

In-wheel Motors for Electric Vehicles

Sichao Yang

Thesis for the qualification of Doctor of Philosophy

Submitted December 2016

School of Electrical and Electronic Engineering

Newcastle University

In memory of Yang Hai 杨海

*Who used to put little Yang on his shoulder
and tell him every secret of the moon and stars*

To Li Xiaoli 李小丽

For your unconditional love and support

ACKNOWLEDGEMENT

I would like to begin by expressing my gratitude to my supervisors Prof. Barrie Mecrow and Dr. Nick Baker. It has been an honour to be your Ph.D. student. I appreciate your contributions of time and ideas to make my 4 years Ph.D. experience productive and stimulating. Your advice and guidance helped me to overcome tough times during this journey. You set good examples for me to look up to and helped me to grow from a fresh *stupid* graduate to an independent researcher. Your good and consistent humour also made each and every Friday's meeting more colourful and less formidable. I am thankful for all the excellent discussions and conversations with both of you.

I also want to thank all of the wise and interesting people whom I had the privilege to meet from the electrical power research group in Newcastle University: Daniel Smith, Richard Martin, Muez Shiref, Kris Smith, Jamie Washington, Juntao Shi, Steven Jordan, Liam Naugher, Ming Zhang, Aslan Jalal, Raihan Nadal, Osama Abushafa, Sana Ullah, Muhsien Yazid, Tahani Al-Mhana and the list goes on. Some of you have thrown me unforgettable quotes and shared your personal stories with me; some of you have cooked and eaten with me; some of you have given me many late night ride home; a few of you have run with me; some of you have stayed in the office with me over numerous weekends and even on one Christmas eve, etc.. Thank you for being part of my life in the past 4 years.

Also, to all of the mechanical workshop technicians, thank you. Without your help, I don't think I have enough fingers to snap while playing with my metal toy.

My gratitude is also extended to the sponsor of this Ph.D. research, the Protean Electric. Thanks for supporting me finically, trusting me and giving me an opportunity to conduct mad academic research and tame my ideas with practicality in an 'industrial sense'. Many thanks to all of you for the discussion and evaluation of my work, including Chris Hilton, Gunaratnam Sooriyakumar, Ioannis Kakavas, Dragica Kostic-Perovic, to name a few.

Lastly, I would like to thank my family for allowing and supporting me to pursue my dream. Grandpa and grandma, you are my biggest fans. Mom, your happy gene helps me to stay optimistic no matter what and thank you for always standing by my side. Isa, I am glad that I have found you here in Newcastle.

ABSTRACT

The in-wheel motor technology as the source of traction for electric vehicles has been researched recently because it is compact and ease-to-integrate. The motor is housed in the wheel. Since the room for the motor is tightly defined by the size of the wheel and there is no gearing system, the motor must have a high torque density to drive the vehicle directly and a high efficiency to keep cool. The existing motor uses a surface-mounted magnet topology. To make it more cost-competitive, the magnet material needs to be reduced while maintaining the torque performance at the rated operating condition. It is the motive of this Ph.D. research.

The thesis starts with a brief introduction on the background of the electric vehicle. Then the major challenges of the in-wheel motor technology are summarised. With the derived specifications, an induction machine and a switched reluctance machine are then simulated and analysed. Still, the permanent magnet synchronous machine is proved to have the highest torque density.

Change from surface-mounted to interior topology, six new magnet topologies are investigated. The V-shaped interior magnet topology shows superior torque-to-magnet-mass ratio and is easy-to-manufacture. It gives 96% torque while using 56% of the magnet mass compared to the existing motor due to the assist from the additional reluctance torque and the lower magnetic circuit reluctance. The key to use less magnet mass while avoiding the demagnetisation is the front iron shielding effect. The analytical explanation on the better resistance to demagnetisation in the V-shaped motor is provided. The magnet loss mechanism is discussed for proper segmentation. Detailed design adjustments are made to compromise between the torque-to-magnet-mass ratio and the manufactural practicality.

Issues regarding to lower mechanical rigidity occurred in initial assembly of the prototype and solutions are proposed. Followed by successful assembly, experimental tests were conducted and results show good agreement with the simulation.

A specific form of torque ripple is found in the V-shaped motor and occurs generally in all fractional-slot concentrated-winding machines with saliency. It is explained by an analytical model. This model is also extended to explain the generally lower reluctance torque in

fractional-slot concentrated-winding machines. Potential design improvements are suggested and simulated for future versions.

TABLE OF CONTENTS

Acknowledgement	iii
Abstract.....	v
Chapter 1. Introduction	1
1.1. Incentive – the role of EVs in a green society	1
1.2. Prior work – Surface mounted PM in-wheel motor	3
1.3. Objectives.....	5
1.4. Structure of the thesis.....	6
1.5. Contribution to knowledge.....	7
1.6. Published work.....	8
Chapter 2. General Background	9
2.1. Electric vehicle.....	9
2.2. Motors for commercially available EV/HEVs.....	12
2.2.1. In-wheel motor v.s. central motor	16
2.3. Challenges of in-wheel motor technology	20
2.3.1. Torque capability – direct-drive mechanism.....	20
2.3.2. Space restriction, positioning	20
2.3.3. Torque quality	23
2.3.4. Fault tolerance - driver safety.....	23
2.3.5. Efficiency and cooling system	24
2.3.6. Speed range – inductance	28
2.3.7. Mechanical aspects.....	28
2.3.8. Demagnetisation.....	29
2.3.9. Design example - the benchmark motor.....	29
2.4. The alternative option – magnet-free/reduced machines	33
2.4.1. Alternative in-wheel machines from literature.....	33
2.4.2. The Induction Machine	37

2.4.3. The switched reluctance machine.....	46
2.5. Conclusion	48
Chapter 3. Design and Improvement	49
3.1. Rotor topologies	49
3.1.1. Surface-mounted topology - optimum split ratio	49
3.1.2. Surface mounted topology - Magnet width, length and the steel filling	53
3.1.3. Alternative rotor topologies.....	59
3.1.4. Conclusion.....	78
3.2. V-shaped Topology Modification	79
3.2.1. Investigation on slot/pole combinations.....	79
3.2.2. Modification based on manufacturing concerns	90
3.2.3. Analysis of structural integrity	93
3.2.4. Conclusion.....	94
3.3. Analysis of Magnet loss and demagnetisation	95
3.3.1. The stator MMF harmonics	95
3.3.2. Magnet loss calculation	101
3.3.3. Magnet segmentation	116
3.3.4. Demagnetisation in in-wheel motors.....	122
3.3.5. Conclusion.....	126
3.4. Optimisation and Finalisation	127
3.4.1. The parameter table of the BMM and V-shaped motor	127
3.4.2. Optimisation of V	128
3.4.3. The final tuning of the V-shaped in-wheel motor	137
3.4.4. Conclusion.....	145
3.5. Parameter Comparison between the BMM and V-shaped motor	146
3.5.1. No load flux linkage	147
3.5.2. Back electromotive force (back EMF)	147

3.5.3. Terminal voltage.....	148
3.5.4. Torque against current alignment angle curve	149
3.5.5. Torque against phase current.....	150
3.5.6. Torque ripple	151
3.5.7. Inductance	152
3.5.8. Torque-speed characteristic curve.....	161
3.5.9. Efficiency map	165
3.5.10. Additional losses	168
3.5.11. the magnet temperature	177
3.5.12. Conclusion.....	179
3.6. Conclusion	179
Chapter 4. Build and Test	181
4.1. Construction of the V-shaped motor.....	181
4.1.1. Introduction	181
4.1.2. The FEA on the V-shape magnets topology	182
4.1.3. Initial assembly and emergent issues	186
4.1.4. Improved methodology	189
4.1.5. Conclusion.....	193
4.2. Test of the V-shaped motor.....	194
4.2.1. Active short current test	194
4.2.2. Drag torque test	196
4.2.3. Back EMF test.....	197
4.2.4. Transient torque test	198
4.2.5. Conclusion.....	199
4.3. Conclusion	199
Chapter 5. Paper Study on Design Improvements.....	200
5.1. Introduction.....	200

5.2. Reluctance torque in fractional-slot concentrated-winding machines with saliency.....	201
5.2.1. A lower reluctance torque in FSCW	202
5.2.2. The stator harmonic effect.....	206
5.2.3. The analytical expression on the flux across the air gap	211
5.2.4. General rules of stator harmonic interaction	214
5.2.5. Design advice on mitigating the torque reduction effect	218
5.2.6. Conclusion.....	218
5.3. Torque ripple analysis.....	219
1.1.1. The RSSH torque ripple forming mechanism	220
1.1.2. Rules for RSSH torque ripple.....	228
1.1.3. Design guidance table with STI	232
1.1.4. Torque reduction in SP selection.....	239
1.1.5. Torque reduction in an FSCW with fixed SP	240
1.1.6. Conclusion.....	251
5.4. Conclusion	252
Chapter 6. Conclusion and Future Work	253
6.1. Conclusion	253
6.2. Future work.....	254
Appendix A: V-shaped motor dimension drawing	257
Appendix B: Inverter control scheme - SVPWM.....	260
Appendix C: Material data	264
Reference	266

LIST OF FIGURES

Figure 1-1 Major OEMs need to cut fleet emissions by ~30% by 2020 to	1
Figure 1-2 Total EV car sales globally, by year [6]	2
Figure 1-3 The hybrid electric car with in-wheel motor traction system	4
Figure 1-4 Protean In-wheel motor exploded view	4
Figure 1-5 The cost breakdown of the BMM	5
Figure 2-1 The components comparison from [20]	9
Figure 2-2 Comparison of carbon dioxide equivalent per mile between electric vehicle and fossil fuel vehicle [25]	10
Figure 2-3 Trending of the price of Neodymium	13
Figure 2-4 EV configuration due to variations in electric propulsion [34]	18
Figure 2-5 The in-wheel motor from Protean Electric and the central motor from Tesla	19
Figure 2-6 Quad-subdivided motor transitioning from cylindrical to toroidal form for better volume specific torque [14]	21
Figure 2-7 The motor shape and its positioning [14]	22
Figure 2-8 2D sketch for the benchmark motor, winding configuration of 1/8 of the full machine shown in the centre.....	22
Figure 2-9 Example of target specification for an EV [45]	26
Figure 2-10 Typical efficiency maps of an induction machine, a switched-reluctance machine, an interior permanent magnet machine and a surface-mounted permanent magnet machine [46]	26
Figure 2-11 Cooling channel of the water jacket.....	27
Figure 2-12 The position of the cooling jacket and the fluid in/outlet	27
Figure 2-13 The demagnetisation test on the BMM – the overload current is 60A and is on the –D axis, the red area is the flux density below the knee point defined at 100°C which indicates the demagnetisation occurred	31
Figure 2-14 The circuit drawing of the BMM	32
Figure 2-15 The phase back EMF at 800rpm	32
Figure 2-16 12/26 segmented-rotor switch-reluctance motors with concentrated-winding. (a) Geometry. (b) Flux path [53]	34
Figure 2-17 Three-dimensional view of 12slot 16 pole axial flux SSRM [54]	34
Figure 2-18 Cross section of 6-stator-segment 5-rotor-tooth Flux-switching Machines: (a) permanent magnet. (b) DC excited. [57]	35

Figure 2-19 A 12slot 10pole flux-switching machine [56]	36
Figure 2-20 Configuration of the claw pole TFM. (a) Conventional claw pole TFM. (b) Novel claw pole TFM [59]	37
Figure 2-21 The torque vs. slip curve for various rotor resistance	38
Figure 2-22 Acceptable λ range in traditional IM design [68]	39
Figure 2-23 Rotor bar selection [69]	41
Figure 2-24 The equivalent circuit of an IM	41
Figure 2-25 the full CR-IM model.....	43
Figure 2-26 The distributed winding from the 8 pole 48 slot combination.....	44
Figure 2-27 The field view of the CR-IM	44
Figure 2-28 The torque, efficiency, RMS voltage and current, power factor against rotor speed of CR-IM	45
Figure 2-29 The switched reluctance models	46
Figure 2-30 The torque against rotor position of different current inputs.....	47
Figure 2-31 The field view of the SRM.....	47
Figure 3-1 The plot of B_g against λ for BMM.....	51
Figure 3-2 The plot of T^* against λ of the BMM.....	53
Figure 3-3 Variables in the benchmark motor: a. magnet length, b. magnet width, c. steel filling.....	53
Figure 3-4 Variables analysis range	54
Figure 3-5 Simplified magnetic circuit for a pole	54
Figure 3-6 Square air gap flux of surface mounted topology	55
Figure 3-7 Magnetic field density plot of magnet length: a. 5mm; b. 2mm at normal operating condition	56
Figure 3-8 The factor K against the variables in THE BMM.....	56
Figure 3-9 The harmonic spectra of the air gap flux density waveforms of models in 180° and 120° magnet span.....	57
Figure 3-10 The torque comparison in models with different magnet width	58
Figure 3-11 Demagnetization analysis on surface mounted motor	59
Figure 3-12 Alternative magnet topologies	60
Figure 3-13 Comparisons between central composite design (CCD), Latin hypercube design and Audze-Eglais design [91]	61
Figure 3-14 The V topology	61

Figure 3-15 The optimisation program.....	62
Figure 3-16 Three methods to form a 3x3 cube using 1/3 of 3^3 experiments [91].....	62
Figure 3-17 The full sampling of a 3x3 cube	63
Figure 3-18 The excel interface	63
Figure 3-19 Peak torque search using static FE simulation.....	64
Figure 3-20 The 3 variables cube – magnet length, rotor outer radius and centre distance	64
Figure 3-21 The field plot of type b with rated current on Q axis, unmagnetised magnets	65
Figure 3-22 Type c. detail geometric view and demagnetisation test	66
Figure 3-23 The field plot of type d with current on Q axis and no magnets.....	67
Figure 3-24 Field plot with Flux flowing direction in V shape design	68
Figure 3-25 The geometrical similarity between C-arc, V and I.....	69
Figure 3-26 Torque vs. current alignment angle	69
Figure 3-27 The torque vs alignment angle in the full V-shaped 16'' in-wheel motor at full load condition ($I_p=30A$ peak).....	71
Figure 3-28 The reluctance torque vs alignment angle in conventional method.....	72
Figure 3-29 The BH curve of the steel lamination in the in-wheel motor model.....	73
Figure 3-30 The programed procedure of the FPT	74
Figure 3-31 Frozen permeability implemented in the reluctance torque calculation	74
Figure 3-32 Torque vs. Current alignment Angle curve in a.) BMM, b.) V-shaped.....	75
Figure 3-33 The demagnetisation area in C-arc	76
Figure 3-34 The demagnetisation area in V-shaped	76
Figure 3-35 The demagnetisation area in I-shaped.....	76
Figure 3-36 The V-shaped magnet with 2mm magnet length	77
Figure 3-37 Magnet utilisation comparison between BMM, I-shaped and V-shape.....	78
Figure 3-38 The geometric drawing of different slot/pole combinations in different topologies.....	80
Figure 3-39 The flux linkage with winding configuration	82
Figure 3-40 The rotor position of the peak back EMF time instant	83
Figure 3-41 The back EMF magnitude difference in each coil	85
Figure 3-42 The coil distribution effect on phase back EMF	85

Figure 3-43 Flux linkage against electric angle in benchmark (surface-mounted) motor BMM.....	87
Figure 3-44 Back EMF against electric angle at 100rpm in benchmark (surface-mounted) motor.....	87
Figure 3-45 The back EMF harmonic spectra in BMM	88
Figure 3-46 The geometric drawing of a.) s9p8 and b.) s9p10 benchmark motors.....	89
Figure 3-47 The torque-speed characteristics of the BMM and the V	90
Figure 3-48 The flux leakage path in the conventional V-shaped magnets	91
Figure 3-49 The V-shaped magnets design variations [98].....	91
Figure 3-50 The field plot of the flux leakage in V – design 5, 6, 7	92
Figure 3-51 Torque performance comparison	93
Figure 3-52 Excitation setup for the magnetic force study.....	94
Figure 3-53 The magnetic force on each piece.....	94
Figure 3-54 A single energised slot from a 9slot, 8pole machine	97
Figure 3-55 The magnet field of single slot on the full machine.....	98
Figure 3-56 H_t distribution in the air gap at an arbitrary time instant	99
Figure 3-57 H_t harmonic spectrum (1st – 52nd) of the 9s8p machine	99
Figure 3-58 The 2nd, 4th and 5th harmonic rotating direction demonstration.....	99
Figure 3-59 The 5 th harmonic magnetic field made from current sheet method	101
Figure 3-60 The magnet loss per pole in a 72s64p surface mounted in-wheel motor....	103
Figure 3-61 The harmonic loss spectrum in a 72s64p surface mounted in-wheel motor	103
Figure 3-62 The equivalent model for the vector potential method	105
Figure 3-63 The H_t field harmonic spectrum of an s9p6 machine	108
Figure 3-64 The loss comparison of an s9p6 machine	108
Figure 3-65 Eddy current loop of 2 nd harmonic in the 72s64p in-wheel motor from FE	110
Figure 3-66 The parameters defined in method 2.....	111
Figure 3-67 Eddy current loop(s) of 5th harmonic in the 72s64p in-wheel motor from FE	113
Figure 3-68 Eddy current loops of 14th harmonic in the 72s64p in-wheel motor from FE	115
Figure 3-69 The magnet loss spectrum.....	115

Figure 3-70 Eddy current loss as a function of the conductor thickness to skin depth ..	117
Figure 3-71 The additional eddy current path introduced after circumferential segmentation.....	119
Figure 3-72 The circumferential segmentation effect on the spatial harmonics	119
Figure 3-73 The circumferential segmentation effect of the 5 th harmonic in 2D field plot	121
Figure 3-74 The 5 th harmonic magnet loss due to the circumferential segmentation in the 72s64p surface mounted in-wheel motor.....	121
Figure 3-75 The total magnet loss due to the circumferential segmentation in the 72s64p surface mounted in-wheel motor	121
Figure 3-76 The demagnetisation prediction for surface-mounted and V models with identical magnet mass in the worst case scenario described in section II (The magnet grade is: Sintered Neodymium-Iron-Boron Magnets – N45SH, the knee point at 100°C is 0.3T.)	123
Figure 3-77 The flux density on the surface of the magnet(s) in SPM and V (the black line is the flux density with the magnets energised; the blue line is when the armature flux from 4th harmonic is opposing the magnet; the red is the worst case scenario with all harmonics included.)	125
Figure 3-78 The flux density plotted with 4th harmonic on –d axis	126
Figure 3-79 The V-shaped motor	127
Figure 3-80 The axial length to outer diameter ratio	127
Figure 3-81 Variables study.....	129
Figure 3-82 The p.u. rated torque response to parameter changes	130
Figure 3-83 Field plot on Q axis at no load of model b. no. 3 and 5.....	131
Figure 3-84 Field plot on Q axis of model c. no.1 and 5	132
Figure 3-85 Optimum magnet position.....	133
Figure 3-86 Magnet length drawing	133
Figure 3-87 Experimental response to magnet length variation	134
Figure 3-88 Magnet width drawing	135
Figure 3-89 Experimental response to magnet width variation.....	135
Figure 3-90 The torque plotted against magnet mass in BMM (benchmark motor) and V	136
Figure 3-91 The air block V drawing	137

Figure 3-92 The torque-speed curve plot of V_32turns	138
Figure 3-93 The torque-speed curve plot of V_30turns	138
Figure 3-94 The torque-speed curve plot of V_11.9mm	139
Figure 3-95 The V with thin back iron	139
Figure 3-96 Drawing example: V2, V3 and V8	140
Figure 3-97 Drawing of V8	140
Figure 3-98 Torque-speed curve of V8 and BMM	140
Figure 3-99 Static demagnetisational resistance analysis	142
Figure 3-100 The bar representation of the worst case scenario	143
Figure 3-101 Transient demagnetisational analysis 1) on BMMr	144
Figure 3-102 Transient demagnetisational analysis 1) on V8	144
Figure 3-103 Transient demagnetisational analysis 2) on BMMr	145
Figure 3-104 Transient demagnetisational analysis 2) on V8	145
Figure 3-105 The rotor geometry in V	146
Figure 3-106 The no load flux linkage in BMM and V	147
Figure 3-107 The phase back EMF in BMM and V at 800rpm	147
Figure 3-108 The line back EMF in BMM and V at 800rpm	148
Figure 3-109 The phase terminal voltage at 800rpm	148
Figure 3-110 The harmonic spectra of the line voltage	149
Figure 3-111 The torque vs current alignment angle in BMM and V	150
Figure 3-112 The torque vs current magnitude in BMM and V	151
Figure 3-113 The torque ripple at maximum torque angle when $I_p=30A$	152
Figure 3-114 The simple magnetic circuit model	154
Figure 3-115 The flux linkage at $I_q=30A$ DC when the magnets are disabled	154
Figure 3-116 The flux sharing path between adjacent phases	156
Figure 3-117 The flux linkage comparison between the actual and the converted one	158
Figure 3-118 The V-shaped motor DQ inductances comparison	158
Figure 3-119 The V-shaped motor torque components comparison	159
Figure 3-120 The flux linkage against current	159
Figure 3-121 The phasor diagram for non-salient and salient rotor in motor mode	161
Figure 3-122 The torque-speed curve of the BMM comparison	163
Figure 3-123 The inductance variation with $I_p=30A$	164
Figure 3-124 Two control methods in FEA	165

Figure 3-125 The starting point of each slice of the torque-speed envelope.....	166
Figure 3-126 The BMM efficiency map.....	167
Figure 3-127 The V efficiency map.....	167
Figure 3-128 The BMM efficiency map provided by Protean	168
Figure 3-129 The stator of the BMM	170
Figure 3-130 The analytical model of the single tooth winding - grey part is the tooth, orange part is the copper conductor.....	170
Figure 3-131 The coil drawing for a phase.....	171
Figure 3-132 The FE model of a half slot copper.....	172
Figure 3-133 The per-unit copper loss in one sub-motor of the BMM	173
Figure 3-134 The skin depth in a circular conductor.....	173
Figure 3-135 The H field loop of the slot flux leakage	175
Figure 3-136 The current density plot of an FE model	175
Figure 3-137 The more accurate FE model	176
Figure 3-138 The AC loss contribution in the total copper loss.....	176
Figure 3-139 field plot of magnet temperature of the BMM and V-shaped motors at rated condition	178
Figure 3-140 magnet temperature vs. time of the BMM and V-shaped motors at rated condition	179
Figure 4-1 The initial rotor assembly attempt	182
Figure 4-2 The V-shape rotor topology with minimised iron ribs.....	183
Figure 4-3 The torque waveforms with DC current input and varying rotor position ...	183
Figure 4-4 The magnetic forces developed on the wedge in the V topology; attraction from the stator tooth and the magnets	184
Figure 4-5 The magnetic force exerted on the magnet in the surface-mounted topology	185
Figure 4-6 Magnetic flux plot in various rotor positions.....	186
Figure 4-7 Force on the wedge at position c.....	186
Figure 4-8 The V-shape slot on the back-iron	188
Figure 4-9 The two channels on the wedge	188
Figure 4-10 The rotor insertion tool	188
Figure 4-11 Illustration on rotor tilting during insertion	189

Figure 4-12 1.a) Improved insertion method – magnets adhered on the wedge prior to the insertion; 1.b) Initial insertion method – magnets adhered on the rotor prior to the insertion; 2.a) the anticipated outcome with a symmetric position; 2.b) the asymmetric position experienced in the initial method.....	191
Figure 4-13 The force for the a. improved method and b. initial method at 1. symmetric and 2. asymmetric positions	191
Figure 4-14 The tool for the push-on method.....	192
Figure 4-15 Rotor insertion with the new adaptor	192
Figure 4-16 The successfully assembled motor.....	193
Figure 4-17 Schematic diagram of the Protean Electric test rig [109]	194
Figure 4-18 The experimental result of the active short circuit test	195
Figure 4-19 The voltage phasor diagram of the short circuited coil.....	196
Figure 4-20 The simulation result of the short circuit test.....	196
Figure 4-21 The experimental result of drag torque test	197
Figure 4-22 Comparison of the simulation and experimental results of the back EMF test	198
Figure 4-23 Comparison of the simulation and experimental results of transient torque test	199
Figure 5-1 Four stator models: A. 48slots, B. 12slots, C. 9slots, D. 6slots	203
Figure 5-2 Double-layer magnets rotor	204
Figure 5-3 Flux plot on Q axis.....	204
Figure 5-4 Rotor modification	205
Figure 5-5 Two checkpoints defined on the graph as torque vs. the current advancing angle	205
Figure 5-6 Torque comparison between four models	206
Figure 5-7 Current sheet model	207
Figure 5-8 Stator Ht harmonic spectra.....	207
Figure 5-9 Torque vs. time with maximum alignment torque of model D.....	208
Figure 5-10 Torque against time with reluctance torque of model D.....	208
Figure 5-11 Torque against the current advancing angle from three models of current sheet	208
Figure 5-12 Torque components breakdown in the p8s12 FSCW	210
Figure 5-13 Torque components breakdown in the p8s9 FSCW	210

Figure 5-14 Torque components breakdown in the p8s6 FSCW	210
Figure 5-15 Hn curve comparison between FE and analytical calculation	213
Figure 5-16 Stator harmonic spectra of FSCWs.....	217
Figure 5-17 Rated torque comparison between 1. V-shaped design with 56% magnet mass, 2. benchmark motor with 56% magnet mass and 3. benchmark motor with 100% magnet mass of 1/8 of the BMM in-wheel motor. Current input condition: $I_q = 30A$ peak, $I_d = 0A$ (rated load).....	220
Figure 5-18 Model O – the original FE model from [43]; model A – the simplified model; model B – the current sheet converted model	222
Figure 5-19 The spatial harmonics of magnetising field strength created by the model A shown in Figure 518	223
Figure 5-20 The sinusoidal rotor	224
Figure 5-21 Torque ripple comparison between model A and B	224
Figure 5-22 The stator H_t harmonic spectrum of the s9p8 machine	225
Figure 5-23 The magnetic field strength H defined in non-salient and salient cases	226
Figure 5-24 Stator harmonic spectrum of a s9p4 FSCW	228
Figure 5-25 Rotor saliency modulation of type A	229
Figure 5-26 Rotor saliency modulation B	229
Figure 5-27 Modulation B in an s9p6 FSCW	230
Figure 5-28 Both modulations in an s9p12 FSCW.....	231
Figure 5-29 Current sheet with rotor saliency of 2 pole, 4 pole and 8 pole rotor.....	236
Figure 5-30 The arbitrarily selected FSCW models	237
Figure 5-31 The torque output of a DC current input and rotating rotor.....	238
Figure 5-32 The torque ripple in the rated operating condition.....	238
Figure 5-33 The four models	239
Figure 5-34 The RSSH component of the torque ripples	240
Figure 5-35 The torque at $I_q = 30A$ $I_d = 0A$	240
Figure 5-36 Rotor skewing with angle $\xi_{cog} = 60^\circ$	242
Figure 5-37 Effect of rotor skewing on cogging torque	243
Figure 5-38 Effect of rotor skewing on the RSSH torque ripple.....	243
Figure 5-39 The 1 st harmonic of the s9p8 FSCW	245
Figure 5-40 Effect of the slot opening width upon the stator magnetising field strength harmonics.....	247

Figure 5-41 Impact of the slot opening upon RSSH torque ripple	248
Figure 5-42 The vector diagram of 11 th and 14 th harmonic	249
Figure 5-43 The uneven slot opening with 11 th harmonic.....	250
Figure 5-44 The RSSH torque output from the 5 th and 11 th harmonics in an s9p8	250
Figure 5-45 The RSSH torque output from all harmonics in an s9p8 current sheet model	251
Figure 5-46 The RSSH torque output from all harmonics in an s9p8 model with actual stator	251

LIST OF TABLES

Table 2-1 Summary of the motors/generators in the key EVs before 2008 [24].....	13
Table 2-2 Data of the most representative EV models on the market after 2008.....	14
Table 2-3 Selected techniques for enhancing heat dissipation in high-speed electric machines (the current density is calculated from RMS value) [47]	28
Table 2-4 The 18'' in-wheel motors data	30
Table 2-5 The recommended flux density in a rotary electric machine	39
Table 2-6 the slot number should be avoided	42
Table 2-7 available rotor slot number [69]	43
Table 2-8 the performance summary of the BMM and IM	46
Table 3-1 The controlled motor parameters from BMM.....	50
Table 3-2 The topology comparison - Notice, the magnet length of the surface-mounted, I-shaped topologies needs to be divided by 2 when compared to C-arc and V because it merges two pieces of C-arc/V to form one	70
Table 3-3 The possible slot/pole combination.....	79
Table 3-4 Torque comparison between s9p8 and s9p10	88
Table 3-5 The geometric parameters in the BMM and V	128
Table 3-6 The designed experimental response to magnet position.....	129
Table 3-7 2D static FE simulation results on magnet length variation.....	134
Table 3-8 2D static FE simulation results on magnet width variation	135
Table 3-9 The data for the 10 designs	141
Table 3-10 The d and q-axis phase inductances	155
Table 3-11 The per-unit inductance.....	155
Table 3-12 The self and mutual inductances	156
Table 3-13 The flux linkage comparison between actual and the DQ converted ones ..	157
Table 3-14 Calculations for the DC copper loss including end-winding	172
Table 3-15 performance summary of the BMM and V-shaped motors.....	180
Table 5-1 Stator harmonic type	228
Table 5-2 The guidance table for SP selection in FSCWs.....	233
Table 5-3 The controlled parameters for all FSCW models. In which, the slot opening ratio is the ratio of the slot opening span to the full slot span.....	236
Table 5-4 The RSSH torque ripple comparison between FE current sheet and STI	236
Table 5-5 The RSSH torque ripple comparison between FE original and STI	238

Table 5-6 The RSSH torque index in an s9p8	250
--	-----

TABLE OF SYMBOLS

EV	Electric vehicle
BMM	Protean Developed 18 inches, benchmark motor
FE	Finite elements
IM	Induction machine
PM	Permanent magnet machine
SPM	Surface mounted permanent magnet machine
IPM	Interior permanent magnet machine
CR-IM	Copper rotor bar induction machine
RMS	Root mean square value
r_{ag}	The air gap radius
l_a	The axial length
I_{rms}	The RMS value of the phase current
N_c	Number of turns per coil
N_s	Number of stator slot
k_w	The winding factor
A	The electric loading
B	The magnetic loading
D_{ag}	Air gap diameter
β	Pitch factor
τ	pole pitch
M_{mag}	The magnet mass
κ	Magnet utilisation factor

K_f	Fill factor
N_{ph}	Number of turns per phase
A_s	The slot area
ρ	Resistivity
B_s	Maximum flux density in the slot
ϕ	Magnetic flux
μ	Magnetic permeability
l_m	Magnet length
T	Electromagnetic torque
p	Pole pair
ψ	Flux linkage
L_q	Q axis inductance
β	Alignment angle
I_p	Peak phase current
θ	mechanical angle
P_{elec}	Electric power
K_p	Winding pitch factor
K_d	Winding distribution factor
ω_e	Electric angular speed
E_c	Back EMF of a single coil
J	Current density
H_t	Tangential magnetic strength
MMF	Magnetomotive force

ν	Harmonic order
λ_s	Slot angular pitch
K_z	The line current
σ	Electric conductivity
A	The magnetic vector potential
w	Magnet width
f_m	Mechanical frequency
g	Air gap length
δ	Skin depth
W_{ag}	Air gap energy
B_r	remanence

Chapter 1. INTRODUCTION

1.1. Incentive – the role of EVs in a green society

The development of internal combustion engine automobiles is one of the greatest achievements of modern technology. However, a highly developed automotive industry and an increasingly large number of automobiles in use around the world is causing serious problems for the environment and for hydrocarbon resources. Deteriorating air quality, global warming issues, and depleting petroleum resources are becoming serious threats to modern life. Hence, more rigorous emissions and fuel efficiency standards from the International Electrotechnical Commission (IEC) [1] have been established in recent decades to stimulate the development of safer, cleaner, and more efficient vehicles. As of 2012, there had been a noticeable gap between the CO₂ emissions of major OEMs and the EU's 2020 target, as is shown in Figure 1-1. It is now well recognised that electric, hybrid electric, and fuel-cell powered drive train technologies are the most promising vehicle solutions [2].

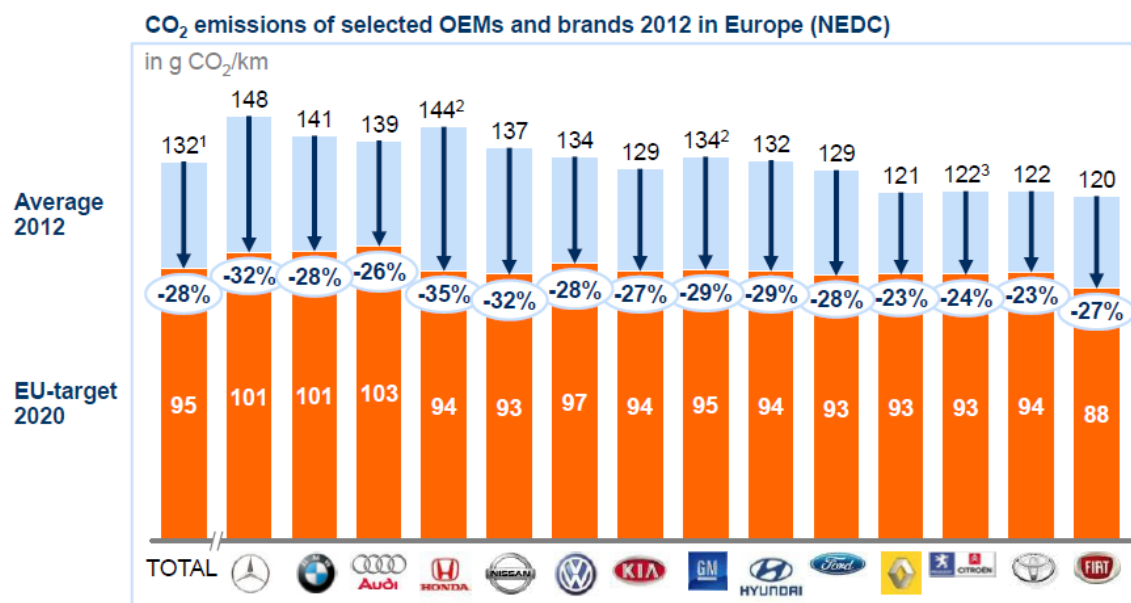


Figure 1-1 Major OEMs need to cut fleet emissions by ~30% by 2020 to meet EU emissions target [3]

Supported by governments worldwide, Electric Vehicles (EVs) have gained great attention due to their high efficiency, zero gas emissions and reduced noise pollution in their driving region. Similarly, major automotive companies have started to produce and sell them in the domestic market at a more affordable price and their performance is now more

comparable to traditional models. In Dec. 2008 [4], the European Commission announced a Europe-wide electromobility initiative, Green eMotion, worth €41.8 million, in partnership with forty-two partners from industry, utilities, electric car manufacturers, municipalities, universities and technology and research institutions. In response, the sale of electric vehicles in the EU-28 has seen exponential growth, as shown in Figure 1-2, the 2015 European Environment Agency report. In 2016, the US Department of Energy (DOE) also announced several financial investments aiming to accelerate the development of Electric Vehicles [5]. Similar government policies are now exercised worldwide.

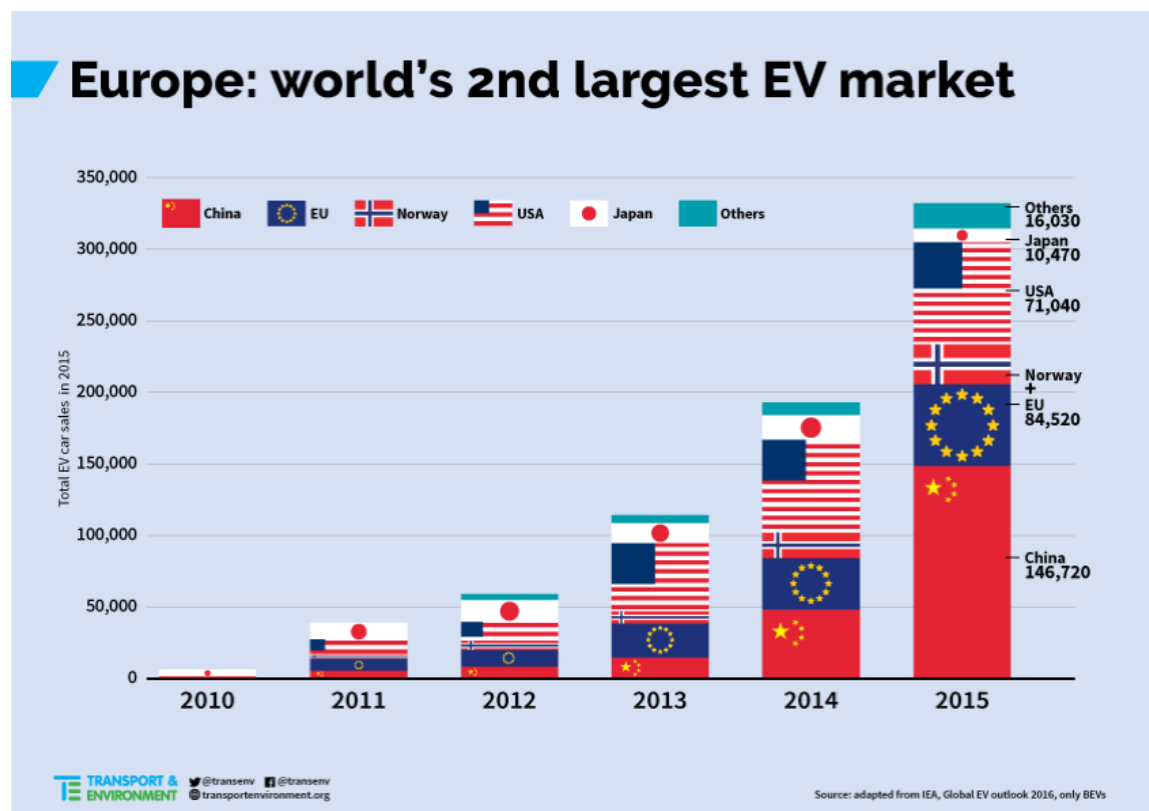


Figure 1-2 Total EV car sales globally, by year [6]

In [7], it is predicted that from 2015 to 2030, on average there will be a 25% growth in the annual sales of compounded zero-emission vehicles worldwide, , so far, more rapid growth has been witnessed in the initial years in China, Europe, Japan, and the U.S. As a result, it is estimated that there will be more than 30 million zero-emission vehicle sales in the four leading markets by 2035, more than 90 million cumulative zero-emission vehicle sales by 2030, and a 35% global zero-emission vehicle sales share in 2035. These goals would roughly translate to 15% of U.S. national automobile usage being from zero-emission vehicles in the four leading zero-emission vehicle markets by 2035.

The energy used to power vehicles is from electricity - a 'secondary energy source'. By switching from an internal combustion engine to an electric motor, dependency on non-renewable primary energy sources – fossil fuels, is broken. Both the UK and China have set a 15% overall target for national energy consumption using renewable sources by 2020 [8, 9] and the US has also set a 20% renewable energy generation target for 2020 [10].

Hence, a change in the type of energy consumption, together with the growth of renewable energy generation, opens up the possibility of having a green and sustainable society. The Electric Vehicle will play a major role in this future society.

1.2. Prior work – Surface mounted PM in-wheel motor

The author's Ph.D. research is based on a collaborative project between Newcastle University Electric Power Group and Protean Electric Ltd. (*Protean Electric is a technology company that has developed an in-wheel electric drive system for hybrid, plug-in hybrid and battery electric light-duty vehicles.*)

There are two major issues in electric vehicle application that need to be addressed. Firstly, the driving range of an electric vehicle is limited by its battery capacity which is much less energy dense compared to fossil fuels: Diesel's specific energy is 48 MJ/kg, whereas it is 0.8 MJ/kg in a Lithium-ion battery [11]. Secondly, the price of the electric vehicle in the current market is higher than traditional fossil fuelled cars. The required high power and torque density combined with the newly introduced super-premium efficiency target [12] has led the majority of designers to use permanent magnet machines along with expensive power electronic inverters and large battery packs.

The first problem has already been tackled in work done prior to this Ph.D. research: the authors of [13] developed this in-wheel propulsion solution for EV applications for its essential merit - integration. By integrating the drive package into the wheels, it frees up the packaging space on the vehicle platform, permitting additional energy storage components or simply more passenger space [14]. By coupling the motor directly with the wheel via an outer rotor arrangement, it ensures that all of the motor torque output is directly available at the wheel, giving the customer better control. Efficiency [15] and compatibility are also improved by eliminating parts of the mechanical design, such as gears and differentials, at a cost to an increase in the size and weight of the motor. It is a high-torque, low-speed, outer rotor permanent magnet motor with a good overload

capability, wide speed control range, and it can also be separated into eight independent sub-motors.

The hybrid electric car powered by the in-wheel motor from Protean Electric is shown in Figure 1-3. Acting as the core of the electric vehicle traction system, the whole package, including the motor, power electronics, brake and capacitors, are integrated into the wheel as is illustrated in Figure 1-4. Inside, the 18 inch' electric motor designed by Protean (the BMM) is taken as the benchmark motor BMM) for this project.



Figure 1-3 The hybrid electric car with in-wheel motor traction system



Figure 1-4 Protean In-wheel motor exploded view

1.3.Objectives

1. The use of permanent magnetic material, produces a high initial cost for the in-wheel motor drive package. According to Protean's cost assessment of the existing in-wheel motor, the magnet cost makes up 23.5% of the total cost, identifying it as the biggest cost contributor of the whole traction package, as shown in Figure 1-5. Hence, finding a way to reduce the use of magnetic material while maintaining its performance sets the major aim of this Ph.D. research.

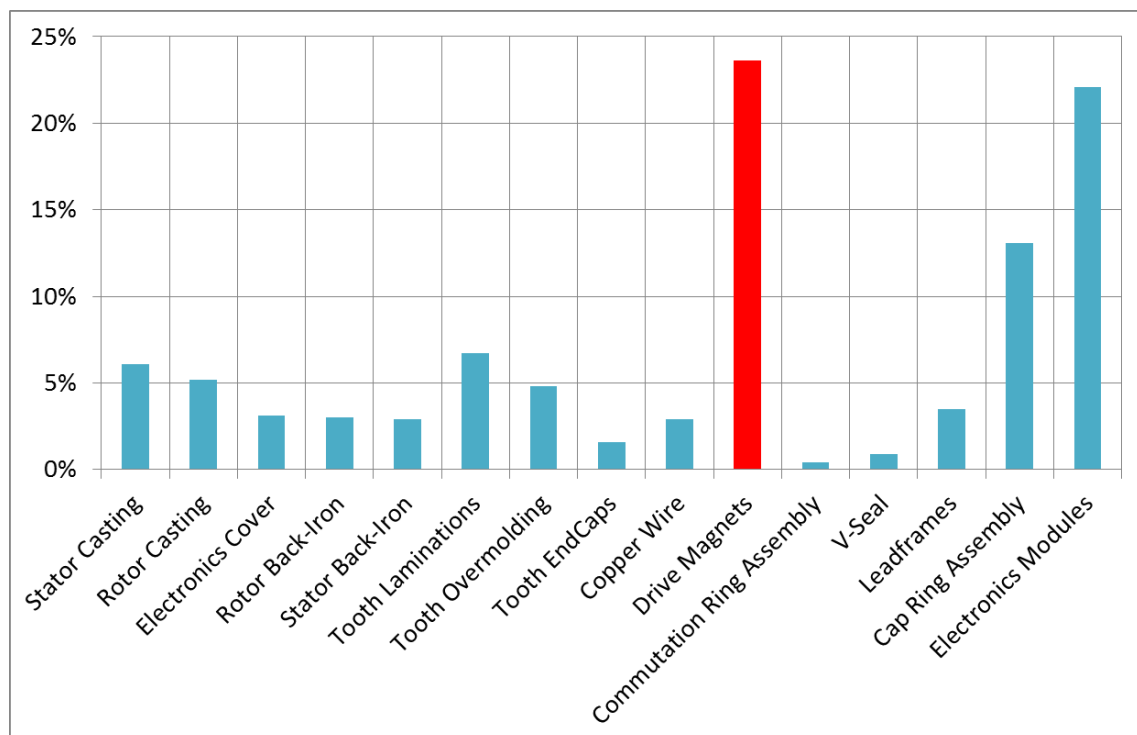


Figure 1-5 The cost breakdown of the BMM

2. The motor needs to provide high torque at acceleration so that it can work at average temperatures close to 100°C with a strong armature field. Demagnetisation needs to be analysed closely and prevented.
3. Because the motor is directly coupled with the wheel, the quality of the torque output can significantly affect driving experience. Hence the torque ripple needs to be kept to a minimum.
4. The efficiency of the next generation motor also needs to be comparable to the BMM.

5. Magnetic loss needs to be minimised in order to prevent an excessive increase in temperature in the magnets.

1.4. Structure of the thesis

This thesis is organised as follows:

In chapter 2, section one, a literature review has been conducted. A report on differentiating the electric vehicle from the internal combustion engine powered vehicle is given. The existing technologies on commercially available EV motors are surveyed. The difference between the in-wheel motor and the central motor is then discussed. In section two, challenges faced by in-wheel motor technology are discussed in detail, including torque capability, space restriction, torque quality (torque ripple magnitude), fault tolerance, operation efficiency, speed range, mechanical integrity and demagnetisation. The surface-mounted in-wheel motor the BMM is taken as an example to be explained. In section three, common magnet-free motor types are researched. A few designs are then tested to see if they meet the torque requirement. An induction motor (IM), and switched reluctance motors (SRM) are presented and compared with the BMM.

In chapter 3, section one, firstly the existing rotor topology from the benchmark motor (BMM) is studied and the optimum split ratio for this topology is calculated analytically. Next, seven alternative rotor topologies are studied to seek a design with the highest torque per magnet mass ratio (Nm/kg). The V-shaped magnet topology is selected. In section two, this V topology is researched in terms of the potential slot/pole combination, the dynamic torque performance is based on the torque-speed characteristic curve and structural integrity. An easy-to-manufacture version of the V motor is selected from several proposed versions. In section three, magnet loss is investigated and demagnetisation resistance is analysed. The rich spatial stator MMF harmonics presented in the air gap have two effects: they generate AC loss in the magnets and they can increase the peak demagnetising field experienced by the magnets. Methods are developed to give greater insight into magnet loss mechanisms, thereby indicating when magnet segmentation is beneficial. The methods are then extended to examine how different rotor designs are affected by both loss and demagnetisation fields, showing major differences between the BMM and V. In section four, the V-shaped motor is further optimised and finalised for practical construction. In section five, the V motor is compared to the BMM in various aspects to show that it matches the benchmark motor's performance: no load flux linkage; back

electromotive force (back EMF); terminal voltage; graph of torque against current alignment angle; graph of torque against current magnitude; torque ripple; inductance; torque-speed characteristic curve; efficiency map; end-winding loss and the AC copper loss.

In chapter 4, section one, the build of the motor is described. Due to the initial construction failure, the influence of removing the steel ribs in the V motor is restudied. This removal poses a significant challenge to the structural integrity of the rotor. New adhesive, assembly tools and insertion methods are then proposed and the V motor is successfully reassembled. In section two, the experimental test results of the V motor are presented against the FE simulation and shown to be a good match.

In chapter 5, it is shown that the V motor (salient rotor) exhibits a higher torque ripple than the BMM. Additionally, a double layer magnetic rotor topology similar to the state-of-the-art BMW-i3 motor is used to demonstrate the significant difference between the achievable reluctance torque of fractional-slot, concentrated-winding and integral-slot, distributed-winding ones. Next, the FE current sheet method is implemented and a theoretical explanation is proposed to reveal the reason behind these two phenomena. Then, general rules are summarised to help retain the reluctance torque capability and reduce the ripple of fractional-slot, concentrated-winding machines. This is done by selecting a certain pole-slot combination and modifying the stator slot-opening width. The concept is demonstrated through modification of the V motor.

1.5. Contribution to knowledge

There are four main aspects of the author's PhD work that are worth mentioning:

1. To reduce magnetic material, V-shaped magnet topology is introduced to replace surface-mounted topology. As a result, the new motor is able to produce a similar rated torque output with 44% of the magnet mass reduction compared to the benchmark motor.
2. The magnet loss in the in-wheel motor is studied in great detail and the V motor is proven to have a higher demagnetisation resistance due to the front iron shielding effect.

3. The torque ripple from stator current harmonics in fractional-slot concentrated-winding machines with saliency is explained in terms of its forming mechanism, effect and treatment.
4. The time-averaged torque from stator current harmonics in fractional-slot concentrated-winding machines with saliency is identified in addition to the well-known alignment and reluctance torque, and its negative effect to the total time average torque is demonstrated.
5. Practical assembly methods are proposed for the V-shaped magnets without retaining bridges.

1.6. Published work

S. Yang, B. C. Mecrow, N. J. Baker, C. Hilton, D. K. Perovic, and I. Kakavas, "Torque ripple reduction in fractional-slot concentrated-winding machines with saliency," presented at the PEMD2016, Glasgow, 2016.

S. Yang, N. J. Baker, B. C. Mecrow, C. Hilton, G. Sooriyakumar, D. Kostic-Perovic, et al., "Cost reduction of a permanent magnet in-wheel electric vehicle traction motor," in Electrical Machines (ICEM), 2014 International Conference on, 2014, pp. 443-449.

S. Yang, N. J. Baker, B. C. Mecrow, D. Smith, G. Atkinson, C. Hilton, et al., "Magnet Losses and Demagnetisation in a Permanent Magnet In-wheel Electric Vehicle Traction Motor," presented at the IEMDC 2015, Idaho, USA, 2015.

S. Yang, I. Kakavas, N. J. Baker, B.C. Mecrow, C. Hilton, D. K. Perovic, "The assembly of a V shape in-wheel motor with reduced mechanical support," presented at the PEMD2016, Glasgow, 2016.

Chapter 2. GENERAL BACKGROUND

2.1. Electric vehicle

In recent years, there has been more and more concern about global warming [16, 17], greenhouse gas emissions and the sustainability of energy sources.

“The atmosphere is a thin shell of gases, particles and clouds surrounding the planet. It is in this thin shell that we are dumping several billion tonnes of pollutants each year. The major sources of this pollution include fossil fuel combustion for power generation and transportation.” [18]

In the transportation sector, international organisations, companies and governments are investing heavily in commercialising the electric vehicle, in an effort to replace conventional fossil fuel vehicles powered by internal combustion engines. There are both political and market demands for electric vehicles (EV).

To start with, this literature chapter will discuss the advantages and disadvantages of the electric vehicle:

Advantages:

- Better driving experience. The electric motor can provide direct torque at a wide range of speeds, it offers smoother and more powerful acceleration without gear changing.
- Little maintenance. There are less moving parts compared to the internal combustion engine [19] which is demonstrated in Figure 2-1.

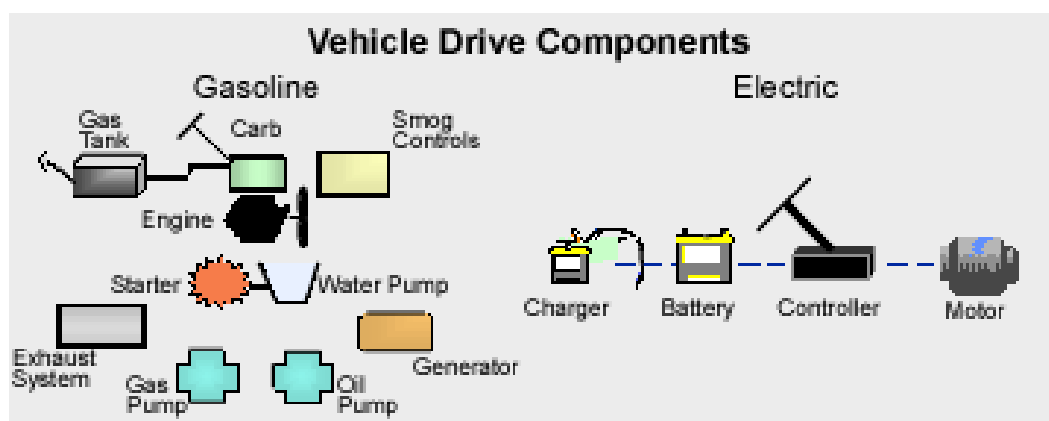


Figure 2-1 The components comparison from [20]

- Lower driving cost. There are many articles [21, 22] suggesting this:

“According to analysis in [23], electric-vehicle drivers can save over \$10,000 on (American) car ownership costs over five years, compared with those driving gas automobiles.”

- Higher efficiency. The drive package of the electric motor and its associated electronics can work at a higher than a 90% efficiency according to the IEC standard [24]. Its regenerative braking can also save more waste energy, compared to gasoline cars, which is especially useful in urban areas where the vehicle is frequently stalled.

Even when taking the energy loss when converting from power plant to EV car battery into consideration, EVs are still generally more efficient compared to conventional cars.

- Zero gas emissions, no local pollution. This is clearly beneficial for big cities with heavy traffic and a dense population.
- According to [25], even when calculating the CO₂ emissions of EVs from well to wheels, it is merely half of that of conventional vehicles. The average carbon dioxide equivalent in grams per mile in the US is shown in Figure 2-2.
- Quiet driving. This is due to its force generation mechanism, which reduces noise pollution in urban areas. If the safety of pedestrians is of concern, artificial sounds could potentially be added [26, 27].

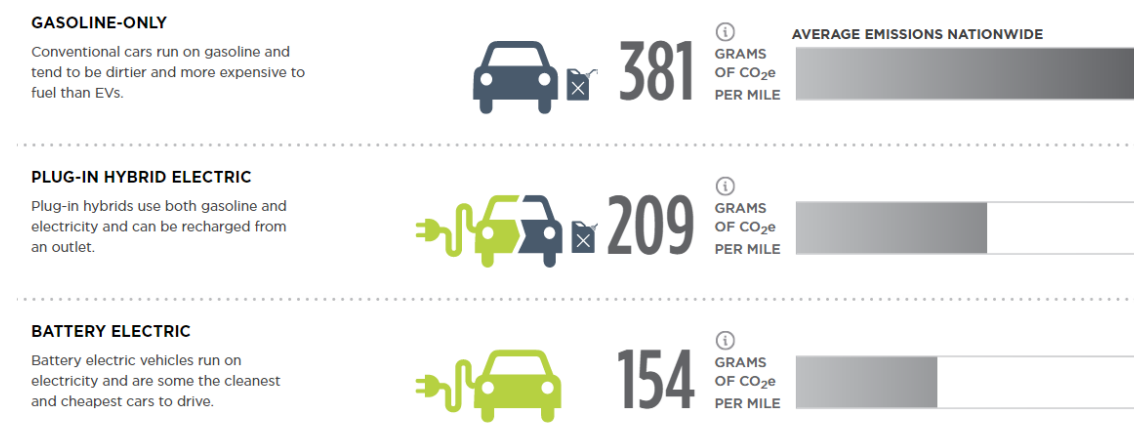


Figure 2-2 Comparison of carbon dioxide equivalent per mile between electric vehicle and fossil fuel vehicle [25]

Disadvantages:

- High initial cost: the initial price of an EV is still higher than its fossil fuel equivalent. To handle this, governments are currently providing various incentives like tax-free purchase policies and subsidies.

From [28]: “ *On June 1, 2010, the Chinese government announced a trial program to provide incentives up to 60,000 yuan (~US\$9,281 in June 2011) for the private purchase of new battery electric vehicles and 50,000 yuan (~US\$7,634 in June 2011) for plug-in hybrids in five major cities.* ”

A high EV manufacturing cost is partly due to battery cost. However, with the development of battery technology, a maturing manufacturing process and an increasing production volume, the price of the battery will likely to keep reducing [29]. Additionally, improved efficiency in late drivetrain, including motor designs will reduce the battery volume required to achieve the same mileage target.

- The battery has a much lower energy storage density compared to fossil fuels. It needs to take up more space and is heavier if the same energy storage capability is desired.

As aforementioned, from [28], the specific energy of the most popular type of automotive battery Lithium-Iron is around 0.8 MJ/kg compared to 48 MJ/Kg from Fuel oil, more than a 50-fold difference.

However, battery density has been improving over the years, as it is put in [30]: “*Since 2008, the cost of Tesla’s battery packs has been cut approximately in half, while the storage capacity has increased by about 60 percent. Tesla didn’t attempt to radically change the chemistry or materials in lithium-ion batteries; rather, it made incremental engineering and manufacturing improvements. It also worked closely with Panasonic to tweak the chemistry of existing battery materials according to the precise needs of its cars.*”

- A lower driving range, due to lower energy storage.

The main focus of the EV is to cover average daily inner-city activities. According to [31], on average, as Americans drive 29.2 miles per day, the average EV model is sufficient. Even for long distance travel, the Tesla Model 3, which is promised to be released in 2017 has a 215mile range. Although this is shorter compared to a 400-mile range from an average fossil fuel vehicle, the average driver would generally not travel

this distance non-stop and the EV can be easily recharged at various road stations while drivers are taking a break.

It is clear that even though the electrification of the fossil fuelled vehicle still currently has some issues, various methods are developing to help break new frontiers. Due to its obvious advantages over traditional technology, it will prevail in due course.






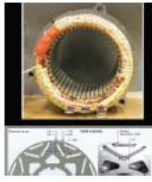


2.2. Motors for commercially available EV/HEVs

At the heart of an electric vehicle lies the electric motor. In order to meet aggressive targets in terms of power density, efficiency and cost of the drivetrain, the current development of the electric motor needs to be studied.

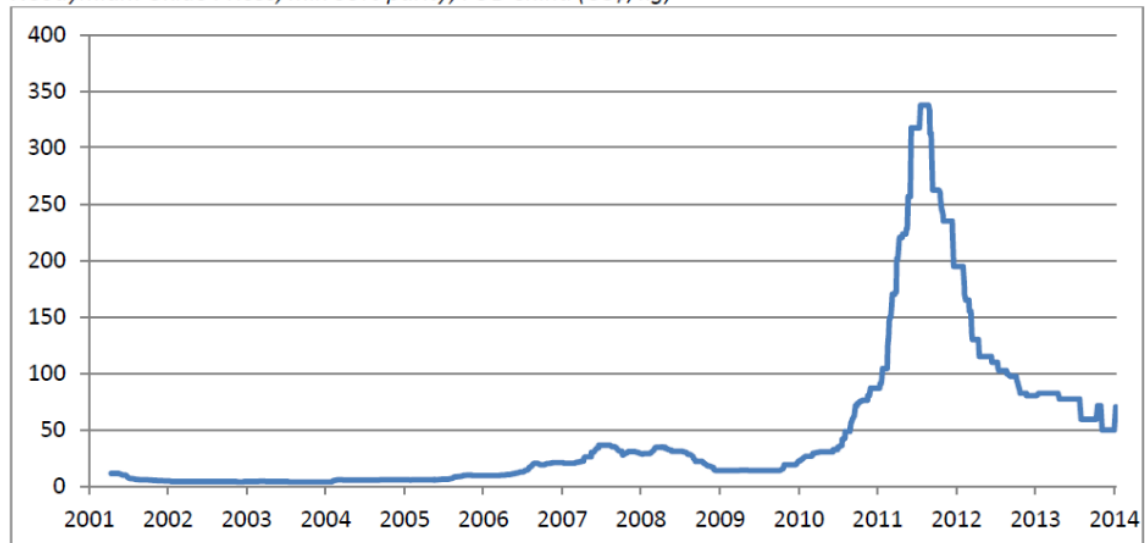
When the power is above 100kW, induction machines tend to dominate. Because the power density requirement is not as rigorous in heavy-duty vehicles, there is generally more space to fit the motor into the vehicle. Induction machines have advantages in terms of partial load efficiency and there are very low drag losses if the machine is running unloaded. Induction machines do not have the issues of fault tolerance (i.e. the braking torque produced in case of a fault) or an uncontrolled generation mode as in the case of a PM machine. However, permanent magnet machines (PM) are the mainstream in terms of medium duty vehicle classes due to their high torque density and efficiency. This is shown in Table 2-1. With the price of Neodymium, the rare earth material for the magnet resettled after 2012 as shown in Figure 2-3, more PMs have been designed in recent EV models such as BMW-i3 and Volkswagen e-Golf in the year 2015 shown in Table 2-2.

Due to space limitation in in-wheel technology, it is both necessary and economically feasible to choose the permanent magnet type of electric machine.

Table 2-1 Summary of the motors/generators in the key EVs before 2008 [24]

Motor/generator				
Vehicle	Honda Insight 2000	Honda Civic 2003	Honda Accord 2005	Honda Civic 2006
Stator	Concentrated winding	Concentrated winding	Concentrated winding	Concentrated winding
Rotor	SPM	SPM	Inset PM	Inset PM
Rating	9.2 kW/83 Nm	12 kW/108 Nm	14 kW/136 Nm	15.5 kW/123 Nm
DC bus voltage	144 Vdc	144 Vdc	156 Vdc	156 Vdc
Motor/generator				
Vehicle	Toyota Camry 2007	Lexus 2005 R × 400h	Toyota Prius 1998	Toyota Prius 2004
Stator	Distributed winding	Distributed winding	Distributed winding	Distributed winding
Rotor	IPM	IPM	IPM	IPM
Rating	105 kW	123 kW	30 kW (33 for 2003)	50 kW/400 Nm
DC bus voltage	244–650 Vdc	650 Vdc	273 Vdc	200–500 Vdc



Neodymium Oxide Prices, min 99% purity, FOB China (US\$/kg)





Source: Industrial Minerals (2012–2014) and Metal Pages (2001–2012)

Figure 2-3 Trending of the price of Neodymium

Table 2-2 Data of the most representative EV models on the market after 2008

Vehicle model	Name	Power rating	Drive motor	Year
	Hyundai Ioniq	87 kW	PM	2017
	BMW i3	125 kW	IPM	2016
	Toyota RAV4	115 kW	IM	2014
	Chevrolet Bolt	150 kW	PM	2017

	Fiat 500e	83 kW	PM	2013
	Nissan Leaf	80 kW	IPM	2011
	Mitsubishi i-MiEV	35 kW	PM	2009
	Kia Soul	81.4 kW	PM	2017
	Ford Focus	107 kW	PM	2011

	BYD e6	160 kW	PM	2011
	Tesla Model S	310 kW	IM	2012

2.2.1. In-wheel motor v.s. central motor

To position the electric motor in the vehicle, the possible configurations are summarised in Figure 2-4. Type f is the in-wheel motor configuration and type c is the central motor configuration. They can be demonstrated by the commercialised models in Figure 2-5.

There are significant advantages with the in-wheel motor configuration:

- It frees up space, otherwise occupied by the central motor on the vehicle platform, permitting additional energy storage components or simply more passenger space.
- The torque of each wheel can be controlled independently, giving better four-wheel drive and response.
- Elimination of gears and differentials produces a simpler and more reliable overall mechanical design and opens up the possibility for a complete vehicle structure redesign.

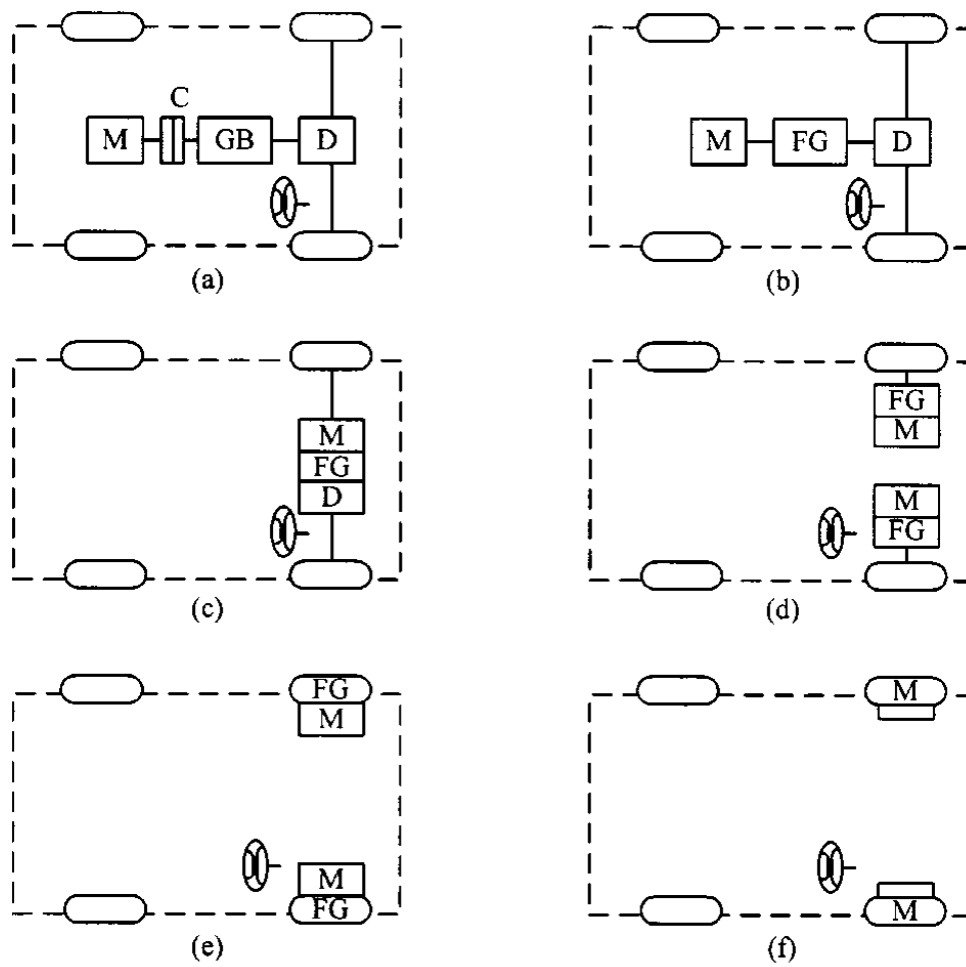
However, as radical as it is, a few concerns arise too:

- Schalkwyk in [32] concluded that there would be a less comfortable driving experience of riding, gripping and handling due to an increase in the vehicle's unsprung mass.

However, as Anderson stated in [33]: While perceptible differences emerge with increased unsprung mass, on the whole they are small and unlikely to be apparent to the average driver. The nature and magnitude of the changes appear to be nothing that cannot be overcome by the application of normal engineering processes within a product development cycle. Conversely, the promise of individual wheel motor control shows good potential for substantial improvements in vehicle behaviour.

- Safety issues when faults occur in the motor, develop an unbalanced torque disturbance. This could be overcome by a fault-tolerant motor design.
- Complicated electronic control and devices are needed to replace the mechanical differential.
- The requirement of high torque density for direct driving and the restriction of space inside the wheel permits only a high level of technology and engineering, meaning the price of two (or four) in-wheel motors would be higher than one conventional, central, bulky motor.
- Potentially higher mechanical failure rates compared to when using a central motor, due to excess vibration, rotor eccentricity and bearing wearing. This would require a more involved mechanical analysis, which is out of the scope of this thesis.

To tackle these aforementioned concerns, the design decisions of the BMM made by Protean will be introduced in the next section.



C : Clutch
D : Differential
FG : Fixed gearing
GB : Gearbox
M : Electric motor

Figure 2-4 EV configuration due to variations in electric propulsion [34]

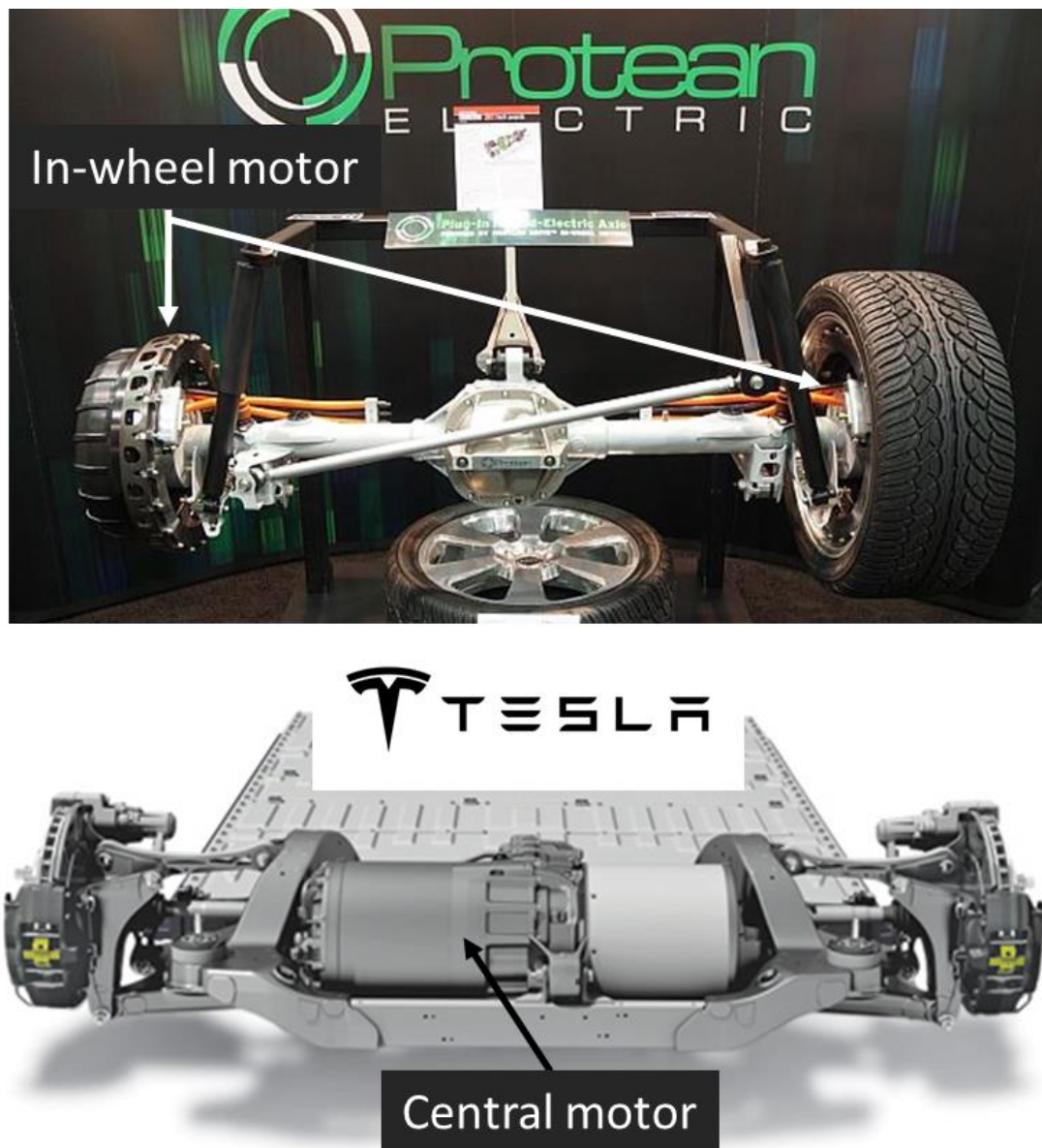


Figure 2-5 The in-wheel motor from Protean Electric and the central motor from Tesla

2.3.Challenges of in-wheel motor technology

In this section, design challenges of the in-wheel motor are firstly discussed in detail, including torque capability, space restriction, torque quality, fault tolerance, operation efficiency, speed range, mechanical integrity and magnet demagnetisation. Then the parameters of the BMM are discussed.

2.3.1.Torque capability – *direct-drive mechanism*

The torque produced by a motor is proportional to the magnetic tangential force and the air-gap radius. The force is proportional to the surface area of the air-gap and the tangential Maxwell stress (BH value). This is because the air-gap flux density B is normally fixed due to saturation, and the H value is related to heat dissipation and is generally determined by the selected cooling method. So, for the same volume and cooling method, the BH value is mostly fixed regardless of its shape, and the torque output is mainly proportional to the motor's active volume.

As there is no gearbox, the torque of the in-wheel motor is directly coupled to the wheel axle and needs to be sufficient for various driving situations. Similarly, if the motor is coupled with the gearbox, it can run at a high speed and generate a low electromagnetic torque while still giving a high shaft torque output after gearing. Hence, the motor volume of the in-wheel motor generally needs to be higher than the high-speed electric motor without considering its associated gearbox. In contrast, the space available to host the in-wheel motor is much more restricted compared to the geared motor.

Therefore, it is necessary to select the permanent magnet machine type due to its widely recognised high torque density in terms of both Nm/Litre and Nm/kg values.

2.3.2.Space restriction, positioning

Torque is proportional to the motor's active volume not its shape. Motors of a different shape but with the same volume produce a similar torque. The active volume of a cylindrical motor can be calculated by its airgap radius r and axial length l , i.e. $\pi r^2 l$. Interestingly, as stated in [14], when the motor shape changes from cylindrical to toroidal, since the active volume $\pi r^2 l$ doesn't relate to the motor's inner radius, the central volume can be removed to increase its torque density (Nm/Litre and Nm/kg values) without affecting its torque output. Hence, a ring-shaped motor topology was chosen as shown on

the right side of Figure 2-6. In order to achieve this shape, a high pole number is necessary to enable low flux per pole and allow small stator and rotor core-back depths.

To couple the motor directly with the wheel and further maximise the air-gap radius, an outer rotor topology was chosen. A surface mounted topology was chosen in the benchmark motor due to its manufactural and control simplicity. Limited by the short axial length, a concentrated winding configuration was selected to give a non-overlapping end-winding, with a minimum inactive axial length. As the minimum manufactural stator tooth segment size is used, this winding configuration also means that the highest possible pole number can be achieved.

The motor's extremely short axial length is due to its unique positioning, sharing the wheel space by sitting parallel with the specifically designed car brake, which is shown in Figure 2-7. The logical reasoning behind this novel brake positioning has been carefully laid out in [14]. The aspect ratio, i.e. overall (active and inactive) axial length to outside diameter, is merely 0.18 in the BMM.

Illustrated in Figure 2-8, A 64 pole, 72 slot combination was selected as a good compromise between frequency-related losses and air-gap radius maximisation. The inner volume of the motor was also removed to reduce weight and save space for other components.

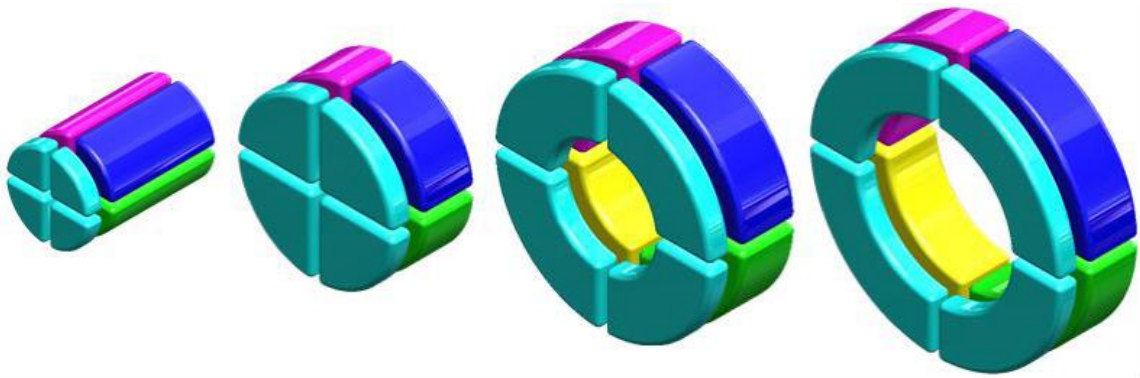


Figure 2-6 Quad-subdivided motor transitioning from cylindrical to toroidal form for better volume specific torque [14]

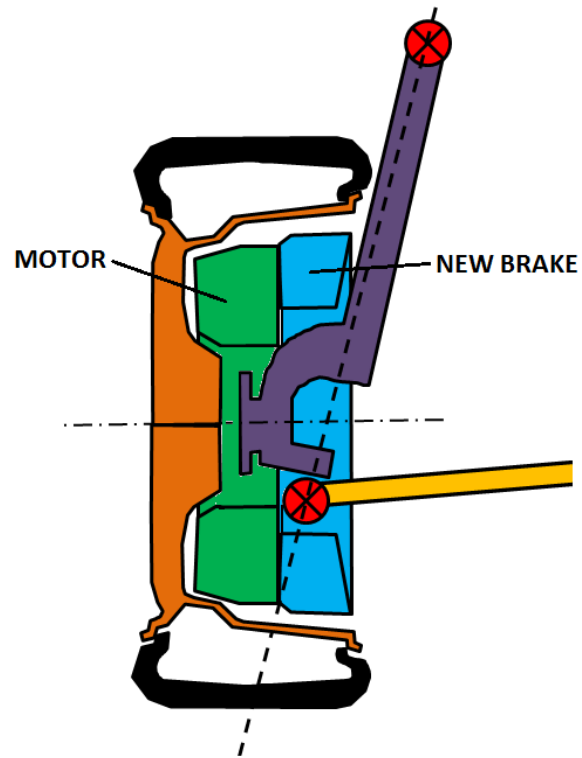


Figure 2-7 The motor shape and its positioning [14]

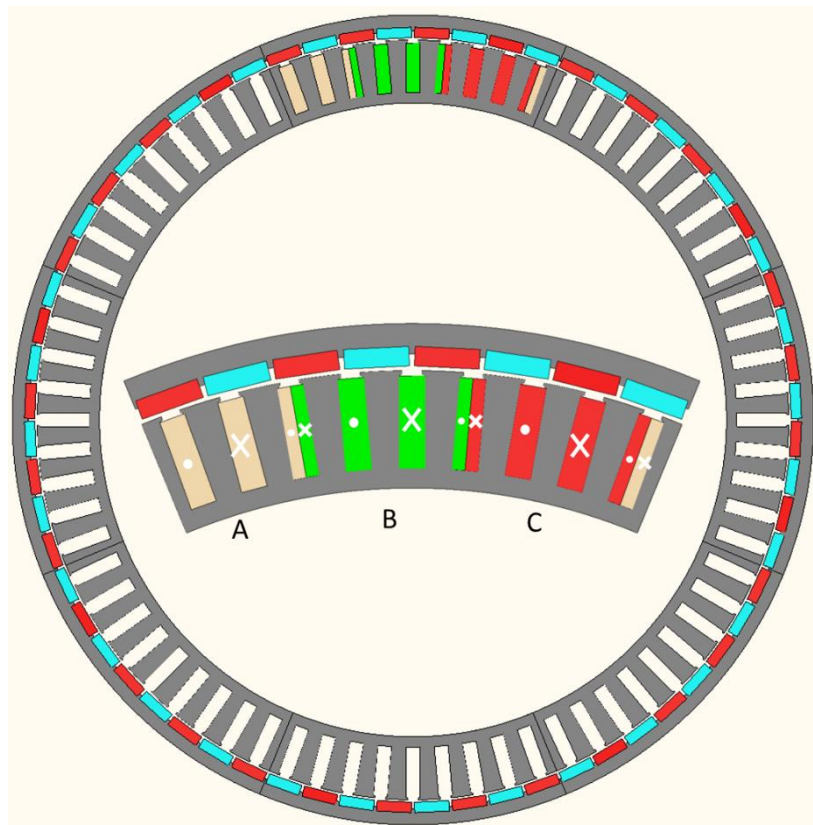


Figure 2-8 2D sketch for the benchmark motor, winding configuration of 1/8 of the full machine shown in the centre

2.3.3. Torque quality

The torque quality affects the noise level of the electric vehicle, but it is much higher in frequency compared to the combustion engine and is easier to be dealt with, as mentioned in [35]. It is also crucial to the driver's driving experience in the in-wheel topology. From Chris Hilton [36], the chief technology officer of Protean Electric: *"The effects of torque ripple from a wheel motor compared to the one from a central motor is different, but it is not clear exactly how or whether one is significantly worse. The driver will feel excessive ripple as vibration at low speeds, and probably as general noise at higher speeds. Depending on the location in the vehicle, different frequencies will tend to transmit through to the driver. A central motor is mounted where the engine is located which will transmit frequencies which I'd guess are of the order of a few 10's of Hz. The ripple will also find its way to the wheel hub to some extent, though everything above about 20Hz would probably get filtered out along the way. Vibration generated in the wheel hub will react back through the suspension which would probably transmit frequencies up to about 20Hz. Neither will affect the handling or safety at the 5-10% level, but they will affect the vibration performance."*

As quoted above, for the same amount of torque ripple on the wheel, there is little difference in terms of the handling and safety of the two motor positions. However, without the damping effect from the flywheel and transmission system, which is usually in cooperation with the central motor or engine, the torque ripple of the in-wheel motor will be directly coupled to the wheel and will need to be kept as low as possible (<2% in the BMM from FE).

The permanent magnet machine type and surface mounted rotor topology permit a low torque ripple. Furthermore, the selection of a fractional number of slots per pole, results in a smaller number of slots for a given number of poles, which is a distinct manufacturing advantage and is also conducive to a low cogging torque.

2.3.4. Fault tolerance - driver safety

According to [37], due to the traction force of the vehicle being developed separately from two or four wheels in the in-wheel motor drive system, it is extremely susceptible to single point failure developing an imbalanced torque among wheels. To prevent this type of

failure, the motor design must incorporate a high level of fault tolerance. There are a few directions to consider.

Firstly, the faulty parts need to be easily isolated from the healthy rest. As discussed in [38-41], the multi-phase (more than three phase) design and single layer winding (i.e. alternative teeth winding) can help to improve the fault tolerance capability by decoupling the phase flux and current from each other. However, a multi-phase motor needs to be driven by a specially designed multi-phase inverter or a few standard three-phase inverters combined. Hence, the electronic power cost is higher in these designs.

Secondly, the magnitude of the faulty current and torque need to be limited. By increasing the phase inductance using a fractional-slot concentrated-winding (FSCW) configuration, the faulty current can be reduced to a level that is not too much higher compared to the rated current ($<150\%$), the level which can cope with the rest of the healthy parts. Because of the rich harmonics from the stator winding in FSCW, the harmonic leakage inductance is much higher than that of a distributed-winding configuration. Hence the total phase inductance is much higher in FSCWs, e.g. the inductance in the 12slot-14pole motor is 6.56 times higher than the one in the 42slot 14pole motor with an equal magnet flux linkage [42].

In the case of the BMM, as can be seen in Figure 2-8, the whole motor is split into 8 sub-motors, each has 9slots and 8poles. They can then be powered by 8/4/2 inverters depending on the level of independence specified. Within each sub-motor, the flux of each phase is confined to three consequent teeth. The surface-mounted magnet topology along with the winding configuration also gives a high inductance to limit faulty currents. This arrangement offers sufficient fault tolerance capability, i.e. when any sub-motor(s) fail the rest would continue to work and compensate the torque loss. Testing of the thermal, mechanical and electromagnetic independence of each sub was conducted in the work prior to this project [43].

2.3.5.Efficiency and cooling system

As energy density in batteries is much lower than that of fossil fuels, both the space for energy storage and energy consumption efficiency is vital to an EV system. Also because of limited space, it is very important to reduce the loss (increase the efficiency) and remove the loss-associated heat from the motor via an effective cooling system.

Efficiency is important at the system level for all speeds. At present EVs are best suited to an urban drive cycle representative of a typical sub-urban daily commute. The frequent operating areas for the drive are located at the low speed, low torque region and are demonstrated as a dotted-line-enclosed box in the torque against speed envelope shown in Figure 2-9. Through comparing the induction machine, interior and surface-mounted magnet machines and switch reluctance machine in Figure 2-10, it can be seen that the permanent magnet machine has the highest efficiency overall and at the targeted region. Though its efficiency is largely reduced at high speed due to iron loss, it is not a concern for a direct-drive low-speed in-wheel motor. Hence, the permanent magnet machine type was selected to maximise the efficiency of motor operation.

The cooling system of the in-wheel motors is a liquid jacket pumped with glycol. As can be seen from Figure 2-11 of the current design, it has two cooling channels, one is inside the stator and one is on the axial side of the stator and next to the inverter modules. Its position and in/outlet are marked in Figure 2-12. Table 2-3 shows a comparison of cooling techniques in high speed electric machines, in which it is suggested that machines with a current density in the range of 10-15 A/mm² should adopt the liquid jacket cooling technique. The calculated current density of the BMM is 19.44. With careful design from Protean Electric, the cooling jacket has been made to work more efficiently than that quoted in literature and is capable of handling this level of current density on the stator. However, with both cooling channels on the stator, it is relatively difficult to remove rotor loss. This means the rotor loss needs to be minimised. The temperature of the surface-mounted magnets in the benchmark the BMM is measured at under 100°C for any given condition [44].

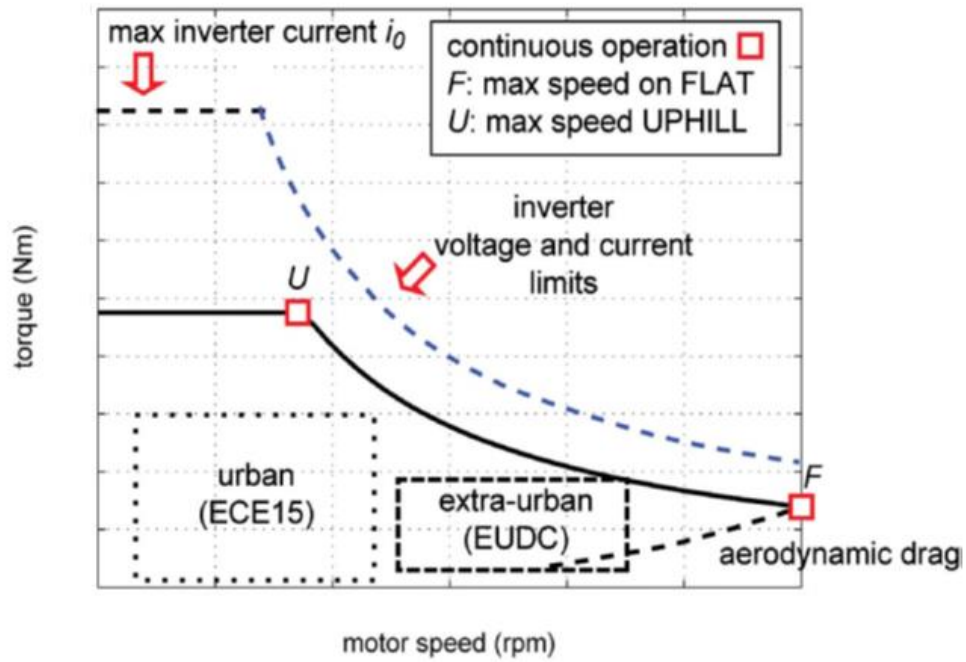


Figure 2-9 Example of target specification for an EV [45]

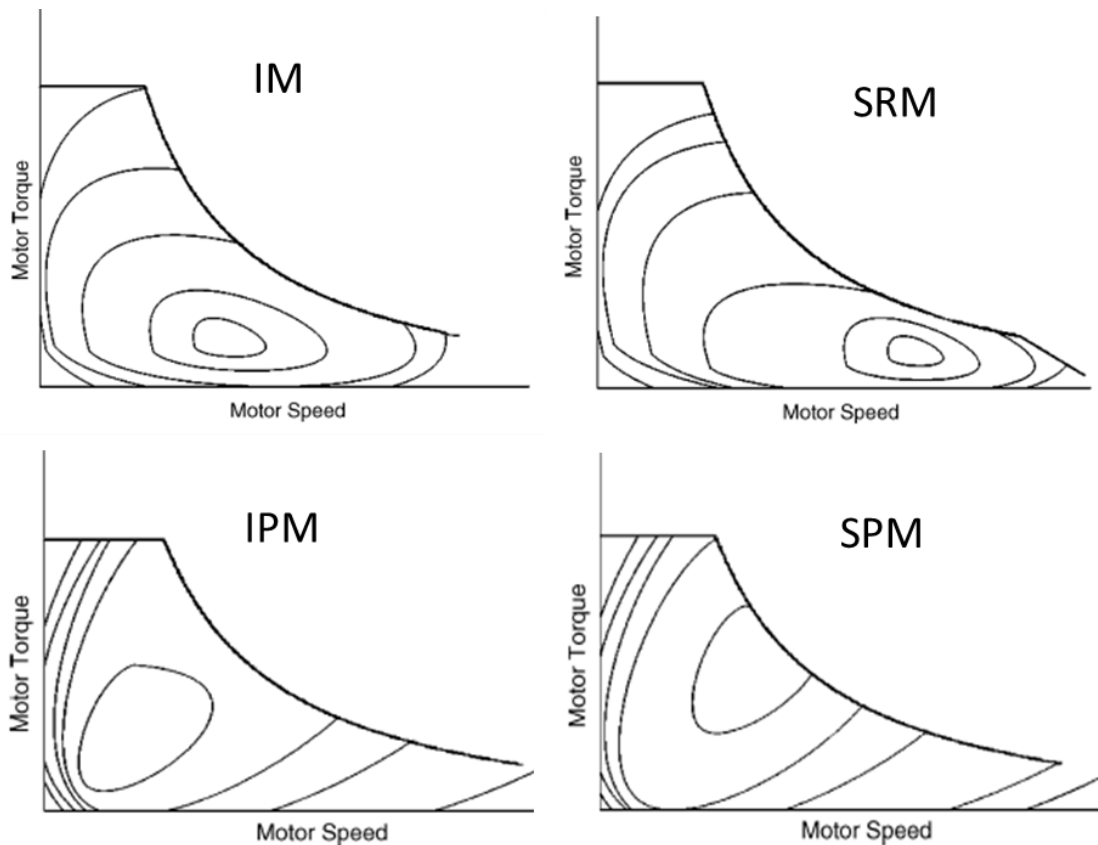


Figure 2-10 Typical efficiency maps of an induction machine, a switched-reluctance machine, an interior permanent magnet machine and a surface-mounted permanent magnet machine [46]

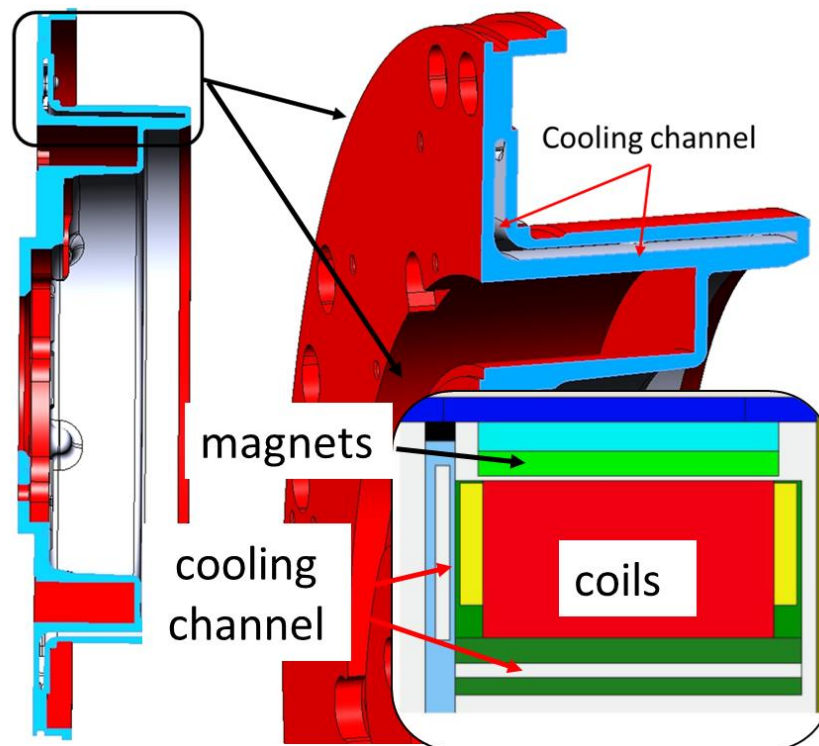


Figure 2-11 Cooling channel of the water jacket

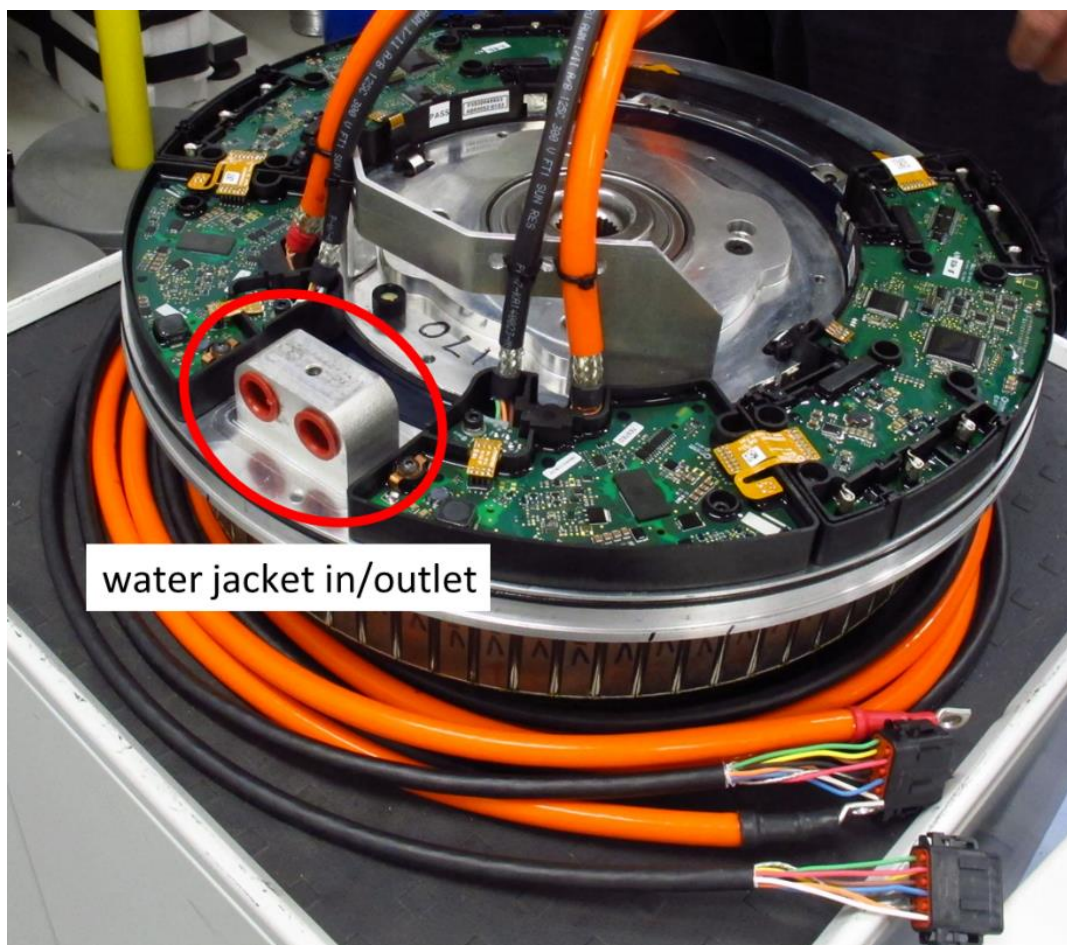


Figure 2-12 The position of the cooling jacket and the fluid in/outlet

Cooling system	Current density A/mm ²	Advantages	Disadvantages
Fins and heat sinks	5 to 8	Simple method	Increase in weight and size
Water or oil jacket	10 to 15	Effective stator cooling	Increase in diameter and weight
Direct liquid cooling and hollow conductors	up to 30	Very intensive cooling of the stator winding	Increase in weight and size Too expensive for machines rated below 200 kW
Spray oil-cooled end turns of rotor winding	over 28	Very intensive cooling of the rotor winding	Wet rotor; contamination of cooling medium (oil) with time
Liquid cooled wedges [166]	8 to 15 (estimated)	Intensive cooling of rotor winding	Does not effectively cool the rotor poles
Cold plates between poles and rectangular wire rotor winding (IPS)	about 22 (estimated)	Intensive cooling of rotor winding	Requires installation of cold plates in rotor and cooling medium circulation

Table 2-3 Selected techniques for enhancing heat dissipation in high-speed electric machines (the current density is calculated from RMS value) [47]

2.3.6.Speed range – inductance

Because it is a direct drive system, the speed range of the motor is not as demanding as that of a high-speed motor with gearbox. The top speed for the BMM is 1600rpm equivalent to 140km/h on the tyre which is the average value of a light-middle class vehicle. However, it can still be beneficial to have a long constant power region when cruising at high speed. By selecting the fractional-slot concentrated-winding (system), a significant increase in phase inductance can be achieved, which facilitates constant power operation over a wide speed range with flux weakening control.

2.3.7.Mechanical aspects

The mechanical study is out of the scope of this thesis. Two main issues are briefly discussed here:

The vibration magnitude of the permanent magnet machine is generally lower than machine types like the switch reluctance machine. A high pole number can also further reduce the radial attractive force per pole. Additionally, in the BMM, the greatest common divisor of the slot and pole number is an even number, which indicates there is no imbalanced radial force for vibration.

To withstand the centrifugal force developed while rotating, thin iron ribs or a full shrink-fitted ring are normally used if it is an internal rotor. However, for this application, outer rotor topology is used meaning the centrifugal force can be counteracted by the rotor housing. Plus, it rotates at a low speed developing a low centrifugal force. So there are few centrifugal related issues.

2.3.8.Demagnetisation

In order to have a high flux density, a neodymium iron boron magnet is selected due to its high residual flux and coercivity. However, this type of material can be demagnetised when its temperature is above 100°C and the opposing flux is strong. The grade of the magnet used in the BMM is N45SH and its characteristic curve is shown in Appendix C. The magnet will be demagnetised at a temperature of 100°C if the flux density of the magnet is below 0.3 T. The magnet temperature is largely related to its loss and cooling. The flux level in the magnet can be drastically repressed if: a. flux weakening is applied at the constant power region; b. there is a faulty condition and the flux generated by the shorted stator coil is opposing the magnet directly. Since the measured magnet temperature in the BMM can reach to 100°C, potential demagnetisation issues in the new design need to be carefully analysed.

2.3.9.Design example - the benchmark motor

The benchmark motor is presented here to demonstrate the design solutions for the challenges discussed. This motor has been designed, manufactured, tested and marketed by Protean Electric to fit into an 18inch wheel. Specifications are summarised in Table 2-4 with FE models shown in Figure 2-8.

Table 2-4 The 18'' in-wheel motors data

Continuous DC Voltage Supply	320	V
Discontinuous DC Voltage Supply	400	V
Continuous Current density in Slot (RMS)	19.4	A/mm ²
Discontinuous Current density in Slot (RMS)	38.9	A/mm ²
Rated Output Torque	695.2	Nm
Corner Speed	728	rpm
Rated Output Power	53.0	kw
Top Speed	1600.0	rpm
Control Strategy	SVPWM	
Cooling Method	Water Jacket	
Magnet Type	NdFeB-N45SH	
Steel Type	Non-Oriented Silicon Steel_M330-50A	
peak continuous phase current	30	A
coil turns	32	-
Magnet Length	5	mm
Magnet Working Temperature	100	deg
Active Axial Length	58.8	mm
Outer Diameter	386	mm
Inner Diameter	302	mm
Air Gap Diameter	364	mm
Air Gap Distance	1	mm
Slot Number	72	-
Pole Number	64	-
magnet mass	2.38	kg
motor weight (based on 2D motor)	20.12	kg

The torque output

The torque output is related to electric loading, magnetic loading and machine volume by eq. (2.1):

$$\begin{cases} T = \sqrt{2}\pi r_{ag}^2 l_a k_w AB \\ A = \frac{2N_c I_{rms} \cdot N_s}{2\pi r_{ag}} \end{cases} \quad (2.1)$$

Where r_{ag} is the air gap radius; l_a is the axial length; I_{rms} is the RMS value of the phase current; N_c is the turns per coil; '2' on the nominator increases with the assumption that a slot is shared by two coils, i.e. double-layer winding; N_s is the number of the stator slot; k_w is the winding factor; A is the electric loading i.e. linear current density with unit A/m; and B is the magnetic loading, i.e. the peak fundamental flux density generated by the

magnet travelling across the air gap with unit Wb/m^2 . The value of B is normally set at about 0.9~1.2 Tesla for high torque density machines, which is normally half of the stator tooth flux density limited by the saturation level of the steel lamination. $k_w = 0.945$ for both winding configurations.

The torque value of the BMM can be estimated analytically assuming that $B=1$. It is 698.9Nm, which is close to the finite element result, 695.2Nm, shown in Table 2-4.

The magnet mass

The current magnet mass in the BMM ensures that the magnet works properly at 100°C with a maximum armature field opposing the excitation field. When reducing the length of the magnet from 5mm to 3mm the demagnetised area is clearly increased.

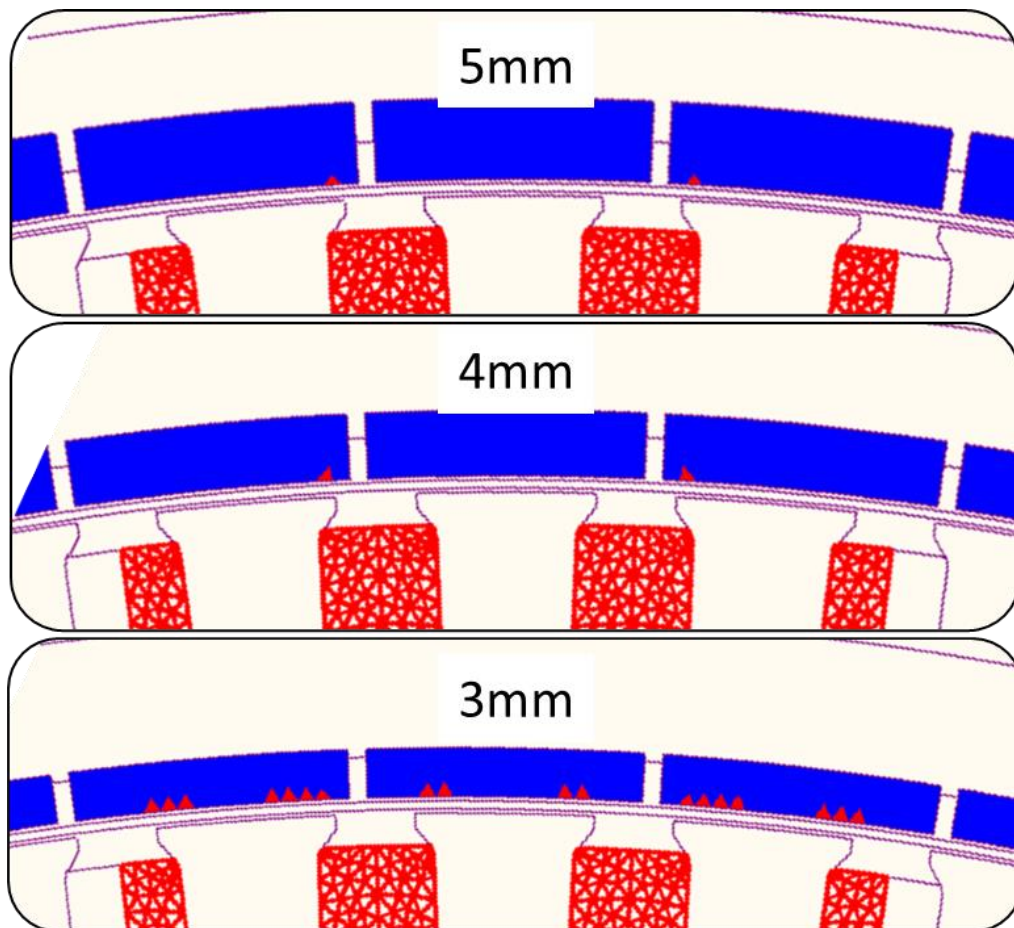


Figure 2-13 The demagnetisation test on the BMM – the overload current is 60A and is on the -D axis, the red area is the flux density below the knee point defined at 100°C which indicates the demagnetisation occurred

The speed requirement

As illustrated in Figure 2-14, there are 8 parallel circuits, each sub-motor is connected with a inverter and powered by the full DC voltage source. The use of multiple inverters helps to increase the speed range and also raise the fault tolerance capability of the BMM at a sacrifice to increased electronic costs. The top speed is 1600rpm in the BMM and the corner speed is 800rpm. The back EMF of one phase, per sub-motor at corner speed is shown in Figure 2-15, which is just within the limits of the maximum DC supply voltage 320V.

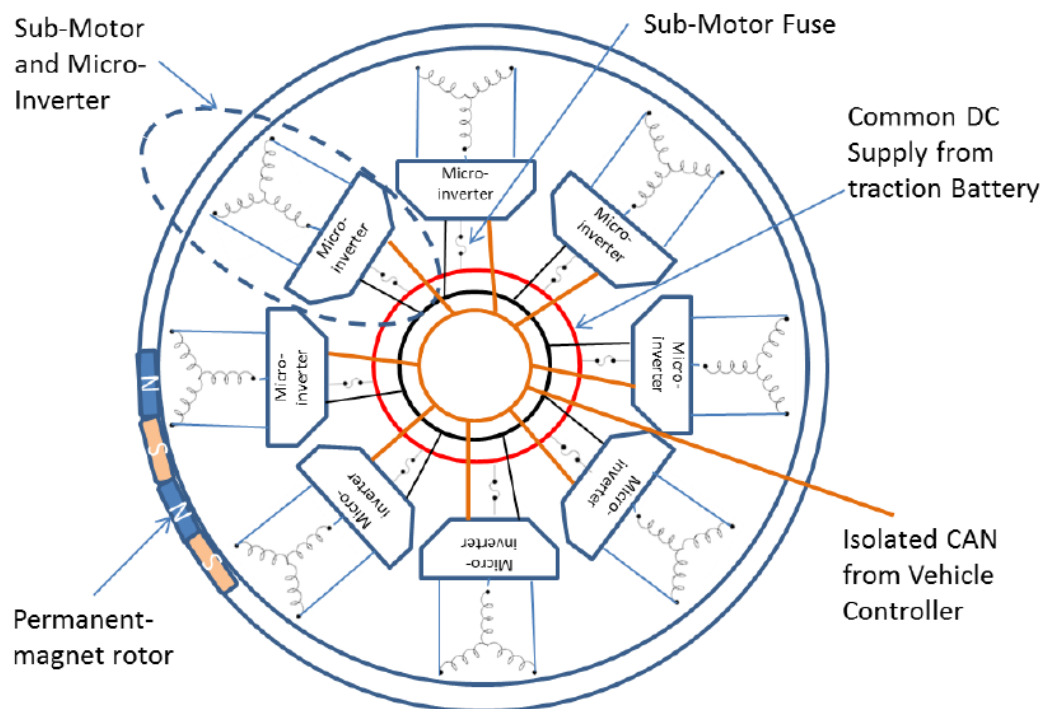


Figure 2-14 The circuit drawing of the BMM

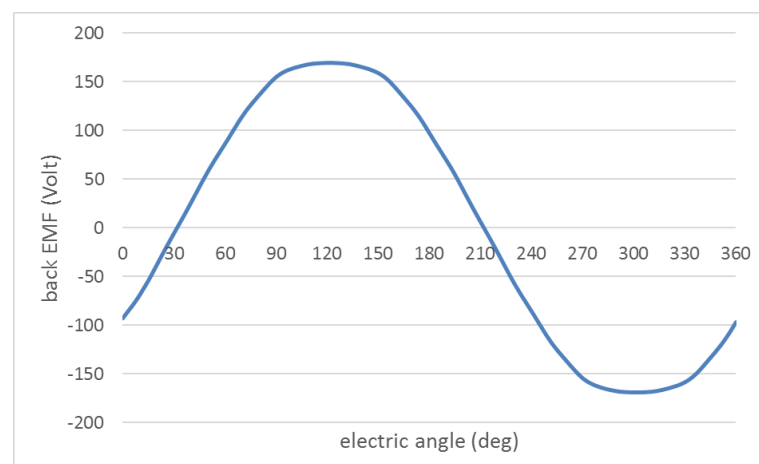


Figure 2-15 The phase back EMF at 800rpm

Different design challenges associated with in-wheel motor application have been discussed. The logical process of designing the existing benchmark motor has been demonstrated in detail. In the next section, a few different machine types will be investigated to seek alternative options.

2.4. The alternative option – magnet-free/reduced machines

In this section, the most common magnet-free/reduced machine types for the in-wheel application are discussed and an attempt is made to compare the designs with the BMM. An induction machine and a switched reluctance machine with similar dimensions are designed and presented.

2.4.1. Alternative in-wheel machines from literature

In-wheel motor technology has been being researched since 1994 [48]. But there is still no commercialised model. Protean Electric, one of the leading companies in this technology, recently opened up a manufacturing factory in TianJin, China in 2016 – a promising sign on its commercialisation [49]. As stated previously, permanent magnet electrical machines are typically the preferred choice in automotive traction applications due to their good torque density and high efficiency. The permanent magnet outer rotor is chosen by all three leading companies on in-wheel motor technology - Protean Electric [50], Elaphe [51], Ecomove [52]. However, the price of these motors is often unacceptable for the automotive market, furthermore, fluctuation in the price of rare earth permanent magnets generates uncertainty and could potentially prohibit long-term design planning. Work on alternative machine types for this application continues. Some designs with physically constructed machines are discussed here:

In Figure 2-16, a segmented-rotor switch-reluctance machine is presented. By using a high number of rotor segments and concentrated winding, the efficiency and torque density is higher than the conventional switch-reluctance machine. Its air-gap radius is also maximised using outer rotor positioning similar to the BMM. The central part of the rotor can also be removed similar to the BMM to further improve the Nm/KG value. However, the torque ripple is still a limiting factor, even with the current chopping method, which is 30% of the average torque in [53].

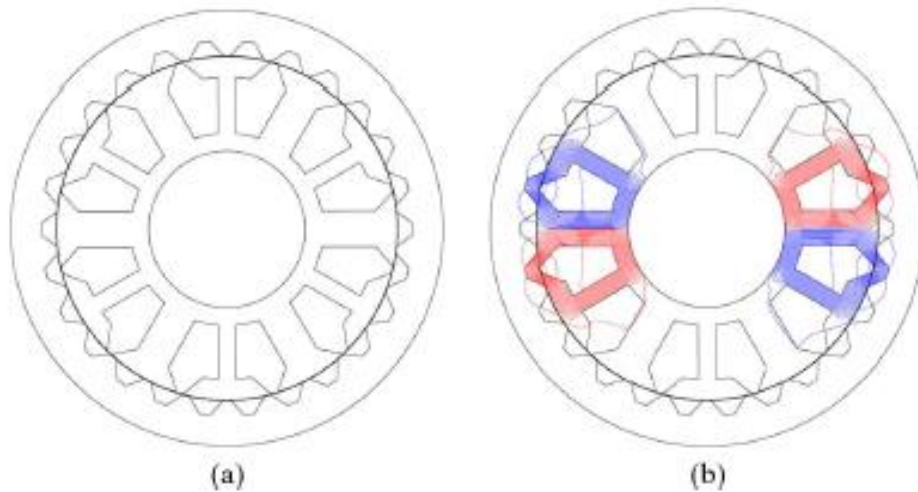


Figure 2-16 12/26 segmented-rotor switch-reluctance motors with concentrated-winding. (a) Geometry. (b) Flux path [53]

The switched reluctance machine can also be implemented on the axial flux machine with dual rotor design, as is shown in Figure 2-17. The flux in this type of machine can travel through the middle part and link both sides in a single circuit. As a result, higher torque density can be achieved by removing the flux return path on the middle part. However, its reported torque density is still lower than the permanent magnet machine.

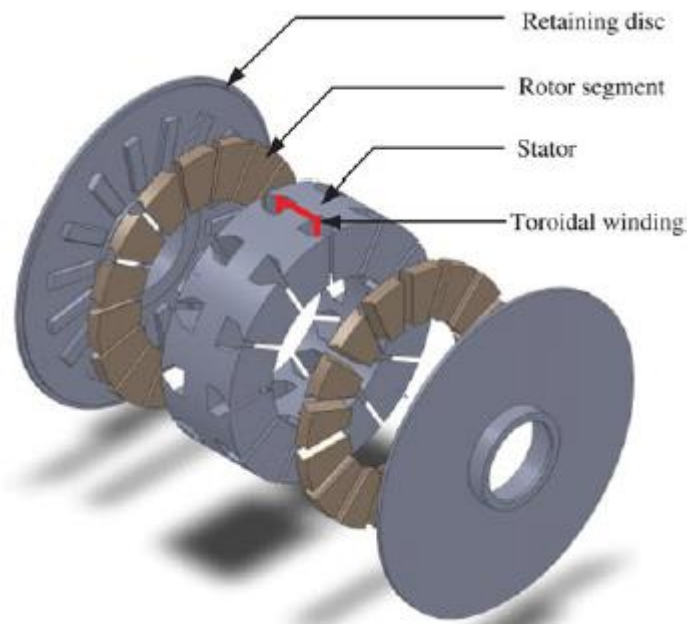
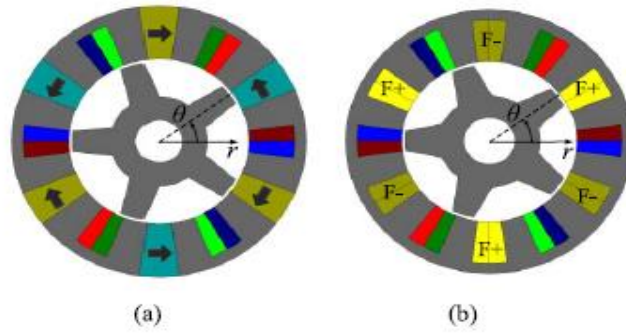


Figure 2-17 Three-dimensional view of 12slot 16 pole axial flux SSRM [54]

Another type of machine is the flux-switching machine. There are many topologies on this type of machine [55], however, the governing principle is the same: shifting the rotor excitation to the stator, which can be seen from Figure 2-18 - the field windings (or permanent magnets) are located in the stator with the armature winding. It combines the

advantages of the high torque density of the SM and the robust rotor structure of the SRM by placing permanent magnets or field windings in the stator. Furthermore, in a flux-switching permanent magnet machine, as shown in Figure 2-18a, the thermal condition of permanent magnets is significantly improved as they are effectively cooled by the stators outer surface, while in a dc-excited flux-switching machine, as shown in Figure 2-18b, the brush is eliminated, thus all the problems caused by the brush in conventional dc-excited machines are solved. However, the additional field winding on the stator reduces the room available for armature winding and tends to have a more complex winding configuration: The end winding length is circa 50% of the overall axial length in [56], shown in Figure 2-19.



*Figure 2-18 Cross section of 6-stator-segment 5-rotor-tooth Flux-switching Machines:
(a) permanent magnet. (b) DC excited. [57]*

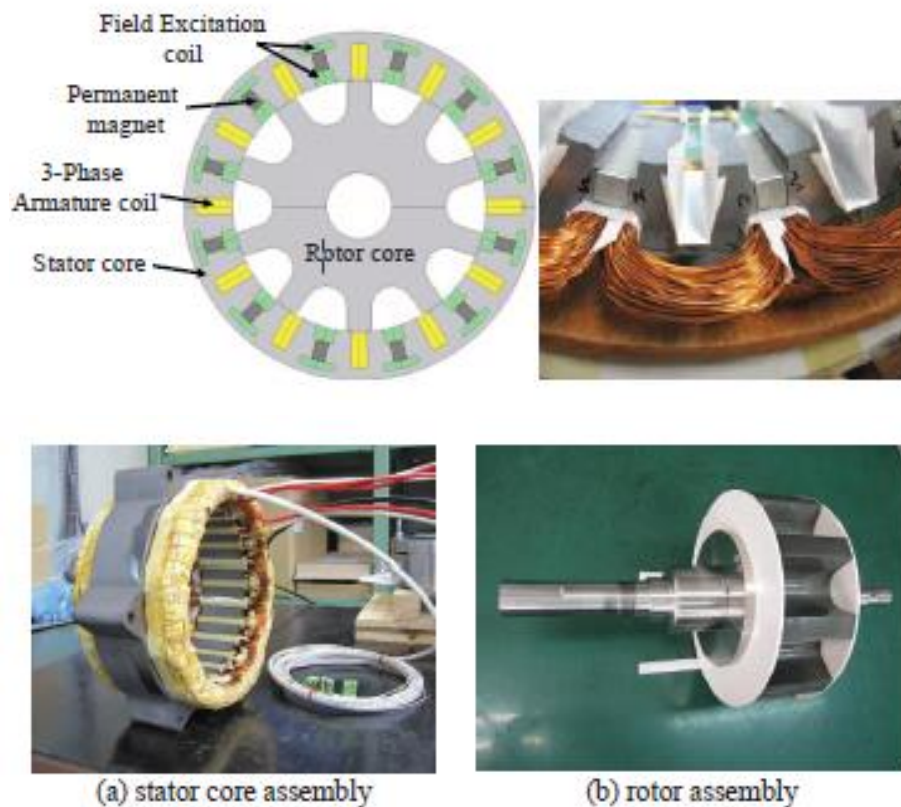


Figure 2-19 A 12slot 10pole flux-switching machine [56]

Finally, the transverse flux machine is known for its high torque density due to the decoupled nature of the electric and magnetic circuits of the machine. In other words, a lower magnet mass can be used to achieve the same torque target. In conventional machines, a doubling in the pole number will lead to a reduction in the armature magnetomotive force per pole of the same proportion. This is due to a reduced slot area leading to a decrease in torque output. In transverse flux machines however, the coil does not share the same circumferential area as the flux path and the magnetomotive force is seen across all of the poles. An increase in pole number does not decrease the available slot area, leading to a corresponding increase in electrical loading and therefore an increase in the torque. In Figure 2-20, a transverse flux machine is demonstrated. It is clear that the structure is complicated, which in turn would increase the manufacturing cost. Furthermore, it is low in power factor due to its unduly high magnetic inductance [58], which means the achievable corner speed of the machine is much lower for the same terminal voltage rating.

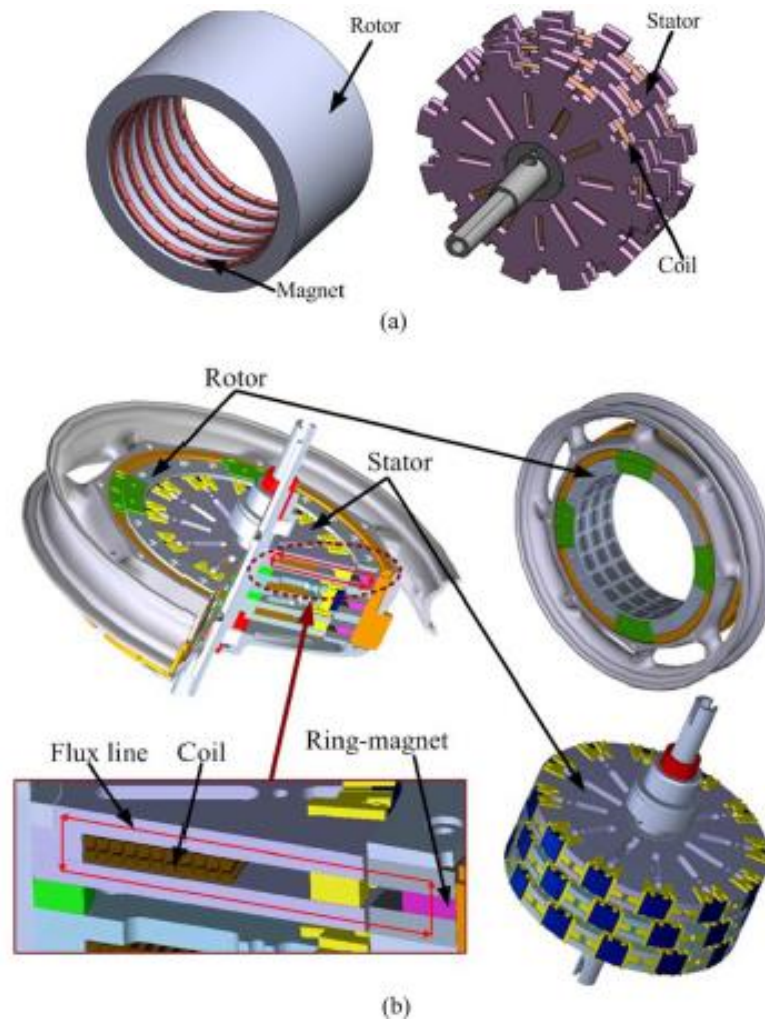


Figure 2-20 Configuration of the claw pole TFM. (a) Conventional claw pole TFM. (b) Novel claw pole TFM [59]

In conclusion, the above magnet-free/reduced machine types have some clear disadvantages against the permanent magnet machine. In order to compare their torque capability directly with the BMM, in the following sections, the technologically-matured machine, the induction machine and the conventional switched-reluctance machine are chosen to sketch some primary designs from and their torque output from FEA are demonstrated. The outer rotor diameter and the stack length are kept the same as the BMM.

2.4.2. The Induction Machine

The induction machine proposed, maintains identical spatial, electronic and thermal constraints to that of the BMM. Conventional inner rotor topology is used for a simpler design process.

Induction machine design

The induction machine is designed with the following considerations:

- a. The induction machine type offers a lower cost solution, however, it's comparatively lower efficiency, power density and power factor is less desirable according to Zeraoulia in [60]. The copper rotor bar induction machine (CR-IM) has been researched recently in [61-63] showing superior efficiency over the traditional aluminium cage. In [64], a copper rotor induction machine is reported to have an equal performance compared to the THS II PM machine from Toyota Prius. This can be explained by the graph in Figure 2-21, the lower the rotor resistance, R_r , the lower the slip of the maximum torque, hence the higher the efficiency will be. It is chosen for the in-wheel IM design. The materials for the stator, rotor core and the winding will be kept the same as the BMM.

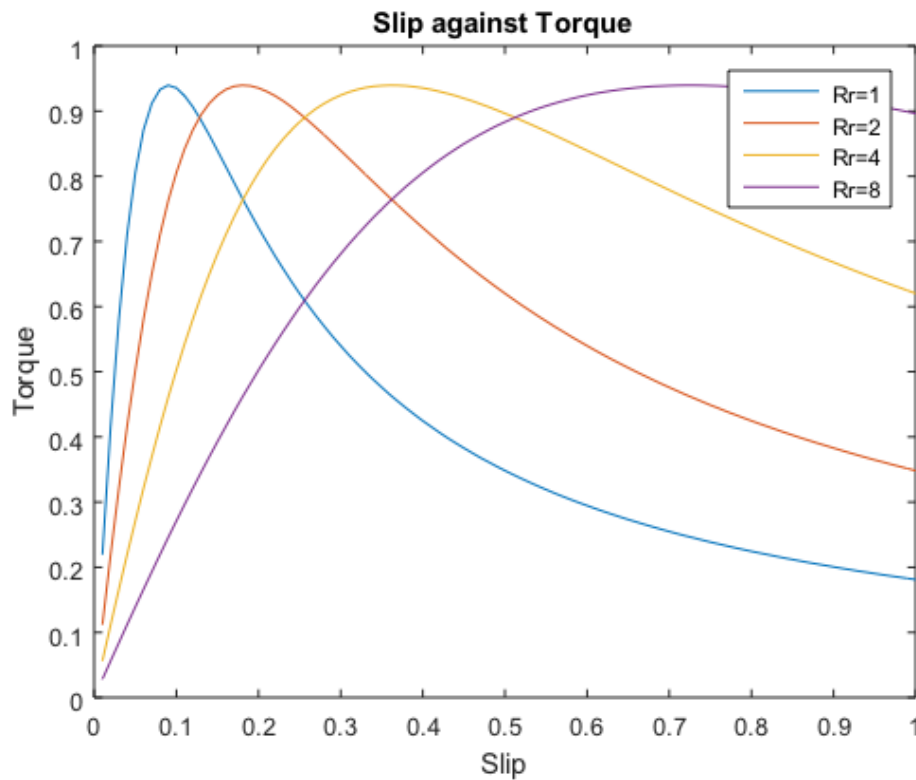


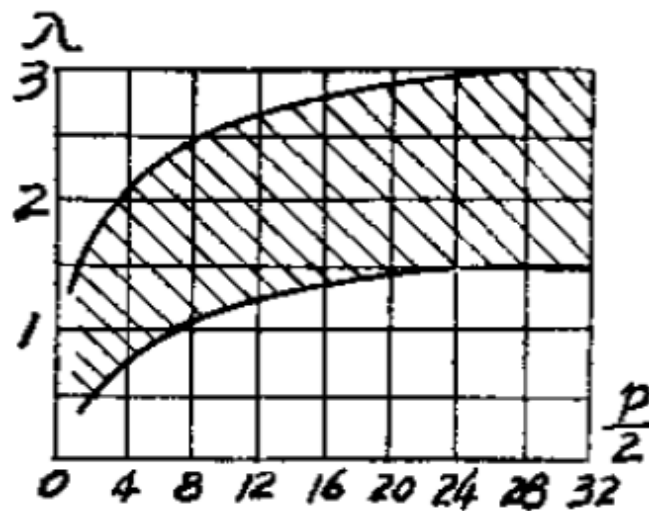
Figure 2-21 The torque vs. slip curve for various rotor resistance

- b. Due to a high torque density demand and rigorous dimension restrictions, the value of the air gap flux density must be maximised while keeping the losses and temperature increase within a tolerable limit. After checking the recommended values from data in Table 2-5, the average air gap density in IM is targeted as 0.9T.

Table 2-5 The recommended flux density in a rotary electric machine

Position	Typical flux density range [65]	Maximum flux density [66]
Airgap Bg	0.65 – 0.82 T (Avg)	0.9 T
Stator yoke	1.1 – 1.45 T	1.7 T
Stator teeth	1.4 – 1.7 T	2.1 T
Rotor yoke	1.2 T	1.7 T
Rotor teeth	1.5 – 1.8 T	2.2 T

- c. Traditionally, in order to achieve good acceleration/deceleration when starting, i.e. reducing the machine inertia, the rotor radius should be kept small with a long stack length [67]. However, if the stack length is too long, the torsional force of the shaft would be too large. The aspect ratio $\lambda = D/L$ (outer diameter/axial length) normally ranges from 0.5 to 1. The pole number can then be selected based on the D/L ratio from Figure 2-22. Though in this design exercise, because the size of the motor is predefined, the aspect ratio is fixed to a 400mm outer diameter over 58.8mm active stack length.

Figure 2-22 Acceptable λ range in traditional IM design [68]

- d. In order to achieve a comparable torque density, the distance of the air gap in the induction machine should generally be smaller than that in the BMM. Bearing in mind thermal expansion and manufactural tolerance, 5 mm has been chosen for the CR-IM.

- e. The slot area in the CR-IM has been increased using a deeper slot compared to the BMM to improve the electric loading. Consequently, the air-gap and inner rotor diameter are reduced.
- f. The cooling method is kept the same as the BMM which leads to a fixed copper loss. The peak value of the phase current is calculated in eq. (2.2) for the CR-IM. A is the slot area, N is the number of slots and n is the number of turns per coil. The slot fill factor is identical in both machines.

$$I_{IM} = I_{BMM} * \sqrt{\frac{A_{IM}}{A_{BMM}} * \frac{N_{BMM}}{N_{IM}} * \frac{n_{IM}}{n_{BMM}}} \quad (2.2)$$

- g. The rotor bar shape, illustrated in Figure 2-23, determines the rotor reactance and resistance in an equivalent circuit as shown in Figure 2-24, which in turn determines the torque output by eq. (2.3). The torque against slip curve with a different rotor resistance value is calculated analytically and plotted in Figure 2-21 to show that a lower resistance gives a lower slip at maximum torque. There are various types of rotor shapes: a.) deep, parallel sided rectangular bar, b.) doubly-casted, deep bar, c.) round tooth tip tapered bar d.) straight tooth tip tapered bar, f.) circular or semi-circular bar, e.) closed type bar, etc. Amongst them, many fast design modifications have been made. The d type bar shape has been adopted mainly because the tooth width can be kept even from top to bottom to ensure minimum local flux saturation. The average width of the bar is determined by the tooth flux level from Table 2-5. Increasing the depth of the bar can reduce the rotor resistance which improves the torque, but also increases the reactance, which in turn reduces the torque. So the depth of the bar is a compromise between these two values.

$$T = \frac{3sE_r^2 R_r}{R_r^2 + s^2 X_r^2} \frac{1}{\omega} \quad (2.3)$$

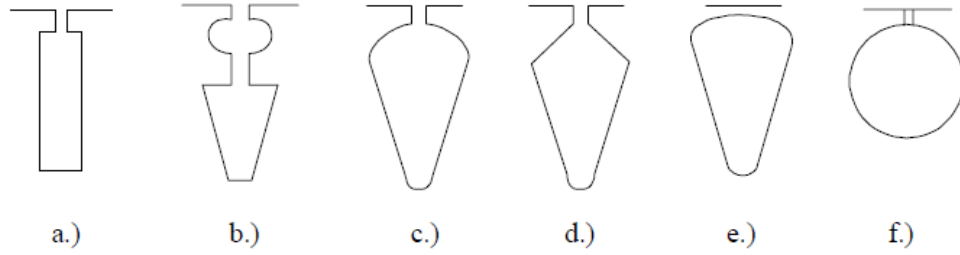


Figure 2-23 Rotor bar selection [69]

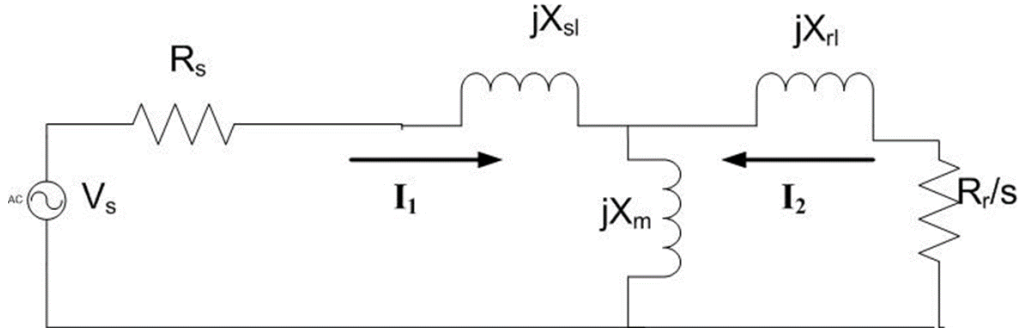


Figure 2-24 The equivalent circuit of an IM

- h. With a higher pole number, the rotor and stator core back can be reduced. However, a smaller pole number can have a lower switching frequency, which leads to a lower electronic cost and smaller losses, and a smaller magnetising current per pole. The equation (2.4) taken from [70] shows the phase magnetising inductance of an unsaturated machine, where l_{ag-ef} is the effective air gap length. In this equation, the inductance is inversely proportional to the square of the pole pair for a given air gap diameter (D_{ag}). Consequently, the torque output is inversely proportional to the pole pair number, since $T \propto pL$. Therefore, in order to achieve a higher torque, a low number of pole pairs should be selected [71], which is contradictory to the space restriction. Looking through literature on high torque SRMs, and IMs, none of them (both) possess a stator slot number higher than 50 and have a good torque density, which further supports this analytical reasoning.

$$L_m = \frac{mD_{ag}}{\pi p^2 l_{ag-ef}} \mu_0 l_a (k_{w1} N_s)^2 \quad (2.4)$$

- i. The fractional-slot concentrated-winding (FSCW) for the BMM is not applicable to the CR-IM. It has been found that there are much higher losses in the FSCW IMs due to rich asynchronous travelling stator harmonic content in [72]. A five-phase FSCW IM has been constructed and tested in [73] to reduce the harmonic content.

However, despite an increased fault tolerance and a reduced core loss and torque ripple, the power density is reduced and both the complexity and copper loss are increased. Hence, distributed winding is selected despite the fact that it is long end-winding: the slot number is 48 and the pole number is 8 making it 6 slots per pole.

- j. Since the winding is distributed, the end winding will be longer than that of the BMM. It can be calculated by an empirical expression (2.5) which has been developed by manufacturing companies and presented in [69]:

$$\begin{cases} l_{end} = 2.y - 0.04 \text{ for } 2p = 2 \\ l_{end} = 2.y - 0.02 \text{ for } 2p = 4 \\ l_{end} = \left(\frac{\pi}{2}\right).y + 0.018 \text{ for } 2p = 6 \\ l_{end} = 2.2.y - 0.012 \text{ for } 2p = 8 \\ y = K_p \tau \end{cases} \quad (2.5)$$

Where K_p is the pitch factor and τ is the pole pitch.

- k. Taken from [66] the rotor slot number selection principle is demonstrated in Table 2-6, a bad choice could cause noise, vibration, cusps in torque speed curve and cogging problems. The rotor slot number has been chosen as 58 from Table 2-7.

Table 2-6 the slot number should be avoided

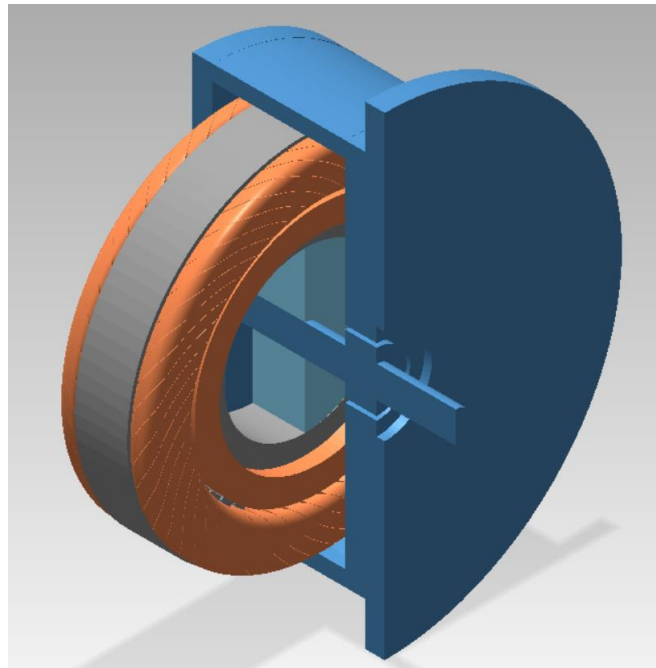
Noise or vibrations	$S_1 - S_2 = \pm 2, \pm(p \pm 1), \pm(p \pm 2)$
Cusps in torque speed curve	$S_1 - S_2 = \pm p, -2p, -5p$
Cogging problem	$S_1 - S_2 = 0, \pm mp$

Table 2-7 available rotor slot number [69]

$2p$	N_s	N_r
2	24	18, 20, 22, 28, 30, 33, 34
	36	25, 27, 28, 29, 30, 43
	48	30, 37, 39, 40, 41
4	24	16, 18, 20, 30, 33, 34, 35, 36
	36	28, 30, 32, 34, 45, 48
	48	36, 40, 44, 57, 59
	72	42, 48, 54, 56, 60, 61, 62, 68, 76
6	36	20, 22, 28, 44, 47, 49
	54	34, 36, 38, 40, 44, 46
	72	44, 46, 50, 60, 61, 62, 82, 83
8	48	26, 30, 34, 35, 36, 38, 58
	72	42, 46, 48, 50, 52, 56, 60
12	72	69, 75, 80
	90	86, 87, 93, 94

FE modelling of the CR-IM and its results

In a semi FE software *MotorSolve*, *Infolytica*, the induction machine has been modelled and the results are shown here. In Figure 2-25, the full model of CR-IM is shown and the winding configuration from the template is demonstrated in Figure 2-26. The flux field plot of the CR-IM is shown in Figure 2-27 and the saturation level decided in the previous section is validated.

*Figure 2-25 the full CR-IM model*

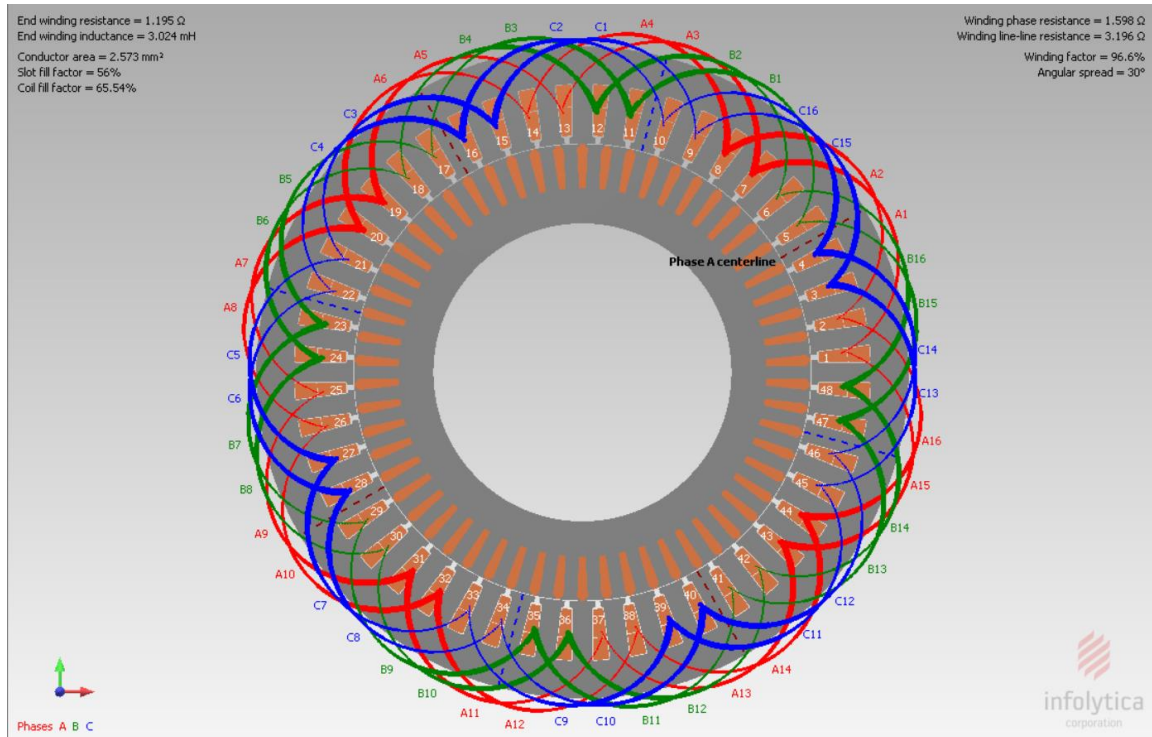


Figure 2-26 The distributed winding from the 8 pole 48 slot combination

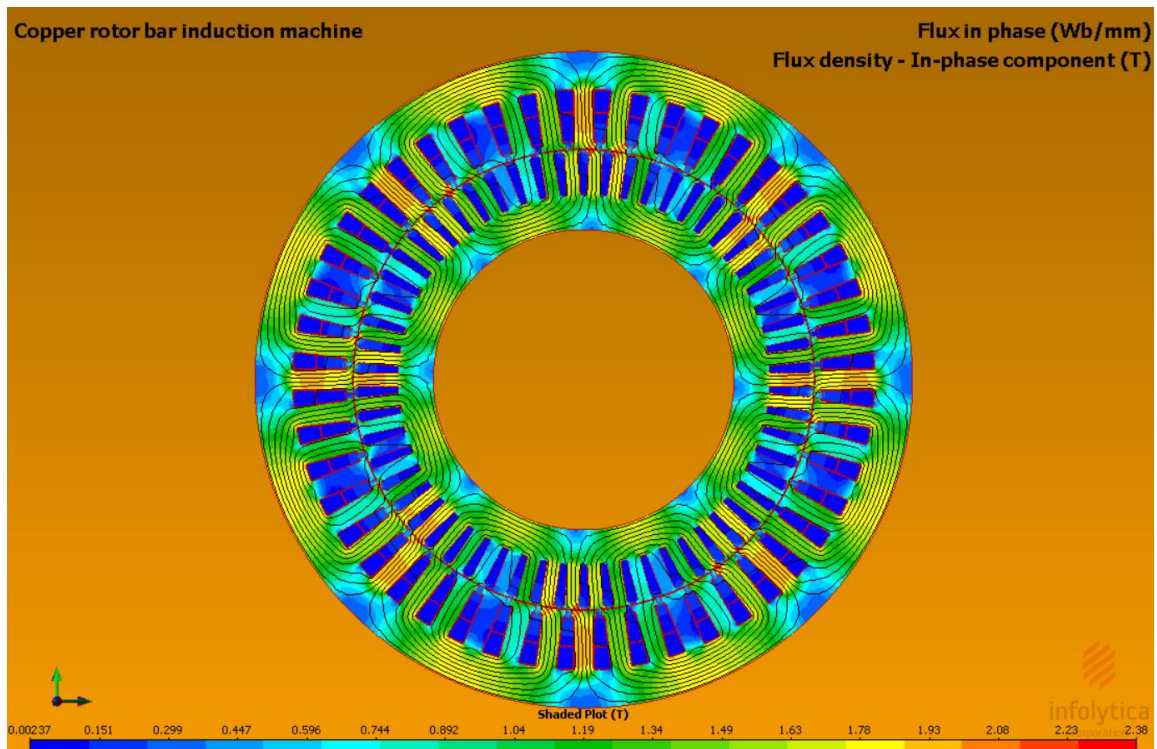


Figure 2-27 The field view of the CR-IM

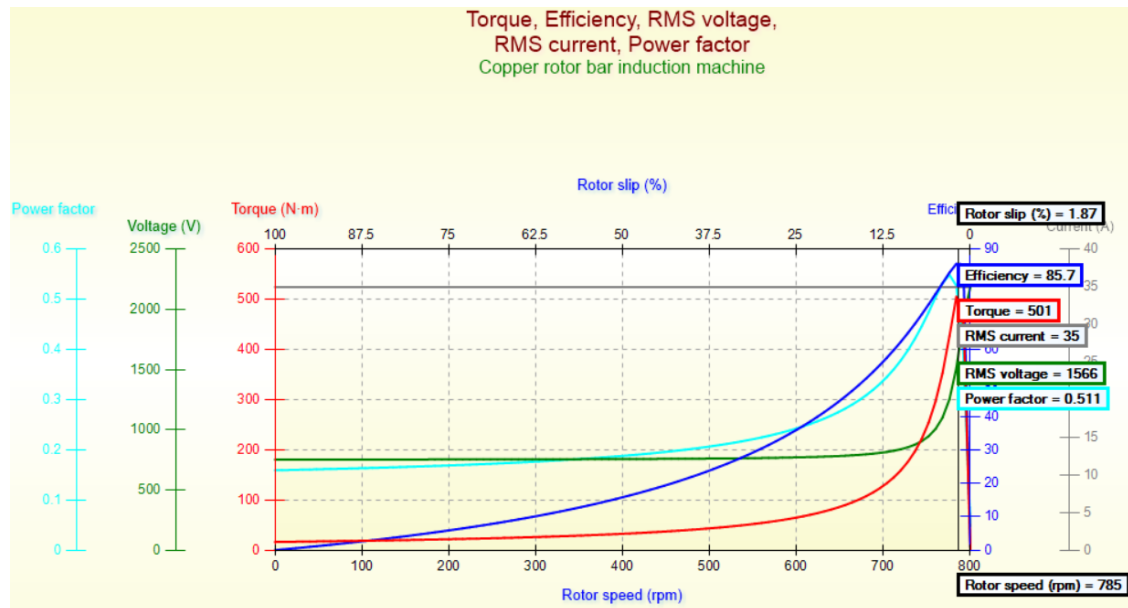


Figure 2-28 The torque, efficiency, RMS voltage and current, power factor against rotor speed of CR-IM

The performance summary against rotor speed at a synchronous speed of 800rpm is plotted in Figure 2-28. The torque-slip curve is shown as a red line. The peak torque is circa 500Nm at slip=1.9% which is 71.5% of the rated torque in the BMM. The RMS line voltage of CR-IM is 1566V and has a 276V peak assuming 8 parallel inverter circuits are used as in the BMM. This is within the limits of the DC voltage supply. However, the power factor is merely 0.5 and the efficiency is 85.7% lower than the BMM.

A lower efficiency and a slightly higher number of coil turns in the CR-IM generates more heat, challenging the existing cooling system. Furthermore, as distributed winding has been chosen, the total axial length of this CR-IM is 51% longer than the BMM. Though it can be mitigated by changing the lap winding to toroidal winding [74], the long inactive length cannot be reduced to a level that's suitable for the current in-wheel package size.

A detailed comparison of the IM and the BMM is summarised here:

Table 2-8 the performance summary of the BMM and IM

	BMM	IM	
Continuous DC Voltage Supply	320.0	268.7	V
Continuous Peak Current per Phase	30.0	50.0	A
Slot Area	2.5	4.6	mm ²
Continous Output Torque	695.0	501.0	Nm
Slot Area	2.5	4.6	mm ²
Continous Output Torque	695.0	501.0	Nm
Power factor	0.84	0.51	-
Efficiency	0.94	0.86	-
Rated Speed	800	784	rpm
Control Strategy	SVPWM		
Coolling Method	Water Jacket		
Steel Type	Non-Oriented Silicon Steel_M250-35A		
coil turns	32		-
Active Axial Length	58.8		mm
Inactive Axial Length	74	108.8	mm
Outer Diameter	386	400	mm
Inner Diameter	302	183	mm
Air Gap Diameter	364	280	mm
Air Gap Distance	1	0.5	mm
Slot Number	72	58	-
Pole Number	64	48	-
magnet mass	2.38	-	kg

2.4.3. The switched reluctance machine

In this section, one switched reluctance machine (SRM) is sketched in *MotorSolve* to compare the torque output with the BMM.

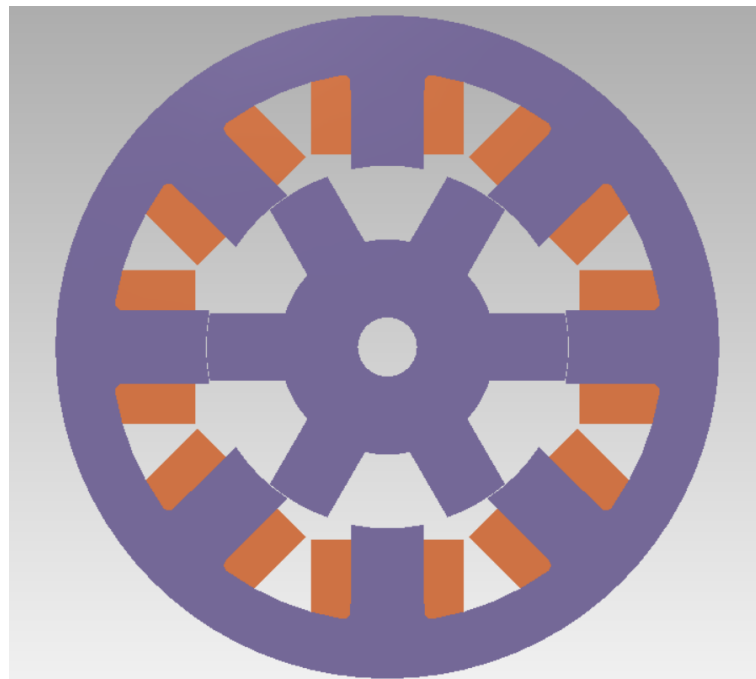


Figure 2-29 The switched reluctance models

In the comparison, again, the total copper loss I^2R is fixed. With a calculated current input, the static analysis of the torque against rotor position is shown in Figure 2-30. At a 100% rated current, the peak torque is 310Nm which is 44% of the BMM.

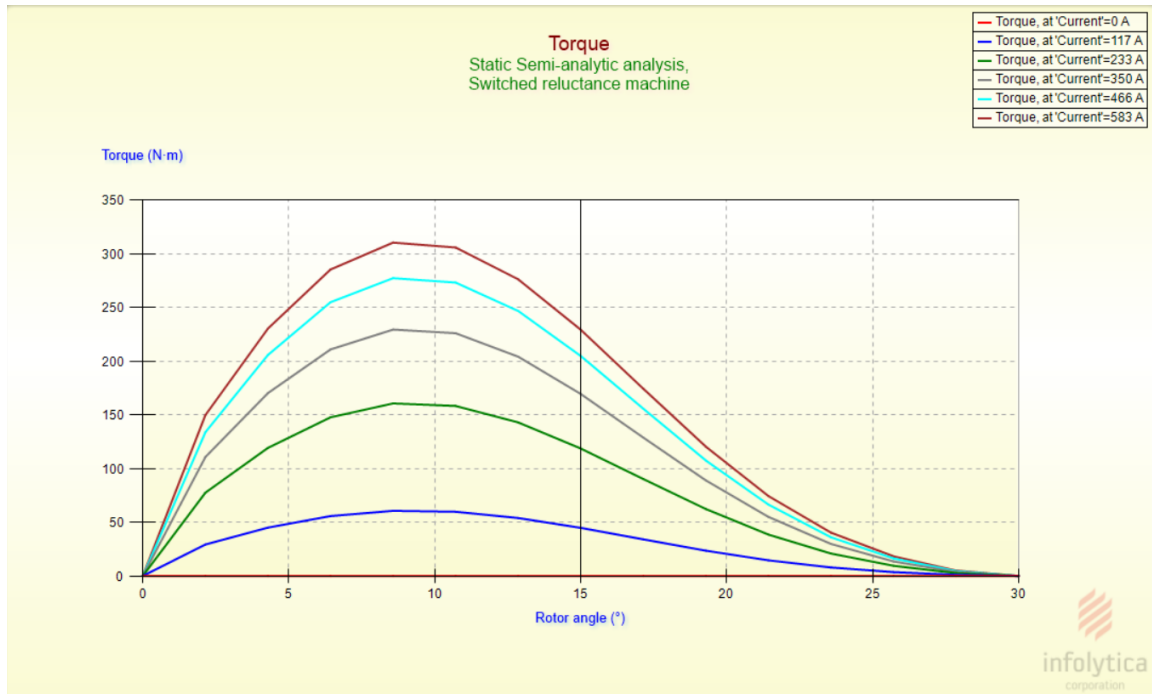


Figure 2-30 The torque against rotor position of different current inputs

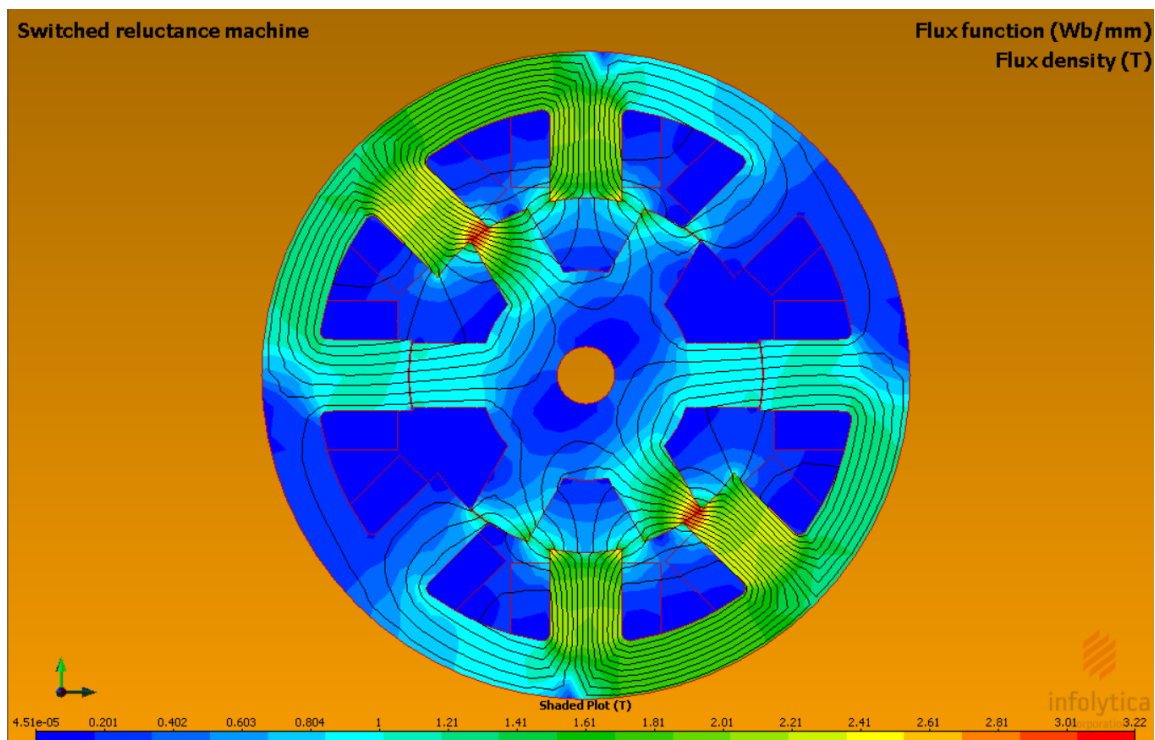


Figure 2-31 The field view of the SRM

2.5. Conclusion

In this chapter, the advantages of the electric vehicle over the conventional fossil fuel powered vehicle have been summarised. The main advantages being zero local pollution and breaking the dependence on fossil fuels. The main disadvantages being a higher purchase cost and lower driving range which can be tackled with a cheaper and more efficient motor design.

Furthermore, commercialised EV models for light-to-middle class vehicles have been surveyed, it was found that a permanent magnet machine has been the prime choice in recent decades for the OEM of almost every major car, due to its high torque density, high efficiency, good power factor and low torque ripple.

In-wheel motor topology was chosen over conventional central motor topology due to distinctive advantages for the components (differential gearing etc.), passenger space saving and an ability to be integrated into any existing vehicle. Though there are a few challenges including high fault tolerance, torque density requirement and strict space limitations, solutions, including using fractional-slots, concentrated-winding, outer-rotor, and a modular design, have been proposed in the existing Protean developed benchmark motor.

Lastly, to reduce or eliminate the use of magnets, a few state-of-the-art alternative machines have been discussed. All of them could not achieve the targeted torque density. A self-designed copper-cage outer-rotor induction machine has been proven to be able to provide 72% of the required rated torque at a lower efficiency, power factor and longer total axial length compared to the BMM. This design can serve as a baseline for further development and optimisation. However, the difference in performance was unable to be overcome without any radical design innovation. Other self-designed SRMs can provide 44% of the torque in the BMM.

The permanent magnet motor type was proven to be the best option in terms of performance. The background has now been fully introduced and in the next chapter the research will proceed into the investigative design stage.

Chapter 3. DESIGN AND IMPROVEMENT

There are two main topologies for the permanent magnet radial flux motor: surface-mounted magnet and interior magnet. According to [75], the interior magnet rotor has a better demagnetisation resistance. Different magnet topologies were studied in [76-83], it is found that an interior topology can produce a higher torque per magnet mass due to additional reluctance torque. Hence, if aiming for the same torque output, magnet mass could potentially be reduced.

In this chapter, together with the surface mounted rotor topology, seven topologies are studied to seek a design with the best ‘magnet utilisation factor’ defined as κ by eq. (3.1):

$$\begin{cases} \kappa = \frac{T_{rated}}{M_{mag}} / \kappa_0 \\ \kappa_0 = \frac{T_{r_BMM}}{M_{mag_BMM}} \end{cases} \quad (3.1)$$

In which T_{rated} is the torque output with the rated current input and M_{mag} is the magnet mass of the designed motor. κ_0 is the original value of the BMM.

The V shaped magnet topology will then be further optimised at critical operation points. Its demagnetisation resistance is also analysed in detail and is proven to be higher compared to the BMM. Various aspects are then compared with the BMM. The V-shaped motor is proven to perform at the same level: match the performance of the BMM with a magnet mass reduction of 44%.

To start with, the surface mounted topology is analysed.

3.1. Rotor topologies

3.1.1. *Surface-mounted topology - optimum split ratio*

Torque is proportional to ‘electric loading’ x ‘magnetic loading’ x ‘air gap surface area’.

A high split ratio (air gap radius over outer radius) can maximise the air gap radius, hence the air gap surface area, for a given machine size. An extremely high value can be achieved by adopting an out or rotor topology. This minimises the area excluding the core back

(because the slot height is mostly longer than the magnet length) and has a high number of poles to minimise the core back area. Magnetic loading is normally fixed if strong magnets like NdFeB are used, so the optimum split ratio is roughly proportional to the pole number. The maximum pole number is limited by the electronic switching frequency.

After the pole number and its corresponding rotor core-back length is determined, the split ratio can be further improved by shortening the magnet length at a cost to lowering magnetic loading. Hence, there is an optimum magnet length and split ratio, for the highest achievable torque in a given machine volume. An analytical model was introduced originally in [84] then developed and expanded in [85, 86] to determine the optimum split ratio for the surface-mounted motor. This model was adopted and modified to analyse the BMM.

Assuming that the rotor back iron thickness, the rotor outer diameter and the stator inner diameter and copper loss are constant/consistent with/ in line with the rest of constants shown in Table 3-1, the main variable is the thickness of the magnets. The peak air-gap flux density B_g can be calculated by eq. (3.2), which is a function of the split ratio λ plotted in Figure 3-1. This curve shows that when the split ratio increases past a certain level. The excitation level cannot be maintained and the air gap flux density starts dipping due to magnet thickness reduction. Now the torque needs to be related to this air gap flux density.

Table 3-1 The controlled motor parameters from BMM

rotor pole number, N_p	64
stator slot number, N_s	72
outer rotor diameter, D_{ro} (mm)	386
inner stator diameter, D_{si} (mm)	302
air-gap length, l_g (mm)	1
active length, l_a (mm)	58.8
fixed rotor back iron thickness, l_{rb} (mm)	6
tooth-tip height, h_t (mm)	1.5
PM remanence, B_r (T)	1.35
PM relative permeability, μ_r	1.05
maximum flux density in the stator tooth, B_{sm} (T)	2

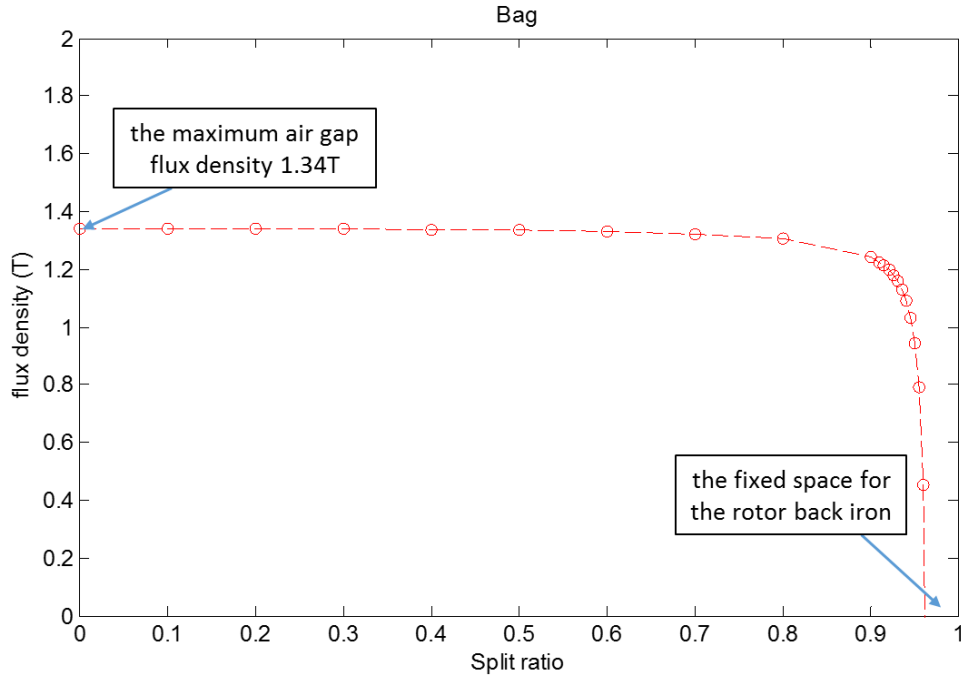


Figure 3-1 The plot of B_g against λ for BMM

$$B_g = \frac{B_r}{1 + \mu_r l_g / \left[\frac{D_{ro}}{2} (1 - \lambda) - l_g - l_{rb} \right]} \quad (3.2)$$

The torque output can be calculated by eq. (3.3), in which I_{ph} is the peak phase value. The copper loss of the whole motor is fixed while varying the split ratio and can be expressed in eq. (3.4), in which N_{ph} is the number of turns per phase, A_s is the slot area, ρ is the resistivity and K_f is the fill factor. By rearranging eq. (3.4) to obtain the expression of I_{ph} and then substituting it into the eq. (3.3) and forming eq. (3.5) the normalised torque density index can be found. This index is a function of the split ratio λ and the slot area A_s . The slot area can be estimated by knowing the tooth width b_t and the stator back iron h_{sbi} (half of the tooth width, eq. (3.8)). b_t is related to the $\frac{B_g}{B_s}$ ratio, eq. (3.7), in which B_s is the maximum flux density allowed in the slot and is set at 2T. The influence of the tooth tip and end-winding, eq. (3.9), are also taken into account. Eventually, when the slot per pole is smaller than 1.5, the torque density index T^* can be expressed as eq. (3.10) [86].

The calculated torque density index against the split ratio of the BMM is plotted in Figure 3-2. The calculated optimum split ratio for the highest torque density is 0.950, which is 366.6mm for the inner rotor diameter. The actual inner rotor diameter of the BMM is 364mm, very close to the analytical prediction.

$$T = 3k_w N_{ph} \frac{D_{ro}\lambda}{2} l_a B_g I_{ph} \quad (3.3)$$

$$P_{cu} = 18N_{ph}^2 I_{ph}^2 \rho \frac{l_a + l_e}{A_s K_f N_s} \quad (3.4)$$

$$T^* = C \frac{T}{Vol} = k_w \cdot \gamma \cdot \lambda \sqrt{\frac{l_a}{l_a + l_e}} \cdot \sqrt{\frac{4A_s N_s}{\pi D_{ro}^2}} \quad (3.5)$$

$$\left\{ \begin{array}{l} \gamma = \frac{B_g}{B_s} \\ C = \frac{1}{B_s \sqrt{P_{cu} K_f / 2 \rho l_a \pi}} \end{array} \right. \quad (3.6)$$

$$b_t = \frac{\pi D_{ro} \gamma \lambda}{N_s} \quad (3.7)$$

$$h_{sbi} = \frac{b_t}{2} \quad (3.8)$$

$$l_e = \frac{\pi^2 D_{ro}}{4N_s} \left[\left(\frac{\pi}{2N_s} + 1 \right) \gamma \lambda + \frac{\varepsilon}{2} - \frac{\sigma}{2} \right] \quad (3.9)$$

$$\left\{ \begin{array}{l} T^* = k_w \cdot \gamma \cdot \lambda \sqrt{\frac{l_a}{l_a + l_e}} \cdot D \\ D = \sqrt{\left[1 - 2\gamma + \frac{\pi}{N_s} \left(2 - \frac{\pi}{N_s} \right) \gamma^2 \right] \lambda^2 + 2 \left[\left(\varepsilon - \frac{\pi \varepsilon}{N_s} + \sigma \right) \gamma - \sigma \right] \lambda - \varepsilon^2 + \sigma^2} \end{array} \right. \quad (3.10)$$

$$\varepsilon = \frac{D_{si}}{D_{ro}} \sigma = \frac{2h_t}{D_{ro}} \quad (3.11)$$

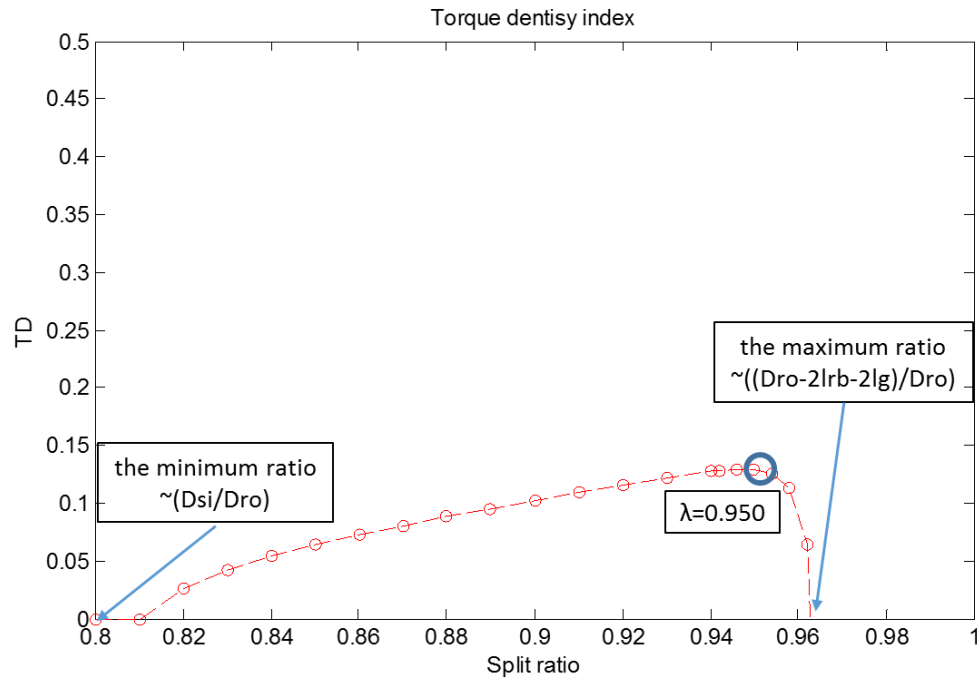


Figure 3-2 The plot of T^* against λ of the BMM

3.1.2. Surface mounted topology - Magnet width, length and the steel filling

Figure 3-3 shows a section of the BMM, in which there are three parameters that can be varied: a. magnet length; b. magnet width; c. steel filling. The experimental ranges are shown in Figure 3-4.

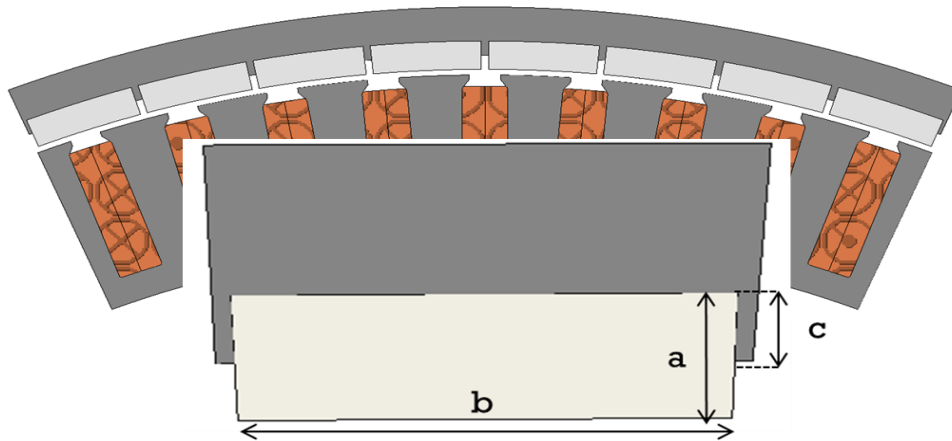


Figure 3-3 Variables in the benchmark motor: a. magnet length, b. magnet width, c. steel filling

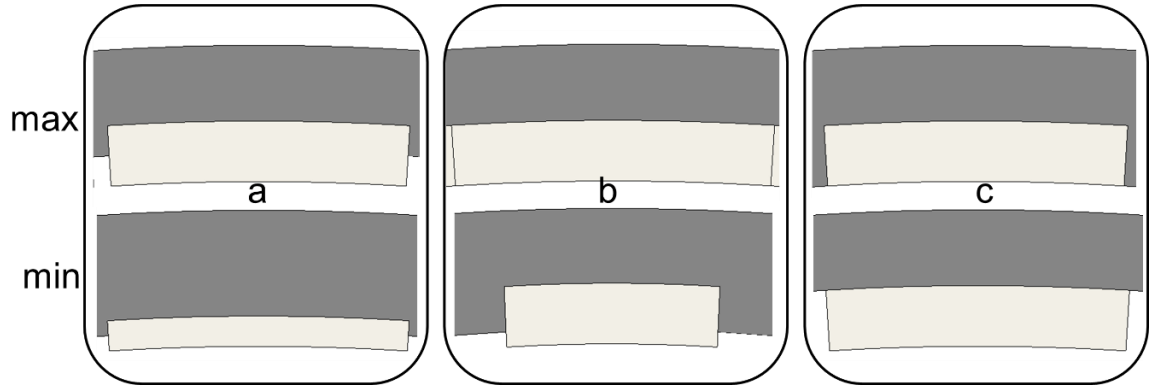


Figure 3-4 Variables analysis range

Discussion on three variables

a.) Magnet length

The magnet length (l_m) is directly proportional to the magnet mass and it influences the flux level (ϕ) in the air gap. This makes it relate to the magnet utilisation factor κ (defined at start of this chapter). As shown in eq. (3.12) and the magnetic circuit in Figure 3-5, when increasing l_m , the ratio of $\frac{l_m}{l_m + l_{ag}}$ and ϕ is increased, assuming l_m is not $\gg l_{ag}$. There is a minimum magnet length that can meet the air gap flux requirement and maximise factor κ . Also, there is a minimum magnet length to avoid demagnetisation issues.

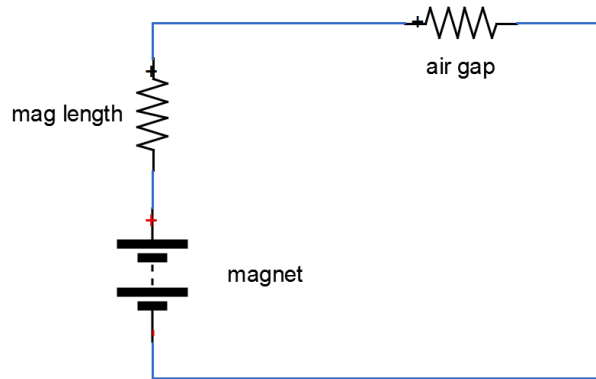


Figure 3-5 Simplified magnetic circuit for a pole

$$\phi = \frac{\text{MMF}_m}{R} = H_c \mu \tau l_a \frac{l_m}{l_m + l_{ag}} \quad (3.12)$$

b.) Magnet width

The magnet width determines the air gap flux waveform shape. With a non-salient rotor and stator, no saturation and a fringing effect, arc-shaped and radially magnetised magnets, the air gap flux waveform is a square wave as is shown in Figure 3-6. The magnet's span

α is determined by the magnet width. The torque output is proportional to the fundamental component of the flux, which can be obtained by Fourier analysis, shown in eq. (3.13).

$$B_1 = \frac{1}{\pi} \int_0^{2\pi} B_g \sin \theta d\theta = \frac{4}{\pi} \int_{\frac{\pi-\alpha}{2}}^{\frac{\pi}{2}} B_g \sin \theta d\theta = \frac{4}{\pi} B_g \sin \frac{\alpha}{2} \quad (3.13)$$

Eq. (3.13) can also be used to calculate the magnitude of the harmonics by modifying ' $\sin \frac{\alpha}{2}$ ' to ' $\sin(v \cdot \frac{\alpha}{2})$ ', where v represents the harmonic order. Hence, the magnetic span is normally chosen to be between 120° and 180° , with the value of $\sin \frac{\alpha}{2}$ ranging from 0.866 to 1.

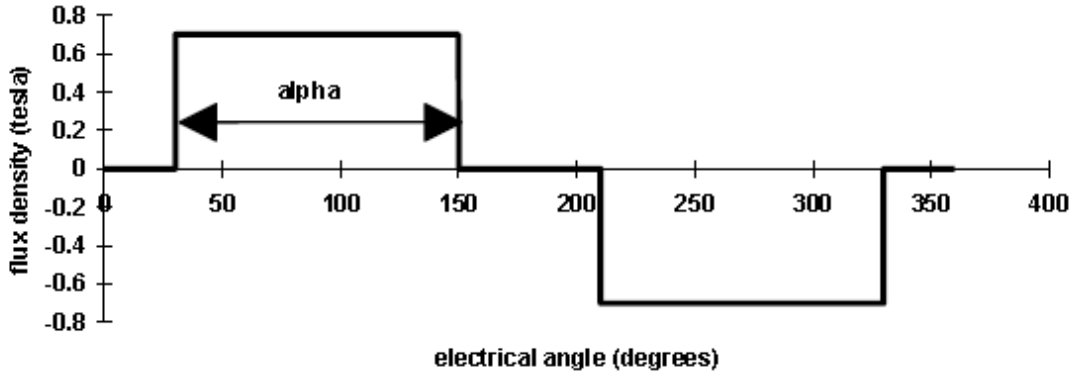


Figure 3-6 Square air gap flux of surface mounted topology

c.) Steel filling

The concept of adding steel teeth between magnets is in order to create inductance variation between the DQ axes. However, the flux leakage between magnets is increased and little reluctance torque is found, which leads to no torque improvement.

Torque response of the variables

Among these three variables, both magnet width and length can have a significant impact on factor κ .

a.) Magnet length

The BH characteristic curve of steel lamination (M250-35A) used in the in-wheel motor is shown in Appendix C. The curve starts to saturate at circa 1.5T and is fully saturated at 2T effectively acting as air. The field plots in Figure 3-7 are to compare the flux saturation

level in two models with different magnet lengths. When the magnet length is reduced from 5mm to 3mm in the BMM, saturation in the rotor core back is removed, which helps to increase factor κ . As the magnet length is reduced from its original value, 4mm (1unit), to 2mm (0.5unit), factor κ in Figure 3-8 is improved to 167%. Therefore, the output torque could be maintained at 82.7% whilst halving the magnet length.

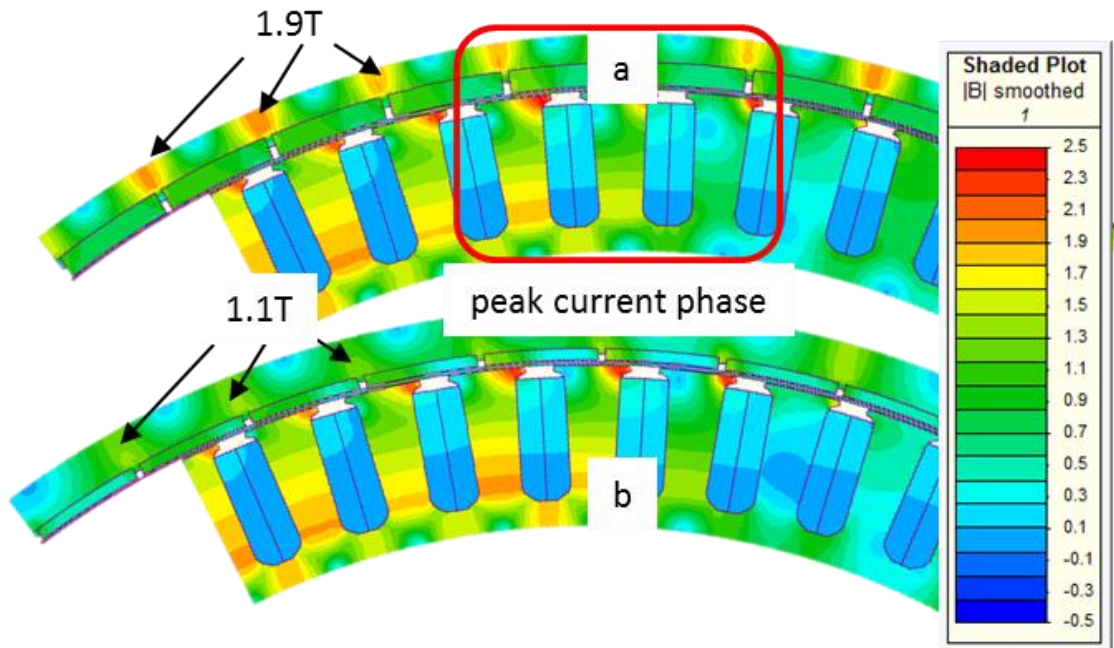


Figure 3-7 Magnetic field density plot of magnet length: a. 5mm; b. 2mm at normal operating condition

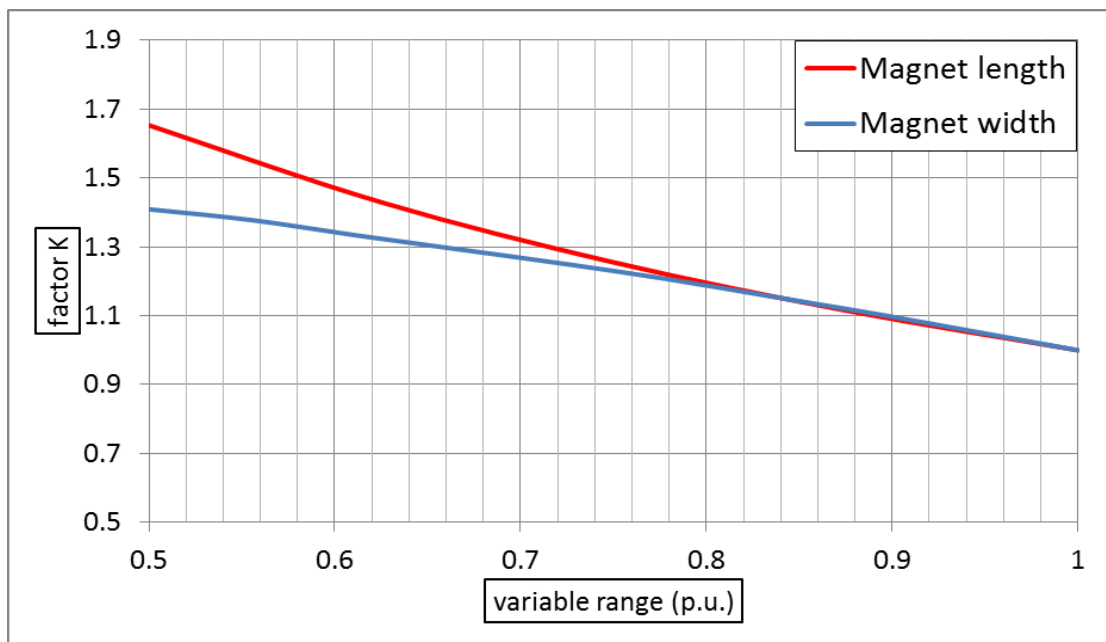


Figure 3-8 The factor K against the variables in THE BMM

b.) Magnet width

By reducing the width of the magnet material, the magnetic circuit is less saturated and there is less flux leakage between adjacent magnets. Factor κ can be improved, increasing from 1 to 1.41. With a reduced magnet span, higher order harmonics can be attenuated, which is analogous to the coil pitching effect. A Fourier transformed harmonic spectra with a magnet span of 180° and 150° is shown in Figure 3-9. Both the 5th and 7th harmonics are largely reduced in the waveform of 150° . When reducing the magnet span from 180° to 120° , the magnitude of the fundamental is reduced by only 13.4%, the torque difference is shown in Figure 3-10, while the magnet mass can be reduced by 33.3%.

The magnet span is selected at 169° for the BMM due to the torque output requirement.

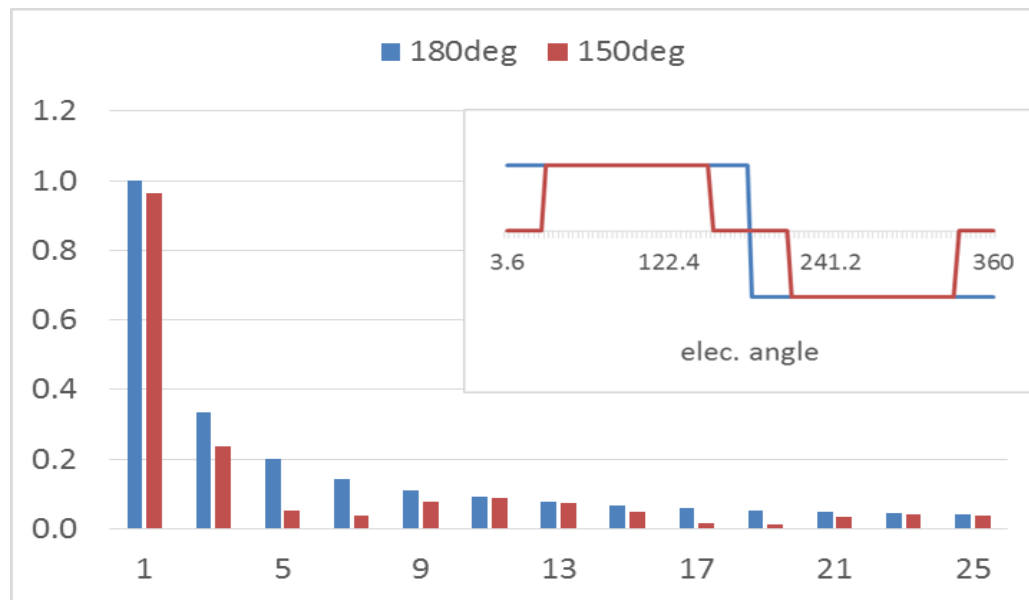


Figure 3-9 The harmonic spectra of the air gap flux density waveforms of models in 180° and 120° magnet span

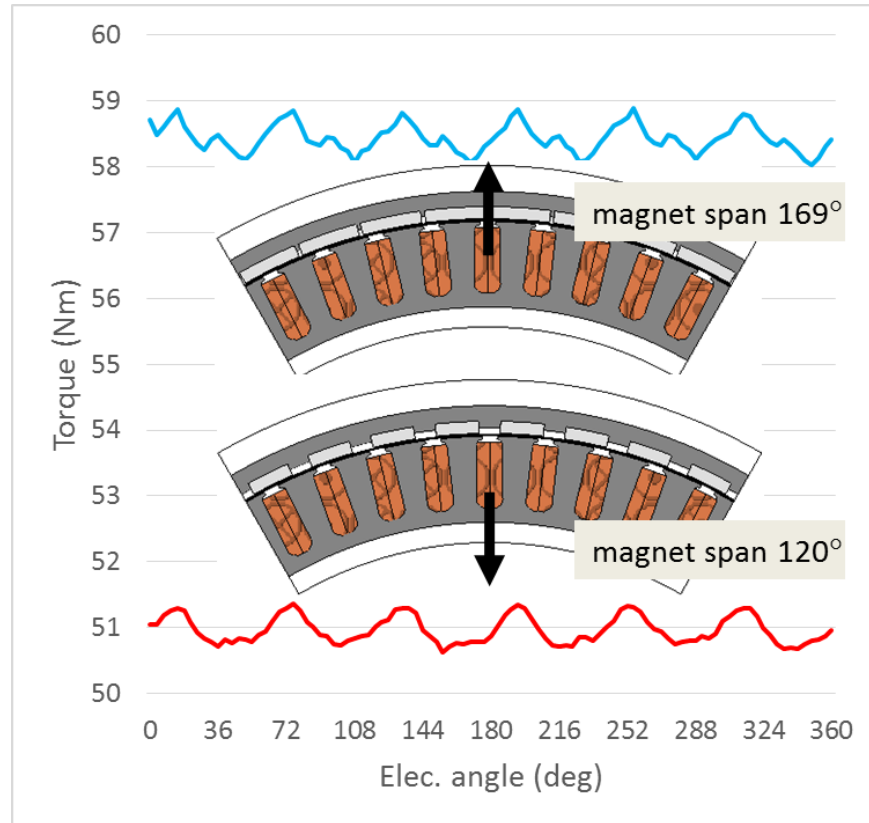


Figure 3-10 The torque comparison in models with different magnet width

Demagnetisation in surface-mounted motors

The surface mounted rotor topology used in the BMM is particularly susceptible to demagnetisation as explained in chapter 3. A worst case scenario is simulated for models of a 4mm and a 2mm magnet length for if the controller is broken and the max overload current is on the $-D$ axis. The results are illustrated in Figure 3-11. The flux density in blue areas is above the knee point showing the magnets to be unaffected, whilst areas in red are below the knee point indicating permanent demagnetisation.

To reduce magnet mass, a simple magnet length reduction method is therefore not practical due to the potential demagnetisation issue. Alternative rotor topologies must be studied to seek better magnet utilisation.

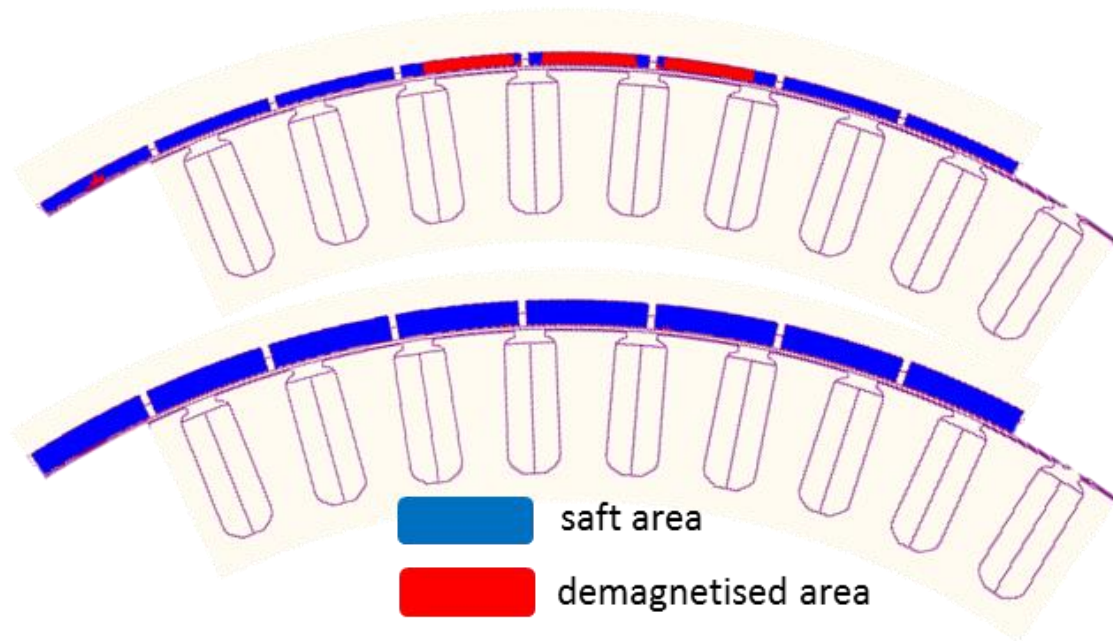


Figure 3-11 Demagnetization analysis on surface mounted motor

3.1.3. Alternative rotor topologies

In the benchmark motor, in order to maximise the air gap radius, the difference between the inner and the outer rotor radii is a mere 11mm, 5.7% of the outer rotor radius. In the surface mounted topology, the magnet length is 5mm which leaves only 6mm rotor core back thickness.

For the alternative magnet topologies, stator dimension is fixed to limit the studying variables. The 11mm rotor thickness presents an extreme limit to the investigation. Illustrated in Figure 3-12 are the six topologies analysed, consisting of a. the slotted, b. the buried, c. the triangular, d. the C-arc e. the I-shaped, f. the V-shaped rotor topologies.

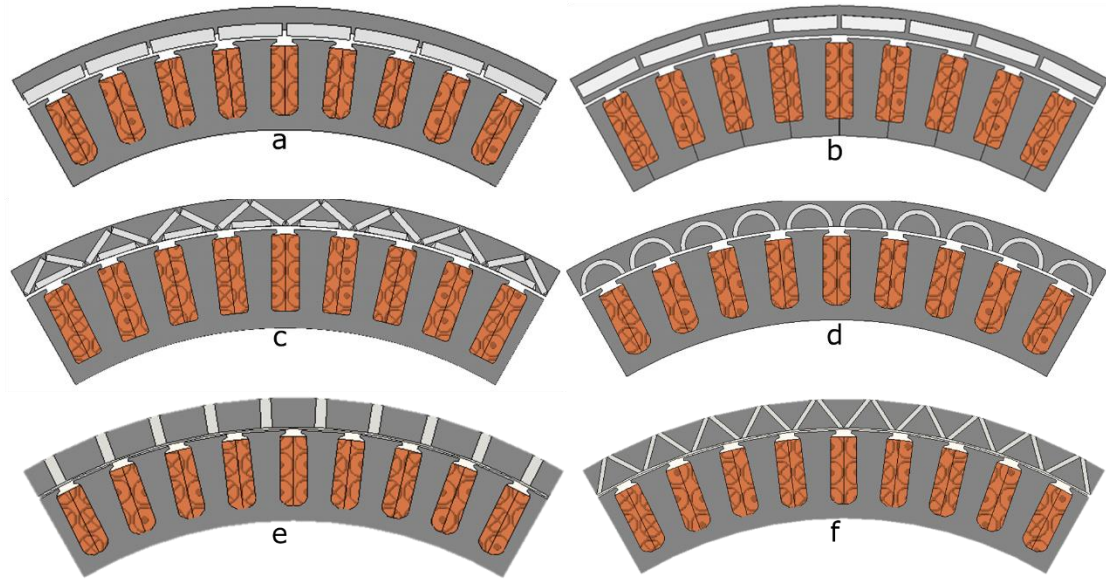


Figure 3-12 Alternative magnet topologies

The optimisation program

Compared to the surface mounted topology, the interior topologies clearly possess a much higher level of geometric complexity. A quick, automatic and systematic optimisation program is necessary.

Popular optimisation algorithms implemented and developed in electromagnetic software are: particle swarm [87], evolutionary [88] and genetic [89] algorithms. There are also methods which have been attempted academically, such as Taguchi and artificial neural network [90]. These methods generally aim to reduce the number of experiments in the process to find the optimal solution. For instance, in the surface response method, the searching surface formed by variables is represented by a reduced number of sampling points, specified by different algorithms shown in Figure 3-13.

In this topology study, after considering the number of the variables, advanced algorithms are not selected. Instead, a simple procedure is created and illustrated in Figure 3-15. It is programmed using Visual basic in *Excel*, executed in *MagNet* (FE software) and post-processed in *Matlab*. The V topology shown in Figure 3-14 is selected to demonstrate the program. There are three variables of the V topology: a. the centre distance; b. the magnet length; c. the rotor outer radius.

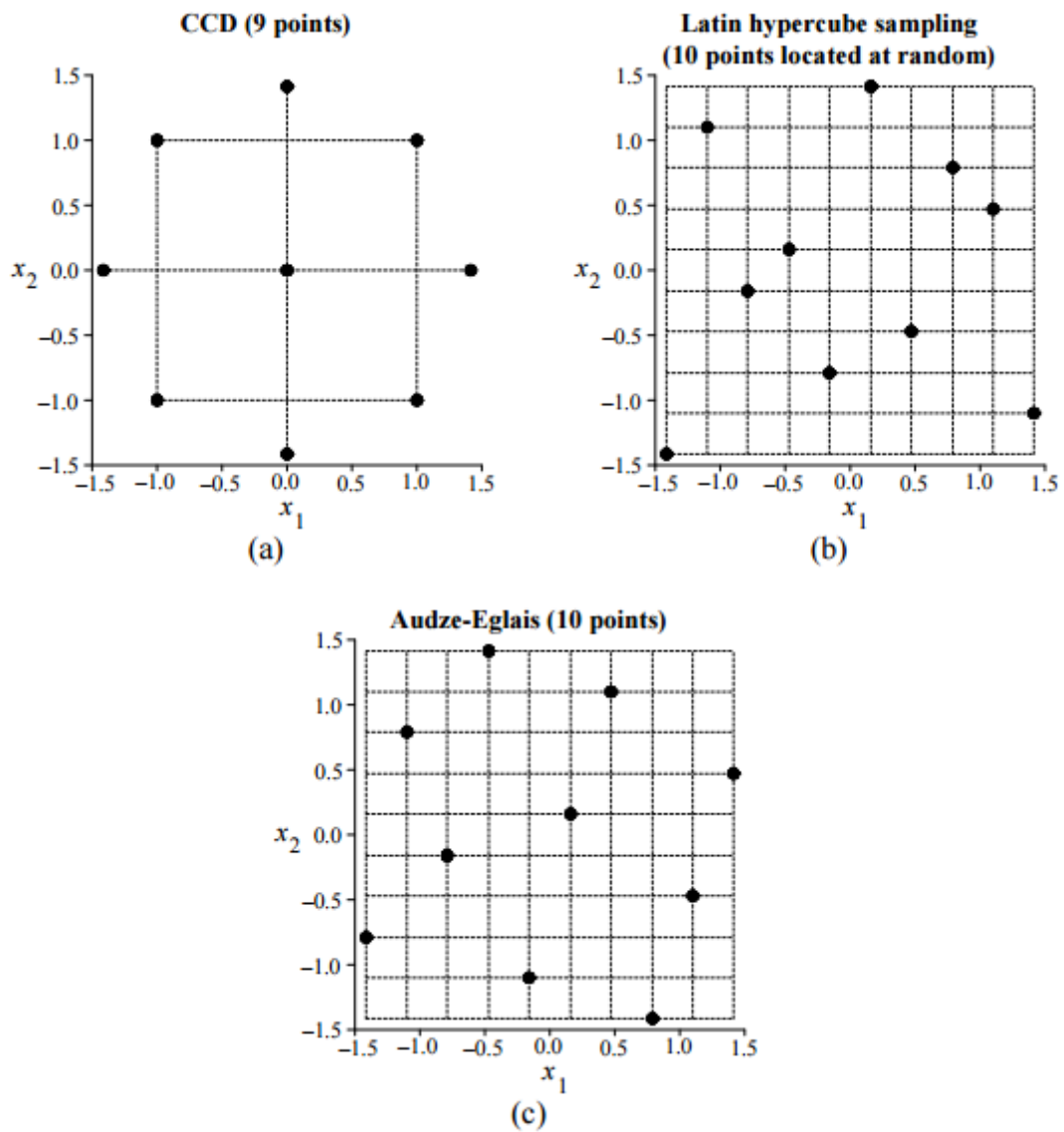


Figure 3-13 Comparisons between central composite design (CCD), Latin hypercube design and Audze-Eglais design [91]

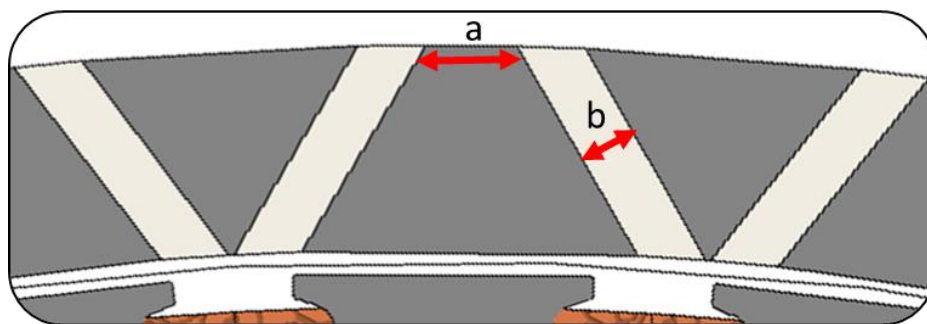


Figure 3-14 The V topology

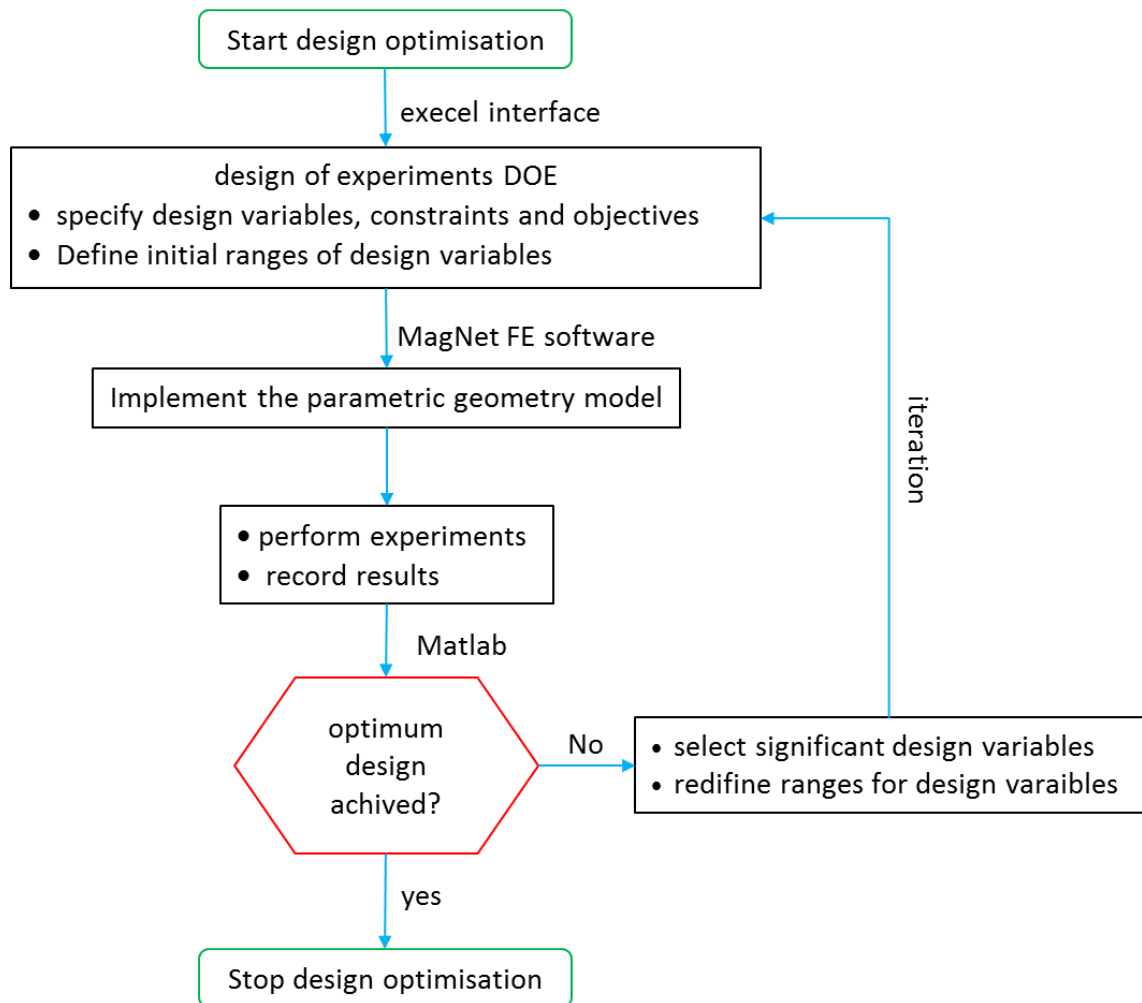


Figure 3-15 The optimisation program

The user interface of excel is demonstrated in Figure 3-18. The parameters of the FE model can be modified in this window and the experimental range of the variables can be set up here. For instance, assuming there are three steps for each of the three variables, the pseudocode for the iteration is shown in Figure 318 a. and the shape of the experiment is formed as Figure 3-17b. There are ways to reduce the number of the experiments to form the shape as is shown in Figure 3-16.

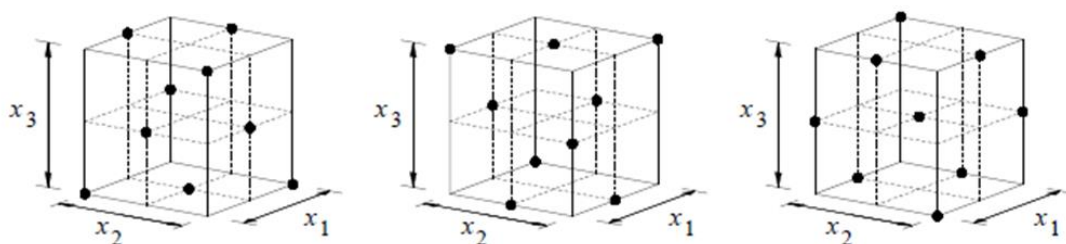


Figure 3-16 Three methods to form a 3x3 cube using $1/3$ of 3^3 experiments [91]

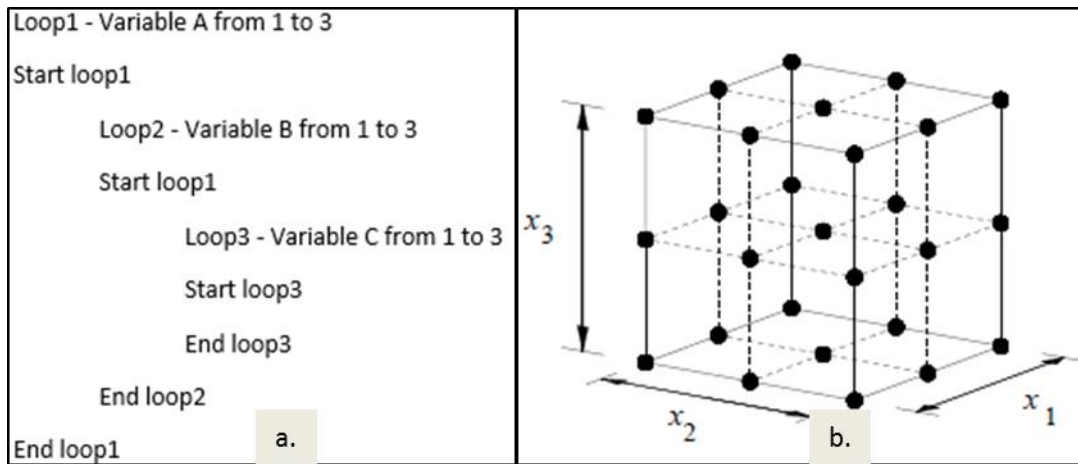


Figure 3-17 The full sampling of a 3x3 cube

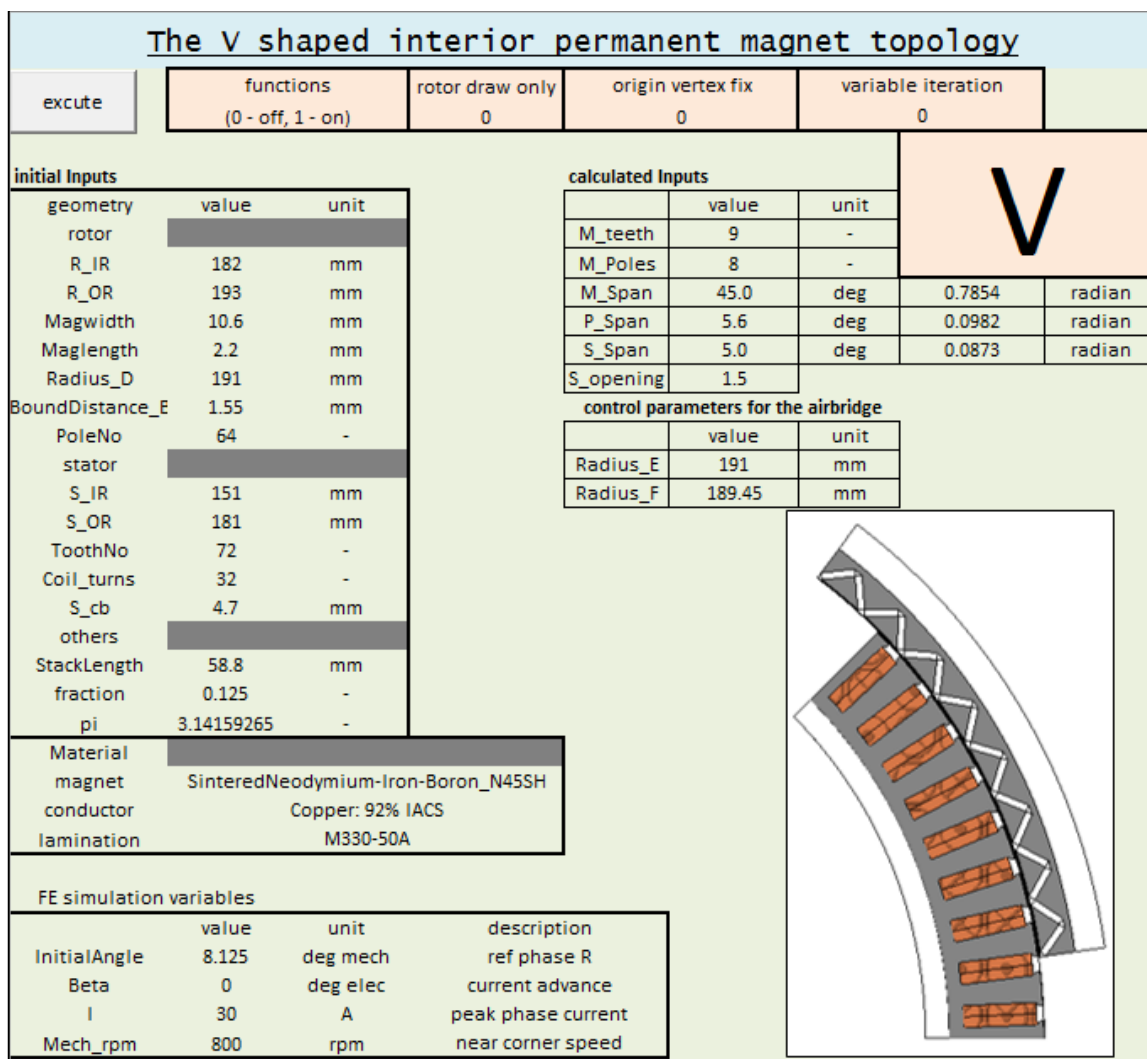


Figure 3-18 The excel interface

For accuracy, 5 steps are chosen for each variable and the full sampling points are obtained to form a cube. At each sampling point, i.e. model (x, y, z), the peak torque output is obtained by changing the current alignment angle, β , from -20° to -10° as is shown in Figure 3-19 (0° is the q axis, -90° is the -d axis).

After all sampling points of the torque response are obtained from the FEA, the cube is formed and shown in Figure 3-20. The 3 dimensions represent 3 variables, the colour of the cube being the experimental response. The redder the node gets, the higher the magnet utilisation factor κ is. The optimum result for these 3 variables in the defined range can then be detected.

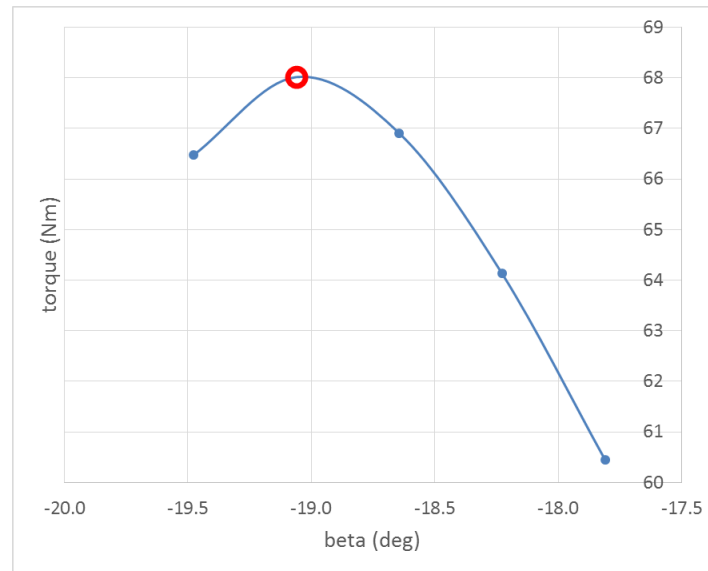


Figure 3-19 Peak torque search using static FE simulation

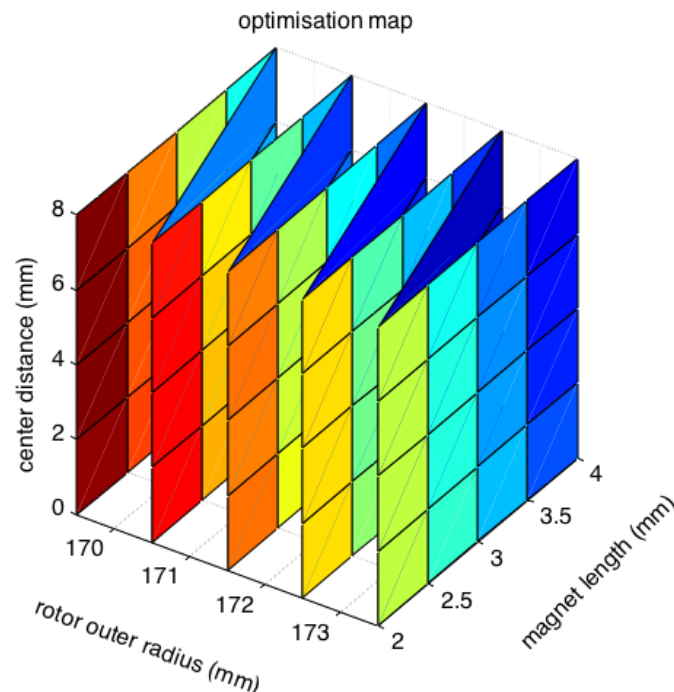


Figure 3-20 The 3 variables cube – magnet length, rotor outer radius and centre distance

After each topology has been optimised, the results are discussed:

Type a. and b. - the variation of surface mounted topology

Type a magnet topology is essentially the same as the surface mounted topology with an additional parameter (steel filling), as discussed in the previous section. The conclusion has already been drawn that little reluctance torque can be found from this topology.

For the buried magnet topology (type b), the idea is to create a less saturated flux path for the armature magnetic circuit, thus increasing the difference between q and d axis inductances. The air barrier on the back of the magnet is introduced to reduce the inductance on the d axis. In Figure 3-21, the q axis flux paths are marked as a black arrow.

Unexpectedly, the flux path in front of the magnet is highly saturated (above 2.2T). The d axis air barrier does reduce d axis inductance, however, open circuit magnetic flux is also dropped. Flux leakage is also much higher. So the best factor κ obtained is 0.83 lower than the value in the BMM.

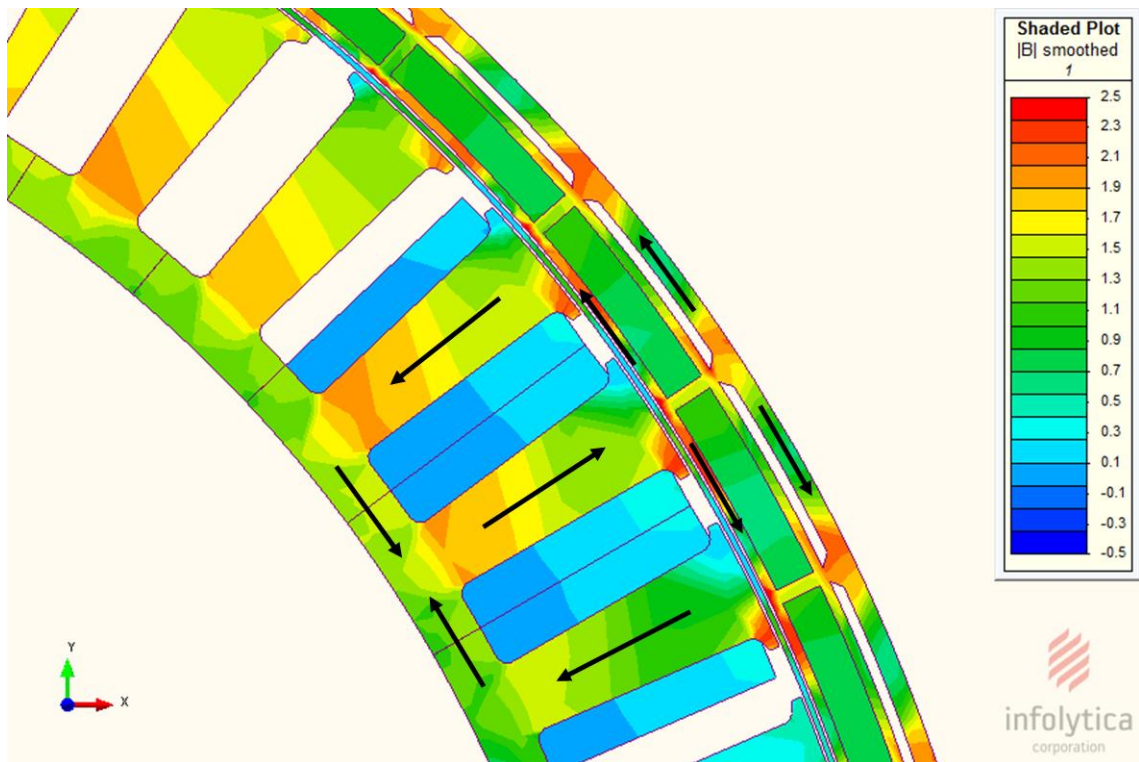


Figure 3-21 The field plot of type b with rated current on Q axis, unmagnetised magnets

Type c. - the triangular topology

A triangular topology (type c) is proposed in [92] and adopted here. After optimisation, the peak magnet utilisation factor can be improved to 1.15, therefore for the same torque output, 13.1% of the magnet mass can be saved using this topology.

However, there are two major concerns about this topology:

1. Geometrical complexity (Figure 3-22): these multi-components with sharp edges have a low manufactural tolerance and the whole rotor structure is mechanically weaker under pressure.
2. The front magnet is 2mm in length and is positioned similarly to that of the surface mounted topology meaning that demagnetisation is an issue in this case.

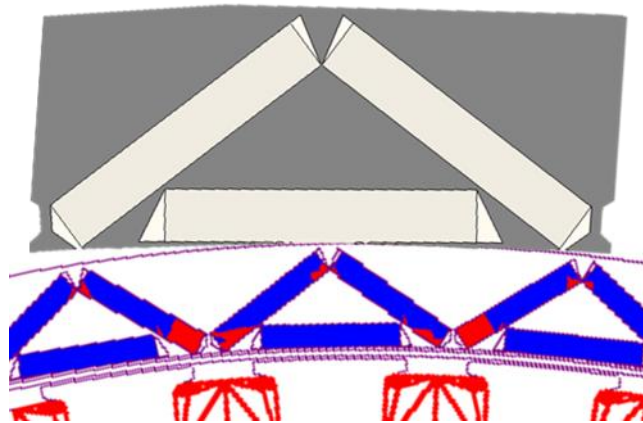


Figure 3-22 Type c. detail geometric view and demagnetisation test

Type d. – the C-arc topology

The aim of the C-arc topology (type d), which is adopted from [78], is to concentrate the flux into the air gap generating a higher air gap flux. The magnet is magnetised radially facing away from or pointing to the centre of the arc which is on the air gap (seen in Figure 334). This flux concentration method is generally used with ferrite magnets to improve the air gap flux level. With mass reduced Neodymium Iron Boron (NdFeB) magnets, the flux concentration method can help to maintain the required flux level.

Furthermore, the flux path on the q axis is made from steel laminations to achieve a higher q axis inductance, as is illustrated by the black arrows in Figure 324. D axis inductance is also expected to be higher due to a smaller magnet length (red arrows marked on Figure 3-23). Hence, both synchronous inductance and inductance difference can be improved.

As a result, this topology can improve factor κ up to 2.06. The only problem is that this shape is harder to manufacture and assemble than square magnets.

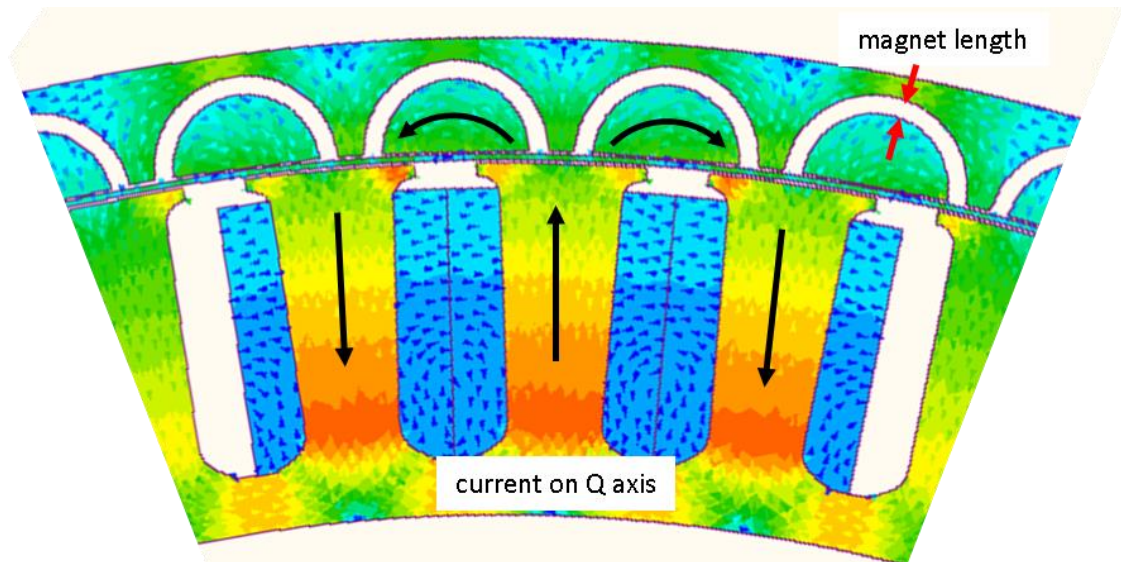


Figure 3-23 The field plot of type d with current on Q axis and no magnets

Type e. and f. – the I-shaped and V-shaped flux concentration topologies

A V-shaped topology is commercially used in the Toyota Prius [93]. Similar to the C-arc topology, the iron piece in front of the magnets creates an easy flux path for armature flux, thus the q axis inductance is improved, resulting in a noticeable amount of reluctance torque. The front iron piece can also act as a flux shield to protect the magnet from high armature flux travelling across the air gap and opposing the magnetic flux, hence the resistance to demagnetisation is improved too. The flux paths and front iron piece are marked in Figure 3-24.

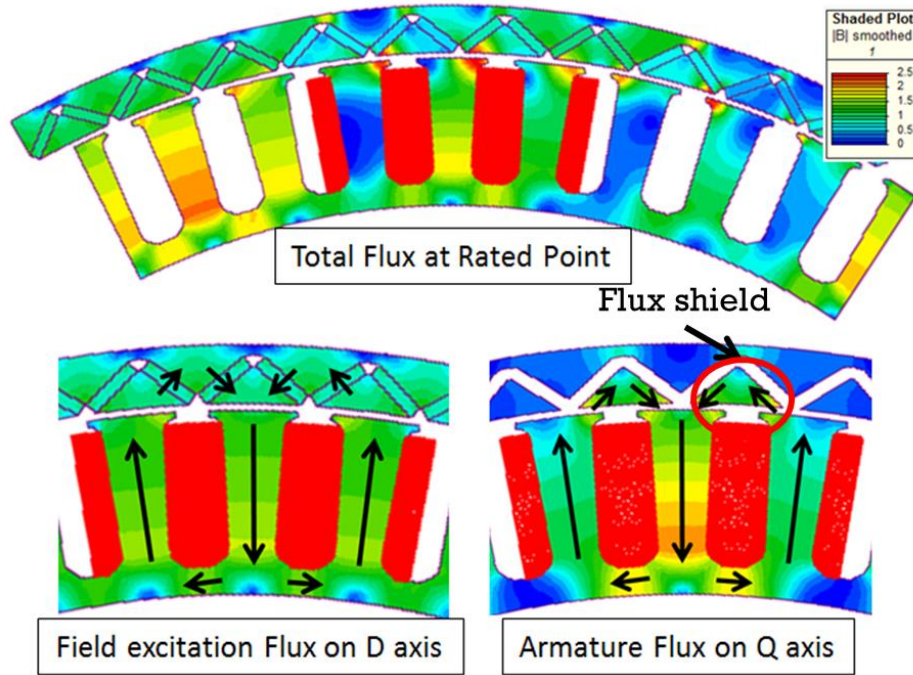


Figure 3-24 Field plot with Flux flowing direction in V shape design

The I-shaped topology is researched academically in [94, 95]. It can be easily related to the other two described in Figure 3-25. The full C-arc can be broken into two pieces to form a V-shaped topology. Two adjacent V-shaped magnets with different polarities can then be merged into one piece by rotating them along their air gap pivot till all pieces pointing radially and until one part of the pole is joined with a part of the adjacent pole.

The V, I and C-shaped topologies all have an easy q axis flux path which helps to create reluctance torque. As can be seen in Figure 3-26, the peak torque of all three types of topology show a bigger phase shift from 0° (the q axis) to -90° (the $-d$ axis) when compared to type a (the BMM), indicating the contribution of the reluctance torque component.

As a result, these three topologies can achieve a similar total torque output with much lower magnet mass, improving factor κ to circa 2.0. The magnet mass used, the torque output and factor κ are recorded in Table 3-2.

Data observation from Table 3-2 shows a clear correlation between the magnet length and the magnet utilisation factor κ . Because of their shorter magnet length, both C-arc and V-shaped topologies give higher values of factor κ compared to the I-shaped topology.

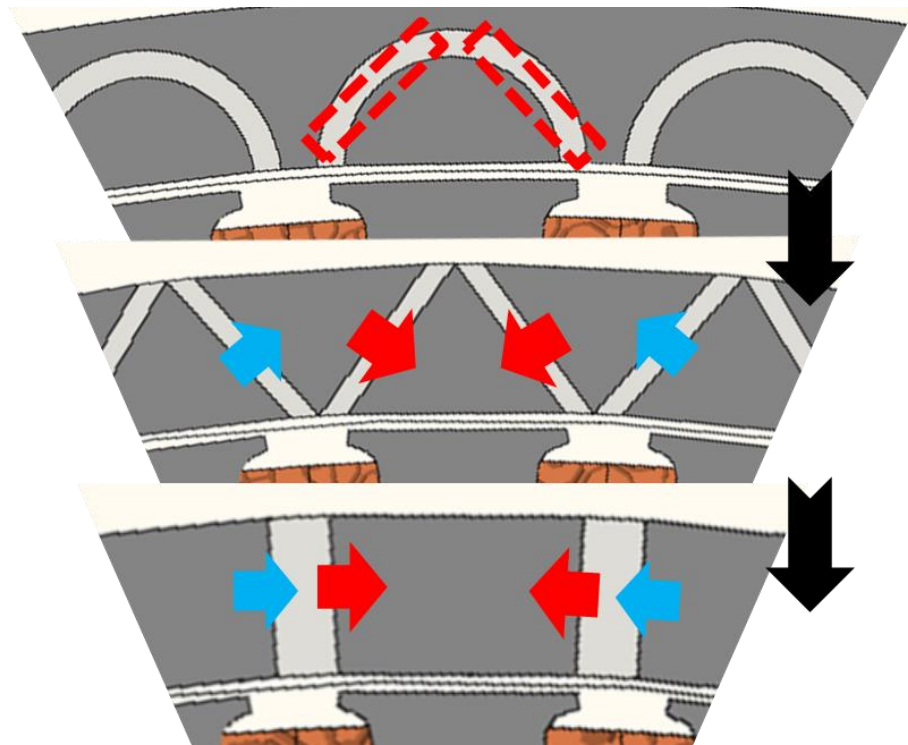


Figure 3-25 The geometrical similarity between C-arc, V and I

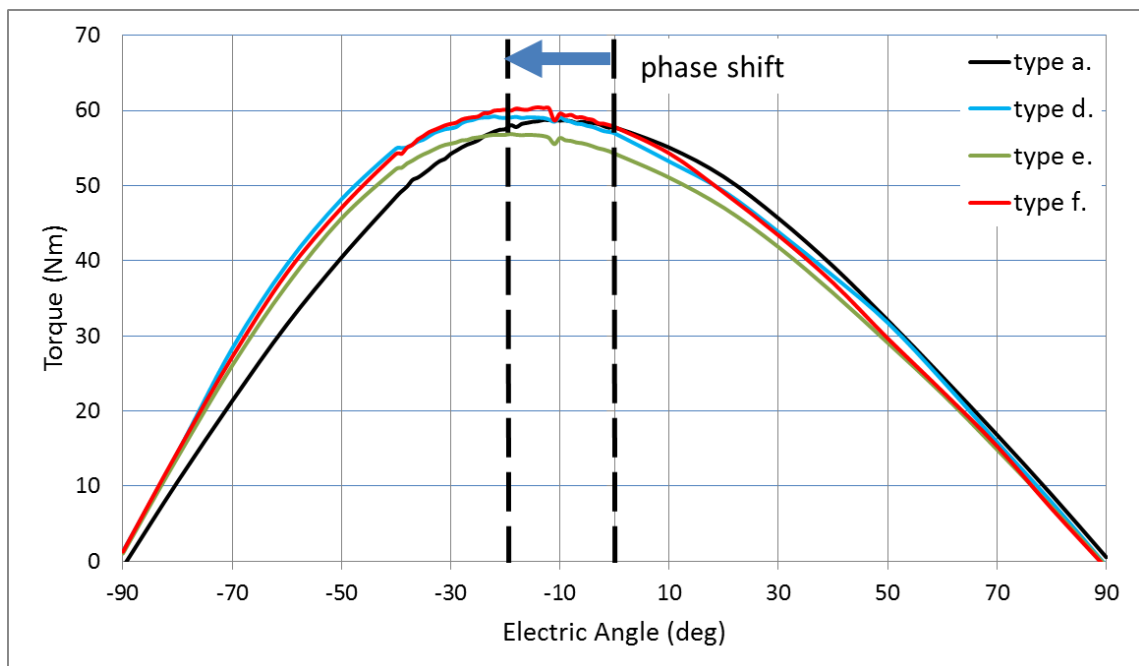


Figure 3-26 Torque vs. current alignment angle

Table 3-2 The topology comparison - Notice, the magnet length of the surface-mounted, I-shaped topologies needs to be divided by 2 when compared to C-arc and V because it merges two pieces of C-arc/V to form one

	Magnet mass		mag length	T		K0	K
topology	kg	ratio	mm	Nm	ratio	Nm/kg	ratio
type a	0.1683	1	4.00	58.59	100%	348.1784	1
type d	0.0823	0.489	1.50	59.23	101%	-	2.07
type e	0.0822	0.488	3.48	53.33	91%	-	1.86
type f	0.0822	0.488	1.74	60.44	103%	-	2.11

Reluctance torque in interior topologies – frozen permeability technique

There are generally two types of torque that can contribute to the time averaged torque, the reluctance torque and the alignment torque. The presence of the reluctance torque component can be detected from the phase shifting phenomenon.

Due to an anisotropic rotor topology, reluctance torque plays a significant role in the makeup of the total torque in the V shaped motor. To analyse this torque component, the frozen permeability technique (FPT) is developed in [96, 97] and adopted here to account for the non-linear permeability of the materials in the model and explained in detail in this section.

The conventional finite element analysis (FEA) used to separate the torque components is firstly discussed.

Conventional FE simulation for the torque components

1. Step 1: total torque

The total time averaged torque at full load condition can be expressed as:

$$T = \frac{m}{2} \cdot p \left(\psi I_p \cos \beta + \frac{(L_q - L_d)}{2} I_p^2 \sin 2\beta \right) \quad (3.14)$$

m – phase number; p – magnetic pole pair; Ψ_f – permanent magnet flux linkage; I_d – current on d axis; L_d – inductance on d axis.

The reluctance torque and the alignment torque in the equation (3.14) are controlled by the phase current magnitude I_p and its alignment angle β ($\beta = 0$ when it is aligned with the q

axis). In FE simulation, the current input value can be set up and the total torque can then be obtained.

In Figure 3-27, the torque is plotted against the alignment angle in a graph with the V-shaped model on the left side. The red line is the q axis of the reference phase, which is in the middle of two adjacent magnet poles. The simulation starts at this point and the alignment angle is gradually reduced from 0 to -90° by rotating the rotor into different positions. The black curve on the right side shows the torque output against the alignment angle.

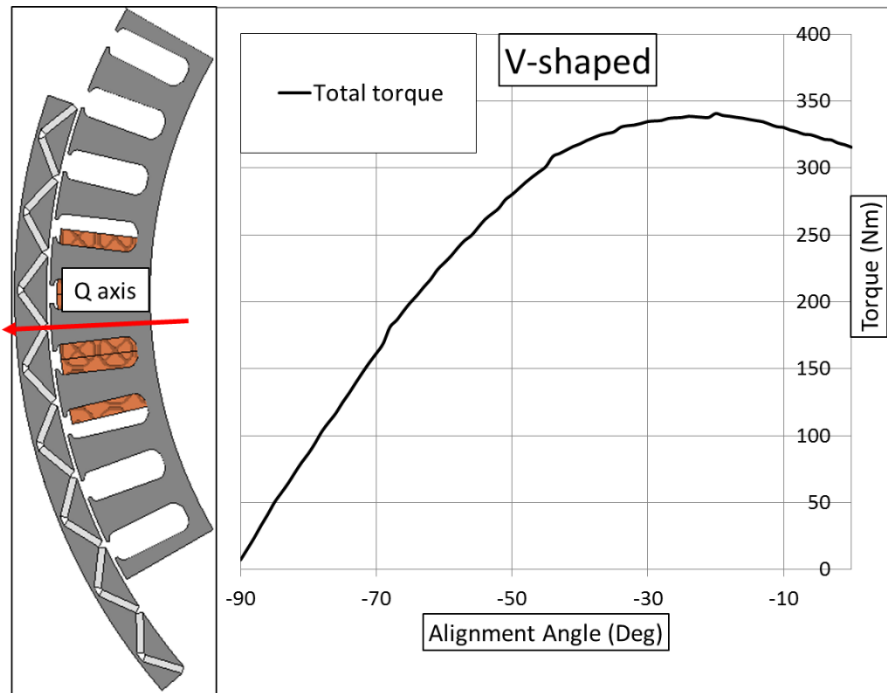


Figure 3-27 The torque vs alignment angle in the full V-shaped 16'' in-wheel motor at full load condition ($I_p=30A$ peak)

2. Step 2: reluctance torque

In order to get the reluctance torque, i.e. the second term $\frac{mp}{2} \frac{(L_q - L_d)}{2} I_p^2 \sin 2\beta$ of eq. (3.14), the magnets are disabled and the same simulation is then performed. The results are shown in Figure 3-28.

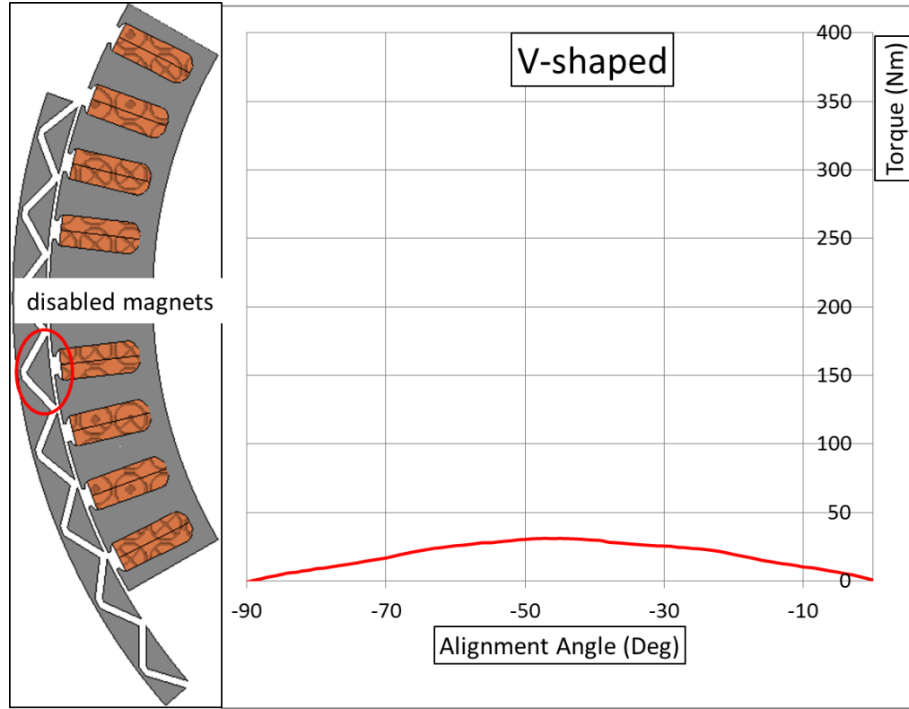


Figure 3-28 The reluctance torque vs alignment angle in conventional method

3. Step 3: alignment torque

Lastly, the alignment torque, i.e. the first term of the equation $\frac{mp}{2} \Psi_f I_p \cos \beta$, is obtained by subtracting the reluctance torque from the total torque.

By using this conventional method, when the magnet is disabled in step 2, the saturation level of the circuit is different from the actual operating condition, which means due to its non-linearity, the value of the relative permeability at step 2 is different from that at step 1. In turn, the value of the d and q inductance will be different from the value at rated operation, leading to errors in the reluctance torque output. This result cannot represent a real time reluctance torque contribution in the rated operation at step 1.

This phenomena can be explained in Figure 330. Permeability is the gradient of the BH curve and can be calculated as $\mu = \frac{B}{H}$. To calculate the reluctance torque at rated condition, the permeability in the lamination that needs to be used is marked as μ_{actual} on the curve. However, in the conventional FEA, at step 2 the permeability μ_{arm} defined by the armature magnetic field strength H_{arm} is the value that is used for the calculation. From Figure 3-29, it is clear that μ_{arm} is not equal to μ_{actual} .

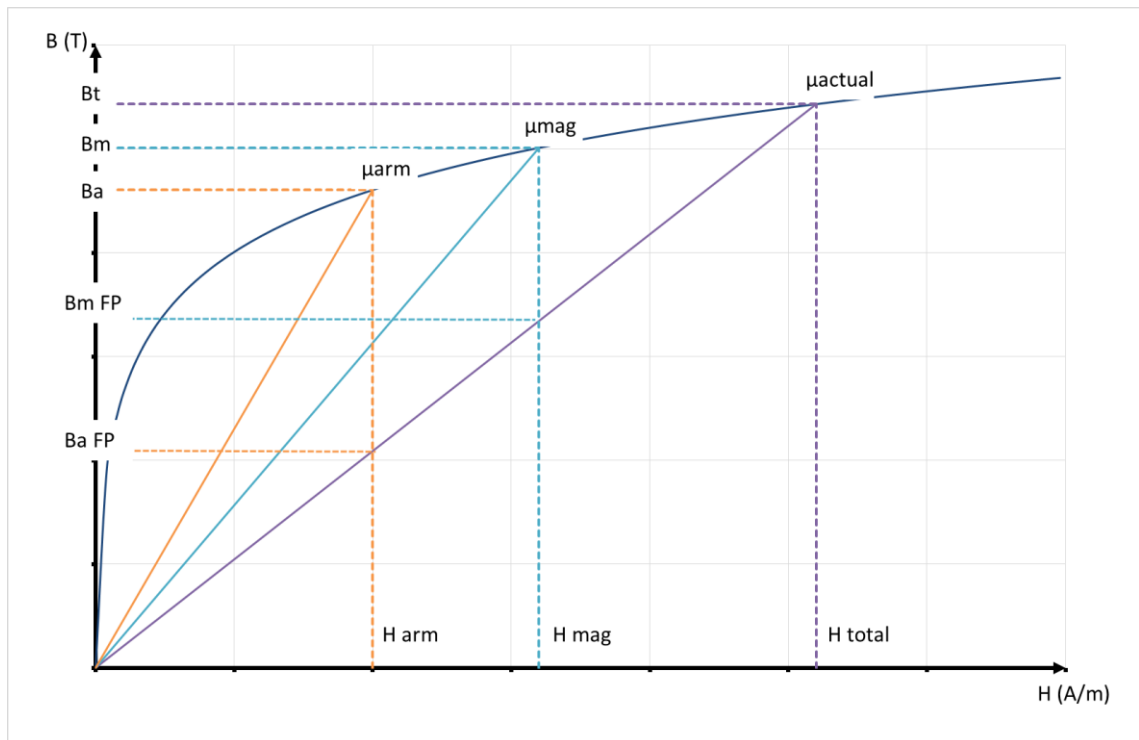


Figure 3-29 The BH curve of the steel lamination in the in-wheel motor model

Saturation level correction with FPT

To solve the issue, the frozen permeability technique is programmed in visual basics and implemented as follows (Figure 3-30):

- Solve the model at the intended condition.
 - 2) Save and freeze the permeability data of every element in the non-linear material.
 - 3) Run the model at other conditions (magnet or armature excitation only) for the torque components.
- Release the permeability data from step 1).
- Set up for the next iteration and repeat step 1-4 (specify new current magnitude and angle).

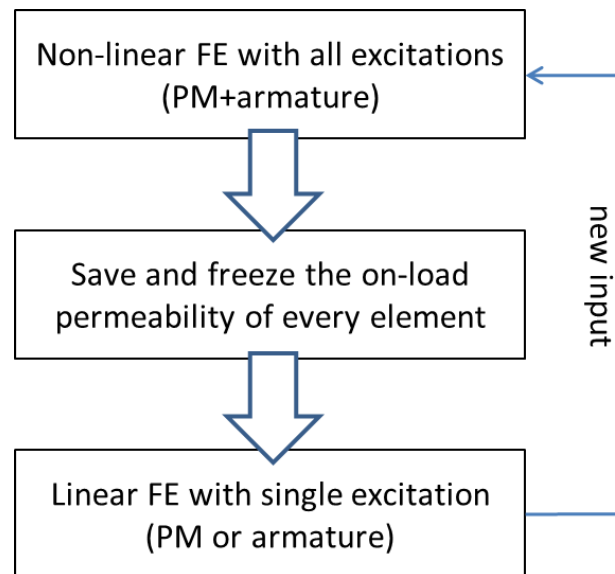


Figure 3-30 The programmed procedure of the FPT

Corrected results with FPT

The reluctance torque with and without FPT are compared in Figure 3-31. With the permeability corrected, the actual reluctance torque of the V is doubled to reach the conventionally obtained value.

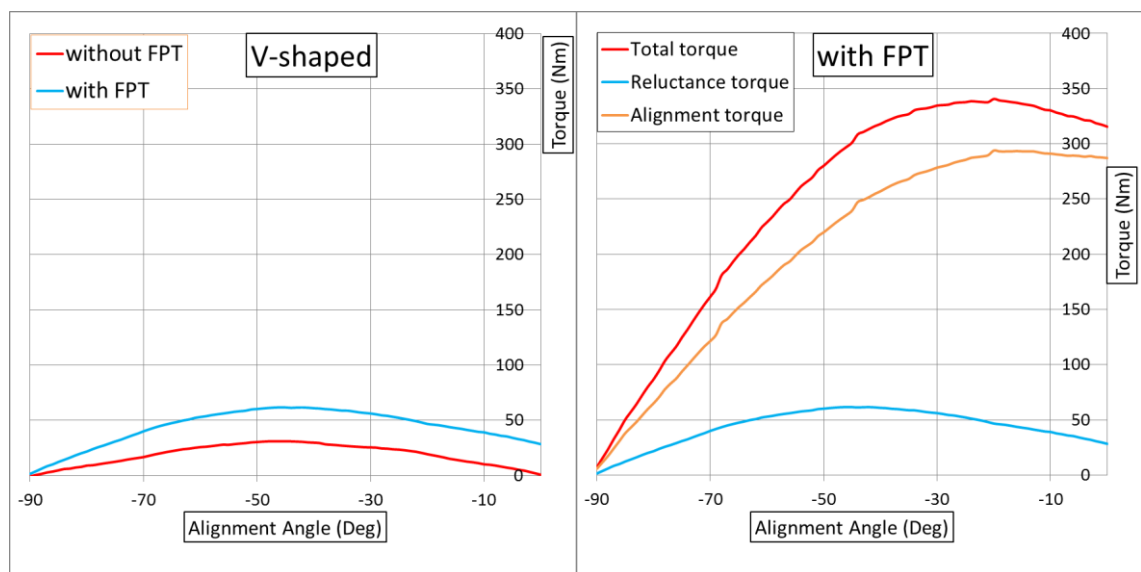


Figure 3-31 Frozen permeability implemented in the reluctance torque calculation

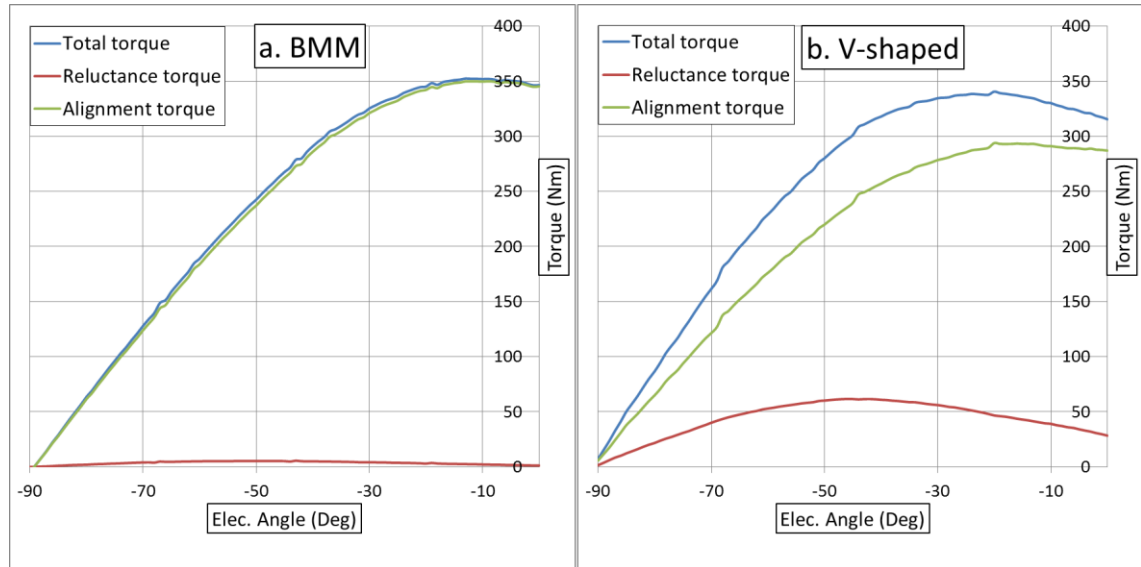


Figure 3-32 Torque vs. Current alignment Angle curve in a.) BMM, b.) V-shaped

In the surface mounted topology, there is no reluctance torque, hence the total torque comes entirely from the alignment torque as can be seen from Figure 3-32. On the other hand, in the interior and V-shaped topologies, the peak reluctance torque can be as high as 18% of the total torque. Hence, the magnet volume can be reduced significantly whilst maintaining the torque output. In other words, the magnet utilisation factor is much higher in the interior topology due to an additional contribution from the reluctance torque.

Resistance to demagnetisation in C, V, I topologies

A magnet with a shorter length normally works at the lower spectrum of its BH characteristic curve for the same required excitation, which is susceptible to demagnetisation issues. Hence, there is a minimum magnet length before it fails to resist the demagnetisation flux.

Demagnetisation analysis is conducted on all three designs in multiple steps of rotor rotation. The maximum armature flux points at different rotor positions relate to the current alignment angle: -135° , -D axis, -45° , etc. In C, I, and V-shaped topologies, the magnet masses are fixed at 0.488 of the BMM and the magnet lengths are shown in Table 3-2.

Like in the surface mounted topology, demagnetisation occurs in the C-arc when the overloading current vector is pointing at the -d axis directly against the excitation flux. As illustrated in Figure 3-33, there is a large area that is demagnetised. A magnet length of 1.50mm in this C-arc model is clearly too thin to resist demagnetisation.

The 1.74mm magnet length is also too thin to resist the armature opposing flux, as is demonstrated in the V-shaped topology. Only the I-shaped design with a length of 3.48mm successfully keeps the flux level in the magnet above the knee point. However, by increasing the magnet length to 2mm or above, both C-arc and V-shaped can safely pass the demagnetisation test, sacrificing their magnet utilisation factor slightly, shown in Figure 3-36.

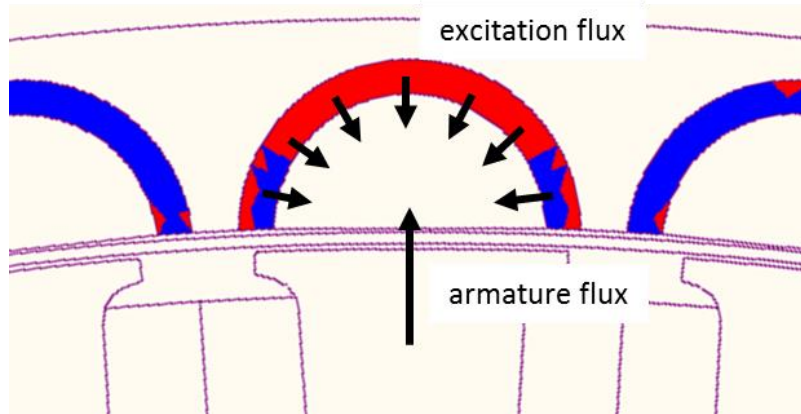


Figure 3-33 The demagnetisation area in C-arc

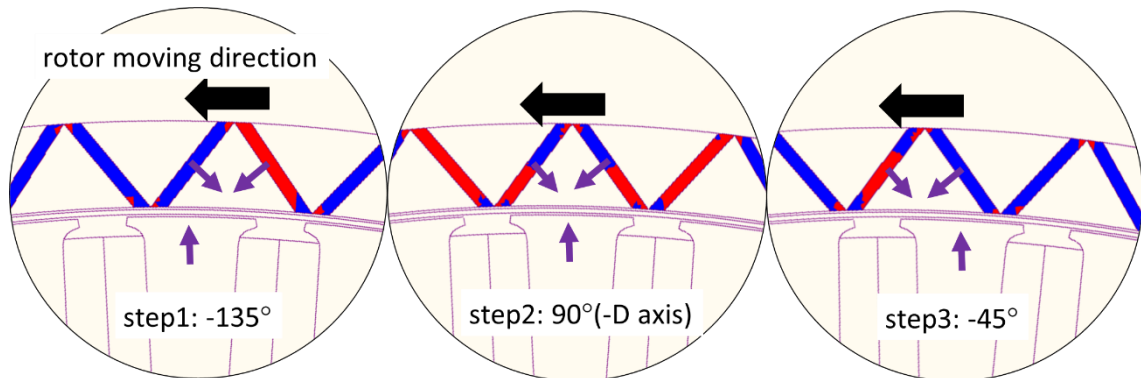


Figure 3-34 The demagnetisation area in V-shaped

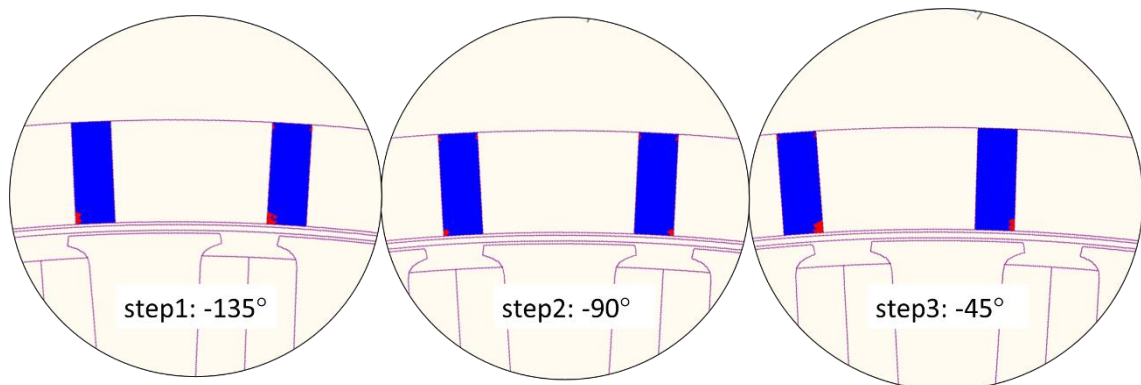


Figure 3-35 The demagnetisation area in I-shaped

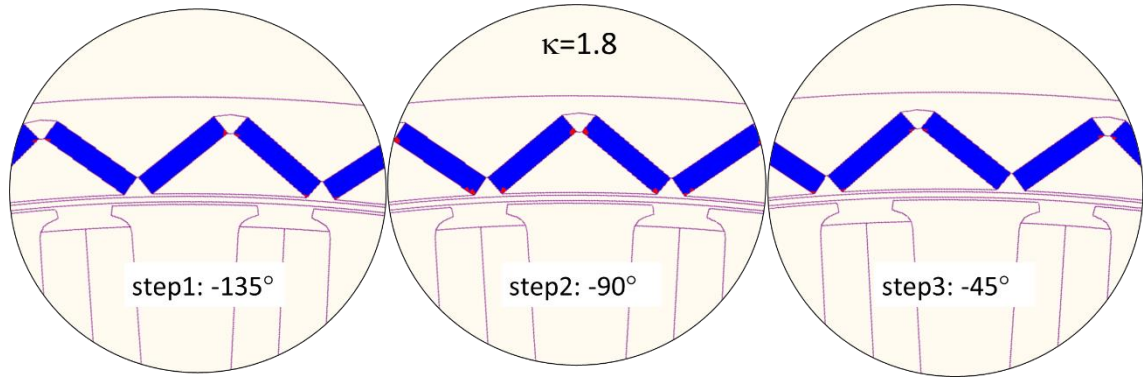


Figure 3-36 The V-shaped magnet with 2mm magnet length

Selection between the C, V and I topologies

The C-arc magnet is closely related to the V-shaped, both offer the highest magnet utilisation factor κ among the seven studied topologies. Nonetheless, C-arc is less practical than V. The brittle nature of the magnet material and the concentric magnetisation direction makes it easy for C-arc magnets to snap. Furthermore, to manufacture the same amount of magnet mass with the specified shape, C-arc magnets require more material compared to rectangular magnet pieces due to the unavoidable wastage in the central area of the arc when stamping. So the V-shaped topology is more preferable.

The V-shaped design has a complete ring-shaped structural support at the back of the magnet pieces, whilst the I-shaped magnets and iron pieces in between need to be bonded when assembled into the full rotor. Furthermore, when changing the magnet length, the magnet utilisation level is higher in the V-shaped design at any given torque or magnet mass, compared to the I-shaped, shown in Figure 3-37.

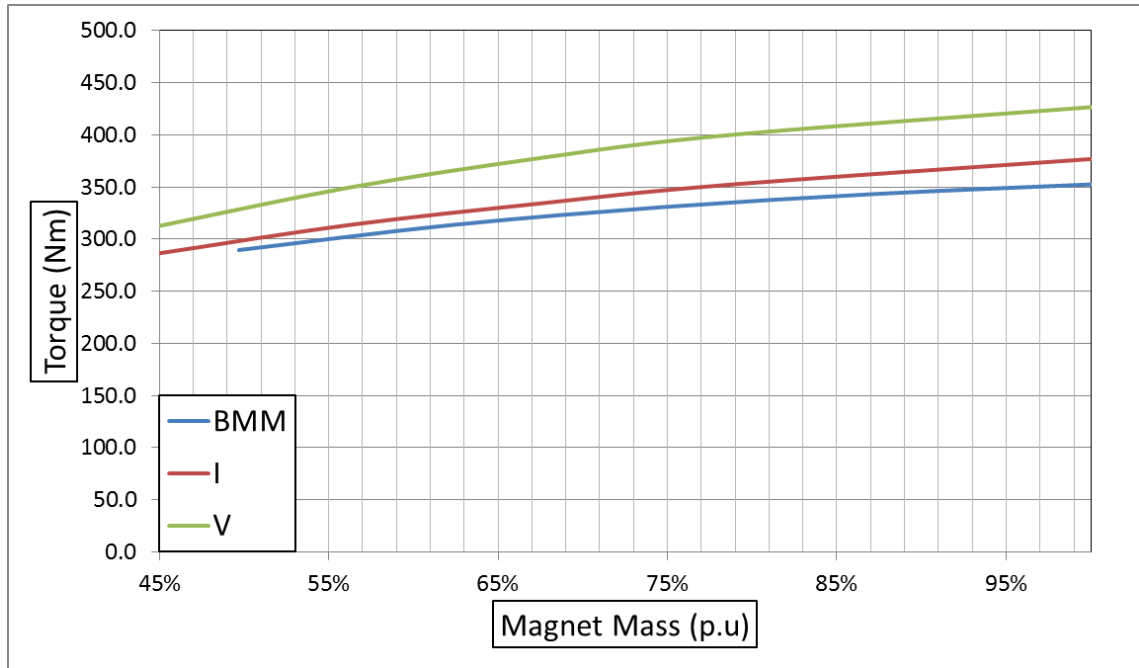


Figure 3-37 Magnet utilisation comparison between BMM, I-shaped and V-shape

3.1.4. Conclusion

In this section, an analytical model is adopted to find the optimum split ratio for the highest torque density in the outer-rotor surface-mounted motor. The calculated ratio is extremely high compared to a conventional inner rotor topology and is in good agreement with the BMM.

With this fixed split ratio, various rotor topologies are then researched. With careful choice, it has been demonstrated that it is possible to greatly decrease the magnet mass employed in the surface mounted motor without a major loss of performance or increased risk of demagnetisation. The surface-mounted magnet topology is replaced with the V-shaped magnet topology, reducing magnet mass by 44% with improved demagnetisation resistance and a matching torque output, seen in Figure 3-37.

The V-shaped topology gives highest magnet utilisation factor due to assistance from additional reluctance torque. The demagnetisation issue is avoided by introducing iron shielding to protect the magnets from the opposing armature flux across the air gap. Also, there would be less loss in the magnets indicating a cooler working temperature in this design.

3.2.V-shaped Topology Modification

In this section, the V-shaped topology is researched in terms of the potential slot/pole combination, the dynamic torque performance based on the torque-speed characteristic curve and structural integrity. An easy-to-manufacture version of the V-shaped motor is proposed.

3.2.1.Investigation on slot/pole combinations

As explained in section one, in order to reduce the magnet material, a motor with the highest level of magnet utilisation while maintaining the rated torque is to be designed. Magnet utilisation is related to magnet length. It is difficult to retain magnet mass per pole when using thinner magnets with a limited magnet length. A higher pole number can be used to maintain the overall magnet mass (hence the torque). Potential slot/pole combinations have been investigated and are shown in Table 3-3 and Figure 3-38. The new combination with a higher pole number, marked in yellow, is found to improve the torque density by 6% in the V-shaped topology compared to the V design in section one [98].

Table 3-3 The possible slot/pole combination

combinations	slots	poles	sub-motors	Harmonic winding factor			
				1st	5th	7th	11th
a	72	64	8	0.945	0.14	0.061	0.061
b	63	56	7	0.945	0.14	0.061	0.061
c	60	64	4	0.951	0.173	0.111	0.045
d	60	56	4	0.951	0.173	0.111	0.045
e	54	60	6	0.945	0.14	0.061	0.061
f	54	48	6	0.945	0.14	0.061	0.061
g	45	50	5	0.945	0.14	0.061	0.061
h	45	40	5	0.945	0.14	0.061	0.061
j	36	48	4	0.866	0.5	0.5	0.5
k	36	40	4	0.945	0.14	0.061	0.061

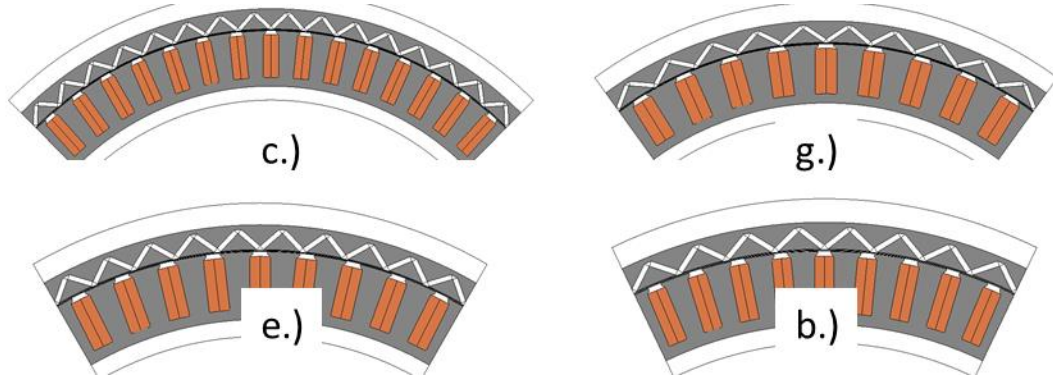


Figure 3-38 The geometric drawing of different slot/pole combinations in different topologies

The winding configuration of this new combination and the classic winding factor calculation are explained in the following section.

The potential combination – s9p10

The selection of slot and pole number determines its harmonic contents and is essential to the winding configuration, fault tolerance and the iron core back thickness. The benchmark motor is a slot, 48pole (54s48p) combination, type f in Table 3-3, and the motor for the BMM wheel is a 72s64p combination (type a) in Table 33. Both of these are multiples of the basic combination - s9p8. The s9p10 combination (type e) can be achieved by simply increasing the pole number without changing the winding configuration and geometrical stator design.

To compare the torque difference between these two combinations, s9p8 and s9p10, relationship between the current, back EMF, torque and angular velocity in the three phase machine, (assuming its lossless during the energy conversion), is shown in the classic eq. (3.15).

$$\begin{cases} P_{elec} = P_{mech} \\ 3EI = T\omega_m \end{cases} \quad (3.15)$$

Where E is the root mean square (RMS) value of phase back EMF (electromotive force), I is the RMS value of phase current input, T is the time average torque output and ω_m is the mechanical angular velocity of the rotor. Assuming that the current value from the inverter and the angular velocity are fixed, then the torque output solely depends on the phase back EMF.

The phase back EMF is the summation of all of the induced voltage of the series connected coils per phase. The stator coils are fixed in the air gap, when the rotor, hence the no-load air gap flux, revolves around the air gap at a certain speed. For a $d\theta$ degree segment of rotor, flux that moves across one slot coil, half of a complete coil in a double layer winding, the induced voltage can be calculated by eq. (3.16).

$$\begin{cases} E_{sc} = \frac{d\psi}{dt} = \frac{d\psi}{d\theta_e} \cdot \frac{d\theta_e}{dt} = \omega_e \frac{d\psi}{d\theta_e} \\ \psi = \phi \cdot N_{sc} \\ \omega_e = p \cdot \omega_m \end{cases} \quad (3.16)$$

Where θ is the rotor position displacement, ψ is the flux linking the coil, ϕ is the flux linking single turn of the coil, N is the number of turns per coil, p is the rotor pole pair and subscripts 'sc' and 'e' mean 'slot coil' and 'electrical', respectively.

The flux that is linking a coil in the s9p8 and s9p10 combinations can be illustrated in Figure 3-39. The reference phase winding configuration is highlighted by the black square in the sub-motor on top. The sinewave graph shows the fundamental flux generated by the magnet that travels across the air gap. The positions of the coil in the air gap from s9p8 and s9p10 are illustrated on the two axes beneath the sinewave axis. The shaded area on the sinewave is the amount of flux that is enclosed/linked by the coil of the s9p8 motor. It can be seen that, even though the coil from s9p10 spans more distance, the flux it encloses is the same as the coil in s9p8 because the flux is cancelled out in the additional enclosed area. The phase segments of s9p8 and s9p10 are also illustrated on the left side. The green lines represent the flux path from magnet excitation.

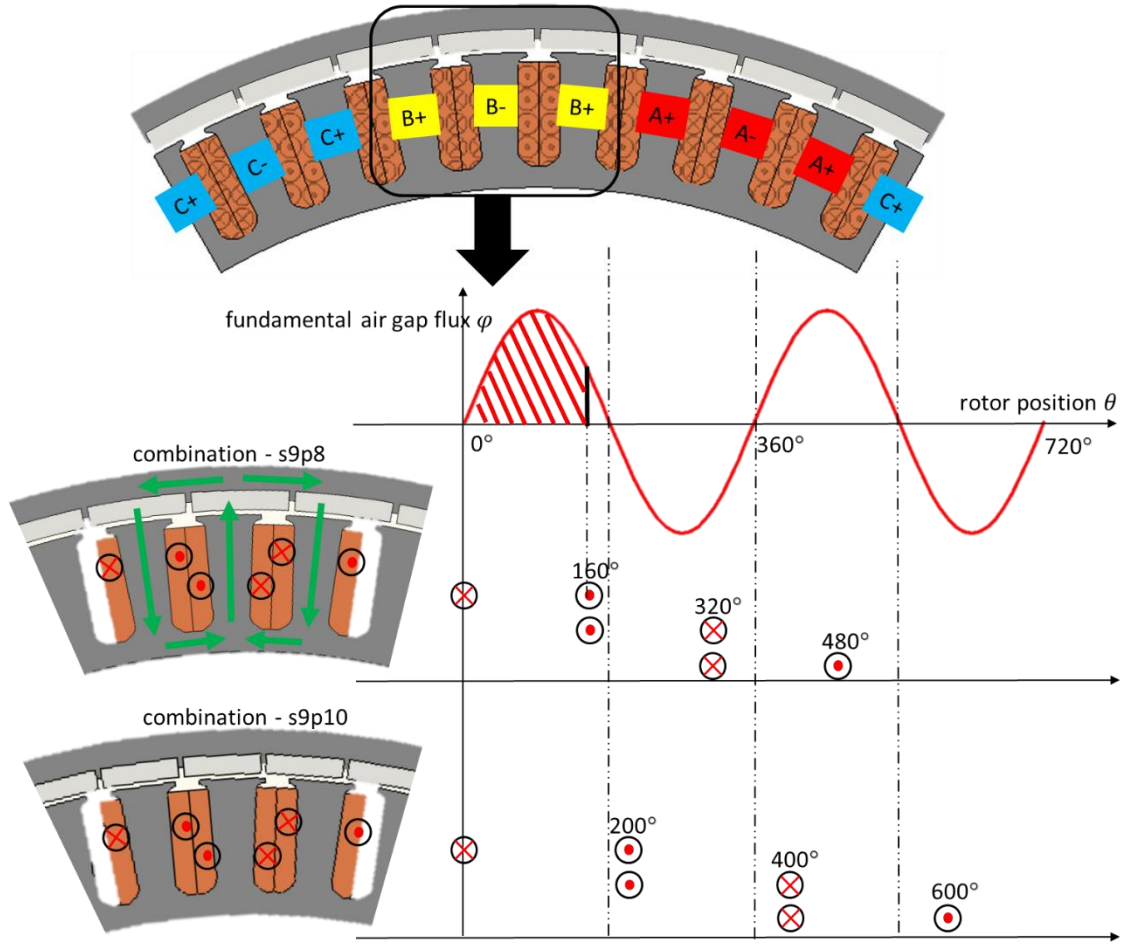


Figure 3-39 The flux linkage with winding configuration

Compared to the fully pitched windings, the coil span is from 0° to 180° , both s9p8 and s9p10 are short pitched by $\alpha = \pm 20^\circ$. These angles can be applied into eq. (3.17) to calculate the winding factor, which indicates how much back EMF can be generated compared to a fully pitched, non-distributed ideal winding configuration. The derivation is included in the next section.

$$\begin{cases} K_w = K_d \cdot K_p \\ K_p = \cos\left(m \frac{\alpha}{2}\right) \\ K_d = \frac{\sin\left(\frac{nm\alpha}{2}\right)}{n \sin\left(\frac{m\alpha}{2}\right)} \end{cases} \quad (3.17)$$

Where, K_w is winding factor, K_p is short pitch factor, K_d is distribution factor and m is the back EMF harmonic order.

Short pitch factor – the back EMF of a coil

The fundamental flux is a sinewave, so the back EMF of a slot coil, half of a coil, is also a sinewave with a 90° phase shifted ahead after the differentiation in eq. (6.3). The $\frac{d\psi}{d\theta}$ term can be represented as $\hat{\psi}\cos\theta$, assuming $\psi = \hat{\psi}\sin\theta$.

The back EMF of a single coil is the summation of the induced voltage on the go side and return side of the coil. The peak value is reached at the time instant shown in Figure 3-40. The value is calculated in eq. (3.18) for fully pitched (first line) and short pitched (second line) coils respectively. The ratio between these two is defined as the short pitch factor of the fundamental, which is equivalent to the second line in eq. (3.17) with harmonic order $m=1$.

$$\begin{cases} [\cos(0) - \cos(\pi)] \cdot \hat{\psi}\omega_e = 2\hat{\psi}\omega_e \\ [\cos(\frac{\alpha}{2}) - \cos(\pi - \frac{\alpha}{2})] \cdot \hat{\psi} = 2\hat{\psi}\omega_e \cdot \cos(\frac{\alpha}{2}) \\ K_{p1} = \cos(\frac{\alpha}{2}) \end{cases} \quad (3.18)$$

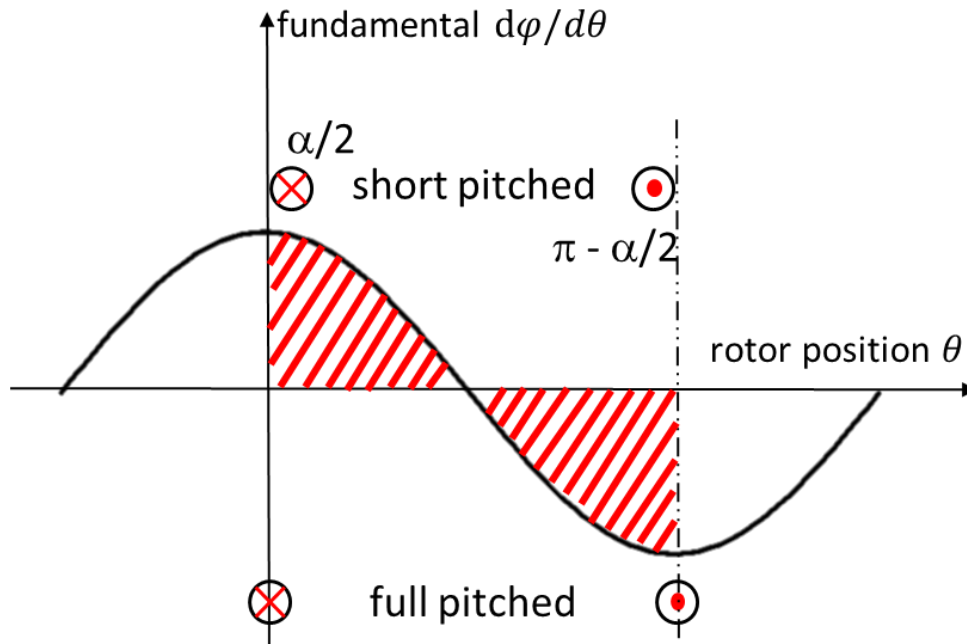


Figure 3-40 The rotor position of the peak back EMF time instant

Distribution factor – the back EMF of coils in series

After the back EMFs of each coil have been calculated, it is necessary to consider the phase difference between each coil in a phase. As it can be seen from Figure 3-39, the first

coil starts at 0° and the second starts at 160° . There is a 160° phase difference. However, because they are wound in opposite direction, the back EMF presented in the equivalent circuit is 20° phase shifted between these two coils. This angle is generally equal to a short pitched angle in a single tooth winding configuration. Notice, in distributed winding, the short pitched and distributed angles could be different because each coil does not need to be concentrated on one tooth.

The magnitude of back EMF in n coils, $n=3$ in both s9p8 and s9p10, can be found by projecting the phase vectors in the red circle onto the black sinewave in Figure 3-41. After summing up these vectors, the magnitude of the resultant vector is the back EMF value of the phase. The phasor summation can be expressed in Figure 3-42. The back EMF for each coil (E_c) can be related to r by the eq. (3.19).

$$E_c = 2r \sin\left(\frac{\alpha}{2}\right) \quad (3.19)$$

The resultant back EMF (E_{res}) is calculated:

$$E_{res} = 2r \sin\left(n \frac{\alpha}{2}\right) \quad (3.20)$$

Rearrange the eq. (3.21) to get:

$$r = \frac{E_c}{2 \sin\left(\frac{\alpha}{2}\right)} \quad (3.21)$$

Substitute eq. (3.20.) into (3.21), get:

$$E_{res} = \frac{E_c \sin\left(n \frac{\alpha}{2}\right)}{\sin\left(\frac{\alpha}{2}\right)} \quad (3.22)$$

If all the coils are non-distributed, then there will be no phase difference between them. The ideal phase voltage will be nE_c . Hence the distribution factor is defined as the ratio between E_{res} and nE_c shown in eq. (6.10).

$$K_d = \frac{\sin\left(\frac{n\alpha}{2}\right)}{n\sin\left(\frac{\alpha}{2}\right)} \quad (6.10)$$

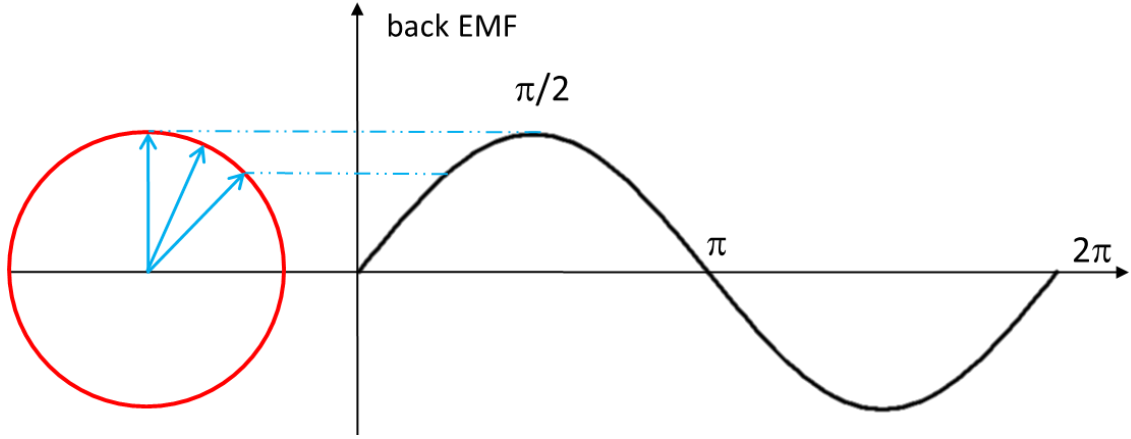


Figure 3-41 The back EMF magnitude difference in each coil

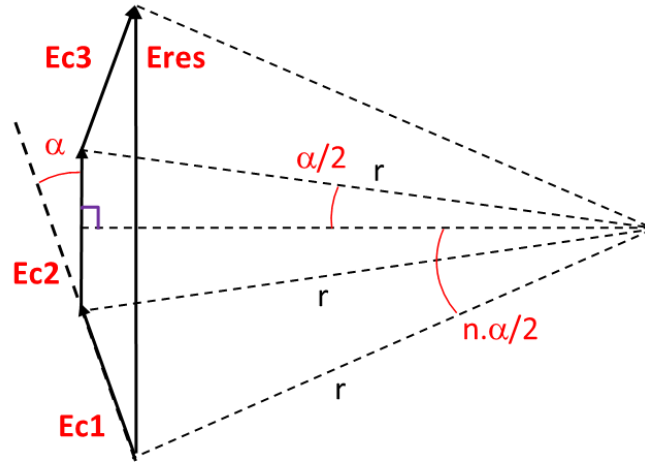


Figure 3-42 The coil distribution effect on phase back EMF

Back EMF difference between s9p8 and s9p10

Upon inspecting the winding factor equation, it is clear whether the short pitching angle α is positive (s9p8) or negative (s8p10), the winding factor will always be between 0 to 1. The result calculated for both s9p8 and s9p10 is 0.945. Plug this into eq. (3.23), and the RMS phase back EMF can be obtained. Where N_{ph} is the coil turns per phase.

$$E_{ph,rms} = \sqrt{2} \cdot K_w \hat{\phi} \cdot N_{ph} \omega_e = \sqrt{2} \cdot K_w \hat{\psi}_{ph} \omega_e \quad (3.23)$$

The flux linkage of 2D transient stimulation on the benchmark motor at 100 rpm is shown in Figure 3-43. It is a sinusoidal shape with negligible harmonics. The peak phase flux linkage is 0.0301 and 0.0255 Wb for s9p8 and s9p10, respectively. Hence, the peak fundamental back EMF of (s9p8)*6 is 7.15 Volts:

$$\hat{E}_{ph} = K_w \hat{\psi}_{ph} \omega_e = 0.945 * 0.0301 * \frac{100}{60} * 2\pi * \frac{8}{2} * 6 = 7.15 \quad (3.24)$$

The ' $\frac{8}{2} * 6$ ' term represents the total pole pairs for the BMM formed by six s9p8 sub-motors. The value of (s9p10)*6 is calculated as 7.42 Volts. This can be confirmed with the FE result.

As seen in Figure 3-44, the back EMF waveforms from FE contain harmonics and are not purely sinusoidal. The data is further processed in *Matlab* and the Fast Fourier Transformed (FFT) harmonic spectra are shown in Figure 3-45. The fundamental from FEA is merely 3.3% higher than the analytical calculation.

In the s9p10 model, there is a 3.9% increase on the back EMF value indicating a torque increase if switching from s9p8 to s9p10. This increase does not come from the winding factor difference or any stator modification but is simply because of a less saturated magnetic circuit. The larger pole number a motor possesses, the thinner core back required for the same level of saturation. Due to a high pole number, the magnetic circuit in the s9p10 is slightly less saturated compared to the s9p8 with an identical core-back.

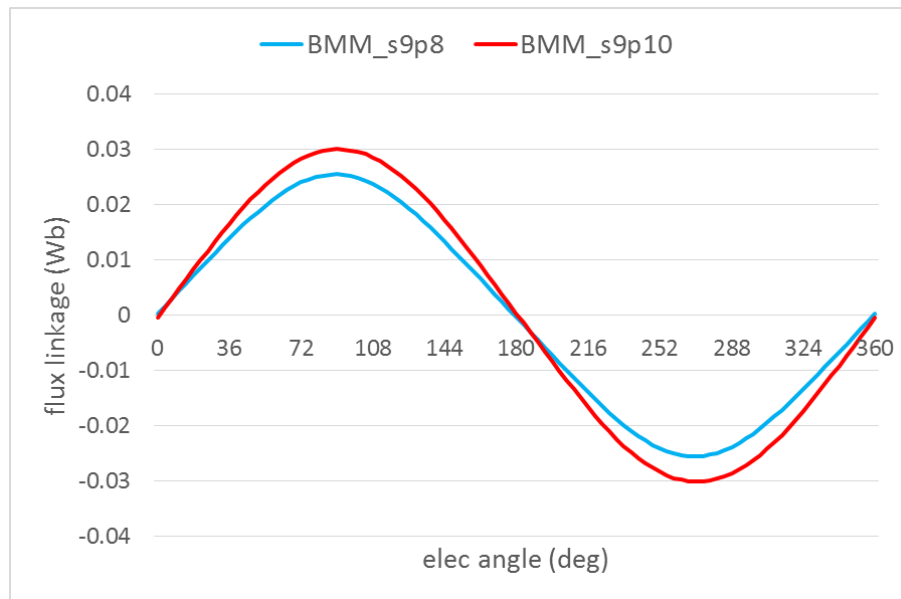


Figure 3-43 Flux linkage against electric angle in benchmark (surface-mounted) motor BMM

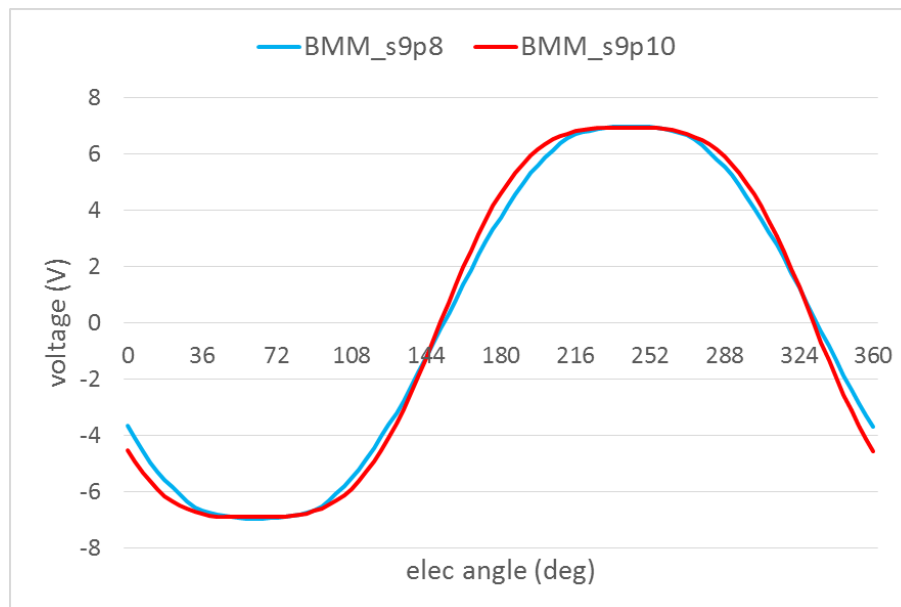


Figure 3-44 Back EMF against electric angle at 100rpm in benchmark (surface-mounted) motor

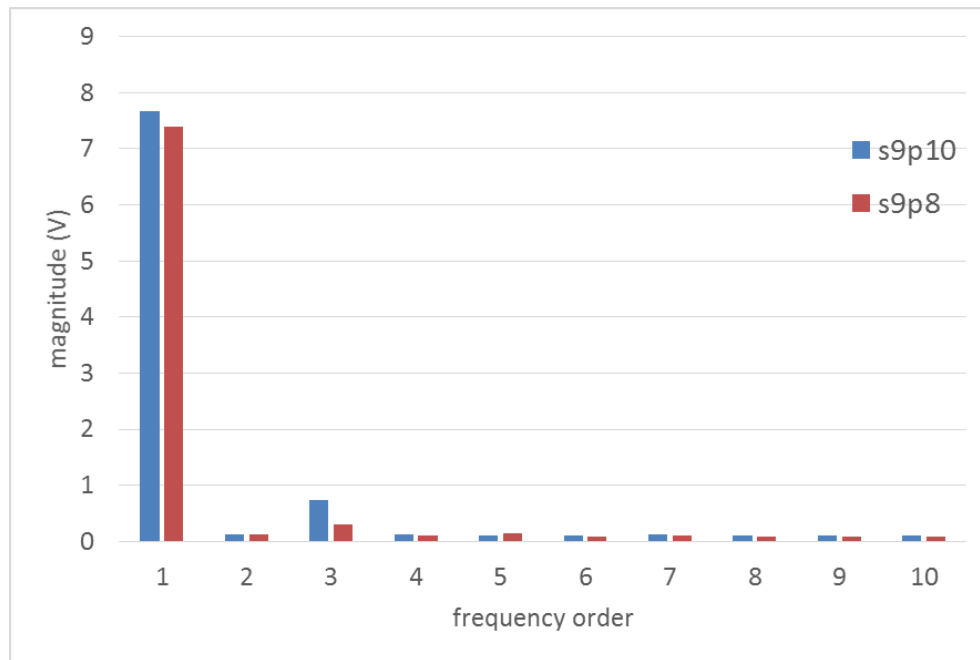


Figure 3-45 The back EMF harmonic spectra in BMM

Torque difference between s9p8 and s9p10

With an increased back EMF, the torque output is expected to be higher in the s9p10 slot/pole combination. The 2D static FE result in Table 3-4 shows that there is a 3.8% torque improvement in the surface-mounted model. Interestingly, the torque ratio is even higher in the V-shaped design. In Figure 3-46, the pole width in the s9p10 is nearly equal to the stator tooth width helping to create a better flux path across the air gap and less leakage.

Table 3-4 Torque comparison between s9p8 and s9p10

rated torque ratio		
BMM	s9p8	1
	s9p10	103.8%
V	s9p8	1
	s9p10	106.6%

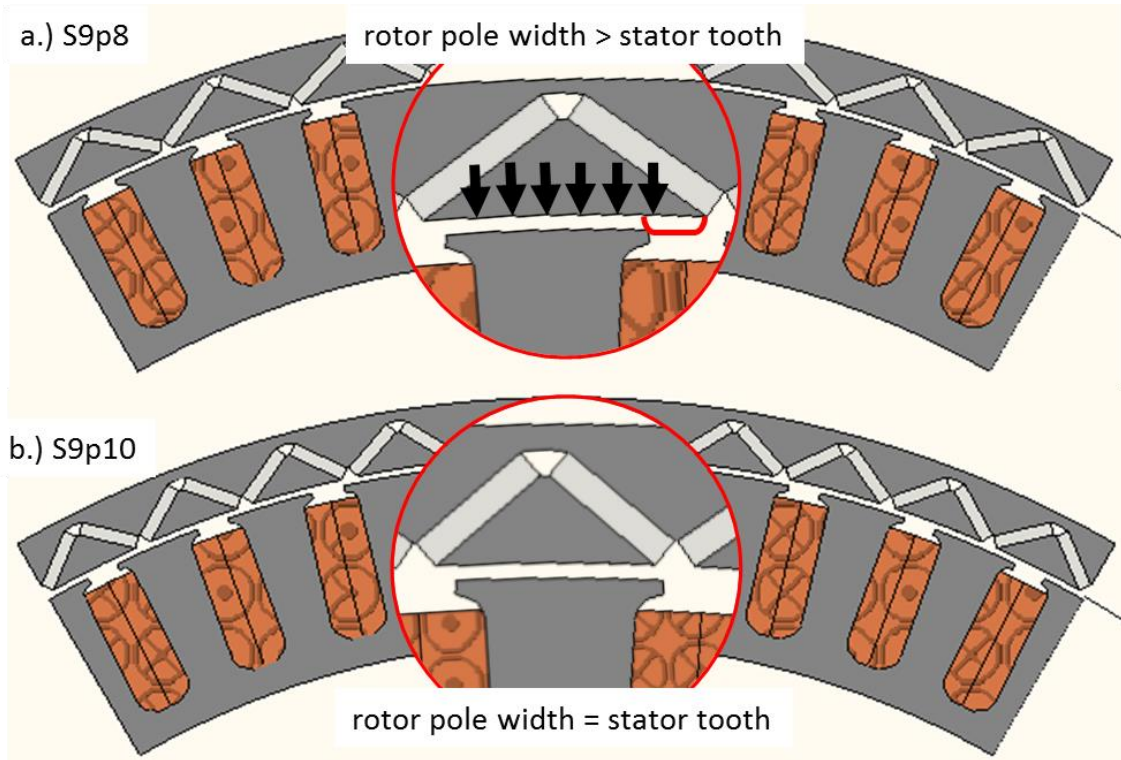


Figure 3-46 The geometric drawing of a.) s9p8 and b.) s9p10 benchmark motors

Impedance difference between s9p8 and s9p10

As static torque output in s9p10 is increased when using the same magnet material, a higher pole option can therefore use less magnet material with the same rated torque target.

However, here a new issue is raised - the impedance is increased. This is because to achieve a certain mechanical speed, the s9p10 one needs to operate at a higher electric frequency resulting in increased synchronous impedance. Consequently, the corner speed is lower in the s9p10 model for the same inverter voltage limit. The torque-speed characteristic curve is illustrated in Figure 3-47. With an identical rated current value and maximum voltage limit for the continuous case, the corner speed of the benchmark motor BMM_s9p8 (surface-mounted), V_{s9p8} and V_{s9p10} is 529rpm, 493rpm and 392rpm, respectively, Figure 348. Notice, the magnet mass is 1:0.56:0.56 in these three models.

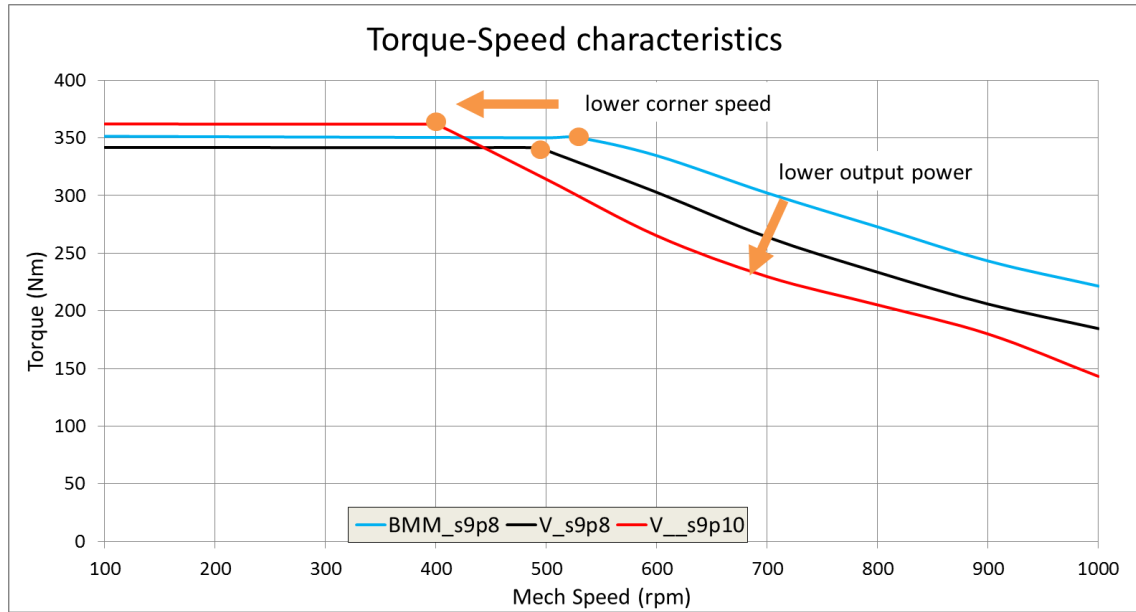


Figure 3-47 The torque-speed characteristics of the BMM and the V

The corner speed of the V_s9p10 is 74% of the BMM_s9p8, which means a 3% higher torque capability is obtained compared to the BMM at a cost to losing 24% of its rated output power on corner speed. In order to maintain the output power, the VA rating of the inverter must be increased, which leads to a higher electronic device cost. On the other hand, the corner speed of V_s9p8 is 93% of the BMM, which means it is possible to retain the original corner speed (529rpm) by outputting 87% of the torque in the BMM.

After discussions with the Protean R&D team, the decision was made to keep the original slot/pole combination (s9p8) because of a higher output power and due to the team's accumulated knowledge and techniques acquired from the s9p8 benchmark motor – the BMM.

3.2.2. Modification based on manufacturing concerns

Figure 3-48 shows the ideal V shape design compared to an easy-to-manufacture version shown in [99-102]. The ideal V design allows for a higher torque capability, whereas the conventional design makes the manufacturing and assembling procedure easier due to a mechanically preferred single piece rotor lamination. Furthermore, features in the red circle in the conventional V can provide necessary mechanical rigidity against any force exerted on the rotor. However, the conventional one [100] permits four flux leakage paths per pole as shown in Figure 3-49 (2), reducing the torque by 20%. These 2 concepts represent the extreme nature of manufacturability verses magnet utilisation.

The seven different variations of the V-shaped design have been investigated to seek the best V option which can accommodate for both ends of the design.

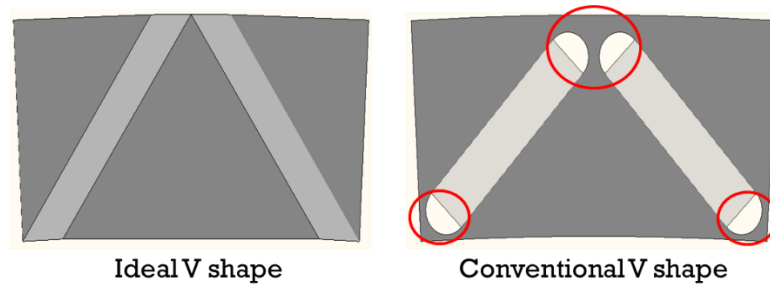


Figure 3-48 The flux leakage path in the conventional V-shaped magnets

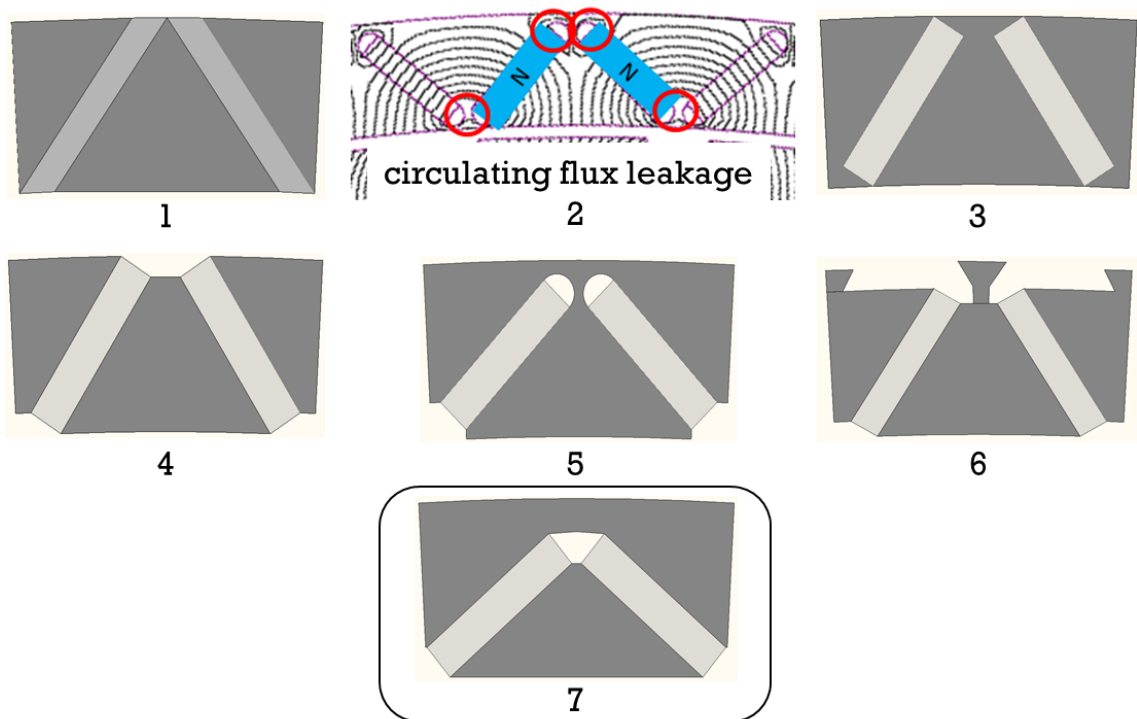


Figure 3-49 The V-shaped magnets design variations [98]

The magnets are made rectangular in design 2 to ease the magnet cutting process and reduce magnet material wastage. However, flux leakage paths are introduced due to the iron ribs used to hold the rotor as a whole piece. The leakage paths can be eliminated in design 4, by making the single piece lamination into a multi-piece lamination, which is clearly more difficult to position, assemble and fix onto the outer rim. To help to locate the pieces during assembly and support them while revolving, a dovetail shaped mechanical feature is introduced in design 6. However, it still results in additional leakage flux, a similar situation occurs in design 5.

A new shape is then invented in design 7. This newly designed shape includes an air bridge on two adjacent magnets which form one pole. The outer/upper leakage flux path is blocked by introducing an air bridge. Also, there is no leakage path on the lower/inner side of the magnetic pole because there is zero iron in that area. Furthermore, there is only one sharp point on each magnet sitting on the periphery of the inner rotor radius and directly against the potential demagnetisation flux. Consequently, demagnetization resistance will be further improved. From the field plot in Figure 3-50, it is clear that the amount of flux short-circuiting at the centre of the V, i.e. the outer/upper leakage flux path, is much less in design 7.

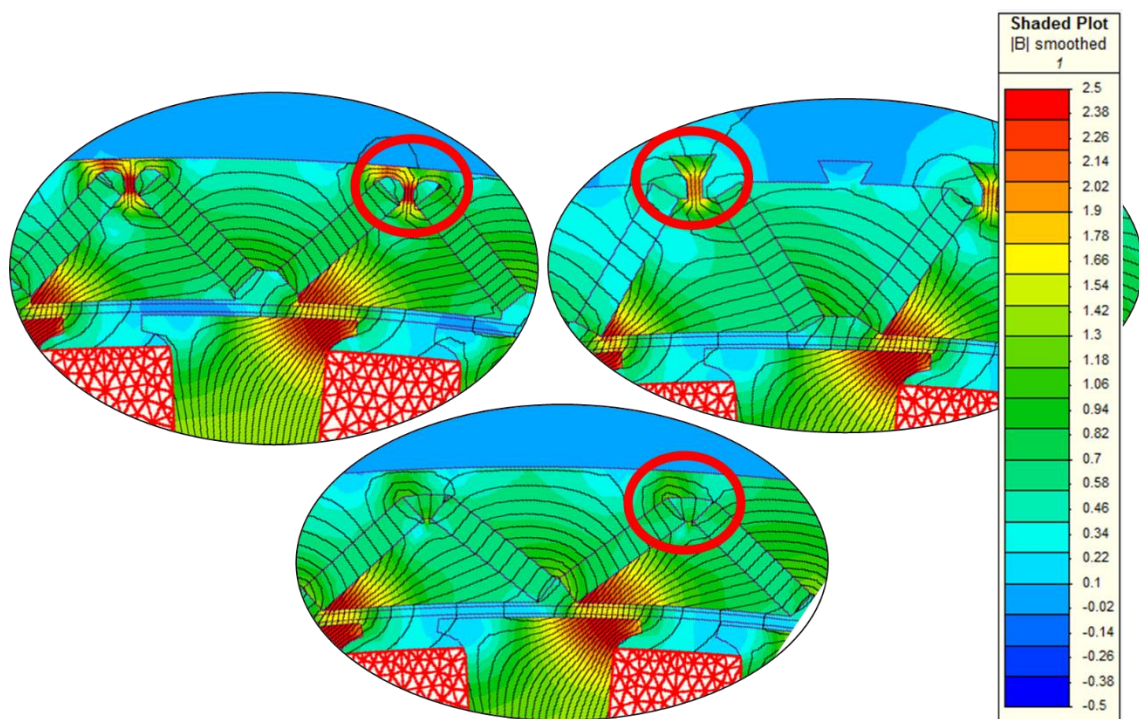


Figure 3-50 The field plot of the flux leakage in V – design 5, 6, 7

Hence, the torque capability in design 7 is expected to be the second highest in relation to the ideal design, i.e. design 1 in Figure 3-49. This is confirmed by 2D static FE simulation at rated current input and fixed at 56% of the original magnet mass in the BMM (surface-mounted magnet) as is shown in Figure 3-51. Design 7 is selected to be taken forward as the best compromise between performance and manufacturability.

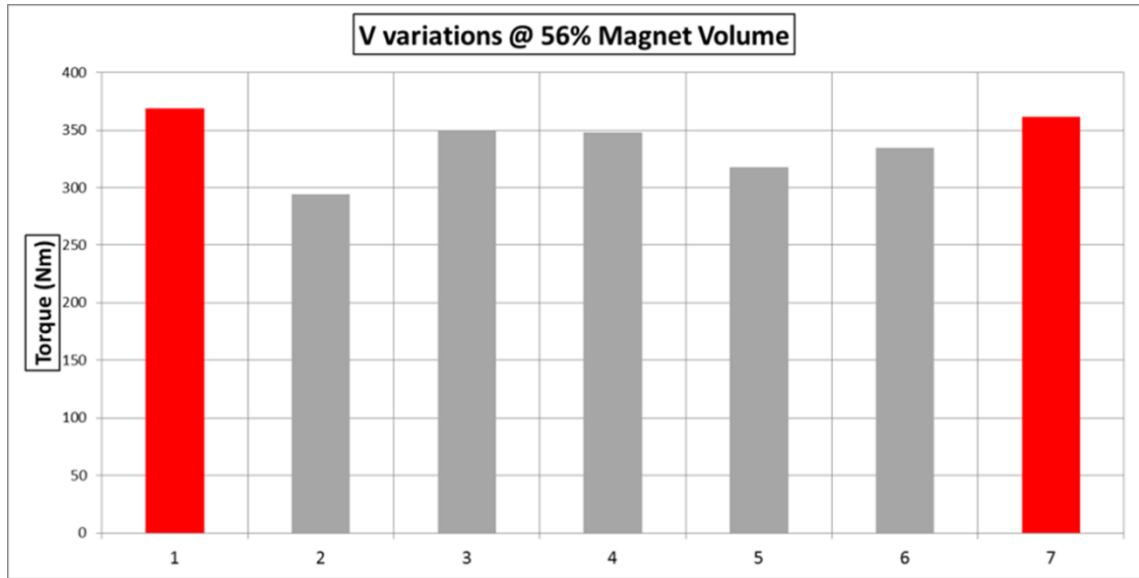


Figure 3-51 Torque performance comparison

In summary, the torque capability of the V shape design, hence the magnet utilisation factor κ , is compromised in a conventional method to allow for an easy manufacturing process. A new air-bridged design (design 7) is created to maintain the torque performance while ensuring a single outer rotor piece for manufacturing consideration.

3.2.3. Analysis of structural integrity

In the modified design (design 7), the front triangular-shaped iron piece and magnet pieces all need to be bonded onto the back rotor ring. Hence, it is necessary to study the force acting on these pieces to determine the mechanical feasibility of the V design concept.

There are two types of force acting on the rotor piece while it is revolving, namely the centrifugal force due to rotation and the magnetic attractive/repulsive force from the adjacent magnets and the stator teeth across the air gap. The centrifugal force on these pieces can be cancelled out by the outer rim holding the rotor as a whole. The magnetic force, however, is complex between rotor pieces. FE analysis is required.

When exciting one phase with the maximum current of opposite polarity to the testing rotor pole, illustrated in Figure 3-52. The air gap distance is kept normal (1mm). The force is simulated in 2D static solution and shown in Figure 3-53. Theoretically his amount of force can be safely counteracted by the chosen adhesive, [103] .

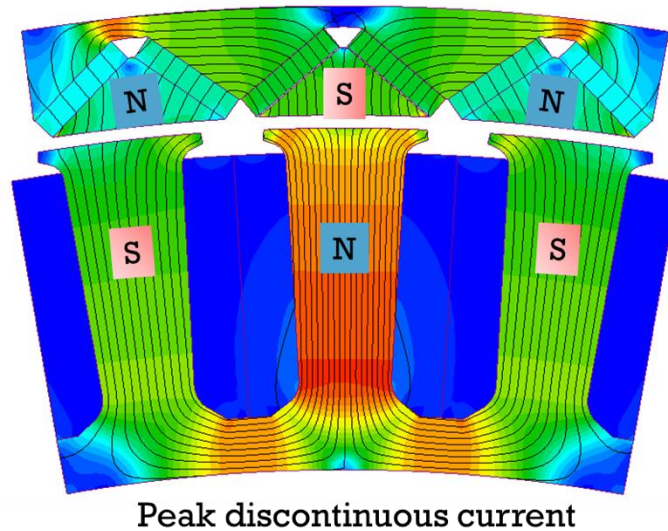


Figure 3-52 Excitation setup for the magnetic force study

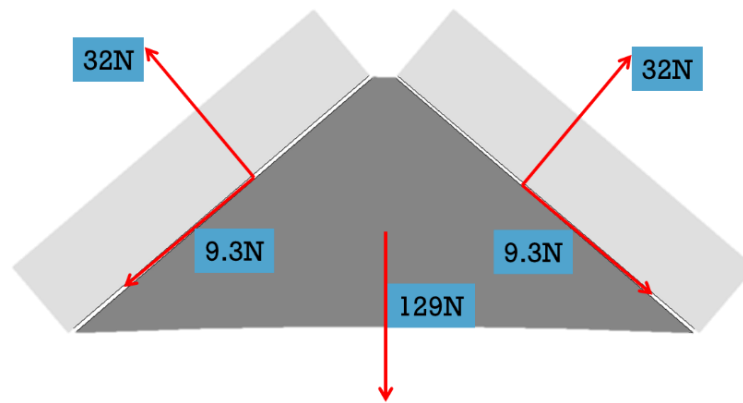


Figure 3-53 The magnetic force on each piece

3.2.4. Conclusion

In this section, an alternative slot/pole combination (s9p10) is shown to give a 6.6% higher torque capability compared to the s9p8 in the V-shaped motor. Due to the increased inductance, the new slot/pole selection works at a lower power factor and consequently a reduced speed range for the given voltage rating and inverter size. A trade-off shall be made depending on the design specification.

The ideal V shape with no leakage path is modified into an easy-to-manufacture version with minimum torque output loss aiming for mass production. The structural integrity is analysed after the choice was made to have an unconventional multiple-piece V topology. The attractive force between the rotor pieces and the stator tooth is small and could be overcome by applying the appropriate adhesive.

3.3. Analysis of Magnet loss and demagnetisation

In this section, magnet loss and demagnetisation are investigated in surface-mounted and interior magnet topologies. [104]

The fractional-slot concentrated-winding configuration helps machine designers to gain significant advantages in increasing the active to overall axial length ratio, fill factor, and thermal conductivity. It also eases the manufacturing and assembly process. However, in addition to the torque producing stator MMF, rich spatial harmonics are generated which may cause strong parasitic effects [105-107].

The rich spatial stator MMF (magneto-motive force) harmonics present in the air gap have three effects on the magnet, particularly: 1. AC losses in the magnets; thus, 2. heat dissipation and temperature increase inside the magnets; 3. an increased peak demagnetising field experienced by the magnets. Analytical models from literature are first introduced and developed to give insight into the magnet loss inducing mechanism, thereby deciding when and how to segment the magnets. Then FEA methods are used to verify the analytical methods for magnet loss and segmentation techniques in the surface-mounted PM motor. Finally, the analysis is extended to examine how different rotor topologies are affected by both loss and demagnetisation fields, showing major differences between the interior and the surface topologies.

3.3.1. The stator MMF harmonics

The moving electric machine is a contraption that can convert energy between electrical and the mechanical states by the medium of magnetic energy. In the machine, the stator MMF produces a travelling magnetic field to synchronise with the rotor converting the energy via the air-gap magnetic field. However, besides the synchronised stator MMF field, there are also many asynchronous fields rotating in different directions in the air gap which are responsible for losses and torque ripple. To represent the harmonics of MMF space distribution in the air gap, an analytical model is developed by applying Fourier analysis.

Assumptions made in this analysis:

- There are time harmonics in the current waveform from electronic switching devices which can cause significant losses [108]. The method to obtain stator MMF spatial

harmonics from the current input with these time harmonics is the same as the method to obtain the current with only a fundamental frequency. Hence, for simplicity, the time harmonics are not considered in the theory inducing section but will be discussed in the magnet losses calculation section.

- Stator iron is assumed to be infinitely permeable, this is a valid assumption due to the high ratio of magnetic permeability between stator iron and the air gap. However, when greater detail and accuracy is needed, FE analysis should be implemented for non-linear behaviour of highly saturated regions, such as the tooth tips.
- Assuming that there is no slot leakage flux, which is a valid approximation in ring-shape in-wheel motors when the slot depth to slot pitch ratio is relatively low.

The tangential magnetic field strength of a single slot

To start with, the relationship between the stator MMF and the air gap magnetic field strength, a.k.a. the linear current density (A/m), of a single slot is introduced.

A single energised slot of a 9slot, 8pole machine is illustrated in Figure 3-54. At any given point in time, the distance integration of the tangential field around the blue dotted flux path is equal to the MMF enclosed, as described in eq. (3.25) by Amperes circuital law. It is assumed that the stator iron is infinitely permeable, the magnetic field strength in the stator iron is negligible and the full field strength is confined to the slot opening, giving an evenly distributed tangential magnetising field at the slot opening but zero for the rest of the dotted line, eq. (3.26).

$$\oint_C H_t(t) dl = \iint_S J(t) dS = MMF_{slot}(t) \quad (3.25)$$

$$H_{t,slot}(t) = \frac{MMF_{slot}(t)}{\chi} \quad (3.26)$$

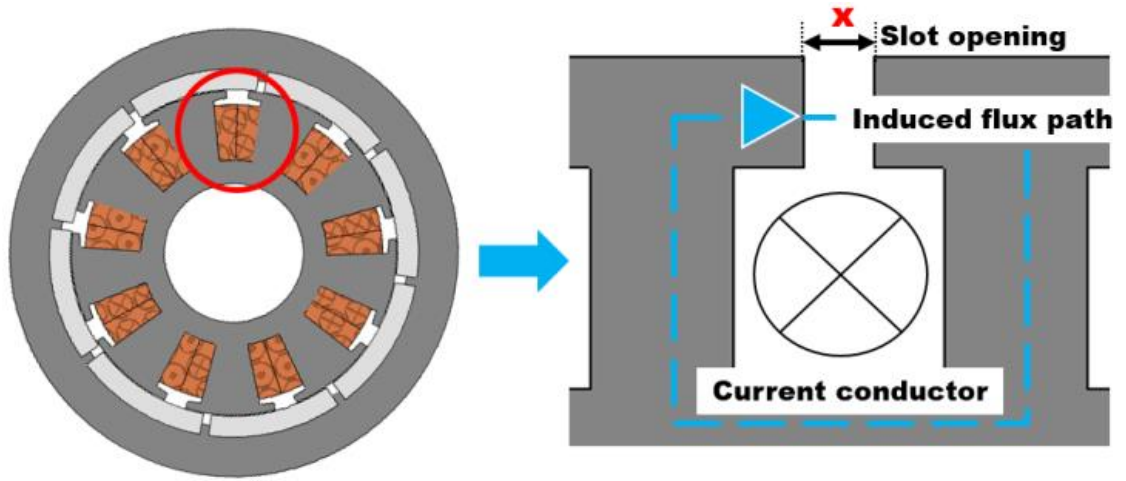


Figure 3-54 A single energised slot from a 9slot, 8pole machine

Fourier transform of the full air gap field distribution

The tangential field strength of each slot in a machine is then plotted against the angular position of the slot in the air gap as is shown in Figure 3-55. A Cartesian coordinate system is chosen over the polar system due to its simplicity in Fourier analysis. When the analysed distance, i.e. the air gap distance, to the machine radius ratio is considerably smaller, the curvature of the model can be ignored and the accuracy remains at an acceptable level, which is a fair assumption in an in-wheel motor with an aspect ratio over 0.9. In Figure 3-55, θ_a and θ_b are the angles defining the slot opening.

From standard Fourier transform, the rectangular waveform of a slot shown on Figure 3-55 can be expressed as eq. (3.27). The first term of the equation is the DC offset, the second term consists of the harmonic, v , magnitude coefficient $\frac{H_t(t)}{v\pi} \sin\left(v \frac{(\theta_b - \theta_a)}{2}\right)$ and the spatial distribution coefficient $\cos\left(v \left(\frac{(\theta_b + \theta_a)}{2} - \theta\right)\right)$.

$$H_t(\theta, t) = \frac{H_t(t)(\theta_b - \theta_a)}{2\pi} + \sum_{v=1}^{\infty} \frac{H_t(t)}{v\pi} \sin\left(v \frac{(\theta_b - \theta_a)}{2}\right) \cos\left(v \left(\frac{(\theta_b + \theta_a)}{2} - \theta\right)\right) \quad (3.27)$$

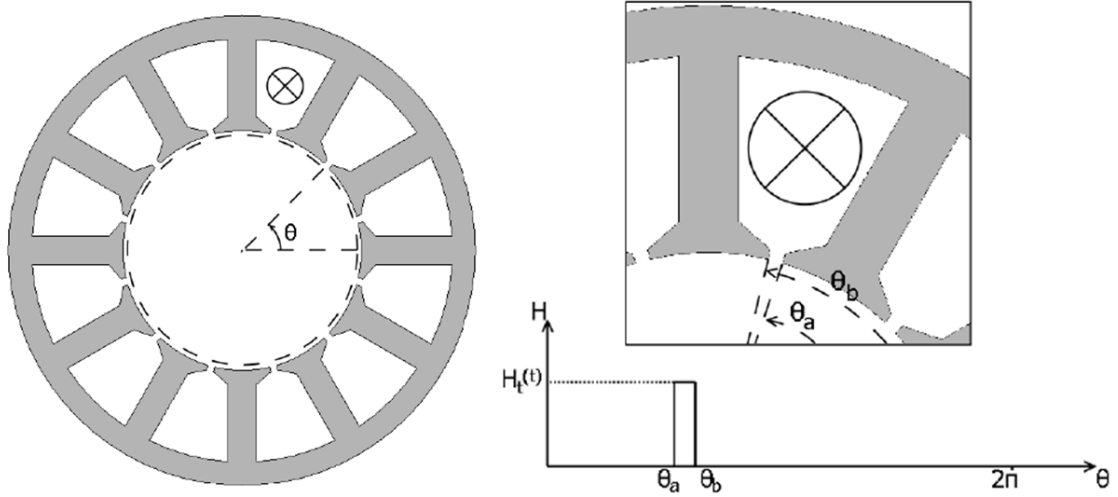


Figure 3-55 The magnet field of single slot on the full machine

The magnetic field of each slot can be obtained by redefining the slot opening angles with slot number m and slot angular pitch λ_s in eq. (3.28). The full air gap magnetic field can then be obtained by the superposition rule and is expressed in eq. (3.29).

$$\theta_{a,b}(m) = \theta_{a,b} + (m - 1)\lambda_s \quad (3.28)$$

$$H_t(\theta, t) = \sum_{v=1}^{\infty} \sum_{m=1}^{slotno} \frac{H_t(t, m)}{n\pi} \sin\left(v \frac{(\theta_b - \theta_a)}{2}\right) \cdot \cos\left\{v \left[\frac{(\theta_b + \theta_a)}{2} + m\lambda_s - \theta\right]\right\} \quad (3.29)$$

The 9slot 8pole machine in Figure 3-54 is taken as an example to showcase the accuracy of the developed analytical model. Two curves of the tangential magnetic field strength from this analytical model and the FE result are plotted against the air gap position in Figure 3-56. It is clear that the two curves are matched closely. The minor oscillation of the analytical model is due to the Gibbs effect. It can be suppressed by increasing the number of harmonics. The harmonic spectra of the H_t field from two methods are also shown in Figure 3-57. In Figure 3-58, a graphical demonstration is made to show the different rotating directions of three example harmonics.

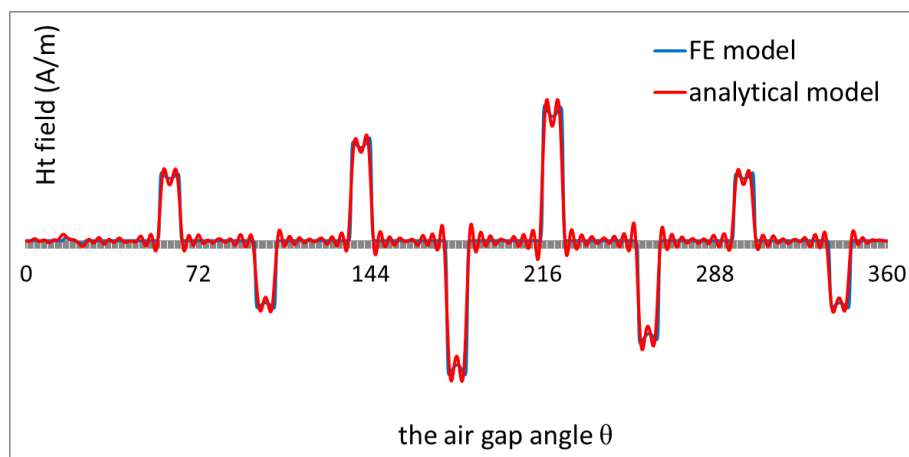


Figure 3-56 H_t distribution in the air gap at an arbitrary time instant

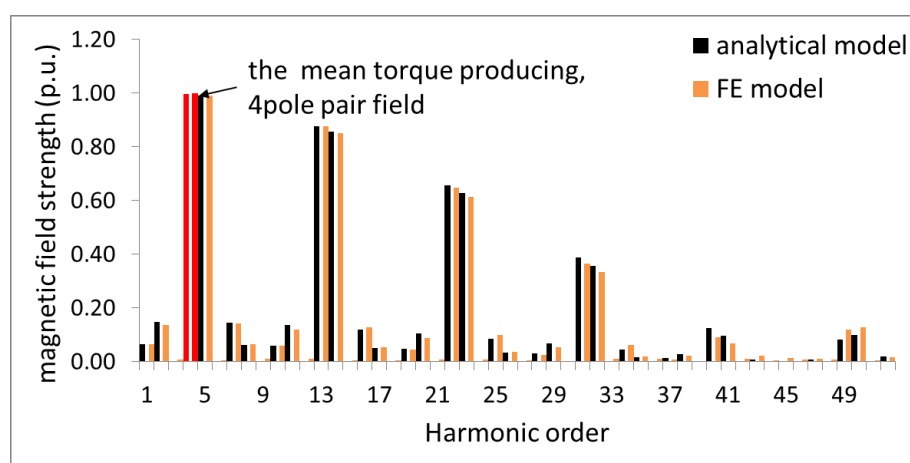


Figure 3-57 H_t harmonic spectrum (1st – 52nd) of the 9s8p machine

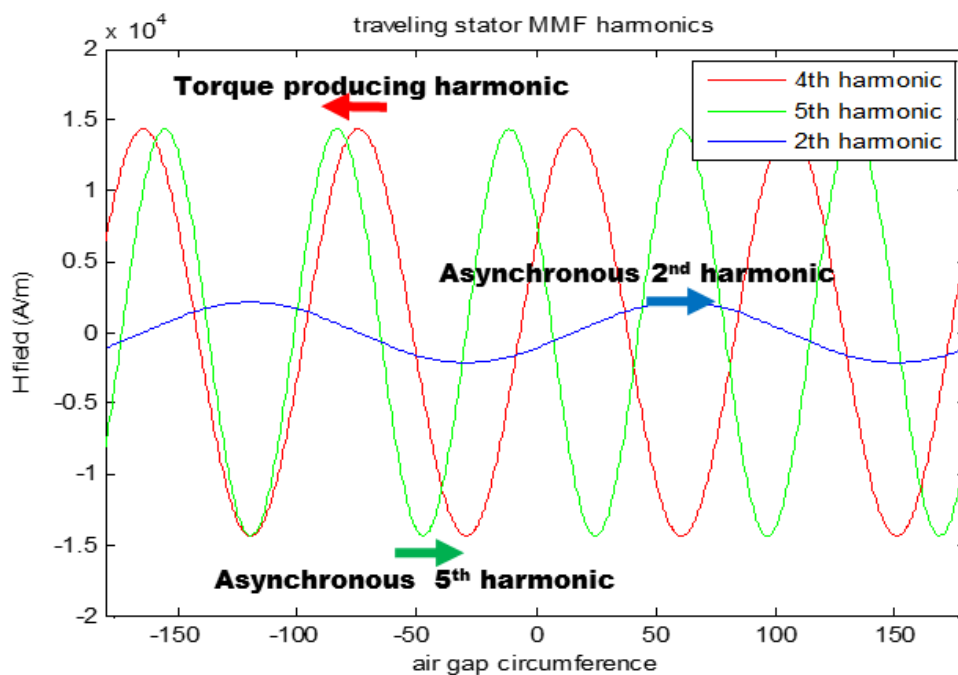


Figure 3-58 The 2nd, 4th and 5th harmonic rotating direction demonstration

The harmonics in the in-wheel motor

The BMM in-wheel motor is 72slot and 64pole, which is essentially eight sub-motors with an MMF pattern of a 9slot 8pole motor repeating eight times round the air gap. To simplify the subsequent discussion, the analysis will be performed on a 9s8p machine: all harmonics can then be multiplied by eight to find their order in the actual machine.

Throughout the rest of the chapter, the torque producing field of the 72s64p in-wheel motor will be referred to as the 4th harmonic, Figure 3-58. This is an 8 pole field in the 8 pole machine and a 64 pole field in the full 64 pole machine. The 2 pole, sub-synchronous-field will be regarded as the first harmonic. This becomes a 16 pole field in the 64 pole machine. Furthermore, there is a large backwards rotating 10 pole field in the 8 pole machine, corresponding to an 80 pole field in the 64 pole machine. This will be referred to as the 5th harmonic, which is illustrated in Figure 3-59.

The high spatial harmonic contents of the stator MMF shown in Figure 3-59 rotate asynchronously relative to the rotor, inducing eddy currents and subsequent heat in the magnets. The heat is hard to dissipate due to there being no direct cooling method applied to the outer rotor. The magnet temperature is measured at 60°-80° Celsius in the benchmark in-wheel motor at a steady state [109]. Although with the existing design there is no risk of demagnetisation as the magnet material is reduced in order to lower cost, this is no longer the case in the surface-mounted topology [98].

By moving from surface mounted magnets to interior magnets, arranged in a V shape, it has been found that the magnet length can be greatly reduced without any risk of demagnetisation. There could be two possible reasons for this: either magnet leakage flux is increased, hence increasing the operating point of the magnet, or somehow the magnet is being screened from the armature reaction flux [110, 111]. Magnet loss is also reduced in the interior topology keeping the rotor cool, which makes demagnetisation less likely and increases the magnet residual flux density, thereby maximising performance.

An insight into why the interior magnet design is less susceptible to demagnetisation will be given in the next section by examining all the spatial harmonics of the stator in turn, understanding whether they penetrate the magnets and whether they cause a significant loss.

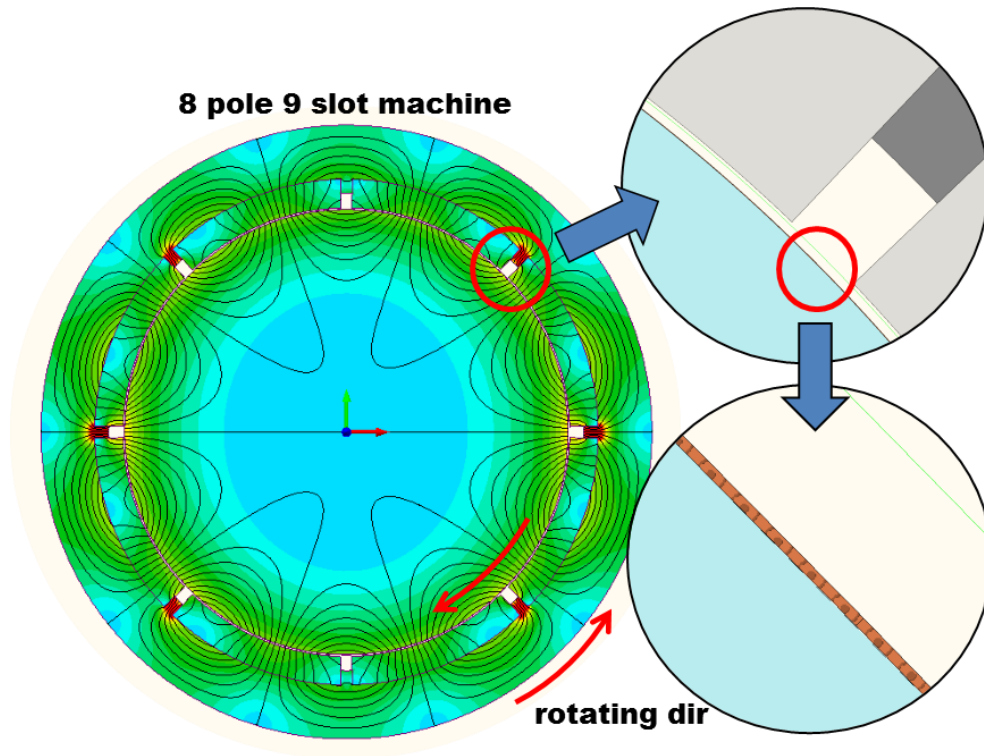


Figure 3-59 The 5th harmonic magnetic field made from current sheet method

3.3.2. Magnet loss calculation

With the magnetic field defined, the magnet loss is calculated in three ways using 2-dimensional finite element analysis and ignoring the end effect on axial dimension:

- 2D FE analysis based on the current sheet representation of the travelling magnetic field harmonics from the stator [112].
- 2D analytical calculation based on fully defined magnetic potential in regions across the air gap [113, 114].
- 2D analytical calculation based on flux integration and classed in cases defined by harmonic wavelength to magnet width ratio [115].

Method 3) is a hybrid approach combining the analytically calculated source field and 2D FE magnet loss calculation, giving a deeper insight compared to full machine FE modelling with an inseparable stator field. This method can be used to evaluate the second and third analytical methods. Hence, it needs to be introduced and validated first.

Notice the computationally expensive 3D approach is demonstrated in some literature[116], but the accuracy of the 2D result is sufficient when explaining the inducing mechanism of the magnet loss.

Current sheet method in 2D FE simulation

In method 3, a current sheet is created with a discretised number of coils to represent any harmonic of a certain magnitude, frequency and rotating direction, such as the 10 pole backward-rotating 5th harmonic field which is illustrated in Figure 3-59. The stator material is on the inner side and is infinitely permeable in order to allow the flux of the coil to be perpendicular to the current sheet surface.

By implementing the current sheet method in 2D FE simulation, magnet loss can not only be calculated by the actual air gap field as is shown in Figure 3-56, but also be separated into single harmonic losses.

To prove the accuracy of this method, the actual travelling harmonic field is generated by re-composing all the harmonics up to the 52nd from the analytical calculation and feeding them into the current sheet model. This range is chosen to balance the computational time and accuracy. The losses over one electric cycle from the current sheet model and the model with a complete stator of the 72s64p surface mounted in-wheel motor are compared in Figure 3-60. This demonstrates that a satisfactory level of accuracy can be achieved using the current sheet model.

As shown by the green line, when the 5th harmonic is taken out from the summed harmonic field, the total loss is reduced to 15% of its original value, indicating its significant effect on magnet loss.

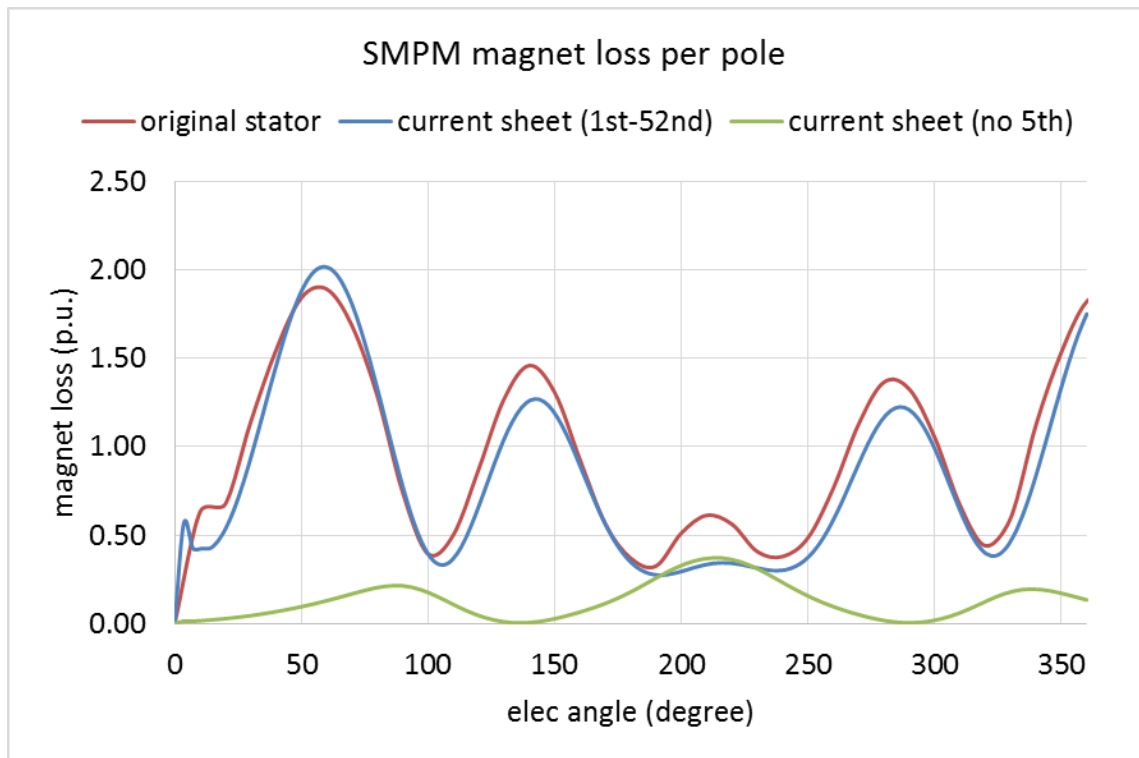


Figure 3-60 The magnet loss per pole in a 72s64p surface mounted in-wheel motor

In Figure 3-61, each H_t field harmonic is individually injected into the current sheet model to examine the effect on magnet loss from a single harmonic. The result shows that 85% of the loss is from the 5th harmonic, again proving the significance of the 5th harmonic in magnet loss.

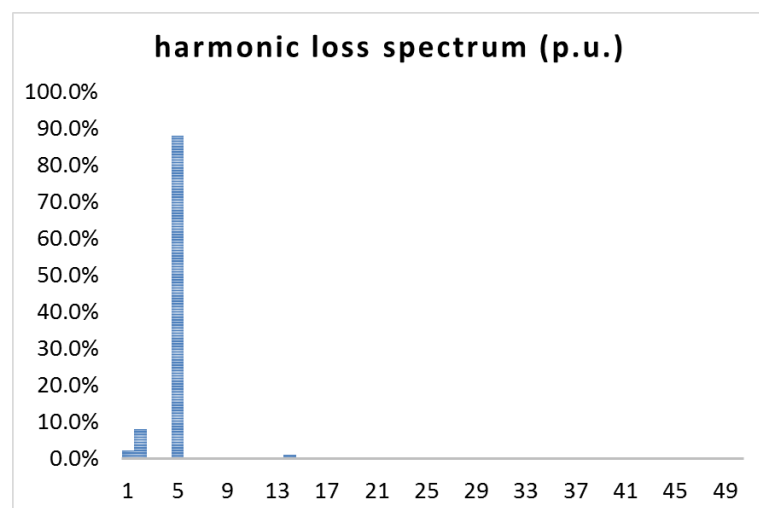


Figure 3-61 The harmonic loss spectrum in a 72s64p surface mounted in-wheel motor

Both simulations identify the 5th harmonic as the biggest loss contributor. Other contributors to loss are the 2nd harmonic, producing 8%, the 1st harmonic, 2 pole field producing 2% and the 14th harmonic producing 1% of the magnet loss. To reduce magnet

loss, its mechanism needs to be understood analytically. To begin with the vector potential method is introduced.

The vector potential method

Method 2 is adopted from R. Stoll's classic work [113] on the travelling magnetic field at a constant distance to a semi-finite conductive plate and is developed by D. Smith [114]. This is analogous to a magnetic field travelling at the stator surface parallel to the magnets located in the rotor.

This method can give an accurate prediction of magnet loss compared to 2D FEA where the air gap radius is high and the air gap distance is low. However, this is because it relies on solving second order partial differential equations (PDEs) simultaneously. When the geometry is complicated, i.e. the interior topology, the number of PDEs and their boundary conditions increase, it makes it laborious to solve by hand. Hence, it is applicable to surface-mounted magnets but not to the V shape.

Figure 3-62 illustrates Stoll's model and the equivalent rotor model used for analysis. In this model a simple, although common, topology is chosen, which consists of full span surface-mounted magnets mounted on a magnetically conductive rotor core back. The current sheet is represented by K_z travelling parallel to, and a distance b from, a plate of thickness a . The form of K_z in eq. (3.30) is taken directly from [114], which is equivalent to the tangential magnetic field strength derived in the previous section with the unit 'A/m', where g is the pole pitch of the current harmonic with the unit of 'meter' and ω is the speed relative to the plate with the unit of 'rad/s'.

$$K_z = \hat{K}_z \cos(\omega t - \pi x/g) = \text{Re}[\hat{K}_z e^{j\omega t} e^{-j\pi x/g}] \quad (3.30)$$

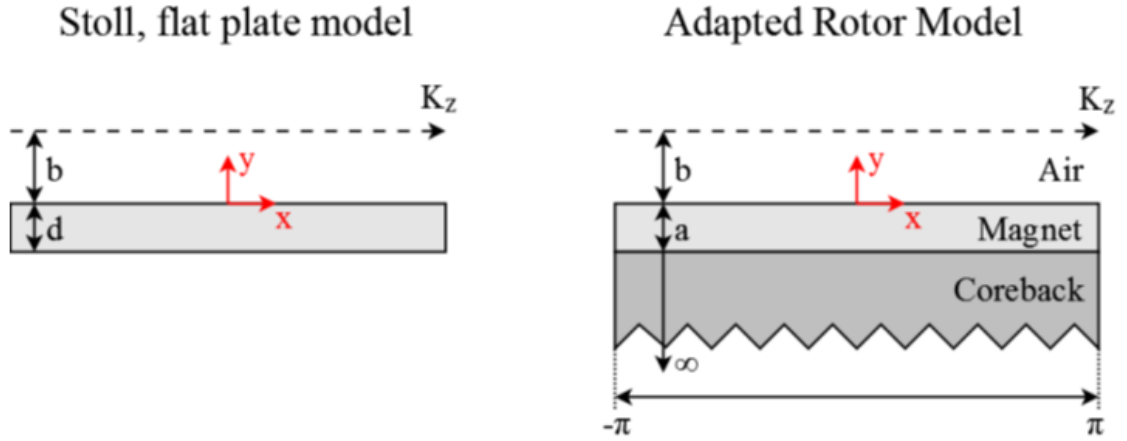


Figure 3-62 The equivalent model for the vector potential method

Obtaining the loss relies on solving a differential equation that defines the magnetic vector potential in any region subject to the boundary conditions posed by the model and the assumptions made. From the magnetic potential, the current distribution J in any conducting region can be defined from eq. (3.31). Finally, the loss in the region can be integrated from the defined current density.

$$\begin{cases} \epsilon = -\frac{\partial A}{\partial t} \\ J = \sigma \epsilon \\ P_{loss} = \int_V \frac{1}{2\sigma} |J|^2 dV \end{cases} \quad (3.31)$$

Where ϵ is the electric field intensity, A is the magnetic vector potential, J is the current density and σ is the conductivity.

The vector potential, A , in the air region with no free charge is defined by Laplace's equation, eq. (3.32), and its general solution is eq. (3.33).

$$\frac{\partial^2 A}{\partial x^2} + \frac{\partial^2 A}{\partial y^2} = 0 \quad (3.32)$$

$$A_{air} = (C_A e^{qy} + D_A e^{-qy}) e^{-jqx} \quad (3.33)$$

Similar equations for any given conducting material are defined by Poission's equation and solved in eq. (3.34) and eq. (3.35).

$$\begin{cases} \frac{\partial^2 A}{\partial x^2} + \frac{\partial^2 A}{\partial y^2} = \alpha^2 A \\ \alpha = \frac{1+j}{\delta} \\ \delta = \sqrt{(2/\omega\sigma\mu)} \end{cases} \quad (3.34)$$

$$\begin{cases} A_{Mag} = (C_M e^{\gamma_m y} + D_M e^{-\gamma_m y}) e^{-jqx} \\ A_{core} = (C_C e^{\gamma_c y}) e^{-jqx} \\ q = \frac{\pi}{g} \\ \gamma = \sqrt{(q^2 + j^2/\delta^2)} \end{cases} \quad (3.35)$$

Where subscript ‘M’ stands for the magnet material and ‘C’ stands for the core back.

D_C in the second line of eq. (9.11) is forced to be zero preventing A_{Core} from trending to ∞ while the core back extends to $-\infty$ on the y-axis direction.

The five constants C_A , D_A , C_M , D_M and C_C are all unknowns to be solved based on the boundary conditions defined in eq. (3.36) due to flux continuity and the field strength on the boundaries of materials. Where subscript n stands for normal direction and t is tangential.

$$\begin{cases} B_{n1} = B_{n2} \\ H_{t2} - H_{t1} = K \end{cases} \quad (3.36)$$

Combining eq. (3.34) and (3.37), the H can be expressed in eq. (3.38).

$$\begin{cases} curl A = B \\ div A = 0 \end{cases} \quad (3.37)$$

$$\begin{cases} H_x = \frac{1}{\mu} \frac{\partial A}{\partial y} \\ H_y = -\frac{1}{\mu} \frac{\partial A}{\partial x} \end{cases} \quad (3.38)$$

Plug eq. (3.38) into the boundary conditions to obtain eq. (3.39) used to solve the 5 unknown parameters. Where ‘i’ stands for the material on the boundary.

$$\begin{cases} \frac{\partial A_{i+1}}{\partial x} = \frac{\partial A_i}{\partial x} \\ \frac{1}{\mu_{i+1}} \frac{\partial A_{i+1}}{\partial y} - \frac{1}{\mu_i} \frac{\partial A_i}{\partial y} = K_{zi} \end{cases} \quad (3.39)$$

Hence, five simultaneous equations at different boundaries can be derived:

$$\begin{cases} \frac{q}{u_0} (C_A e^{qb} - D_A e^{-qb}) = \hat{K}_z e^{j\omega t} \\ C_A + D_A = C_M + D_M \\ \frac{q}{u_0} (C_A - D_A) = \frac{q}{u_M} (C_M - D_M) \\ C_M e^{-\gamma_m a} + D_M e^{\gamma_m a} = C_C e^{-\gamma_c a} \\ \frac{\gamma_m}{\mu_M} (C_M e^{-\gamma_m a} - D_M e^{\gamma_m a}) = \frac{\gamma_c}{\mu_C} C_C e^{-\gamma_c a} \end{cases} \quad (3.40)$$

After obtaining the five coefficients from eq. (3.40), the vector potentials can be fully defined in all regions. The losses can then be calculated using eq. (3.31). The developed analytical model is compared to an FE model of an s9p6 machine with the stator harmonic spectrum shown in Figure 3-64. As can be seen, the accuracy of the analytical calculation is reasonably accurate.

This method is good for loss estimation and can be integrated into any analytical design iteration. The loss contribution from each harmonic can also be estimated. However, there is a more straightforward method to understand the relationship between the magnet width, harmonic wavelength and its loss.

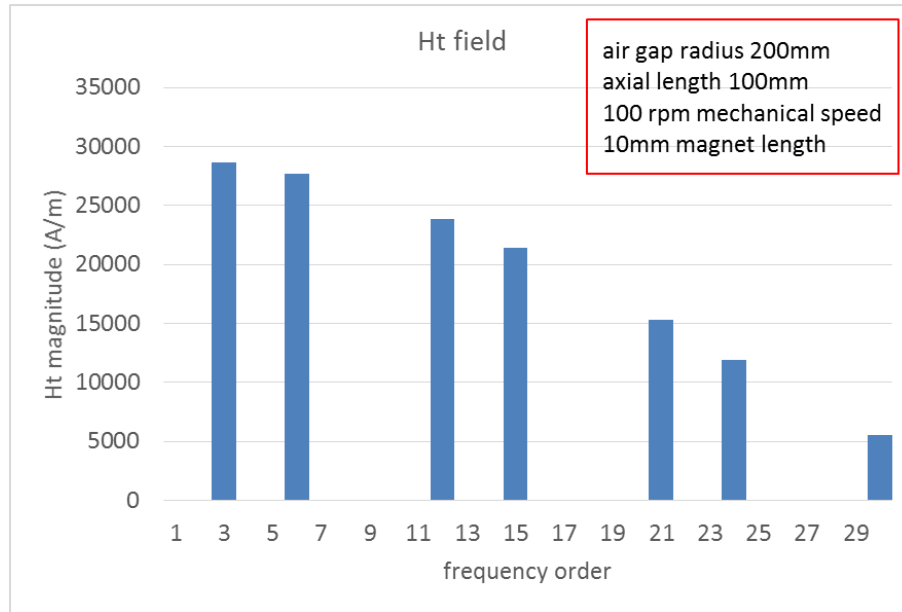


Figure 3-63 The H_t field harmonic spectrum of an s9p6 machine

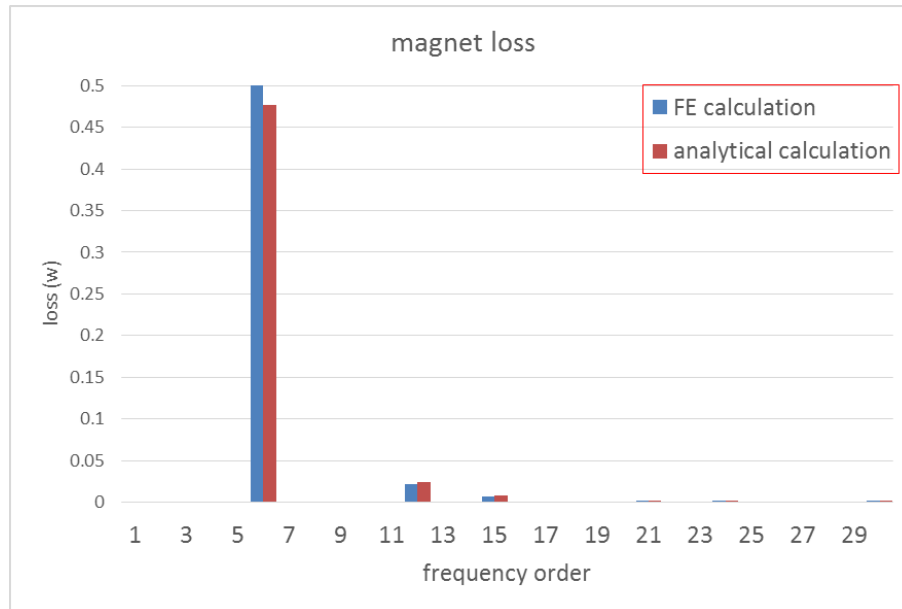


Figure 3-64 The loss comparison of an s9p6 machine

The flux integration method

Method 3 is adopted from [115]. Though no magnet loss can be analytically calculated just using this method without knowing the flux on the magnet surface, a magnet loss index can be generated for indication. The skin effect in the conducting magnet is not considered which leads to a less accurate loss estimation for high frequency harmonics. Nevertheless, it gives a deep insight into magnet loss inducing mechanism and is used to develop the magnet segmentation rule for the 72s64p in-wheel motor.

The eddy current loss density in the magnet at any given point in space varies sinusoidally in time in response to a single travelling harmonic source field. Hence, the loss density at that position has a DC value and a twice frequency oscillation, $(I \sin)^2 R$. The average time loss can be defined by averaging the maximum and minimum value of loss oscillation. Finding the right position in time for the extreme values of the loss becomes key to the calculation.

The eddy current inducing mechanism for all magnetic field harmonics can be classified into three categories in eq. (3.41) based on the harmonic wavelength to magnet width ratio $(\frac{\lambda_n}{w})$. Sub-harmonics of the pole number and those near to the pole number, act differently towards higher frequency harmonics, so they will be discussed separately.

$$\left\{ \begin{array}{l} \text{case A: } 2 < \frac{\lambda_v}{w} \\ \text{case B: } 1 < \frac{\lambda_v}{w} < 2 \\ \text{case C: } \frac{\lambda_v}{w} < 1 \end{array} \right. \quad (3.41)$$

Case A: sub-harmonics

Firstly, consider the 2nd harmonic, which produces a 32 pole field in the 64 pole machine. This type of harmonic has a wavelength at least 2 times larger than the rotor magnetic pole span.

The maximum instantaneous loss occurs when the normal flux enters the magnet on one side of the magnet and exits it on the other side. This is illustrated in Figure 3-65 by applying the 2nd harmonic in the current sheet model. The minimum instantaneous loss position is when the flux is centred over the magnet and the loss is nearly zero. Negligible eddy current is formed due to lack of current return path.

At the point of greatest loss, the eddy currents flow in a single loop down one side of the magnet and up the other. The loss gradient is pointing from the centre to the sides, which is represented by the colour darkening in the figure.

From the figure, it is clear that this harmonic penetrates fully through the magnet due to its large wavelength to magnet width ratio. The eddy current is distributed evenly throughout the magnet length in a radial direction.

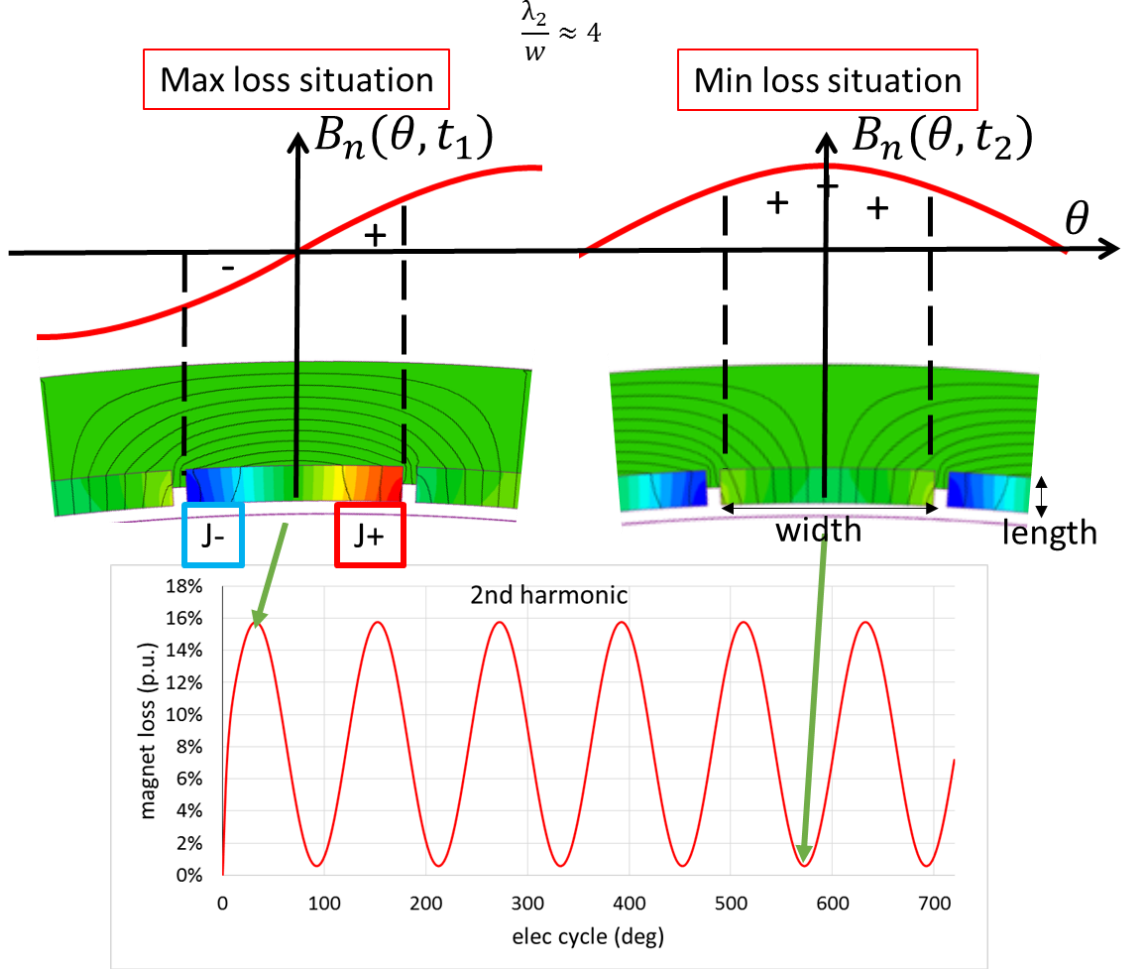


Figure 3-65 Eddy current loop of 2nd harmonic in the 72s64p in-wheel motor from FE

The analytical model is formed and derived in [115] based on the above observation. The parameters used are defined in Figure 3-66. The flux enclosed by the elementary eddy current path is first integrated in eq. (3.42) to obtain eq. (3.43). The resistance of the elementary path is defined in eq. (3.44). The eddy current loss of this path can then be calculated by eq. (3.45), which is essentially the classic equation of V^2/R .

The $\cos^2(\omega_n t)$ term in eq. (3.45) mathematically proves that the first maximum point occurs when $t=0$ and $B_n(x, 0) = B_n \cdot \sin\left(\frac{2\pi}{\lambda_n} x\right)$, which matches with the left side of Figure 3-65. The first minimum point is when $\omega_n t = \pi/2$, and the loss is zero. So the average loss of this elementary path can be calculated by eq. (3.46). Finally, the total loss

is obtained by integrating the elementary path circumferentially along the magnet width. The loss per volume index is calculated in eq. (3.47).

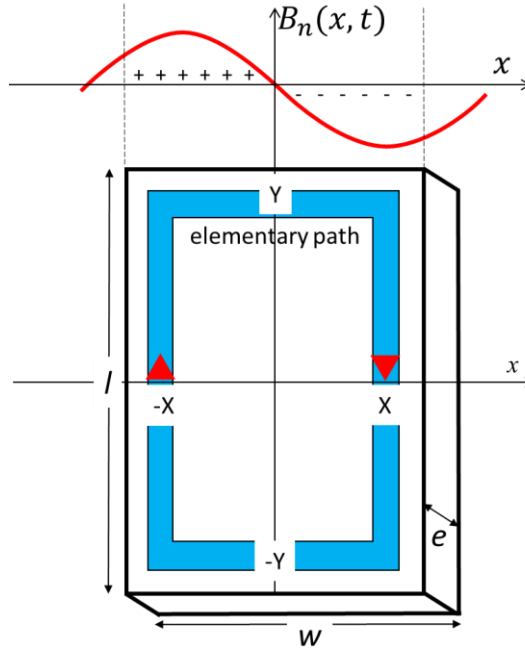


Figure 3-66 The parameters defined in method 2

$$\begin{cases} \Phi_e(X, t) = \int_{-X}^X B_v(x, t) ds \\ ds = 2\alpha X dx, \alpha = \frac{Y}{X} = \frac{l}{w}, B_v(x, t) = B_v \cdot \sin\left(\omega_v t + \frac{2\pi}{\lambda_v} x\right) \end{cases} \quad (3.42)$$

$$\Phi_e(X, t) = \frac{2\alpha X B_v \lambda_v}{\pi} \sin\left(\frac{2\pi}{\lambda_v} X\right) \sin(\omega_v t) \quad (3.43)$$

$$R_e = \rho \frac{4Y}{e \cdot dX} + \rho \frac{4X}{e \cdot dY} = \frac{4\rho X(\alpha^2 + 1)}{e \cdot \alpha \cdot dX} \quad (3.44)$$

$$dP_e = \frac{\left(\frac{\partial \Phi_e(X, t)}{\partial t}\right)^2}{R_e} = \frac{\alpha^3 e \cdot B_v^2 \cdot \omega_v^2 \cdot \lambda_v^2}{\pi^2 \rho (\alpha^2 + 1)} \cdot X \cdot \sin^2\left(\frac{2\pi}{\lambda_v} X\right) \cdot \cos^2(\omega_v t) \cdot dX \quad (3.45)$$

$$\bar{dP_e} = \frac{1}{2} (dP_{e,t=0} + 0) \quad (3.46)$$

$$\begin{aligned}
(P_{per.vol})_a &= \frac{\int_0^w dP_e}{magnetvolume} = \frac{\int_0^w dP_e}{e\alpha\omega^2} \\
&= \frac{\alpha^2 \cdot B_v^2 \cdot \omega_v^2}{2\pi^2\rho(\alpha^2 + 1)} \cdot \left[\frac{\lambda_v^2}{16} + \frac{\lambda_v^4}{32\pi^2 w^2} \left(1 - \cos\left(\frac{2\pi}{\lambda_v} w\right) \right) - \frac{\lambda_v^3}{16\pi w} \sin\left(\frac{2\pi}{\lambda_v} w\right) \right]
\end{aligned} \tag{3.47}$$

Where R_e is the resistance of the elementary path, ω_n is the angular velocity of the harmonic field, ρ is the magnet resistivity. Subscript 'a' in $(P_{per.vol})_a$ stands for the case a. The reason why the loss is larger on the edge can be explained by term $X \cdot \sin^2\left(\frac{2\pi}{\lambda_v} X\right)$ in dP_e .

Case B: transient harmonics

Consider now the 5th harmonic, which produces an 80 pole field in the 64 pole machine. This type of harmonic has a wavelength close to the magnetic pole span (1-2 times). The flux positions of the maximum and minimum losses in this case are the same as case A, as is shown in Figure 3-67. Again, in the maximum case, the currents flow in a single loop and the majority of the loss is at the circumferential edges of the magnet. However, in the minimum position, there are two loops formed because the wavelength to magnet width ratio is smaller in this case permitting the flux polarity to change over half of the magnet pole.

Notice, because the harmonic wavelength of the magnet is smaller and the time frequency is higher, even with a stronger harmonic magnitude, there is less penetration through the magnet in a radial direction in the 5th compared to the 2nd harmonic. Therefore, the current density is not evenly distributed in a radial direction.

The equation $\frac{\left(\frac{\partial \Phi_e(X,t)}{\partial t}\right)^2}{R_e}$ used above becomes inaccurate due to: 1. The flux travel through the back being smaller than the surface of the magnet leading to a lower $\left(\frac{\partial \Phi_e(X,t)}{\partial t}\right)^2$. 2. The resistance R_e in higher harmonics being higher due to a smaller path width in the radial direction, 3. The . As a result, the loss calculated by V^2/R is bigger in the analytical model compared to the actual case. This inaccuracy is observed in Figure 3-69.

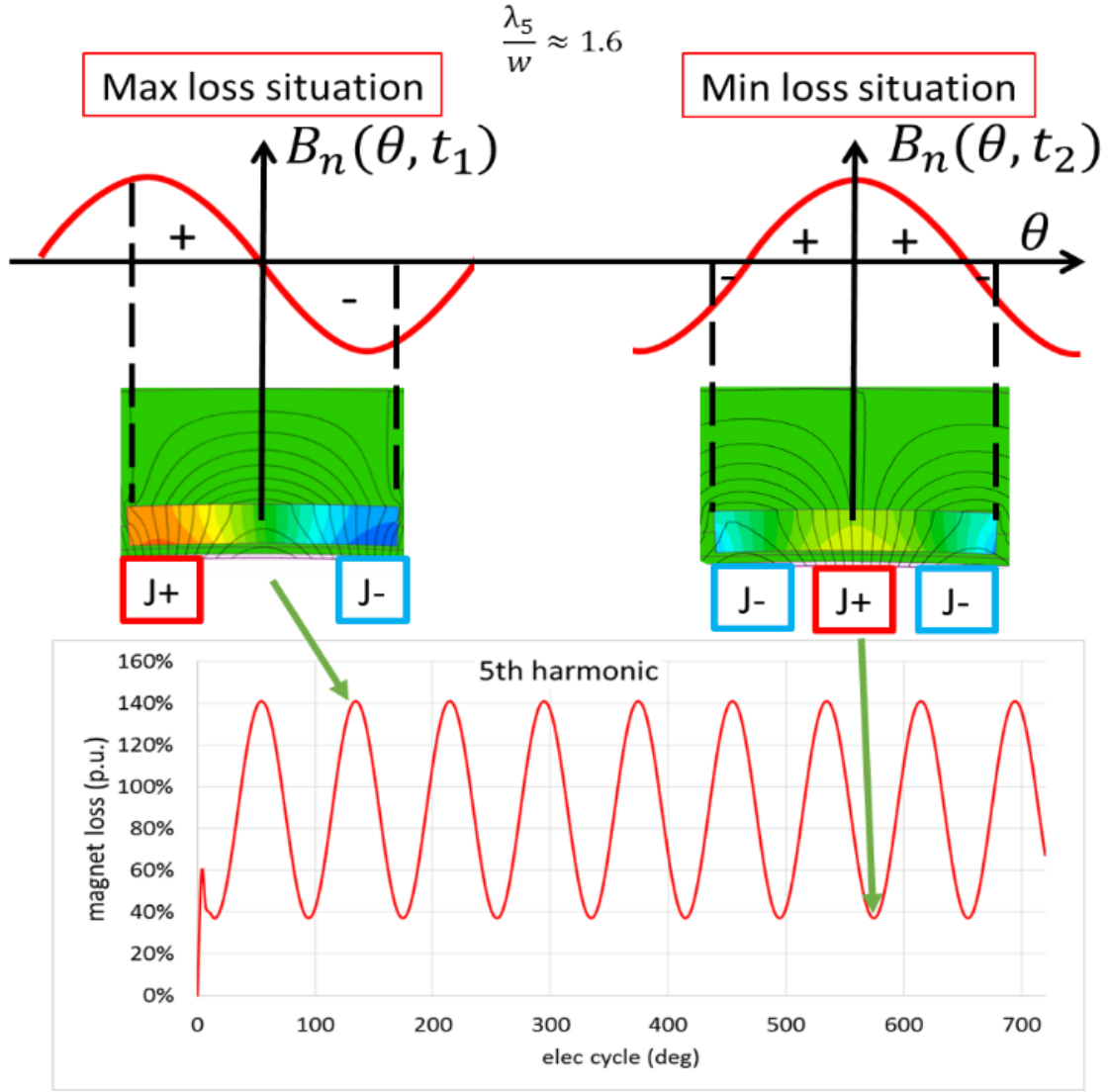


Figure 3-67 Eddy current loop(s) of 5th harmonic in the 72s64p in-wheel motor from FE

Analytically, the equation of eq. (3.48)-(3.50) can be obtained by the same process described in eq. (3.42)-(3.47).

$$\begin{aligned}
 (P_{per.vol})_{b,max} = & \\
 2 \cdot \frac{\alpha^2 \cdot B_v^2 \cdot \omega_v^2}{2\pi^2 \rho (\alpha^2 + 1)} \cdot \left[\frac{\lambda_v^2}{16} + \frac{\lambda_v^4}{32\pi^2 w^2} \left(1 - \cos\left(\frac{2\pi}{\lambda_v} w\right) \right) - \frac{\lambda_v^3}{16\pi w} \sin\left(\frac{2\pi}{\lambda_v} w\right) \right] & \quad (3.48)
 \end{aligned}$$

$$\begin{aligned}
& ds(P_{per.vol})_{b,min} \\
&= \frac{(\frac{4w^2\alpha^2}{\lambda_v(2w-\lambda_v)})B_v^2 \cdot \omega_v^2}{2\rho\pi^2 \cdot (1 + (\frac{4w^2\alpha^2}{\lambda_v(2w-\lambda_v)}))} \left[\frac{(2w-\lambda_v)\lambda_n^3}{16w^2} \left(1 + \frac{2}{\pi^2} \right. \right. \\
&+ \left. \frac{2\lambda_v^2}{\pi^2} \left(\frac{1}{w^2} - \frac{1}{(w-\lambda_v)^2} \right) \right) + \frac{\lambda_v^4}{16\pi w^2} \sin\left(\frac{2w\pi}{\lambda_v}\right) \\
&+ \frac{\lambda_v^5}{16\pi^2 w^2 (2w-\lambda_v)} \left(1 + \cos\left(\frac{2w\pi}{\lambda_v}\right) \right) \\
&- \frac{(2w-\lambda_v)^2 \lambda_v^4}{8\pi w^3 (w-\lambda_v)} \sin\left(\frac{w\pi}{\lambda_v}\right) \\
&\left. - \frac{\lambda_v^5 (2w-\lambda_v)(2w^2-\lambda_v(2w-\lambda_v))}{8\pi^2 w^4 (w-\lambda_v)^2} \cos\left(\frac{w\pi}{\lambda_v}\right) \right] \tag{3.49}
\end{aligned}$$

$$(P_{per.vol})_b = \frac{(P_{per.vol})_{b,max} + (P_{per.vol})_{b,min}}{2} \tag{3.50}$$

Case C: super harmonics

Finally, consider the 14th harmonic, which is the only super-harmonic to produce a significant loss in this category. In this case, the maximum loss occurs when there are three eddy current loops, with four current loops at the minimum loss time instant. The loss is distributed throughout the magnet in a circumferential sense, but is concentrated at the magnet surface because the high pole number flux does not penetrate so much through the magnet.

A comparison between the analytical model and the 2D FE model is given in Figure 3-69. It is inaccurate in showing the exact loss contribution from different harmonics due to the assumptions made about constant flux penetration along the radial direction. Nonetheless, the analytical model can still correctly predict the major loss contributor. Its value lies in revelations about the relationship between magnet width and wavelength, which serves as part of the theoretical background on magnet segmentation.

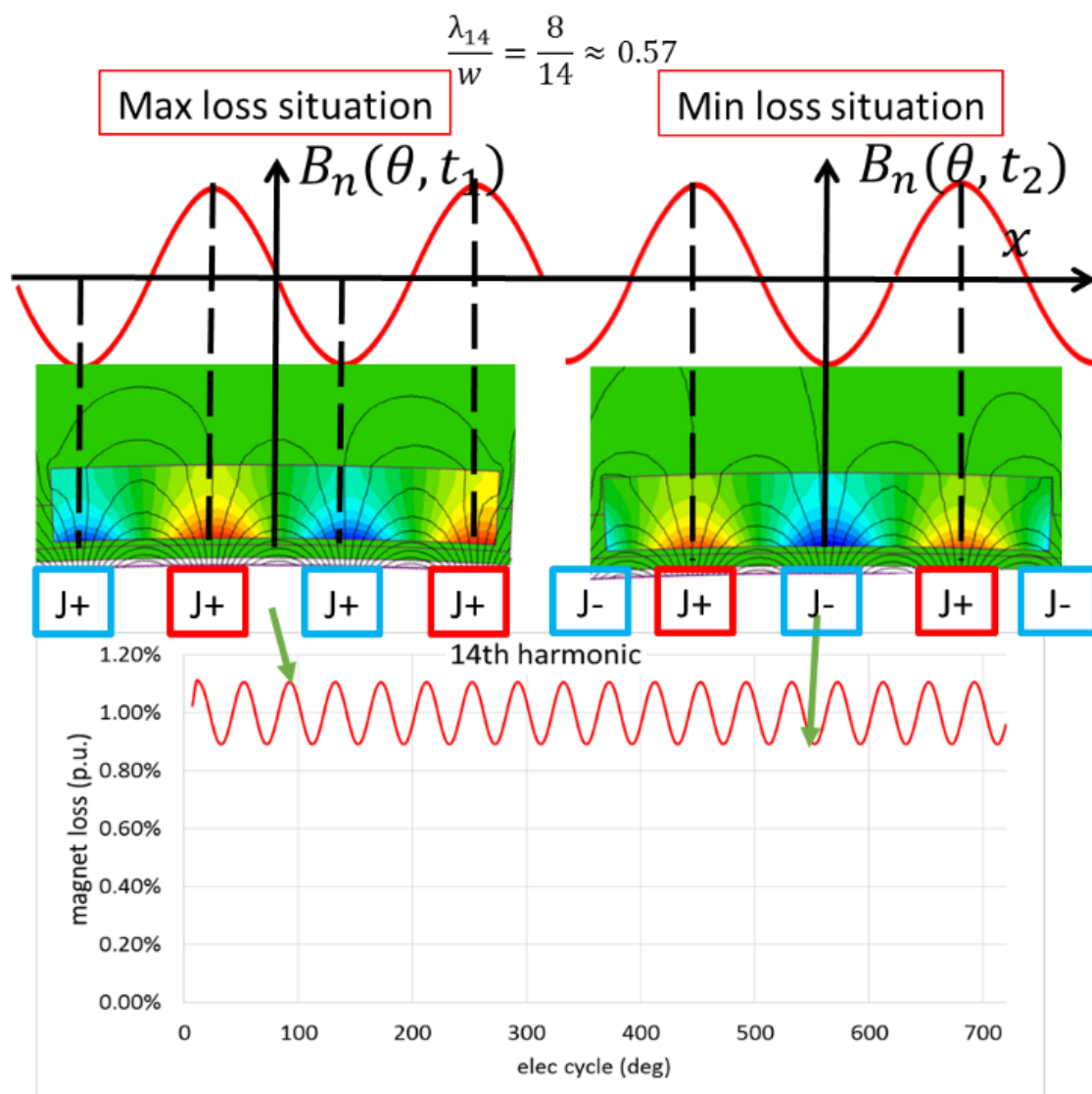


Figure 3-68 Eddy current loops of 14th harmonic in the 72s64p in-wheel motor from FE

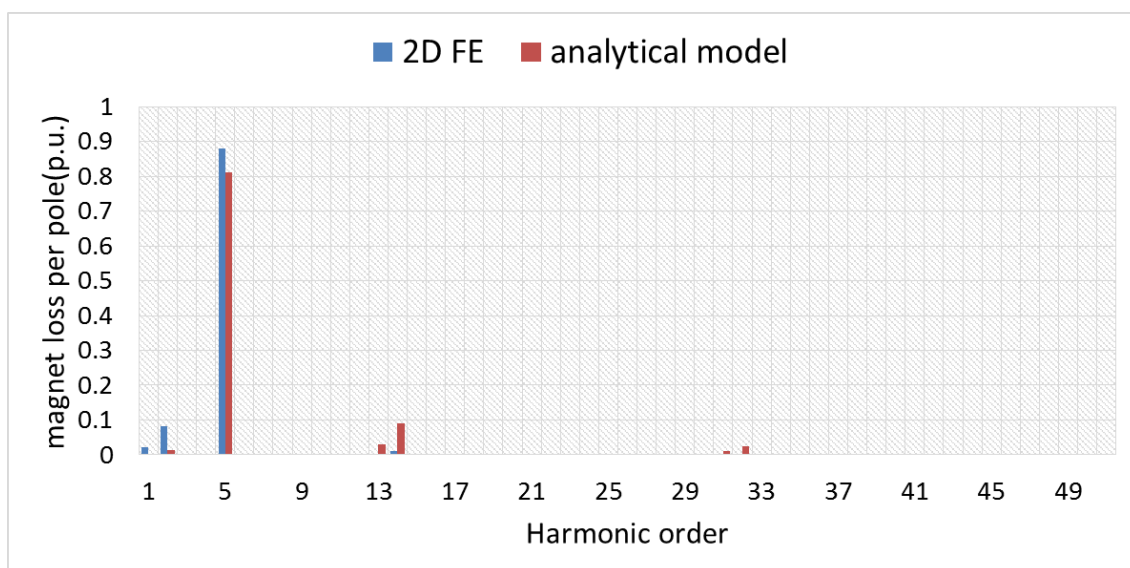


Figure 3-69 The magnet loss spectrum

3.3.3. Magnet segmentation

Normally, the magnets can be segmented along axial and/or circumferential directions. A segmentation choice without an understanding of the magnet loss origin can sometimes result in an increase in magnet loss [117]. Hence, harmonic effects that have been discussed in the previous section are summarised for the magnet segmentation selection criteria.

The linear current density harmonic is expressed as $\hat{K}_z \cos(\omega t - \pi x/g)$, and its corresponding harmonic loss is influenced by time frequency ωt and $\pi x/g$ spatial wavelength. The time harmonic and spatial harmonic affect the magnet loss differently.

Harmonic effect

The eddy current induced in the conducting material is an alternating current, hence, due to the skin effect, it tends to flow on the surface of the material when the time-varying frequency of the current is high.

Depending on the ratio between conductor thickness and skin depth, the eddy current loss can be categorized into three regions: a. the resistance limited case, b. transitional period and c. the inductance limited cases which is illustrated in Figure 3-70 [112]. The conductor thickness, i.e. the skin depth, of the magnet is defined by the circumferential distance of half of the eddy current loop.

Both analytical methods introduced in this chapter assume that magnet loss is in the resistance limited case - the skin depth is thicker than the magnet length. This means that the whole magnet is conductive whether segmented or not. Hence, power loss can be expressed as V^2/R , in which V is related to the changing rate of flux and remains constant. Hence, in this case, simple magnet segmentation creates a longer eddy current flow path to increase resistance and is proved to be effective in loss reduction.

However, when skin depth is much shallower than conductor thickness, the current tends to flow on the 'skin' of the conductor: in a surface-mounted magnet, that is the side that faces along the radial direction. Hence, only the skin area is conducting and experiencing flux change to induce a voltage. If segmenting the magnet, both the conducting path length and the conducting area will be increased. The resistance and the voltage increase proportionally keeping the current constant. Therefore, power loss should be expressed as

I^2R meaning magnet loss is actually increased with increased resistance from segmentation. This is the inductance limited case.

Hence, it is important to be able to first identify the main harmonic(s) causing magnet losses and then understand which case it (they) belong(s) to.

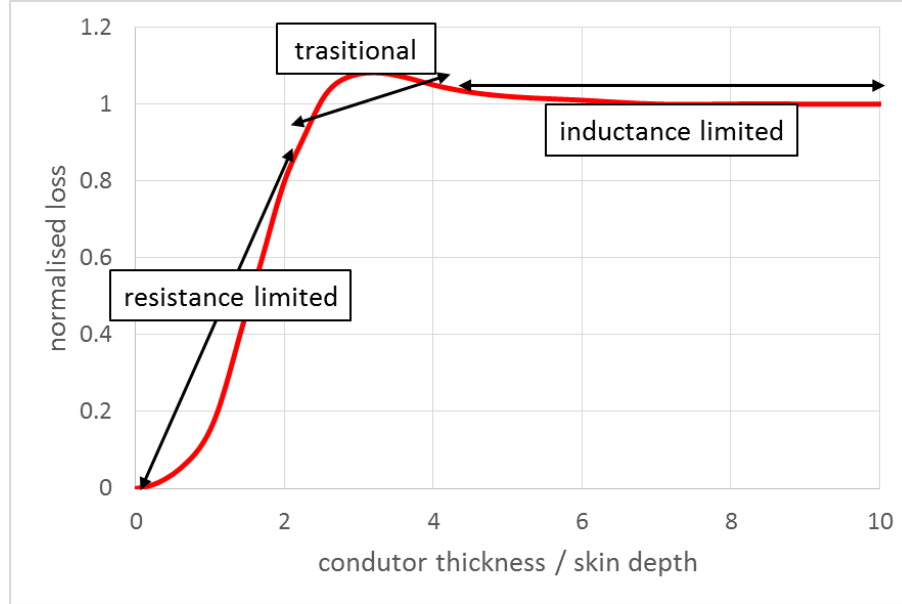


Figure 3-70 Eddy current loss as a function of the conductor thickness to skin depth

The skin depth of a conductor is defined as $\delta = \sqrt{2/(\omega\sigma\mu)}$, the alternating speed ω determines the skin depth. The speed can be defined in eq. (3.51) for the synchronously rotating rotor. The \pm in the equation represents the rotating direction of the harmonic relative to the rotor. The pp is the pole pair of the rotor and v is the harmonic spatial order.

$$\text{synced rotor: } \omega = 2\pi \cdot f_m \cdot (v \pm pp) \quad (3.51)$$

It is clear that the speed increases as the order of the spatial harmonic increases. Whereas, the conductor thickness, half of a conducting loop length circumferentially, is reduced due to the reduced wavelength of the harmonic. Assuming the slot current waveform is sinusoidal without any time harmonic, the harmonic losses from the chosen spatial harmonic spectrum in the in-wheel motors (s72p64) are all in the resistance limited region shown in Figure 3-70.

The effect of time harmonics, if considered, generated by the switching devices can also be explained by Figure 3-70. The loss estimation follows the same logical process, the only difference is that for each spatial harmonic, the alternating frequency is now

multiplied by the time harmonic order. This reduces the skin depth of all spatial harmonics while the wavelength of the spatial harmonics remains fixed.

In the in-wheel motor, due to a relatively low speed range (0-1600rpm), the skin depth of the main loss producing spatial harmonic 5th is 14.83mm at a 1600rpm maximum speed and half of the magnet length (conductor thickness) is 8.34mm. Hence, it is well into the resistance limited region. Thus, increasing the resistance by segmentation is effective for the 5th harmonic loss reduction. Furthermore, at 1600rpm the electric frequency is 853.3Hz and the switching frequency is 16k Hz as reported from Protean Electric, which means the time harmonic from the carrier is fairly low. Hence, the loss effect from the time harmonics other than the fundamental is neglected.

Segmentation choice

As discussed, the spatial harmonics of the in-wheel motor are all in the resistance limited region. Therefore, by increasing the resistance, magnet loss can be reduced. However, the resistance of the eddy current flow path only increases when the number of eddy current loops are bigger than the original one after segmentation, as shown in Figure 3-71. If there are already two loops, then there will be no new loop formed after segmentation. Hence, the number of segmentations needs to be selected carefully.

Axial segmentation

When segmenting one magnet into two along the axial direction, the resistance can always be increased. Nonetheless, if the axial length to magnet width ratio is too high, the gained resistance from the additional circumferential eddy current flowing path is relatively short and does not significantly contribute to the total resistance. Thus, in order to effectively reduce magnet loss, it is suggested that the ratio between the axial length and the width of the magnet should be reduced to below '1'. Hence, the in-wheel motor with a ratio of 3.46 will be segmented into 10 pieces axially to reduce the ratio to 0.346.

Circumferential segmentation

Consider an unsegmented magnet with a very large length along the circumferential direction, the eddy current loop length is limited only by the spatial harmonic wavelength of the source field as is shown in Figure 3-68. Hence, in order to form new loops, the segmented pieces need to be smaller than the wavelength. Because the magnet width is already smaller than the wavelength of the 5th harmonic, main loss contributor,

circumferential segmentation is always effective. Based on the analytical model described in the third method, Figure 3-72 is created to demonstrate magnet loss against segment-width-to-harmonic-wavelength ratio.

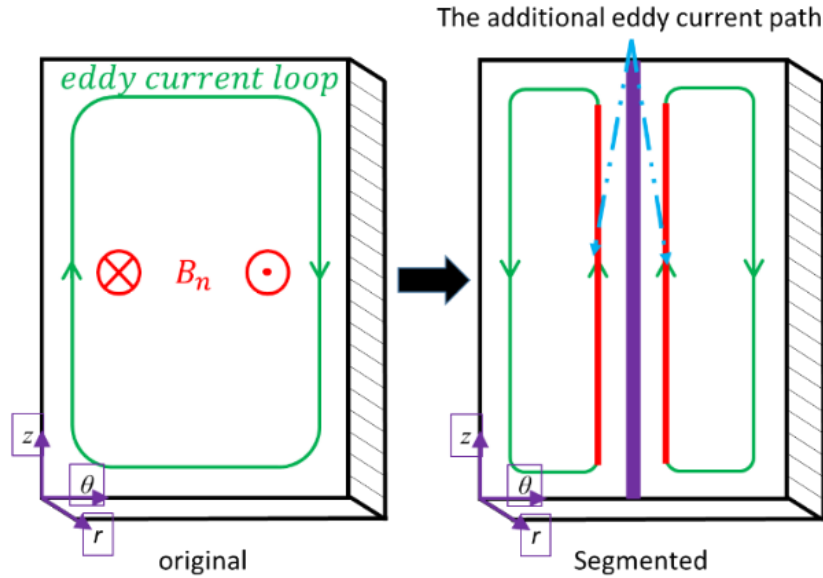


Figure 3-71 The additional eddy current path introduced after circumferential segmentation

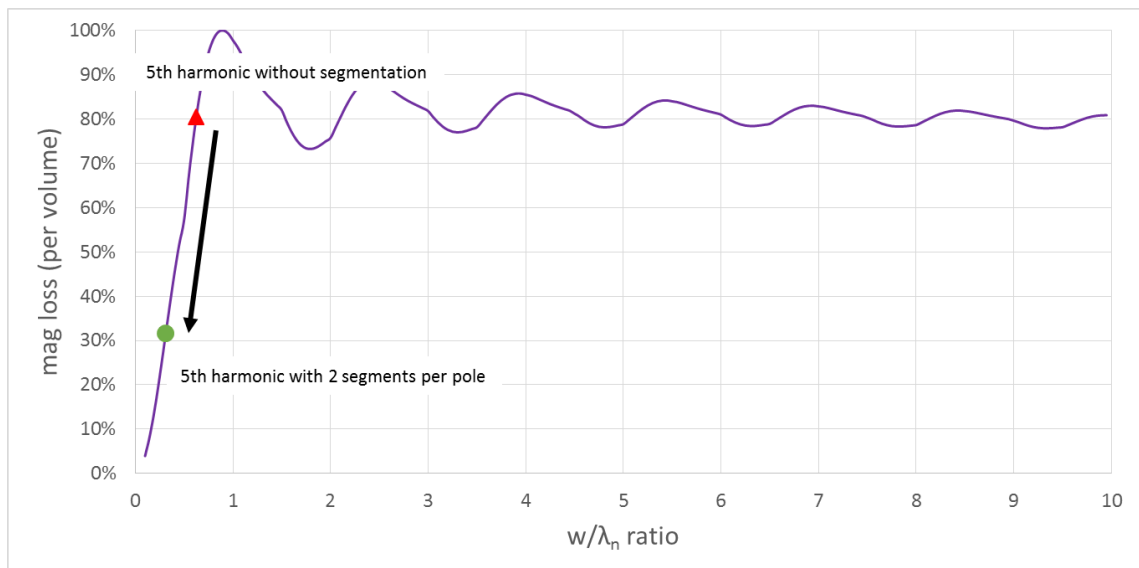


Figure 3-72 The circumferential segmentation effect on the spatial harmonics

The original magnet width per pole, w , is 1 unit. If the magnet is segmented into two pieces, the equivalent magnet width is reduced to $\frac{1}{2}$ a unit. Hence, the $\frac{w}{\lambda_5}$ ratio of the 5th harmonic is changed from 0.6125 to 0.31 on the graph and the loss per volume is reduced from 0.8 to 0.32 per unit. More than half of the magnet loss can be reduced as shown in Figure 3-72.

Besides the increased resistance in the eddy current loop, the flux linking the loop is also much less for each segmented piece. Observing eq. (3.43), flux linkage is not only related to loop distance 'X' but also modified by the value of ' $\sin(\frac{2\pi}{\lambda_n}X)$ '. Maximum flux linkage is achieved when X equals to $\frac{1}{4}$ of the wavelength. That is when the magnet span equals half of the wavelength, i.e. the main (4th) harmonic. Therefore, when segmented, the value of ' $\sin(\frac{2\pi}{\lambda_n}X)$ ' changes from '0.96' to '0.79'. In essence, circumferential segmentation can increase the value of the denominator and also reduce the value of the numerator of V^2/R , rendering it extremely useful for reducing the 5th harmonic loss.

To verify this prediction, the original magnet is segmented into 2 pieces. The eddy currents from the 5th harmonic can no longer flow in a single loop, two loops are created. The loss field plot comparison is shown in Figure 3-73. It shows the effect upon magnet loss as a function of time. The loss comparisons are also made for both the 5th harmonic and the total magnet loss in Figure 3-74 and Figure 3-75. It shows that the loss reductions from the 5th harmonic (by 65%) can be successfully transferred onto the total loss reduction (by 65%).

Note that for the 14th harmonic, two-pieces segmentation will not significantly reduce its loss, because each segment is still greater than a single harmonic pole span and the eddy current can still form a complete loop with unaffected peak flux linkage. In order for segmentation to be effective it would have to be such that each segment spanned only a harmonic pole or less ($\frac{w}{\lambda_5} < 2$), which would require at least 4 segments per pole.

To conclude, circumferential segmentation is extremely useful for the sub-harmonics and harmonics near the fundamental which have small number of eddy current loops, including the main loss producing 5th harmonic and the 2nd harmonic in the BMM. Hence, 2-pieces-per-pole magnet segmentation is chosen to reduce magnet loss in the surface-mounted topology. Since each pole is formed by 2 magnet pieces in the V-shaped design, if unsegmented, the magnet loss in the V-shaped motor will be intrinsically lower than the surface-mounted motor.

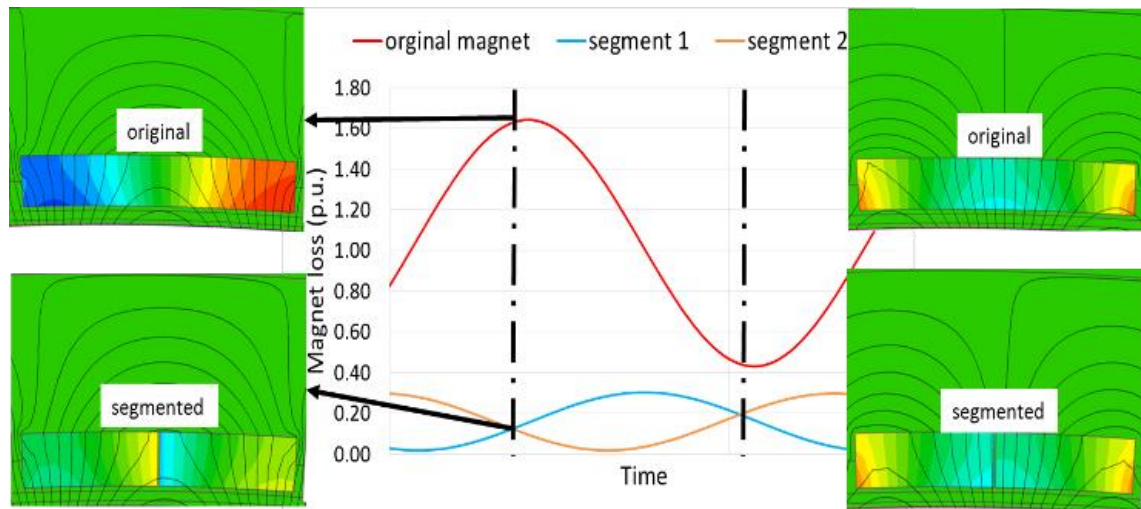


Figure 3-73 The circumferential segmentation effect of the 5th harmonic in 2D field plot

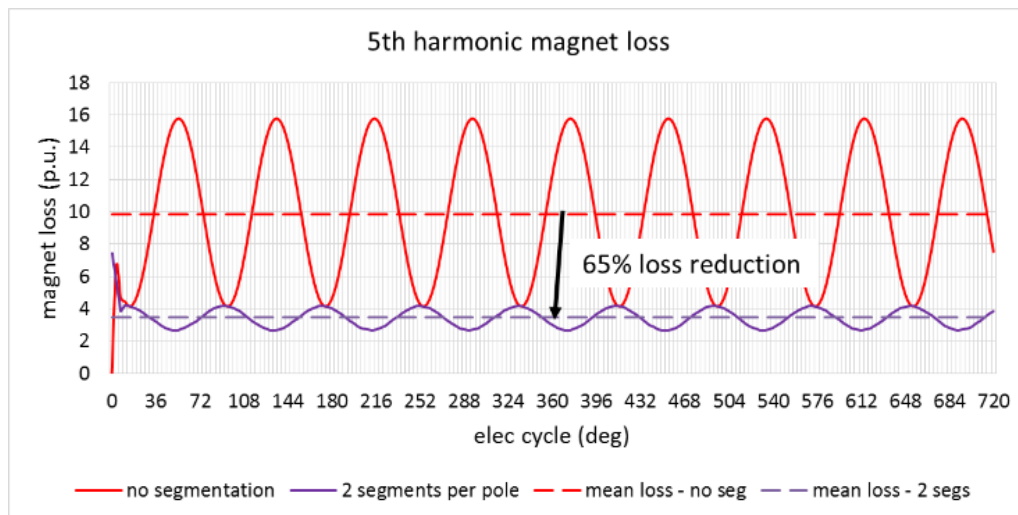


Figure 3-74 The 5th harmonic magnet loss due to the circumferential segmentation in the 72s64p surface mounted in-wheel motor

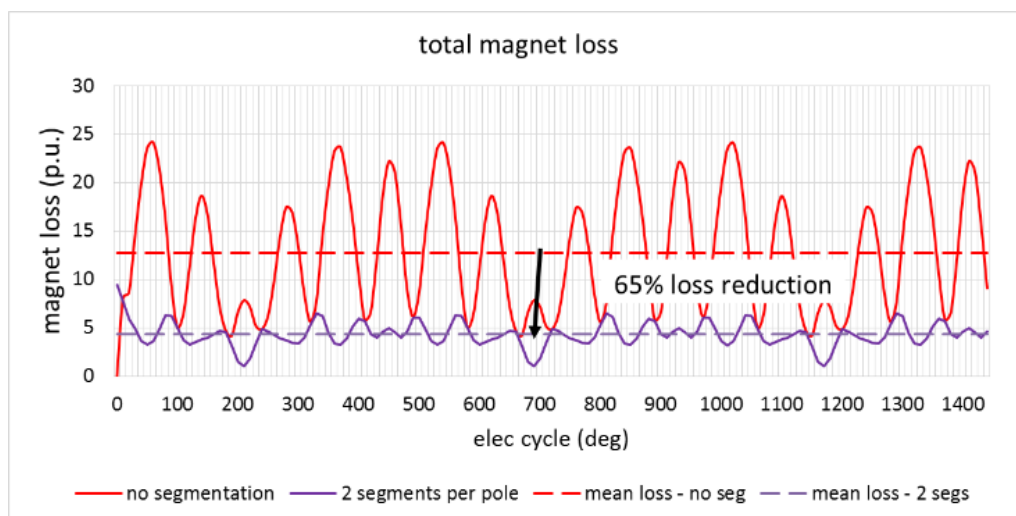


Figure 3-75 The total magnet loss due to the circumferential segmentation in the 72s64p surface mounted in-wheel motor

3.3.4. Demagnetisation in in-wheel motors

Segmentation reduces loss and therefore temperature, which makes the magnets more resistant to demagnetisation. However, it does not reduce the magnitude of the demagnetising field, which is the source of demagnetisation. To reduce material cost, the magnet length is made shorter than the benchmark motor increasing the risk of demagnetisation. At the peak demagnetising current, the magnets move over the knee of the B-H curve and can be permanently demagnetised, as shown in Figure 3-76(a). The demagnetising field that magnets experience varies with time. The peak demagnetising field occurs at the time instant when the peak 5th harmonic field coincides with the peak of the main torque producing field. The sum of these two fields acts on the third magnet from the right in Figure 3-76(a) and makes the majority of the piece demagnetised.

Compare Figure 3-76(b) with that of (a). In (b) the magnets have been changed to an interior V shape. It uses the same magnet mass and electric loading, there is no demagnetisation. Figure 3-77 and Figure 3-78 attempt to illustrate why V-shaped magnets are much less prone to demagnetisation.

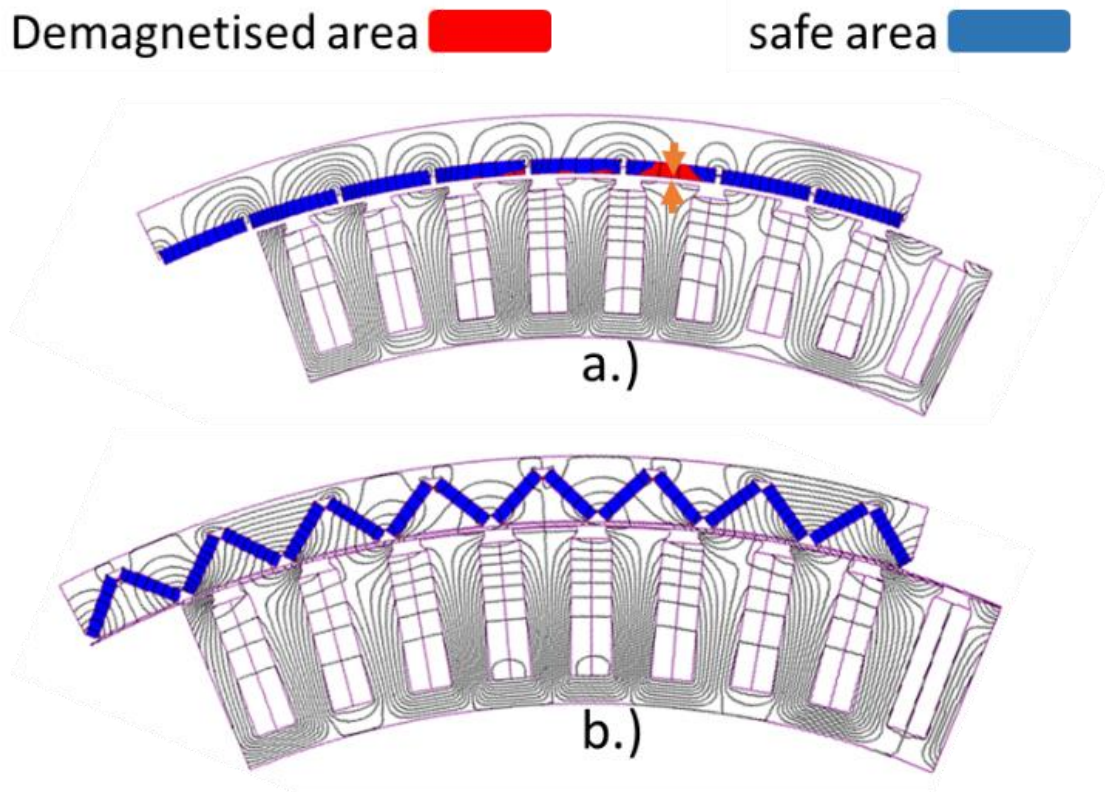


Figure 3-76 The demagnetisation prediction for surface-mounted and V models with identical magnet mass in the worst case scenario described in section II (The magnet grade is: Sintered Neodymium-Iron-Boron Magnets – N45SH, the knee point at 100°C is 0.3T.)

Figure 3-77 shows the magnet operating point along the magnet surface. In black, is the no-load operating point for each case. Both magnets operated with a flux density close to 0.8 Tesla, with the circumferential ends of the magnets having a lower flux density due to the slotting effect. The average flux is lower in the V model because of the magnet's increased surface area. The flux drop in the middle of the V is due to the opposing leakage flux from both sides of the magnetic pole.

In blue is the impact of the torque producing 4th harmonic, though in this case it is positioned on the negative d-axis directly opposing the rotor field from the magnets. Magnets in both designs experience a significant drop in flux density, but remain safely above 0.3 Tesla, which is the point of irreversible demagnetisation at 100°C.

Finally, in red, is the case with all of the stator harmonics included and overlapped to oppose the rotor field. The flux density of the majority of the surface-mounted magnets dropped below the knee point line in the graph, whilst the V-shaped magnet arrangement remains safely above, apart from the edges of the magnets sitting in the air gap.

There are two reasons for a higher resistance to demagnetisation in V: 1. all higher order harmonics are screened out by the triangular iron piece in front of the magnets. High pole number fields enter and leave this triangle without ever linking the magnet. In the 64pole-72slot machine, the screening of the 5th harmonic field is only partial because it is close to the pole number, but this is still enough to significantly reduce its impact. The second reason is that the front piece can also act as a flux distributor, the flux is averaged out by the front iron due to its non-linear permeability before entering the V magnets, whereas the peak flux is directly opposing the magnet in the surface mounted one. This can be observed by checking the field colour on the surface of the magnets in Figure 3-78.

Furthermore, in the case discussed above the electric loading and magnet mass are fixed in the two designs. However, if targeting the same torque output with the same magnet mass, much less electric loading is required, hence lower stator harmonics, in the V-shaped motor due to the assistance of the reluctance torque. This means not only is there a higher resistance to demagnetisation, but also the demagnetising field is much smaller in the V-shaped motor.

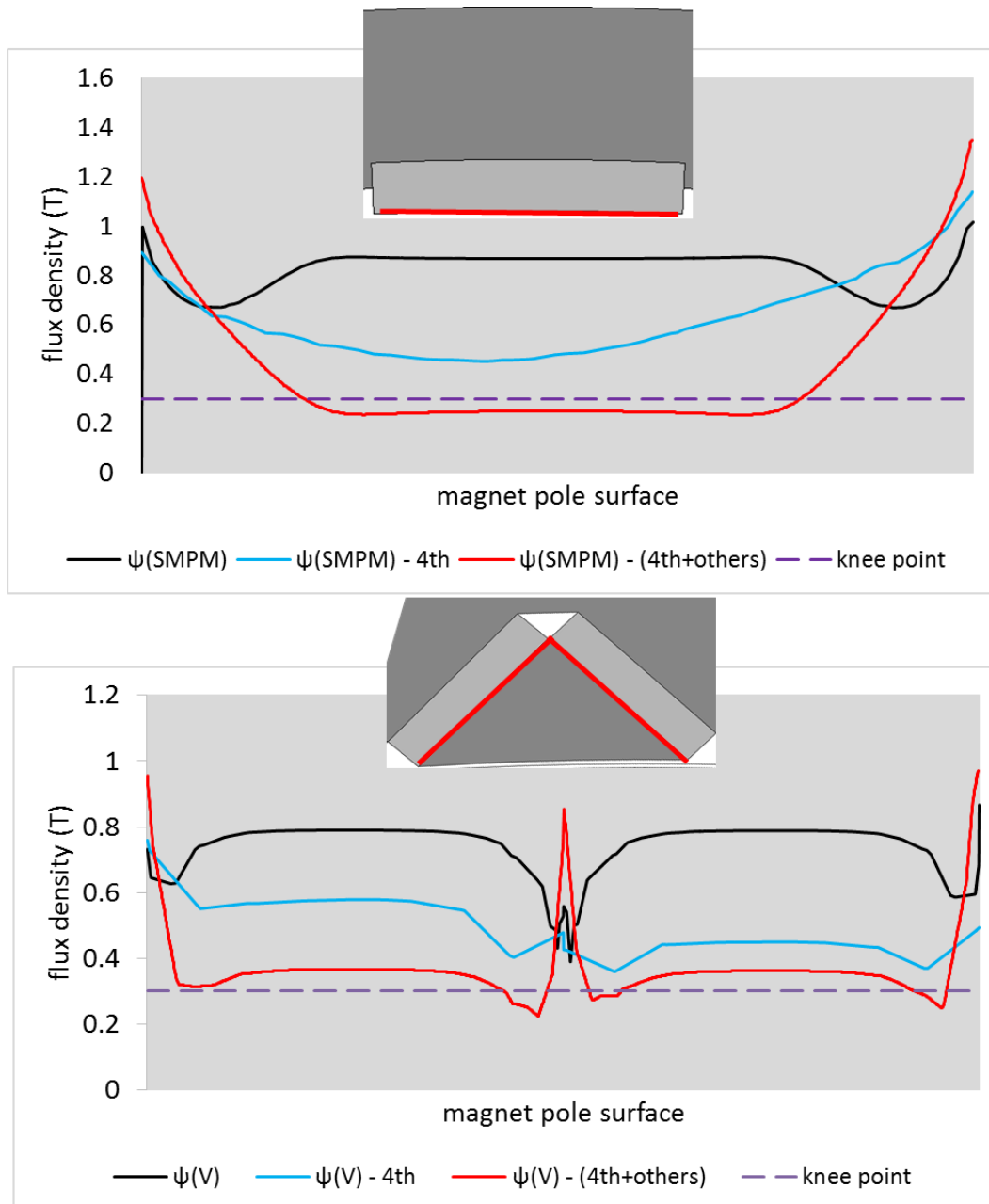


Figure 3-77 The flux density on the surface of the magnet(s) in SPM and V (the black line is the flux density with the magnets energised; the blue line is when the armature flux from 4th harmonic is opposing the magnet; the red is the worst case scenario with all harmonics included.)

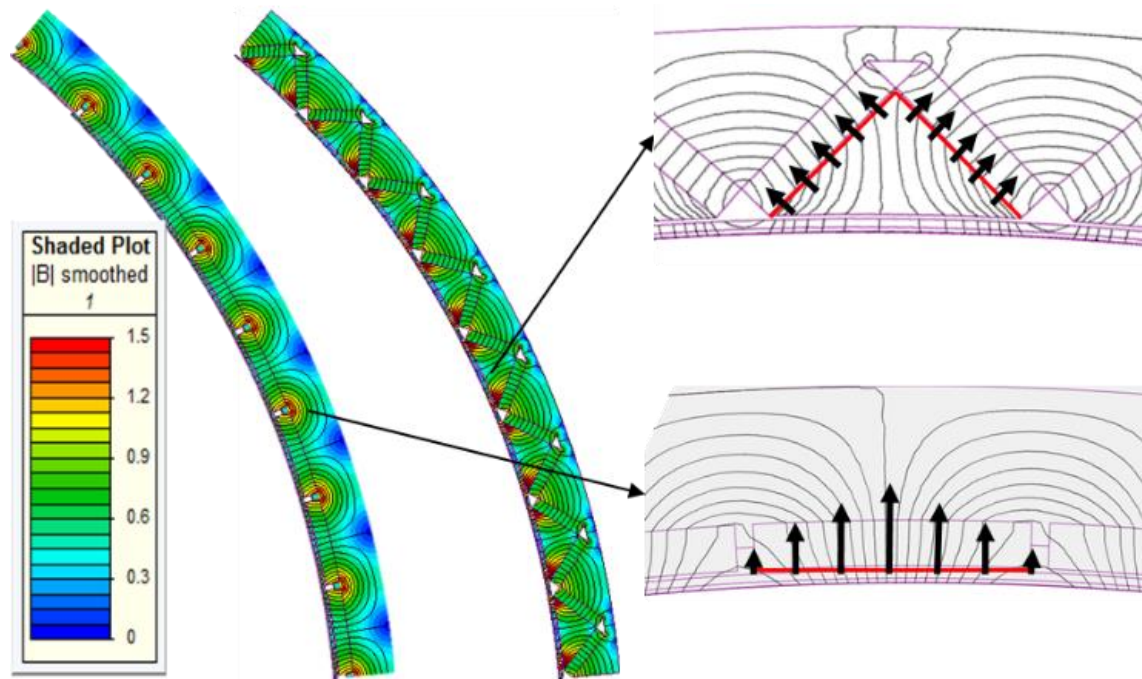


Figure 3-78 The flux density plotted with 4th harmonic on $-d$ axis

3.3.5. Conclusion

The magnet loss of the PMs is explained thoroughly in this section. Firstly, the analytical model of the source field from the stator harmonics is introduced. It is then verified by the current sheet method in 2D FEA. With the source field known, two analytical and one hybrid method to calculate magnet loss are discussed. Deeper insight is gained into the magnet loss inducing mechanism in the BMM (64pole and 72slot). Magnet loss is shown to be dominated by the presence of a negatively rotating 80 pole field, and it is shown how this loss can be reduced by 65% by segmenting the magnets into two circumferential parts. To reduce costs, magnet mass reduction is desirable, it is shown why by adopting V-shaped magnets in an interior configuration, this can be achieved with reduced risk of irreversible demagnetisation.

3.4. Optimisation and Finalisation

In this section, the V-shaped design is optimised and finalised for prototype construction. A detailed optimisation procedure is presented. The demagnetisation issue and the torque-speed characteristic curve are also analysed in detail.

3.4.1. The parameter table of the BMM and V-shaped motor

The parameters of the magnet of the V-shaped motor are defined in Figure 3-79. The aspect ratio (the active axial length to outer diameter) of the BMM is 0.15 and is shown in Figure 3-80. Dimensions of both models are listed in Table 3-5.

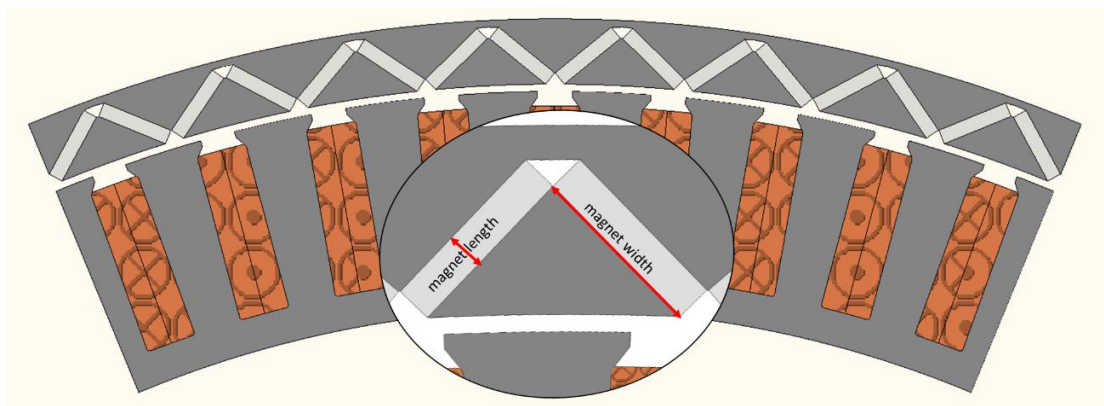


Figure 3-79 The V-shaped motor

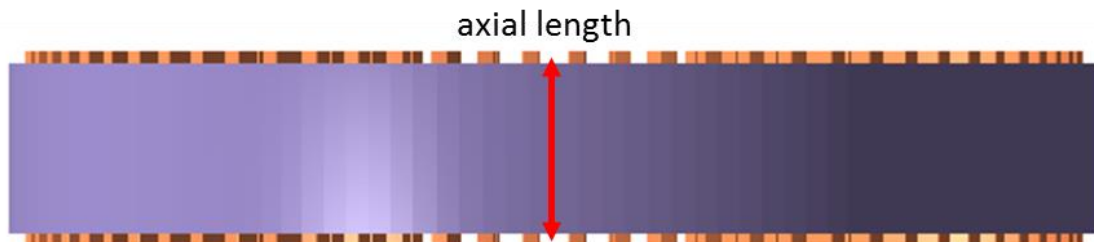


Figure 3-80 The axial length to outer diameter ratio

Table 3-5 The geometric parameters in the BMM and V

PD18	BMM	V
mag width (mm)	17	10
mag thickness (mm)	5	2
mag pole pitch (deg)	169	-
air gap (mm)	1	
axial length (mm)	58.8	
rotor outer radius (mm)	193	
rotor inner radius (mm)	182	
stator inner radius (mm)	151	
magnet pole number	64	
slot number	72	
sub motor number	8	

3.4.2.Optimisation of V

For traction motors in an EV, the torque-speed characteristic curve is an important performance metric and contains the main optimisation objectives. The V-shaped motor needs to provide the same rated torque output as the BMM in the constant torque region and the same corner speed point for the same VA rating. The back EMF and synchronous inductance are key factors that affect the torque output and terminal voltage rating if the current input is fixed.

The optimisation strategy used here is: first, select the computationally inexpensive 2D static FE simulation to optimise the torque output by changing the magnet position and shape; then, apply the 2D transient FE simulation to tune the torque-speed curve so that it matches up with the BMM. 3D FEA is not used since both the benchmark and the V-shaped motor share very similar end effects by using the same stator. The optimisation method is the same as what has been described in 3.1.3.

Notice, the multi-piece design (Figure 3-85) is chosen to be used for magnet optimisation due to its simpler geometry compared with the final design (Figure 3-79).

Optimum V position

There are 5 position parameters defined as independent variables and investigated in 5 sets of experiments. Each variable is varied in 5 equal steps with the remaining four variables controlled (kept constant). The variables are illustrated in Figure 3-81 with step numbers marked from 1 to 5 and variables named from a.) to e.). The rated torque responses are illustrated in Figure 3-82.

In all sets of experiments, the inner rotor diameter, which is related to the active machine volume and thus the torque, is fixed. Hence, with the magnet shape unchanged, the outer rotor must change according to the value of b., c. and e. variables. It is then decided that the effect of varying the outer radius should first be studied. All results from the simulation are collected and tabulated in Table 3-6.

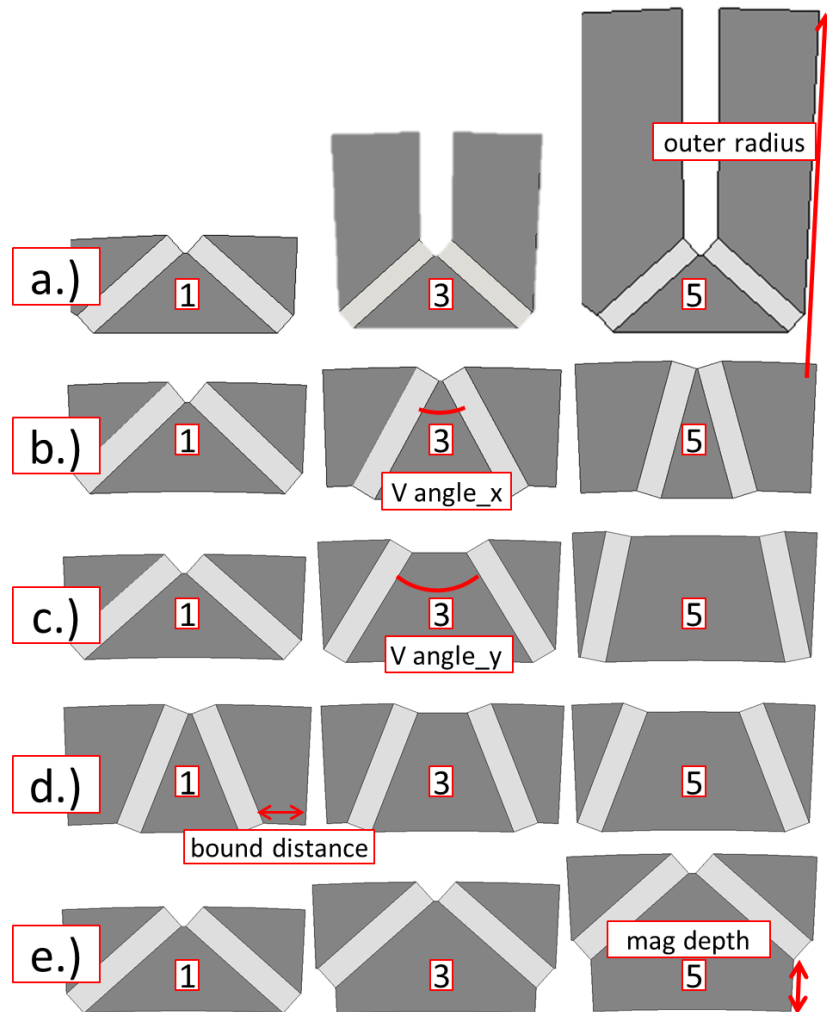


Figure 3-81 Variables study

Table 3-6 The designed experimental response to magnet position

a.)	torque	b.)	torque	c.)	torque	d.)	torque	e.)	torque
mm	Nm	deg	Nm	deg	Nm	mm	Nm	mm	Nm
190	706.6	99.5	707.0	99.5	707.0	5.1	658.2	0	707.0
195	704.5	80.1	717.9	75.6	698.7	4.3	667.0	1	661.9
200	703.9	61.8	696.6	61.9	693.7	3.4	686.4	2	632.1
205	704.1	45.1	658.2	46.7	688.8	2.6	692.0	3	600.5
210	703.7	32.9	580.8	22.9	683.2	1.85	688.1	4	570.9

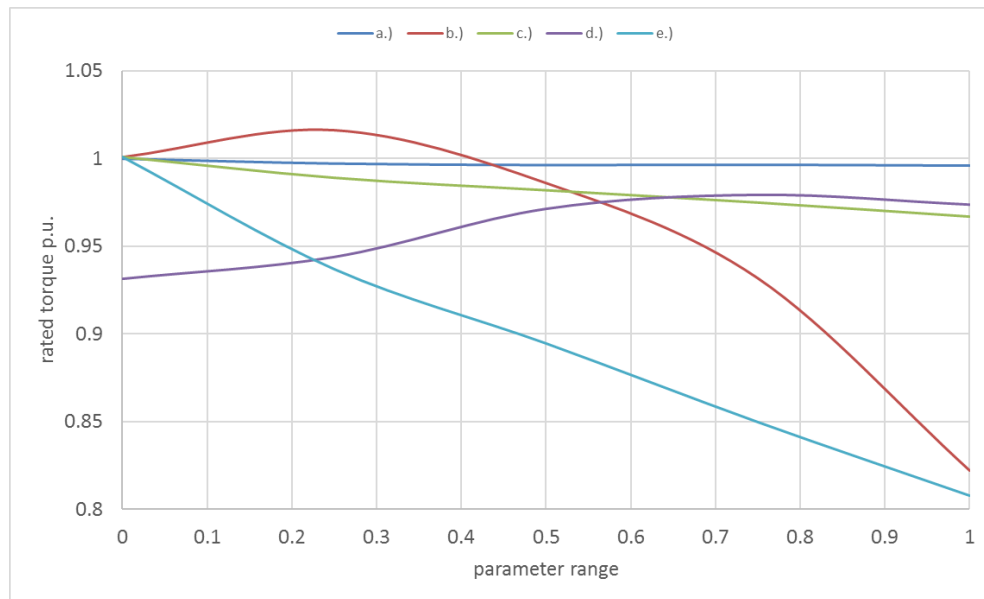


Figure 3-82 The p.u. rated torque response to parameter changes

a.) Outer radius

The independent variable, the outer radius, is changed from 190 to 210 mm in 5 steps and the torque performance drops by less than 1% from step 1 to 5. Therefore, difference in the rotor thickness in the following experiments will not be the main contributor to the torque output difference.

b.) V angle - leg

The variable 'V angle' is varied from 99.49° (maximum allowable) to 32.9° by squeezing its legs towards the centre. The torque reaches its optimum value at step 2, indicating that there is an optimum magnet position for flux concentration. It starts dropping noticeably from step 4 at 45° . The reason for the drop is that the flux is overly compressed and the area of the flux path is heavily restricted to the tooth tip when the flux enters the stator. Consequently, the saturation level is highest in step 5 as can be seen from the area circled in Figure 3-83.

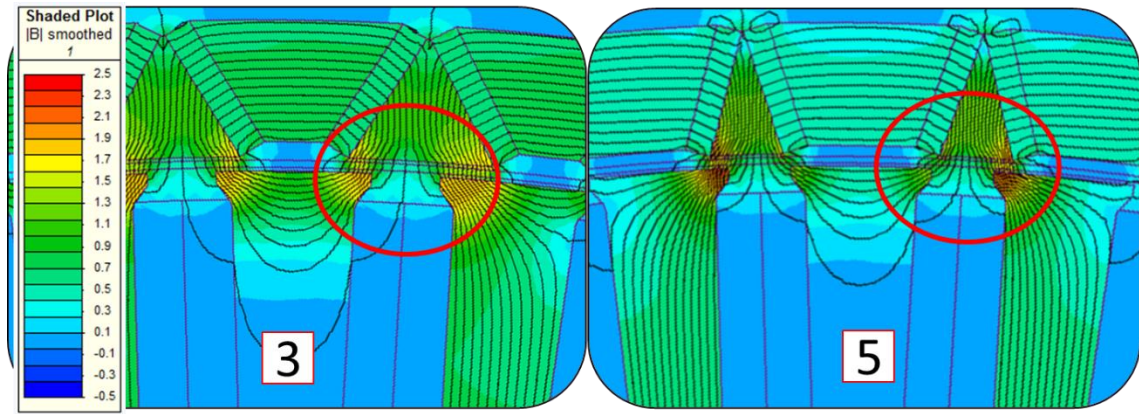


Figure 3-83 Field plot on Q axis at no load of model b. no. 3 and 5

c.) V angle - head

As is shown in the third line of Figure 3-81, the V magnets open from the head and the V angle is reduced from 100° to 23° . The torque output drops by 3.4%. This drop is due to an increased flux leakage.

This phenomenon can be demonstrated in Figure 3-84. When at no load, the flux on the top edge of the magnets in model 5 leaks through the outer air region and fails to contribute to the air gap flux. This is because the flux from the magnet in model 5 points less towards the air gap compared to model 1. The fluxes from two oppositely magnetised magnets inevitably meet in the middle of a pole and, analogous to a water stream, part of it is deviated outwards radially away from the air gap creating leakage flux. Furthermore, the flux leakage path is much shorter in model 5 making it easier to form. The leakage flux and the flux deviation point are illustrated by the red circles in the field plot of model 5 and compared with model 1 in Figure 3-84.

Incidentally, in an extreme condition, the two magnets in model 5 can be merged into one and the leakage flux on top will be at its maximum, which helps to explain the lower magnet utilisation factor in the I-shaped magnet design.

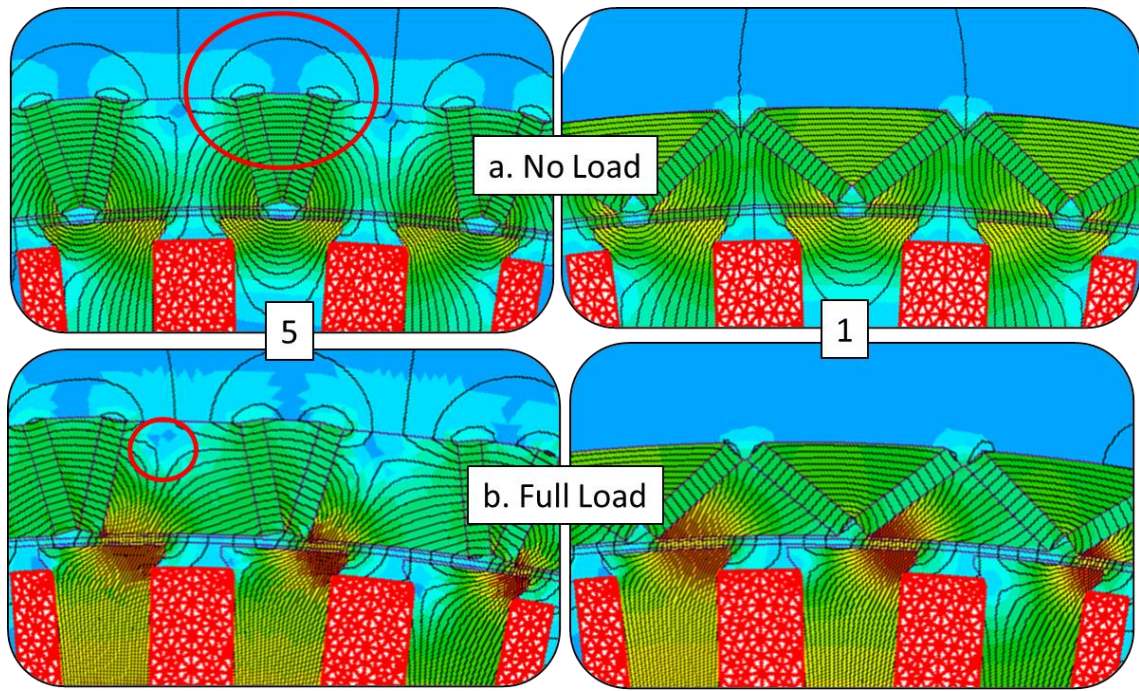


Figure 3-84 Field plot on Q axis of model c. no.1 and 5

d.) Bound distance

As is shown in the fourth line of Figure 3-81, by changing the variable, bound distance, the two magnets that formed one pole can be moved away from each other with a fixed angle x and y . The torque output is 4.5% higher when they are placed at a maximum distance away from each other. This can be explained by the combining effect from tooth tip saturation phenomena in set b and the flux leakage effect in set c.

e.) Magnet depth

When inserting V deeper into the rotor frame from step 1 to 5, the torque ripple is reduced from 3.3% to 2.5% and the magnet loss is reduced slightly too. However, the mean torque is reduced by 19.3% due to a large flux leakage formed around the leg of the magnets. Hence, the magnet should be kept close to the air gap.

Conclusion

In order to reach an optimum torque output, the two magnet legs (the side closer to the air gap) of a pole should be placed away from each other to avoid tooth tip saturation and their heads are required to stay close together to form the optimum flux concentration angle ($70^\circ - 100^\circ$) and prevent flux leakage.

The design in Figure 3-85 delivers the optimum torque, which is very similar to the original one (Figure 3-79) in terms of magnet position choice transferred from the 16'' frame.

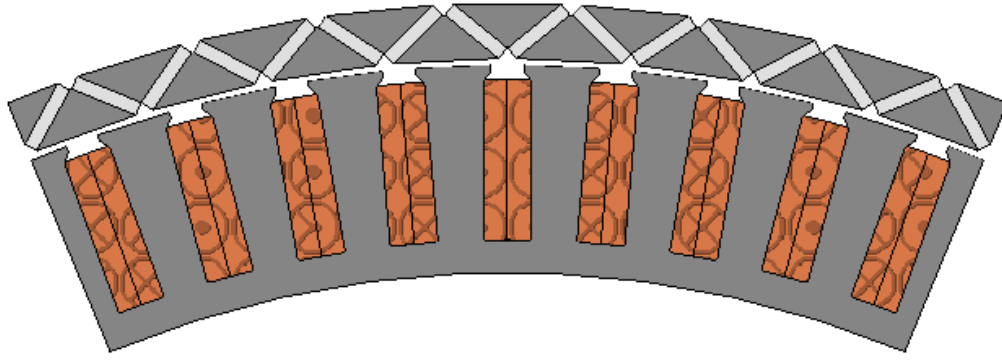


Figure 3-85 Optimum magnet position

Optimum magnet shape

The size of a V magnet is determined by its radial length, width and axial length. It is suggested that the axial length should be fixed for better integration with the existing components. Hence, the 2 studied variables are magnet a. width and b. length and each varies again in the 5 steps.

a.) Magnet length

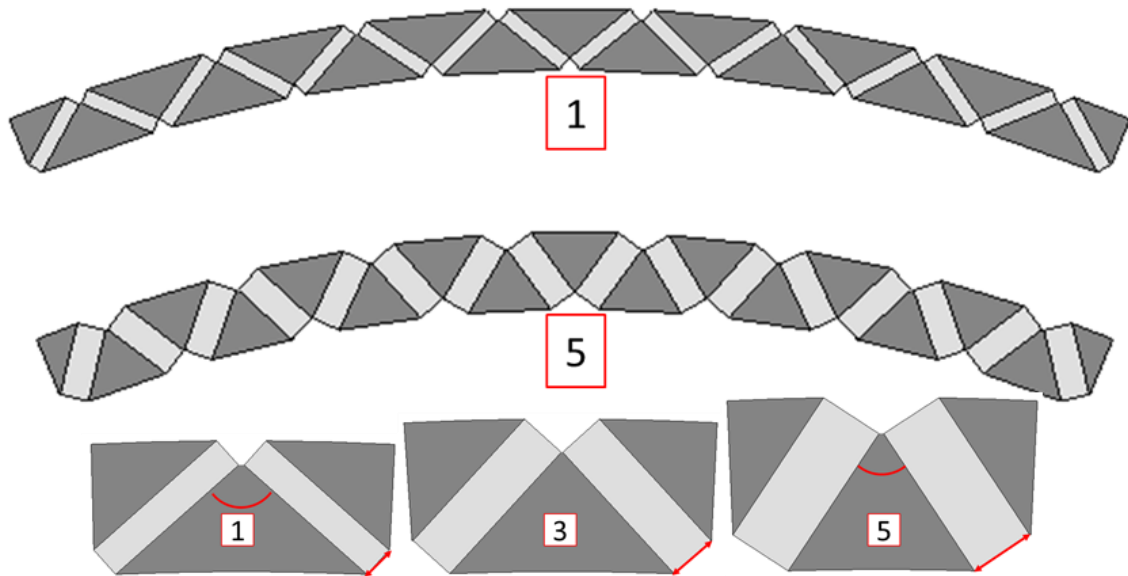


Figure 3-86 Magnet length drawing

The magnet length is changed from its initial length of, 2mm in design 1, to 4mm in design 5 as can be seen from Figure 3-86. The magnet mass is also changed from 0.47 to 0.99, the unit of the original magnet mass in the BMM. The results are graphed in Figure 3-87. Where the red line is the magnet utilisation value defined in chapter 5 and the black line is the torque output of the whole motor. The magnet utilisation is less effective with a higher magnetic loading and a more saturated circuit in the lamination. Furthermore, due

to its fixed core back depth, the magnet V angle is forced to be reduced from 96° to 66° shown in Table 3-7, which further increases the saturation level around the tooth tip area. When the saturation level increases, the difference between the inductance on the d and q axes reduces meaning the reluctance torque of model 1 is higher than model 5. This can be approved by checking the current alignment angle, beta.

To conclude, the magnet length should be kept to its minimum value, in order to achieve the highest magnet utilisation level without demagnetisation. The value of 2mm is selected based on the analysis of demagnetisation from the BMM. It is also considered to be the minimum length achievable in current mass production means.

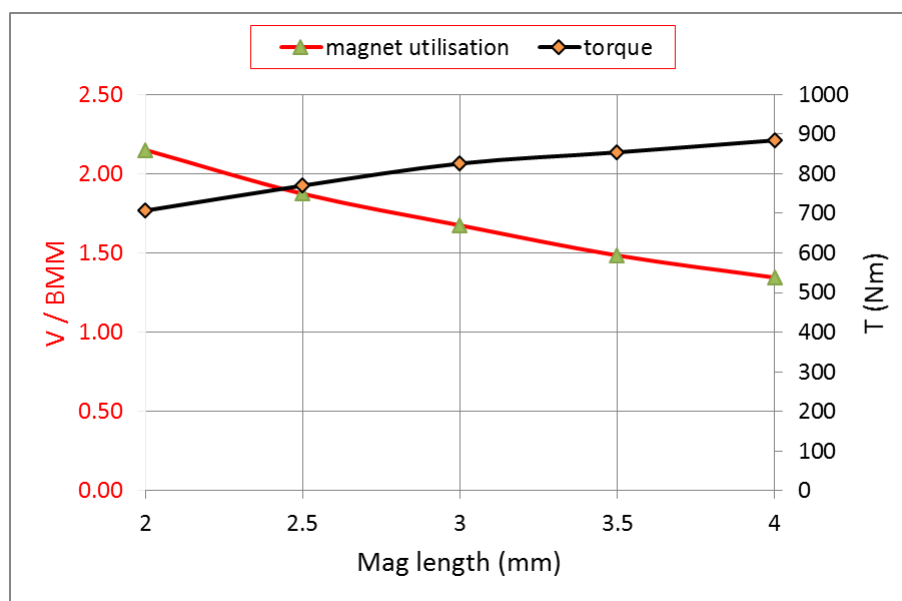


Figure 3-87 Experimental response to magnet length variation

Table 3-7 2D static FE simulation results on magnet length variation

test variable		fixed width at 10mm					
Mag length	Beta	Torque	V Angle	Mag Mass	T/M		
step No	mm	deg	Nm	deg	kg	Nm/kg	ratio
1	2	-21	707.03	96.44	1.13	626.27	2.15
2	2.5	-21	770.22	92.16	1.41	545.79	1.87
3	3	-23	825.98	84.66	1.69	487.75	1.67
4	3.5	-23	854.24	77.53	1.98	432.38	1.48
5	4	-15	884.49	66.53	2.26	391.73	1.35
BMM	5	-12	694.04	-	2.38	291.20	1

b.) Magnet width

In this test, the width changes from 8mm to 12mm and is marked by a red arrow in Figure 3-88. The magnet length is fixed at 2mm. The results are graphed in Figure 3-88. The magnet utilisation at step 1, 2 in set b.) is higher than the best one, step 1, in set a.). However, in order to meet the torque requirement, magnet width of 10mm at step 3 should be set as the minimum value. All the data are tabulated in Table 3-8.

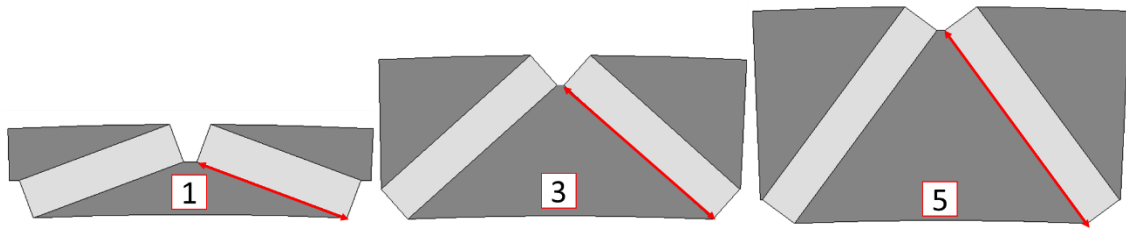


Figure 3-88 Magnet width drawing

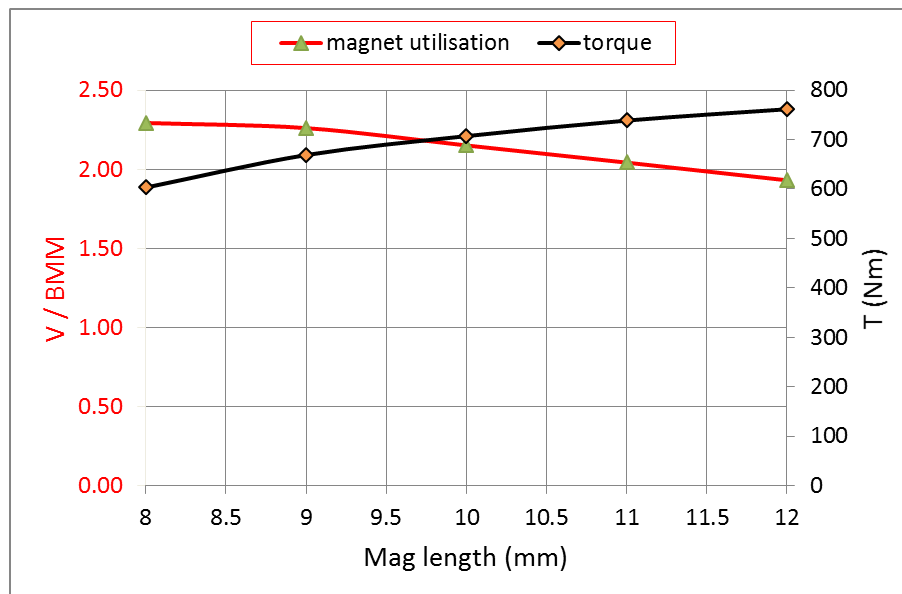


Figure 3-89 Experimental response to magnet width variation

Table 3-8 2D static FE simulation results on magnet width variation

test variable		fixed thickness at 2mm					
Mag width	Beta	Torque	V Angle	Mag Mass	T/M		
step No	mm	deg	Nm	deg	kg	Nm/kg	ratio
1	8	-21	602.97	119.68	0.90	667.62	2.29
2	9	-22	668.79	115.00	1.02	658.22	2.26
3	10	-21	707.03	96.44	1.13	626.27	2.15
4	11	-21	738.53	80.51	1.24	594.70	2.04
5	12	-21	761.48	68.55	1.35	562.08	1.93
BMM	17.1	-12	694.04	-	2.38	291.20	1

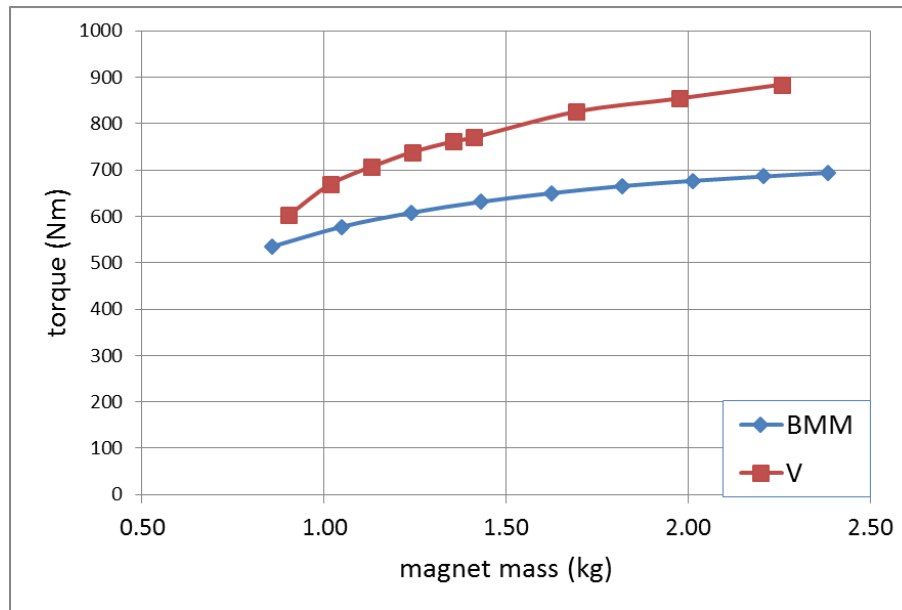
Torque against magnet volume

Figure 3-90 The torque plotted against magnet mass in BMM (benchmark motor) and V
 The torque output is plotted against the magnet mass for both the benchmark and the V-shaped designs in Figure 3-90. The magnet mass in the benchmark motor is changed by varying the magnet thickness only. The torque curve of the V-shaped design is made by collecting the best results at each magnet mass point from Table 3-7 and Table 3-8. It is clear that much more torque can be exerted from the V design when magnet mass is the same as the BMM. Or much less magnet material can be used in the V-shaped design for the same torque requirement.

Modification of V

As mentioned, the V model used in the magnet position and shape optimisation process is a multi-piece version. The next step is to change the V design into an easy-to-manufacture version of V - design 7, Figure 3-49. With identical magnets used, a 10mm magnet width and a 2mm magnet length, the rated torque is dropped from 707.03Nm to 683.43Nm in the ‘air block V’, about 3.3% of the ‘multi-piece V’. The models of these two V versions are shown in Figure 3-91.

Conclusion

The ‘air block V’ of a 10mm width and a 2mm length is chosen after optimisation with a 1.8% lower torque compared to the BMM. In the next section, accounting for the torque-speed characteristic curve, the magnet size will be finalised.

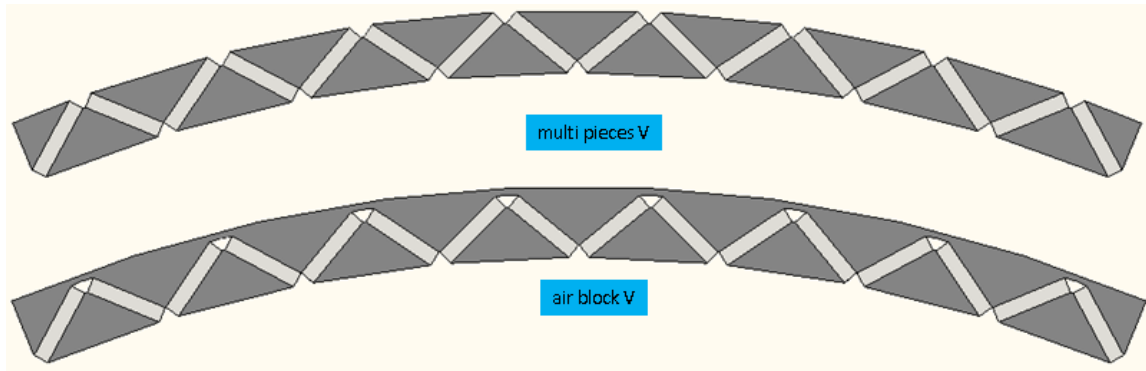


Figure 3-91 The air block V drawing

3.4.3. The final tuning of the V-shaped in-wheel motor

Torque-speed characteristic curve tuning

It is vital for a direct-drive traction motor to produce sufficient torque at a full speed range. The torque-speed curve can directly demonstrate the motor's torque performance over a full speed range. Hence, it is necessary to analyse the curve of the V-shaped motor and compare it with the benchmark motor BMM (surface-mounted). There are many types of control methods to generate the torque-speed curve. The one used here is “maximum torque control”.

The magnitude of the input current, voltage limit and rated power for the V-shaped motor is identical in both the BMM and the V design and the aim is to generate the same torque-speed curve. The two curves of the BMM and the optimised V from the last section were obtained by 2D transient simulation and graphed in Figure 3-92. The torque output of V is slightly lower (1.8%) than the BMM in the constant torque region. In the constant power region, as experienced in the BMM in Figure 3-47, the V-shaped motor has a corner speed 5.3% lower than the BMM due to a higher back EMF constant (Volts per krpm) and is circa 8% lower than the BMM in rated output power.

Hence, it is necessary to tune both corner speed and torque output to match the torque-speed curves.

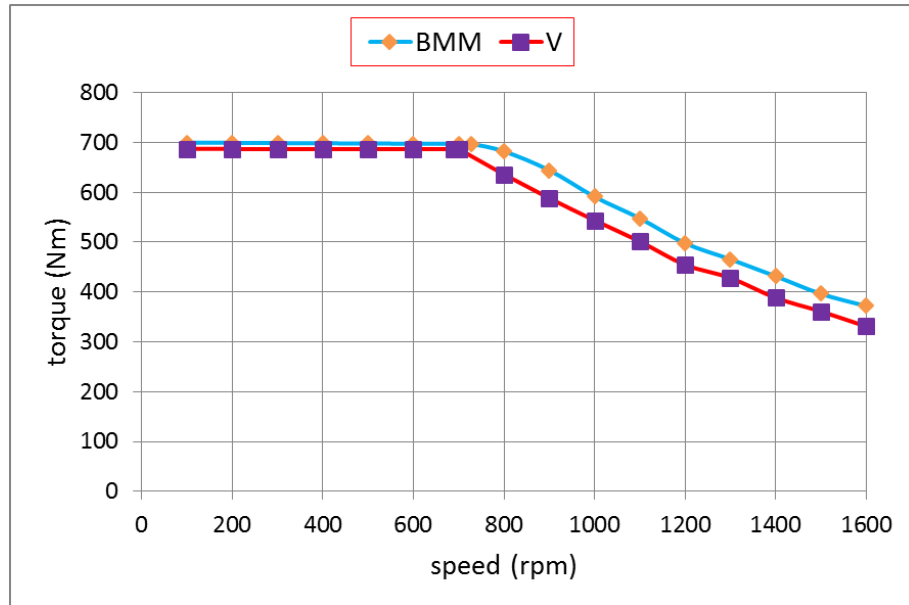


Figure 3-92 The torque-speed curve plot of V_32turns

A. Corner speed tuning

The corner speed is dependent on the back EMF, which is proportional to flux linkage, and hence coil turns. By simply reducing the number of coil turns by circa 6.25% in the V design, the corner speed can be increased by $\frac{1}{1-6.25\%} - 1 = 6.6\%$. The result of changing coil turns from 32 to 30 is illustrated in Figure 3-93, with corner speed of the V increasing to 745rpm compared to 728rpm in BMM. Thus, the corner speed of the two motors is matched. The reduced coil turns also allow a larger gauged wire to be selected, which in turn slightly reduces coil resistance, and in turn copper loss reduction.

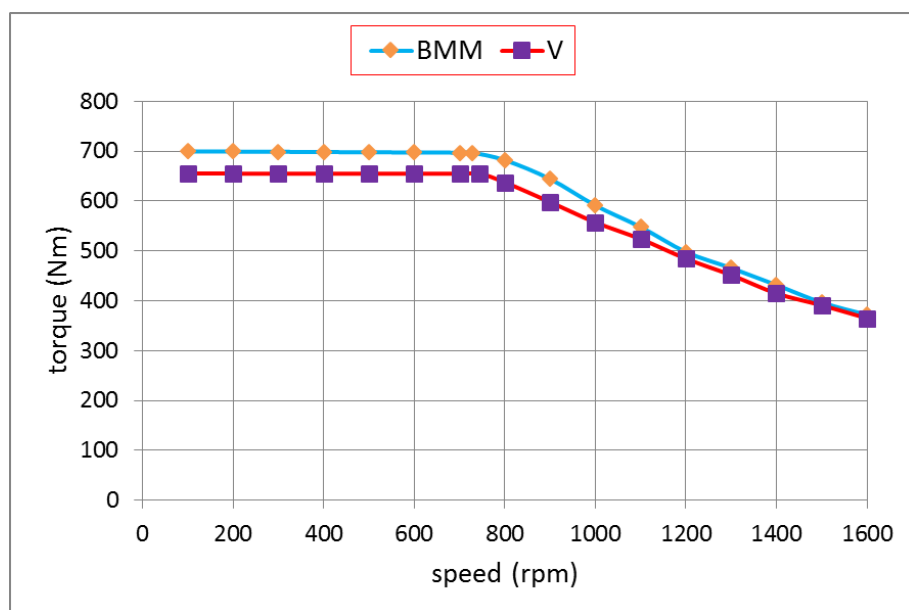


Figure 3-93 The torque-speed curve plot of V_30turns

B. Torque output tuning

As shown in Figure 3-93, the rated torque is lower in the V design with 30 turns. To improve the torque performance, slightly more magnet material is used. The magnet width is increased from 10mm to 11.9mm which makes the magnet mass increase from 54% to 56% of the BMM. The torque-speed curve of V can then be matched with the BMM in Figure 3-94.

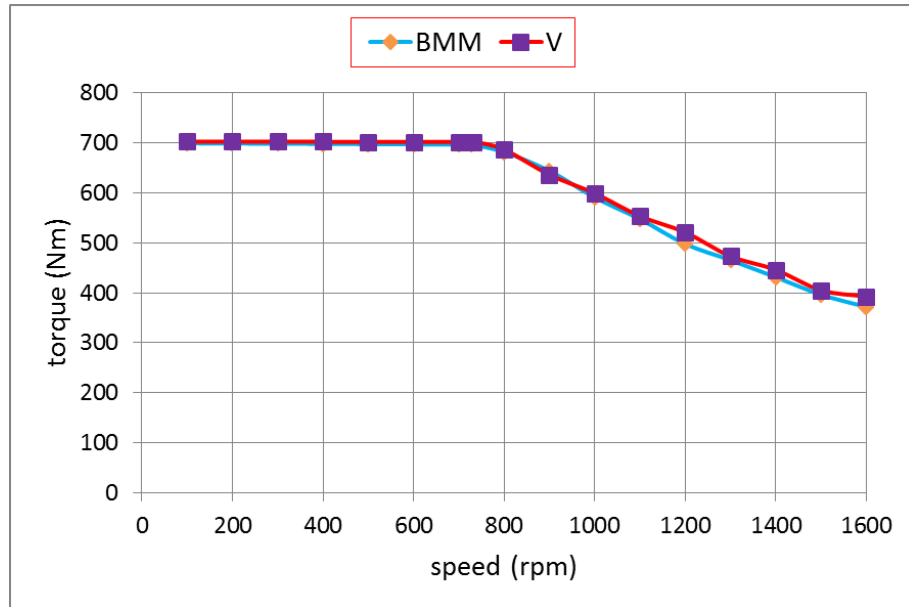


Figure 3-94 The torque-speed curve plot of V_11.9mm

C. reshape the V

The iron bridge thickness of this magnet-length-increased V design is merely 0.5mm as shown in Figure 3-95. This will impose a big challenge on the mechanical stress handling and manufactural approach. After discussion with mechanical engineers from Protean, it was decided that 2mm is the minimum acceptable iron bridge thickness.

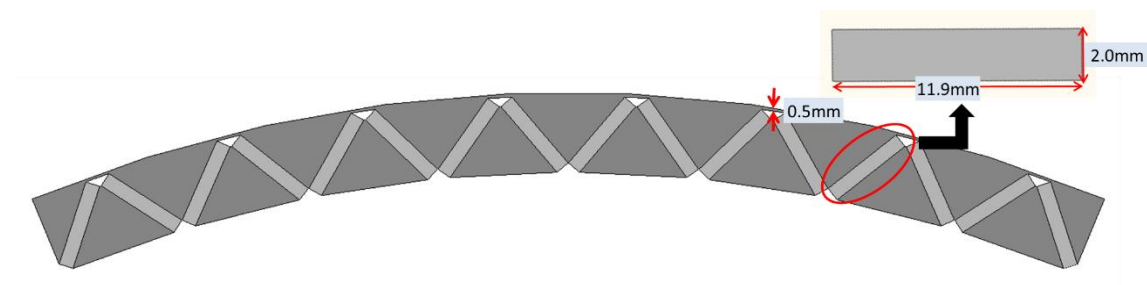


Figure 3-95 The V with thin back iron

The magnet width and length are then arbitrarily mutated around the original values with constraints of a 2mm back iron and torque requirement. Ten designs with the highest

possible magnet utilisation level are compared and their width, length and magnet mass differences are recorded in Table 3-9. V2 is the original design shown in Figure 3-95 and its torque-speed curve matches that of the BMM in Figure 395. From V3 to V10 are the optimised designs with the minimum allowable back iron thickness, 2mm. V3 and V8 are taken as examples in Figure 3-96. As is shown in Table 3-9, both the torque output and magnet utilisation in V8 are close to V2. Hence, V8 is selected for the final design. The geometric drawing and torque-speed curve are illustrated in Figure 3-97 and Figure 3-98, which gives a 4% lower torque in the constant torque region.

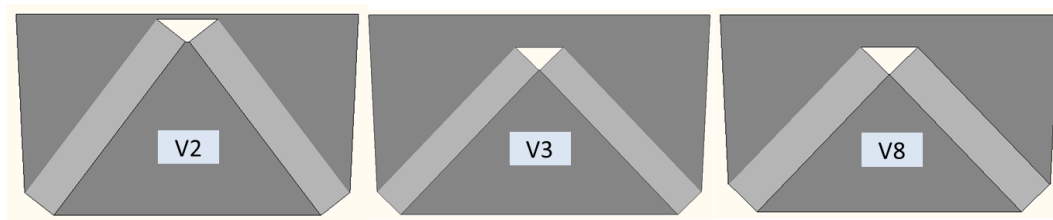


Figure 3-96 Drawing example: V2, V3 and V8

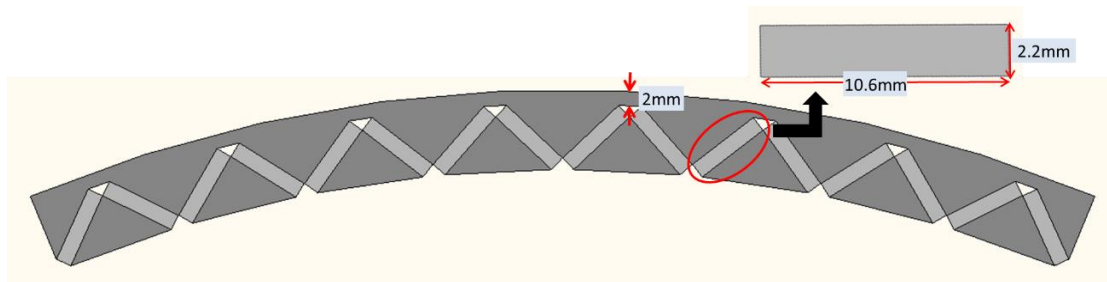


Figure 3-97 Drawing of V8

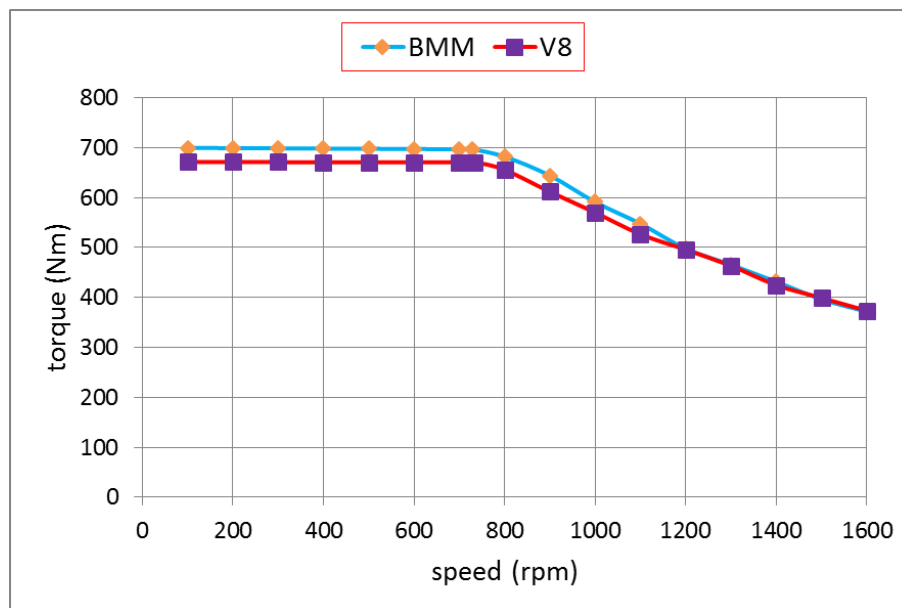


Figure 3-98 Torque-speed curve of V8 and BMM

Table 3-9 The data for the 10 designs

motor type	Torque		magnet shape		magnet utilisation	
	one sub	whole	length	width	Nm/kg	per unit
	Nm	Nm	mm	mm		
BMM	86.91	695.25	17	5	289.70	1.00
V1	82.01	656.09	10	2	581.15	2.01
V2	91.72	733.76	11.9	2	546.17	1.89
V3	82.01	656.07	11	1.8	586.99	2.03
V4	83.50	668.02	10.9	1.9	571.43	1.97
V5	84.96	679.69	10.8	2	557.45	1.92
V6	86.30	690.37	10.7	2.1	544.29	1.88
V7	86.98	695.83	10.65	2.15	538.35	1.86
V8	87.60	700.79	10.6	2.2	532.36	1.84
V9	88.14	705.11	10.55	2.25	526.23	1.82
V10	88.92	711.33	10.5	2.3	521.80	1.80

Demagnetisation resistance analysis

Demagnetisation of the V-shaped magnet is analysed thoroughly in this section to verify the final design. The magnet temperature in the V and the BMM is set to be identical - 100°C for its maximum operating temperature.

The full analysis is conducted in three models: 1) the BMM; 2) the V8; 3) the BMMr (the benchmark motor with reduced magnet length - from 5mm to 2.77mm). Their magnet mass ratio is 1:0.55:0.55. There are 2 sets of 2D FE analyses used.

Set a.) Static analysis

The static analysis is conducted under three conditions:

- Normal: current aligned with the q axis with a peak phase value of 30A;
- Overload: overloading current input on the q axis with a peak phase value of 60A;
- Worst case scenario: overloading current on the -d axis, i.e. armature flux opposing magnet flux, i.e. $I_{q,pk} = 0A$, $I_{d,pk} = -60A$.

From the results shown in Figure 3-99, it can be seen that in the worst case scenario the BMMr magnets exhibit a large red area indicating the V-shaped motor's superior resistance to demagnetisation when the magnet mass is the same. The percentage of the demagnetised area is shown in Figure 3-100. For the V shape, it is near 0% at both normal and overload conditions and <4% of the magnet is demagnetised in the worst case scenario

around the edge. The BMMr experiences more than a 43% demagnetisation in some magnets in the worst case scenario.

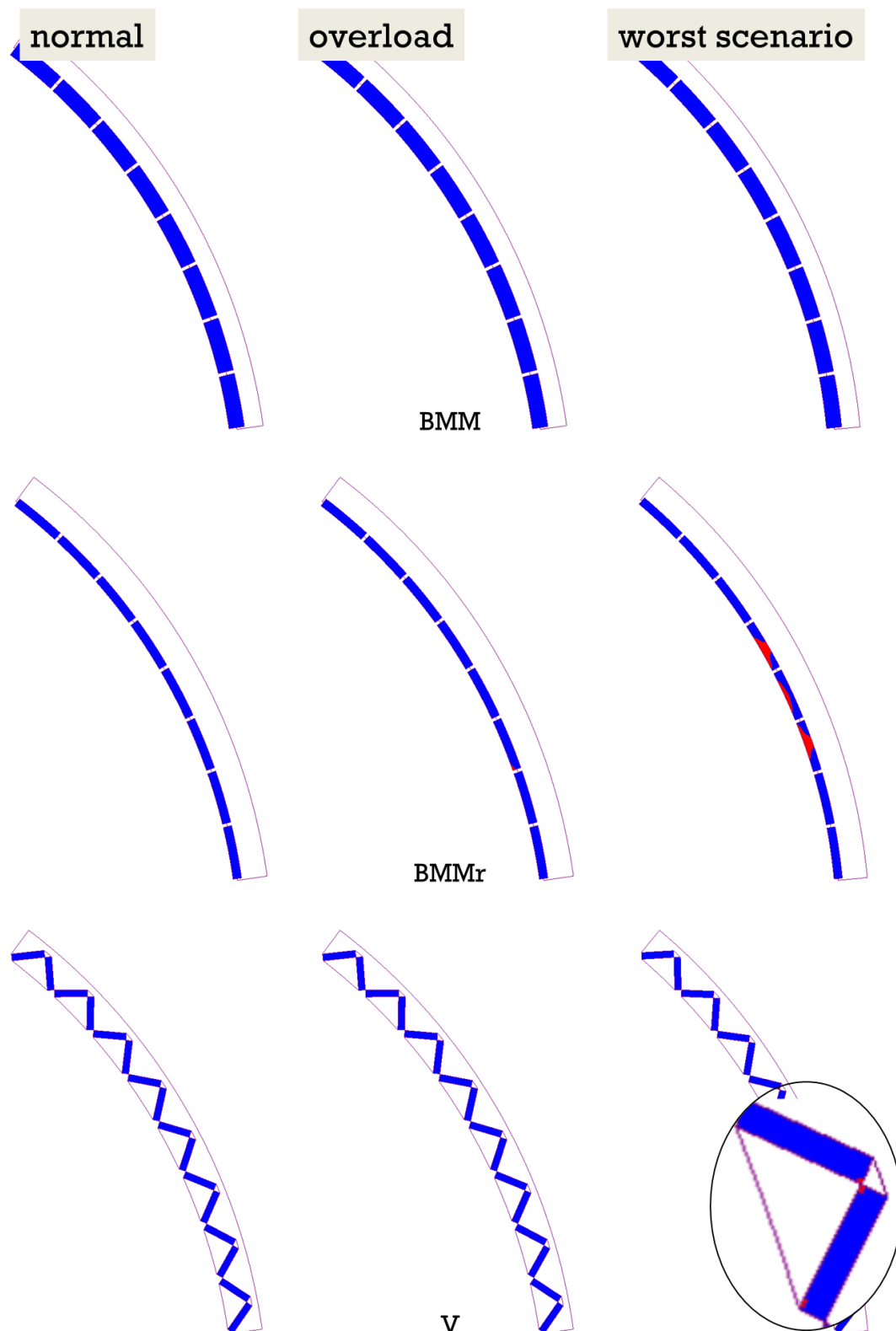


Figure 3-99 Static demagnetisational resistance analysis

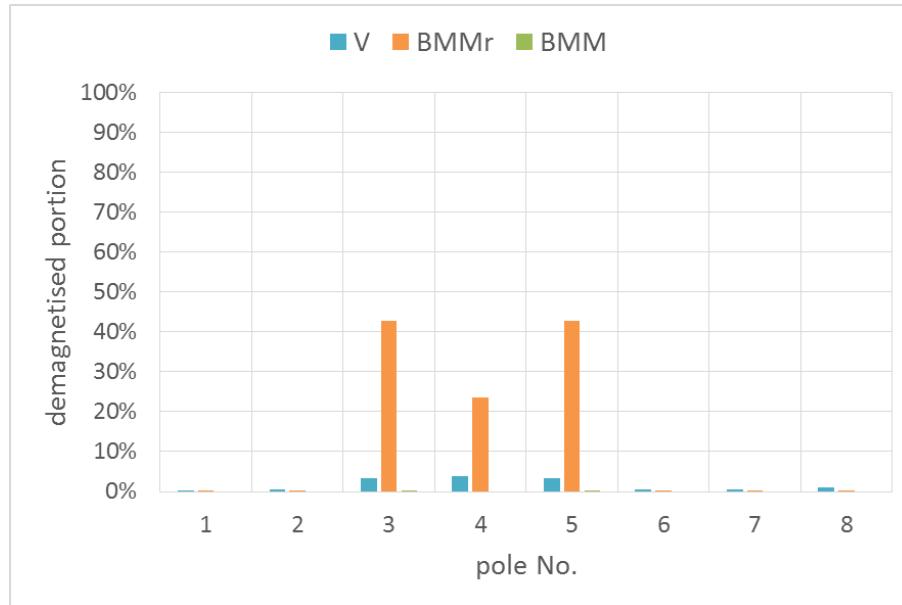


Figure 3-100 The bar representation of the worst case scenario

b.) Transient analysis

Besides a different current input, the relative rotor and stator positions can also affect demagnetisation. Hence, transient analysis is conducted in two cases:

- a. DC current, 60A for reference phase and 30A for the other two phases, with the rotor rotating;
- b. AC current, 60A sinusoidal waveform, with rotor fixed.

Each simulation is set to run 4 electrical cycles which is one full mechanical cycle of a sub-motor. The simulation results are illustrated in Figure 3-101 to Figure 3-104. It is clear that in both cases, every magnet in the BMMr will be demagnetised by at least 50% after a few cycles, whereas V magnets only experience <2% demagnetisation.

To conclude, the V-shaped motor can remain safe at any given condition during a healthy or faulty operation.

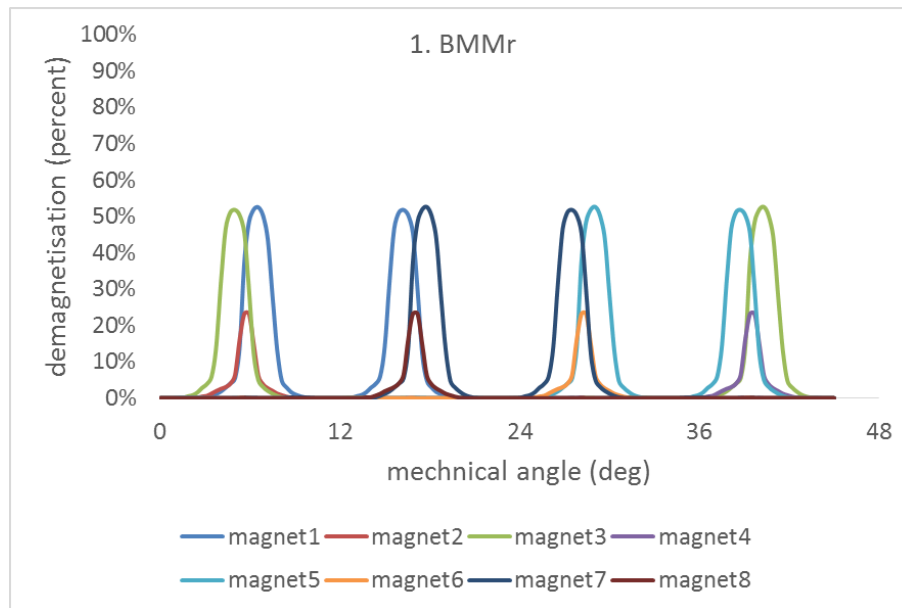


Figure 3-101 Transient demagnetisation analysis 1) on BMMr

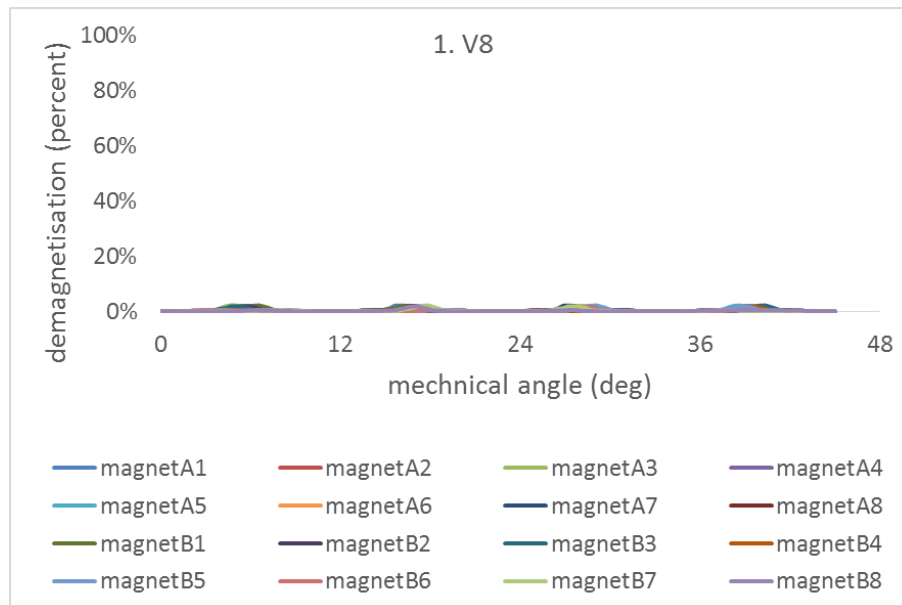


Figure 3-102 Transient demagnetisation analysis 1) on V8

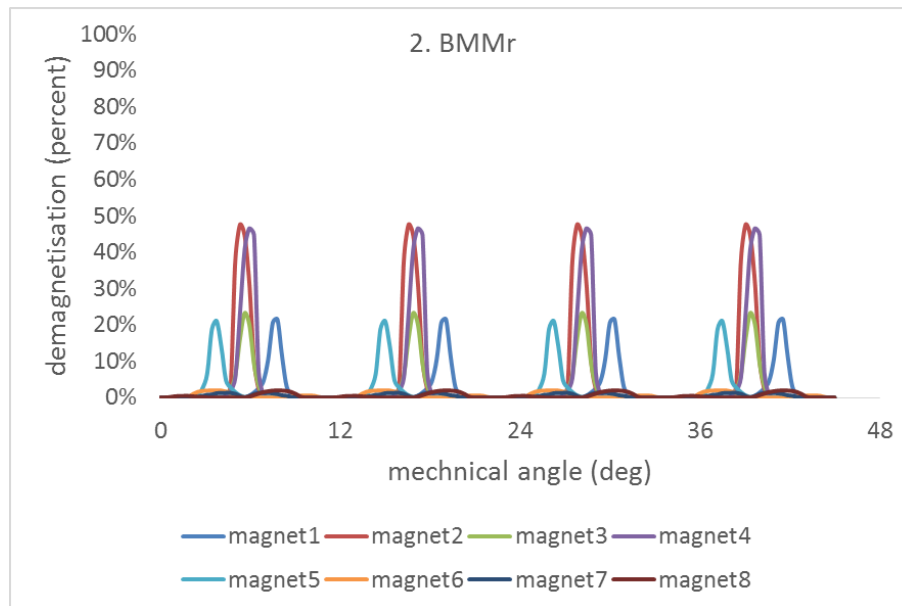


Figure 3-103 Transient demagnetisation analysis 2) on BMMr

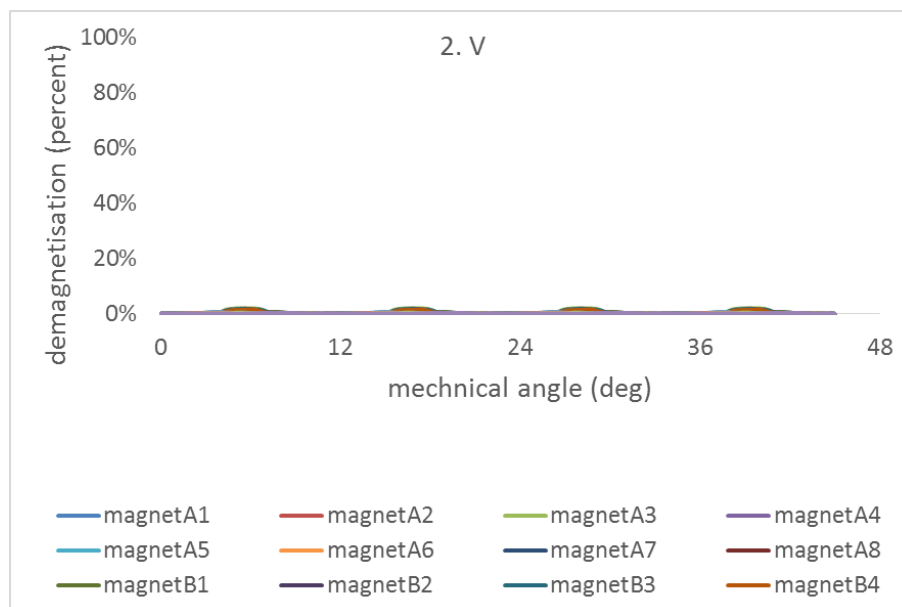


Figure 3-104 Transient demagnetisation analysis 2) on V8

3.4.4. Conclusion

The optimisation procedure of the V-shaped motor is discussed in great detail. The torque density can be optimised by maximising the angle of the V magnet and minimising the magnet length while resisting demagnetisation. The V-shaped motor with a 10.6mm magnet width and a 2.2mm magnet length is selected to match the same torque-speed curve as the BMM. Then the flux density of each magnet is examined at various rotor positions and in the worst case scenario. Demagnetisation is not an issue in the V-shaped motor.

3.5. Parameter Comparison between the BMM and V-shaped motor

In this section, the final design of the V-shaped motor is compared to the BMM from the following aspects:

1. No load flux linkage;
2. Back electromotive force (back EMF);
3. Terminal voltage;
4. Torque against current alignment angle curve;
5. Torque against current magnitude curve;
6. Torque ripple;
7. Inductance;
8. Torque-speed characteristic curve;
9. Efficiency map;
10. Additional losses;
11. The AC copper loss;
12. The magnet temperature.

The vibrational test and the duty cycle analysis has been conducted on the BMM in the research prior to this thesis by [44]. The V-shaped motor is deemed to have similar characteristics, so these two analysis is not included.

The V-shaped motor's dimension is recalled in Figure 3-105:

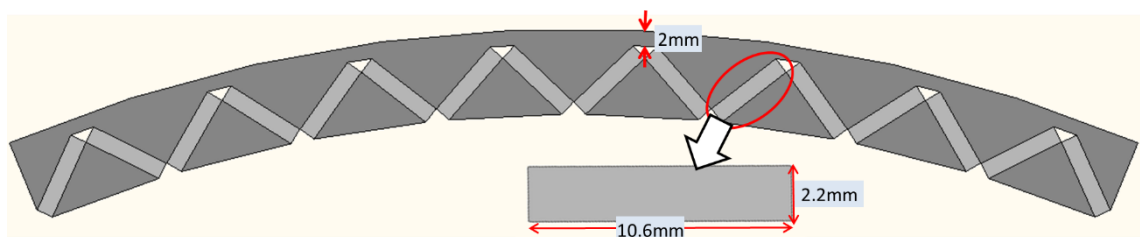


Figure 3-105 The rotor geometry in V

3.5.1. No load flux linkage

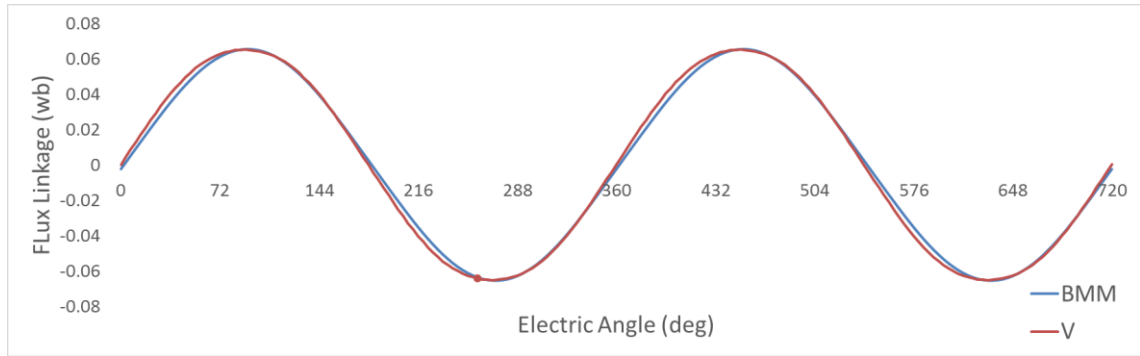


Figure 3-106 The no load flux linkage in BMM and V

In Figure 3-106, the flux linkages from the BMM and from the V are compared and the flux linkage is found to be 0.4% higher in the BMM motor due to having more magnet material. The phasor diagram is illustrated in Figure 3-121, the flux linkage is 90 degrees lagging the armature flux induced by the Q-axis current I_q . I_q is aligned with the back EMF to generate the alignment torque by energy conversion equation $EI = T\omega$.

3.5.2. Back electromotive force (back EMF)

The phase back EMF is proportional to the speed and the phase flux linkage. The FE result of one sub motor is shown in Figure 3-107. There is more 3rd harmonic in the V-shaped motor making its peak value 10% higher than the BMM. However, when the motor is connected to the inverter circuit, the inverter sees the link voltage across the motor and the line voltage of the V-shaped motor is 4% higher. The difference is halved due to cancellation of the 3rd harmonic when converting to line voltage.

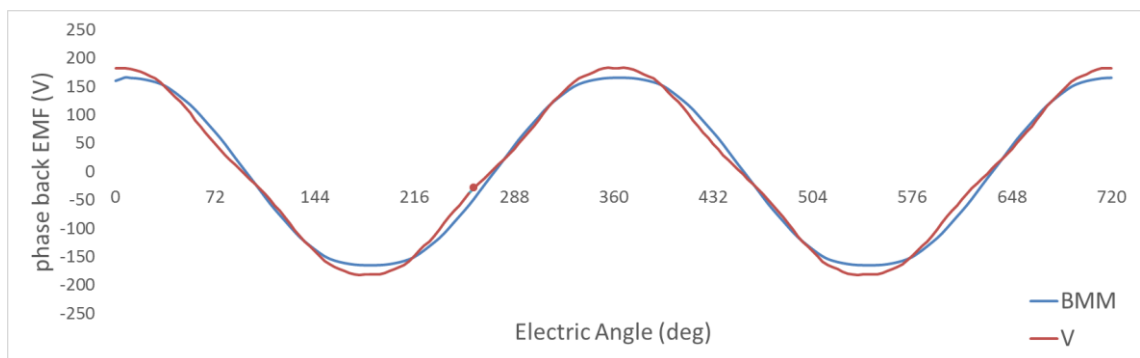


Figure 3-107 The phase back EMF in BMM and V at 800rpm

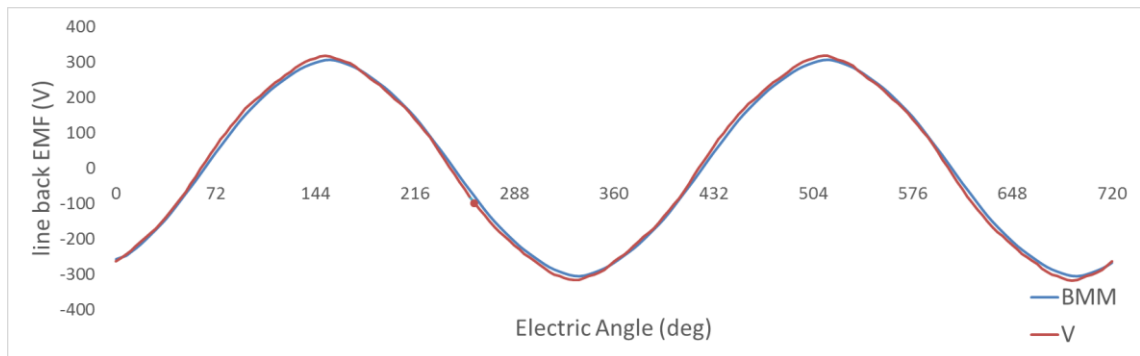


Figure 3-108 The line back EMF in BMM and V at 800rpm

3.5.3. Terminal voltage

In Figure 3-109, the terminal voltage is compared between the BMM and the V. There is a rich 3rd harmonic in the phase voltage waveform in both cases. However, the 3rd harmonic is cancelled in the line voltage. The line voltage magnitude is also 8% higher in V. The harmonic spectra comparisons are provided in Figure 3-110. Both the fundamental and 3rd harmonics are higher in the V-shaped motor.

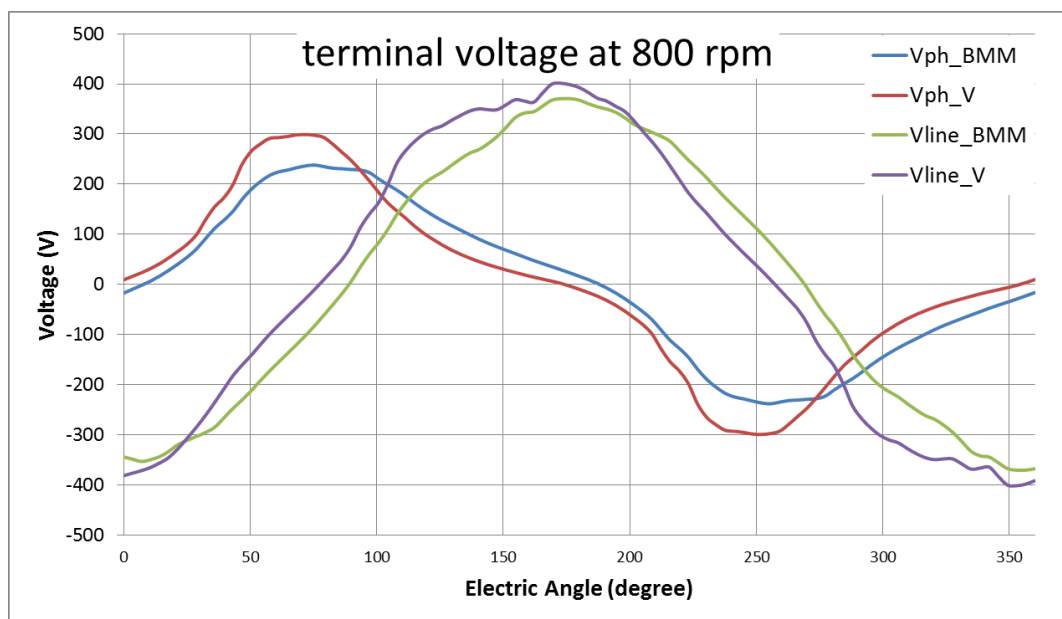


Figure 3-109 The phase terminal voltage at 800rpm

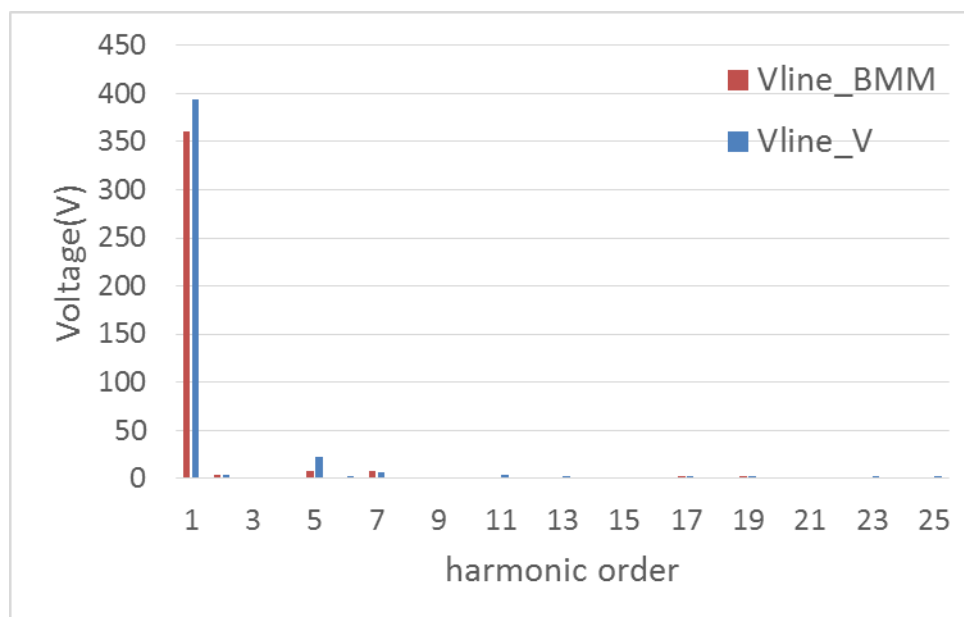


Figure 3-110 The harmonic spectra of the line voltage

3.5.4. Torque against current alignment angle curve

To control the torque accurately by advancing the current alignment angle, the torque against current alignment angle at different current values needs to be recorded. The angle for the peak torque is not fixed and is dependent on the current magnitude in the V-shaped motor due to d/q axis inductance variation, which in turn increases the control complexity.

In Figure 3-111, the torque waveform of the V, the red line, leans away from 0° (the q axis), this proves there is a noticeable reluctance torque contribution in V when the current input is 30A. However, when the phase current magnitude increases from the rated load value of 30A to the overload value of 60A, the reluctance torque contributes less in proportion, thus the total torque difference between the BMM and V is increased. Because a higher saturation in the circuit reduces the difference between the d and q axis inductances, the peak torque angle is changed from -21° to -16° in the V and the shape of the peak is more rounded.

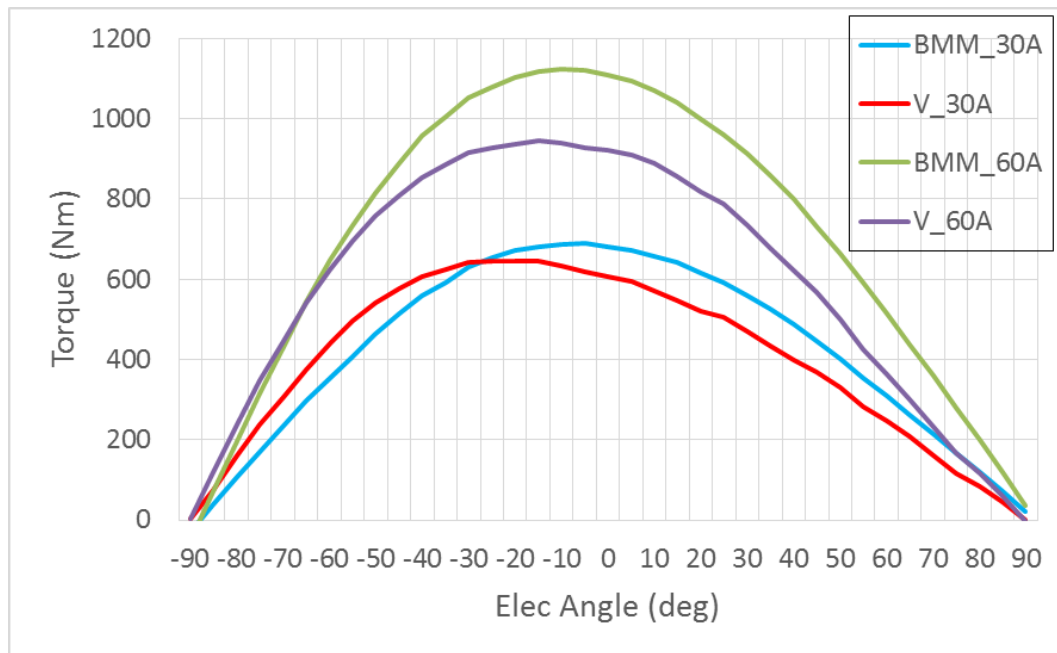


Figure 3-111 The torque vs current alignment angle in BMM and V

3.5.5. Torque against phase current

The gradient of the torque to current magnitude in the V-shaped motor starts dropping much quicker than it does in the BMM when the peak phase current increases above 25A, as can be seen from Figure 3-112. The red curve represents the alignment torque in the V-shaped motor and is the same as the one in the BMM until the $I_{ph} > 15A$. When the current angle is advanced, the torque from the V-shaped motor can keep up with the BMM up until 25A and is 4.5% less at a 30A rated condition. Due to a smaller air gap distance, the magnetic circuit saturates much earlier in the V-shaped motor.

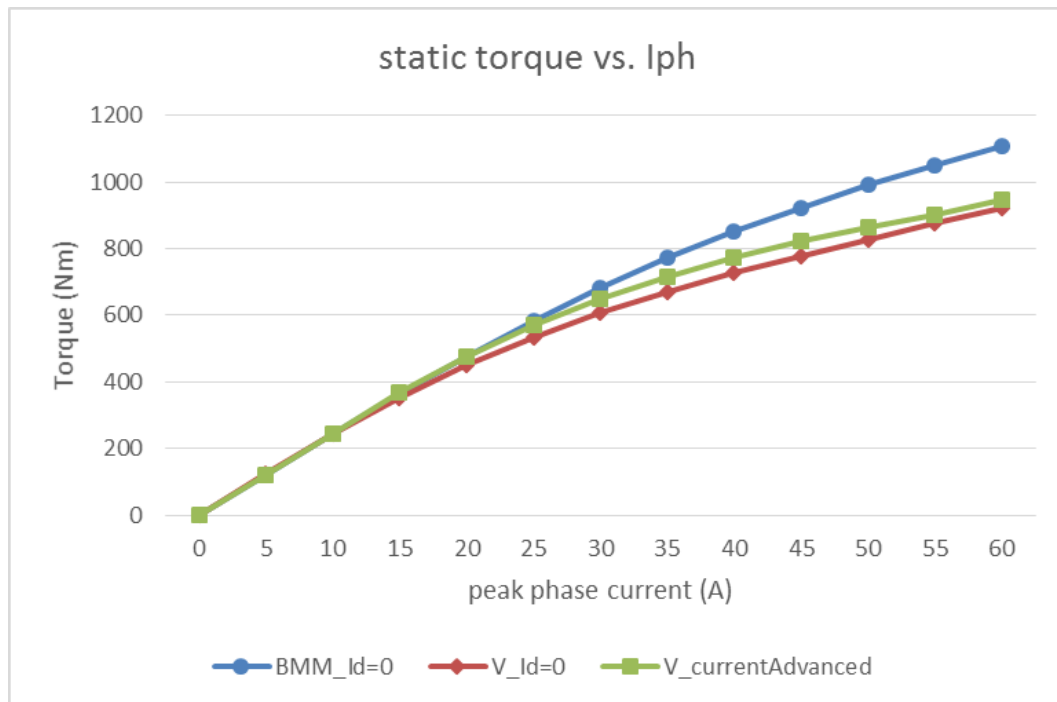


Figure 3-112 The torque vs current magnitude in BMM and V

3.5.6. Torque ripple

Due to additional reluctance torque the V shape magnet can produce a similar torque density using fewer rare earth materials. However, it is suggested that a slightly increased torque ripple could be a potential problem in terms of driving experience, especially when at a low speed and/or when accurate control of the vehicle is required, such as parking and starting the car.

In Figure 3-113, the torque ripple is recorded at a rated operating condition with the current alignment angle controlled to achieve the maximum torque. The peak to peak value of the torque ripple is 1.9% of the average torque in the BMM and 3.6% of the V.

A detailed analysis of the torque ripple will be given in chapter 10.

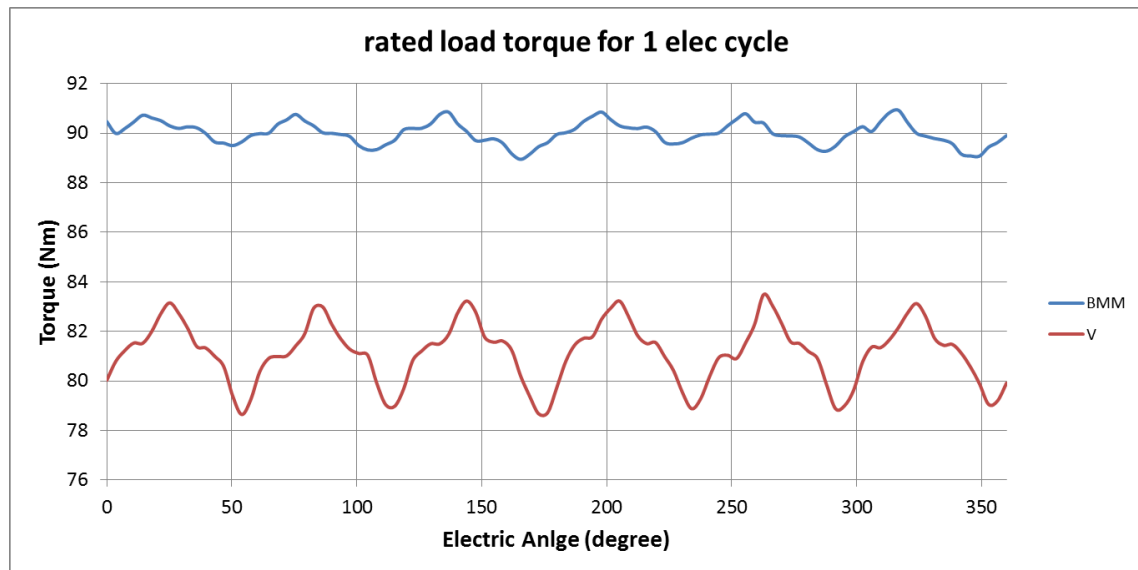


Figure 3-113 The torque ripple at maximum torque angle when $I_p=30A$

3.5.7. Inductance

Inductance, denoted as 'L', is the property of an electrical conductor by which a change in the current flowing through it induces an electromotive force in both the conductor itself and in any nearby conductors by mutual inductance. It is an important property of a motor which has the following uses:

- 1) To regulate the terminal voltage - the lower the phase inductance is, the closer the terminal voltage and back EMF are, as can be seen in Figure 3-121 ($X = j\omega L$).
- 2) To reflect the flux inducing capability - the higher the inductance is, the more flux can be induced by the current or the magnet depending on which axis the inductance refers to.
- 3) To indicate the fault tolerance capability – the higher the inductance, the lower the fault current that can be induced in the short circuit is. [118, 119]
- 4) To be used to control the machine, lower inductance faster current response.
- 5) To indicate the flux weakening capability – the higher the d axis inductance, the stronger the opposing flux.

In the electric motor, there are two fundamental equations that can be used to calculate the inductance value:

4. A time-varying magnetic field induces an electromotive force in nearby conductors

The back EMF of a motor is induced by the changing flux linkage of the rotating rotor and it is calculated as:

$$E = -\frac{d\psi}{dt} = -L \frac{di}{dt} \quad (3.52)$$

In which, E is the back EMF, ψ is the flux linkage.

5. A steady current creates a steady magnetic field

When the rotor is kept stalled and the flux is generated from the coil with a DC current, the inductance can be calculated as:

$$L = \frac{\psi_{dc}}{I_{dc}} \quad (3.53)$$

Based on these two equations, there are several methods developed to calculate inductance.

Inductance via an analytical method in simple geometry

From the simple geometry shown in Figure 3-114, the inductance can be calculated by its geometric parameters. The blue part of this magnetic circuit is an infinitely permeable, ideal material. The magnetic flux is flowing in a circle and across the air gap on the right side. The flux that links the coil can be calculated by eq. (3.54), and the inductance is obtained by eq. (3.55). Where MMF is the MagnetoMotive Force (A), N is the coil turns, A is the cross-section area of the air gap (m^2), l is the air gap distance (m).

$$\psi = N\phi = NBA = NA\mu_0 \frac{MMF}{l} = NA\mu_0 \frac{2NI}{l} \quad (3.54)$$

$$L = \frac{\psi}{I} = 2N^2\mu_0 \frac{A}{l} \quad (3.55)$$

The geometry and conditions are much more complicated in the actual machine, this simple example can serve as an introduction to a more complicated method – the lumped magnet circuit calculation [120]. FEA methods can also be used to determine the accurate value of inductance. Next, the inductance of the V-shaped motor and the BMM are calculated using 2D FEA methods neglecting the end-winding effect:

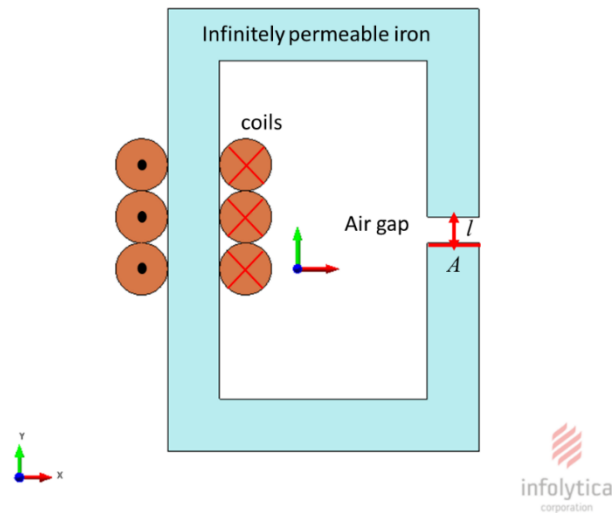


Figure 3-114 The simple magnetic circuit model

Inductance calculation via 2D FEA – DC current

The stator current is locked with the DC value – 30A for the reference phase and -15A in the other two phases – and the magnets are replaced with air. The phase flux linkage variation against the rotor position is shown in Figure 3-115. The d-axis phase inductance L_d is calculated when the flux linkage reaches its minimum value, meaning that the reluctance of the magnetic circuit is at its highest level [121]. The L_q is obtained when the flux linkage is at its highest point. The d and q inductances are listed in Table 3-10. The difference of the d and q inductances in the V-shaped motor is much more significant compared to the BMM.

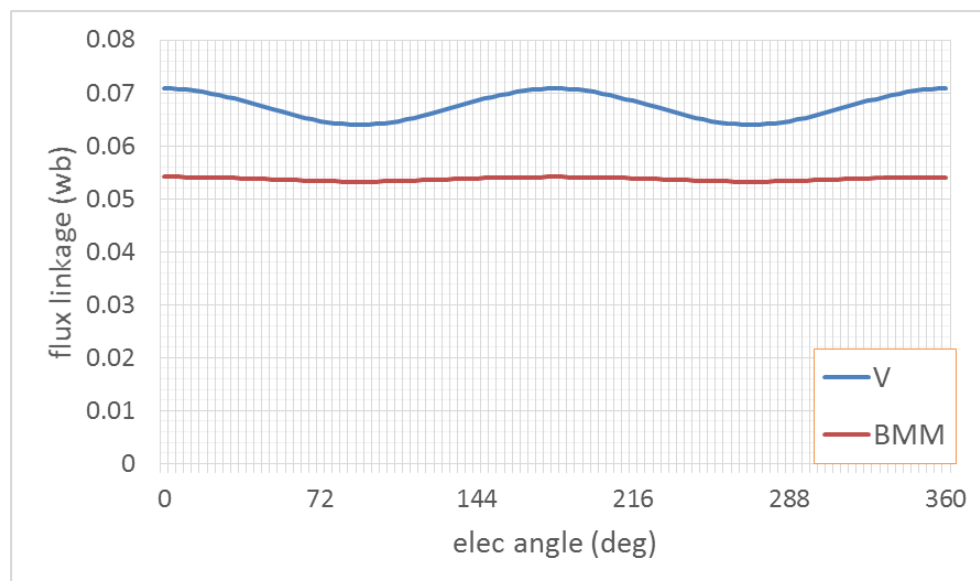


Figure 3-115 The flux linkage at $I_q=30A$ DC when the magnets are disabled

Table 3-10 The d and q -axis phase inductances

1	V	BMM	
ψ_{min}	0.06401	0.05323	Wb
L_d	0.00213	0.00177	H
ψ_{max}	0.07084	0.05411	Wb
L_q	0.00236	0.00180	H

The fault current tolerance capability can be indicated by per-unit inductance calculated in eq. (3.56). Here, the value of L_{sync} is the synchronous phase inductance which is the average value of L_d and L_q , φ_{mag} is the peak value of the phase flux linkage when the magnet is magnetised and there is no current in the stator coils.

$$L_{pu} = L_{sync} \frac{\hat{I}_{rated}}{\hat{\varphi}_{mag}} \quad (3.56)$$

Table 3-11 The per-unit inductance

2	V	BMM	
\hat{I}_{rated}	30.00000	30.00000	A
$\hat{\psi}_{mag}$	0.06512	0.06541	Wb
L_{sync}	0.00225	0.00179	H
L_{pu}	1.04	0.82	-

When the per-unit inductance is close to 1, the designed motor possesses a good fault current tolerance, meaning that the maximum fault current in the worst case – a short-circuited coil – is limited to the value close to the rated current.

Both the BMM and the V have a good fault current tolerance due to high inductance in the fractional-slot concentrated-winding configuration as explained in chapter 3. The per-unit inductance in the V-shaped motor is even higher due to a smaller equivalent air gap distance.

Mutual phase inductance, which could indicate the coupling influence of the faulty phase on other normal operating phases, is also tested with rated current in one phase and no current in the other two phases, the magnet is disabled and the rotor placed at the d axis. The results are recorded in Table 3-12. In both designs, the d axis mutual inductance is less than 10% of the total phase inductance. The flux plot shown in Figure 3-116 illustrates

that there is little flux sharing the tooth with other phases, which is one of the advantages of the concentrated winding configuration.

Table 3-12 The self and mutual inductances

3	V	BMM	
ψ self	0.06500	0.05012	Wb
ψ mutual	0.00591	0.00415	Wb
L self	0.00217	0.00167	H
L mutual	0.00020	0.00014	H

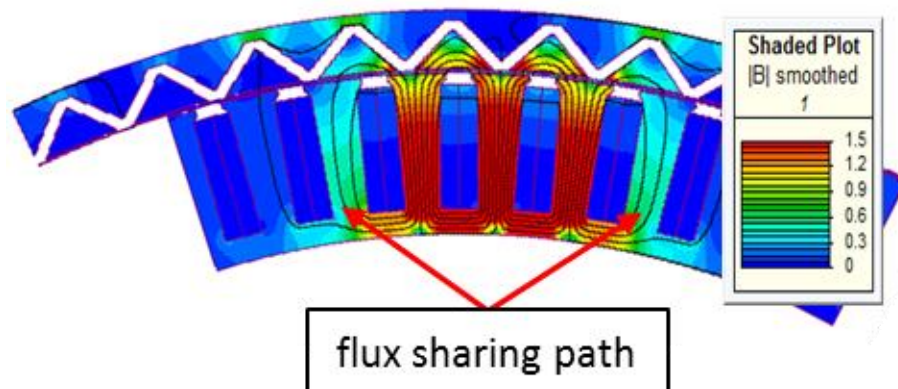


Figure 3-116 The flux sharing path between adjacent phases

Inductance calculation via 2D FEA – with a Frozen Permeability Technique

In the previous section, the d and q inductance for the rated condition were calculated from the magnetic circuit excited by the current alone (magnets disabled). However, this calculation is an approximation neglecting the non-linearity of the material.

In the rated operation condition, it is the total flux from both the magnet excited flux and the armature flux that determines the saturation level of the circuit. Whereas in the aforementioned FEA, the saturation level is only determined by the armature flux. By coupling the FEA with the frozen permeability technique (FPT), introduced in chapter 5, the issue can be solved.

To start with, the accuracy of the FPT is demonstrated on the BMM motor with the magnet magnetised. From Table 3-13, the phase current magnitude (I_{ph}) is fixed at 30A and the current alignment angle beta varies from -90° (–d axis) to 0° (q axis), shown in the 1st column. The I_q and I_d components are calculated and shown in the 2nd and 3rd columns.

Firstly, the FE model is solved statically at a certain current alignment angle β and the flux linkage is recorded in the 4th column. Then the permeability of the model at this angle is frozen and the rotor is rotated from the beta angle to the $-d$ or q axis. The I_d or I_q current input is set to the value in the 2nd or 3rd column, and the model is solved statically. Finally, the flux linkages on the d and q axis are recorded in the 5th and 6th columns.

Table 3-13 The flux linkage comparison between actual and the DQ converted ones

beta (deg)	lph (A)	30	ψ_{total} (Wb)			
-	I_d	I_q	actual	d	q	calculated
-90	30.0	0.0	-0.01149	-0.01149	0.00000	-0.01149
-80	29.5	5.2	-0.01012	-0.01240	0.01069	-0.01036
-70	28.2	10.3	-0.00622	-0.01511	0.02100	-0.00701
-60	26.0	15.0	-0.00022	-0.01953	0.03042	-0.00171
-50	23.0	19.3	0.00748	-0.02546	0.03880	0.00544
-40	19.3	23.0	0.01640	-0.03262	0.04571	0.01404
-30	15.0	26.0	0.02607	-0.04075	0.05099	0.02378
-20	10.3	28.2	0.03559	-0.04919	0.05385	0.03378
-10	5.2	29.5	0.04428	-0.05724	0.05404	0.04328
0	0.0	30.0	0.05202	-0.06447	0.05202	0.05202

The d and q components of the flux linkage are then converted back to the total flux using eq. (3.57), recorded in the final column and are compared with the actual result in the 4th column. The two curves representing the actual and FPT results are plotted against the beta angle in Figure 3-117. It is clear that using FPT, the total flux linkage at any given beta angle can be dissected to the flux-linkage components on the d and q axes.

$$\psi_{actual} = -\psi_d \cdot \sin\beta + \psi_q \cdot \cos\beta \quad (3.57)$$

The verified FPT is now applied to obtain the armature flux component of the total flux on the d and q axes. In order to obtain the component, the magnets need to be disabled after obtaining the permeability at a certain beta angle. The others then need to be done the same as described above.

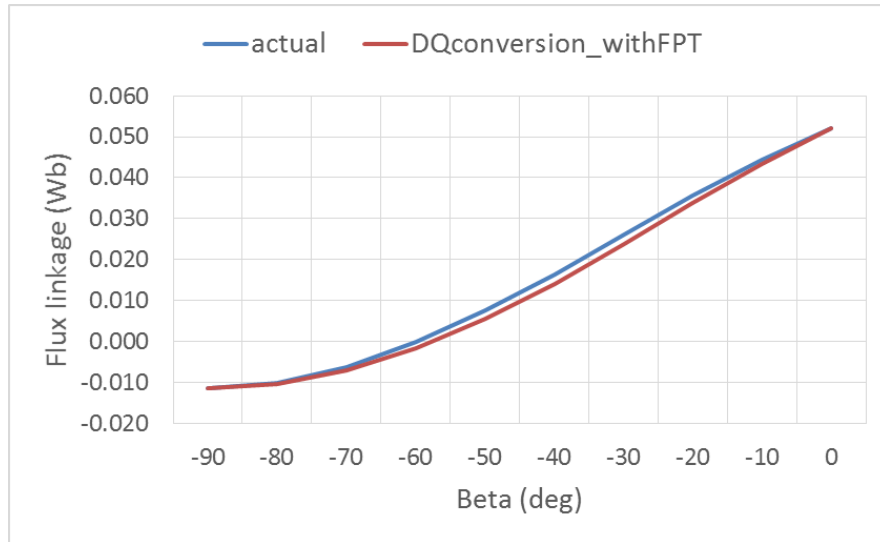


Figure 3-117 The flux linkage comparison between the actual and the converted one

In Figure 3-118, the d/q inductances in the V-shaped motor are compared with the result without using the FPT. There is clear disagreement between these two methods. To validate the FPT method, these inductance values are then fed into eq. (3.14) in chapter 5 to calculate the torque and are compared with the FE result in the torque against beta angle plot. The results in Figure 3-119 show that the technique using FPT has a much better approximation compared to the conventional technique, indicating a much better accuracy of the inductance value.

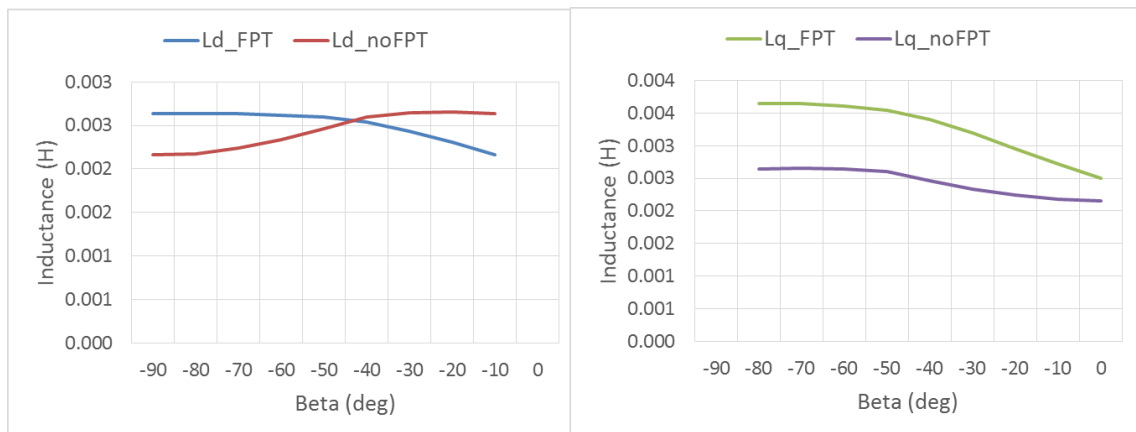


Figure 3-118 The V-shaped motor DQ inductances comparison

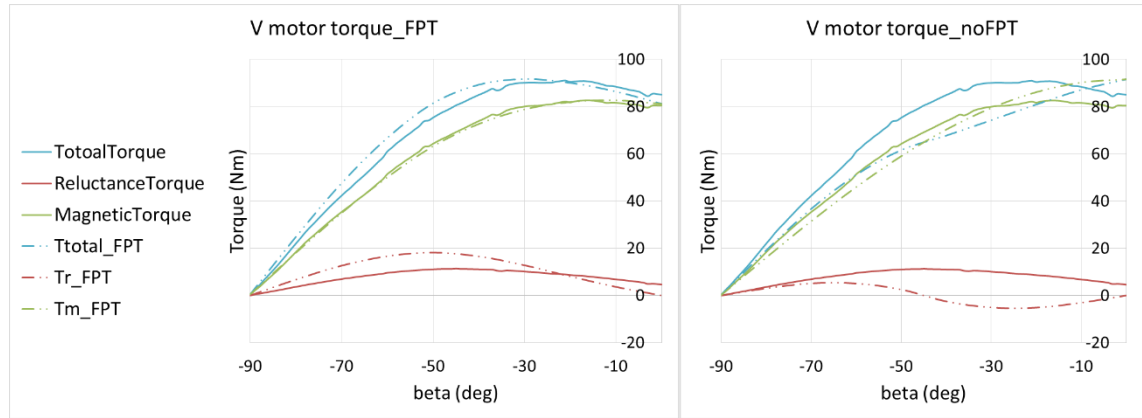


Figure 3-119 The V-shaped motor torque components comparison

Other inductance calculation methods in 2D FEA

There are a few other methods that can be implemented in the FEA, they are briefly described here.

DQ current method

The current alignment angle is locked on the d/q axis, so the inductance of the d/q can be calculated using incremental values of the flux linkage and current in eq. (3.58), assuming that the inductance is linear in the small increment.

$$L = \frac{(\psi_0 + \Delta\psi) - \psi_0}{(I_0 + \Delta I) - I_0} \quad (3.58)$$

The value of ψ , I can be obtained from the FEA, and ψ against I of the V-shaped motor as shown in Figure 3-120.

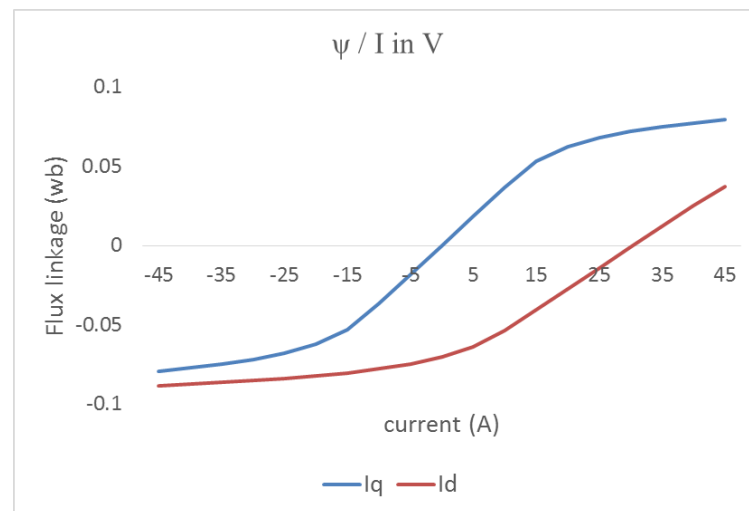


Figure 3-120 The flux linkage against current

Energy method

If there is a single energised coil in a model, the total of the stored magnetic energy W can be used to obtain its inductance (or the equivalent inductance of several coils) when knowing the total current entering the device [122]. To start with, the general expression relating the total magnetic energy W to the total magnetic power P is:

$$W = \int P dt = \int (L \frac{dI}{dt} * I) dt = \frac{1}{2} \int L d(I^2) \quad (3.59)$$

$$L = 2 \frac{dw}{d(I^2)} \quad (3.60)$$

$$L = 2 \frac{W_2 - W_1}{I_2^2 - I_1^2} \quad (3.61)$$

Impedance method

Knowing the information on the current and the resultant voltage, the inductance can also be calculated using the impedance equation:

$$V = V_0 e^{j\omega t} \quad (3.62)$$

$$I = I_0 e^{j(\omega t + \vartheta)} \quad (3.63)$$

$$Z = j\omega L = \frac{V}{I} \quad (3.64)$$

So:

$$L = \frac{\text{Im}\left\{\frac{V}{I}\right\}}{\omega} = \frac{-V_0 \sin \vartheta}{\omega I_0} \quad (3.65)$$

In eq. (3.65), I_0 is the amplitude of the current's fundamental and ϑ is the phase shift between the current and voltage fundamentals. Note that for a positive inductance, $\vartheta < 0$, since the current lags the voltage.

3.5.8. Torque-speed characteristic curve

The torque-speed characteristic curve is the primary performance indicator for an electric traction motor and it can be calculated analytically or numerically. Both ways are discussed here.

The analytical method

This method is derived from the phasor diagram shown here:

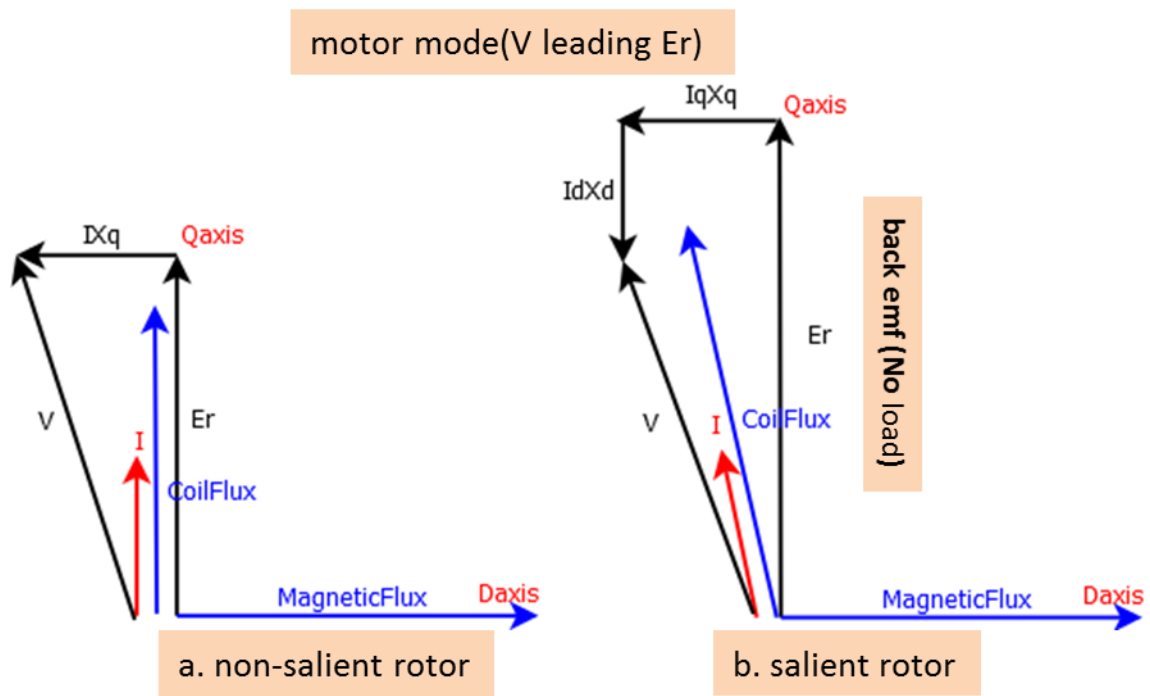


Figure 3-121 The phasor diagram for non-salient and salient rotor in motor mode

The terminal voltage limit is fixed at 320V DC for the BMM in-wheel motor. When increasing the speed, the terminal voltage quickly reaches its limit entering the constant power region. In this region, the current alignment angle is advanced to cancel the flux excited by the magnet and keep the terminal voltage at its limit. The equations to determine the current alignment angle β in the constant power region are derived here:

$$V^2 = (E + I_d X_d)^2 + (I_q X_q)^2 \quad (3.66)$$

$$\begin{cases} E = \psi \omega_e \\ X = 2\pi f_e L \\ I_q = I \cos \beta \quad I_d = I \sin \beta \end{cases} \quad (3.67)$$

$$\left((IX_d)^2 - (IX_q)^2 \right) (\sin \beta)^2 + 2EI X_d \sin \beta + E^2 - V^2 + (IX_q)^2 = 0 \quad (3.68)$$

The equation (3.68) is a quadratic equation in $\sin \beta$, its root $\sin \beta$ can be calculated by the classic equation: $\frac{-b \pm \sqrt{b^2 - 4ac}}{2a}$. In this equation, the rotating speed, the current value is known, the reactance X_d and X_q are related to the inductance and the back EMF is related to the flux linkage. Both inductance and flux linkage can be obtained from FEA. Hence, the angle β can be calculated for each speed point.

The I_q value can be obtained after knowing β and the torque output is determined by eq. (3.69)

$$T = \frac{3EI_q \cdot k}{2\omega_m} k = 0.92 \quad (3.69)$$

Where the values used in eq. (3.66)-(3.69) are all peak values and the subscript ‘m’ means mechanical and ‘e’ means electrical. Factor k is the factor that takes the motor losses into account when relating electric input power to mechanical output power which is taken from the efficiency obtained from FE shown in section 8.9.

The analytically calculated curve of the BMM motor is compared with the FE result in Figure 3-122. The accurate result can only be obtained using the analytical method with an accurate inductance input. In order to obtain a more accurate result, FE is necessary.

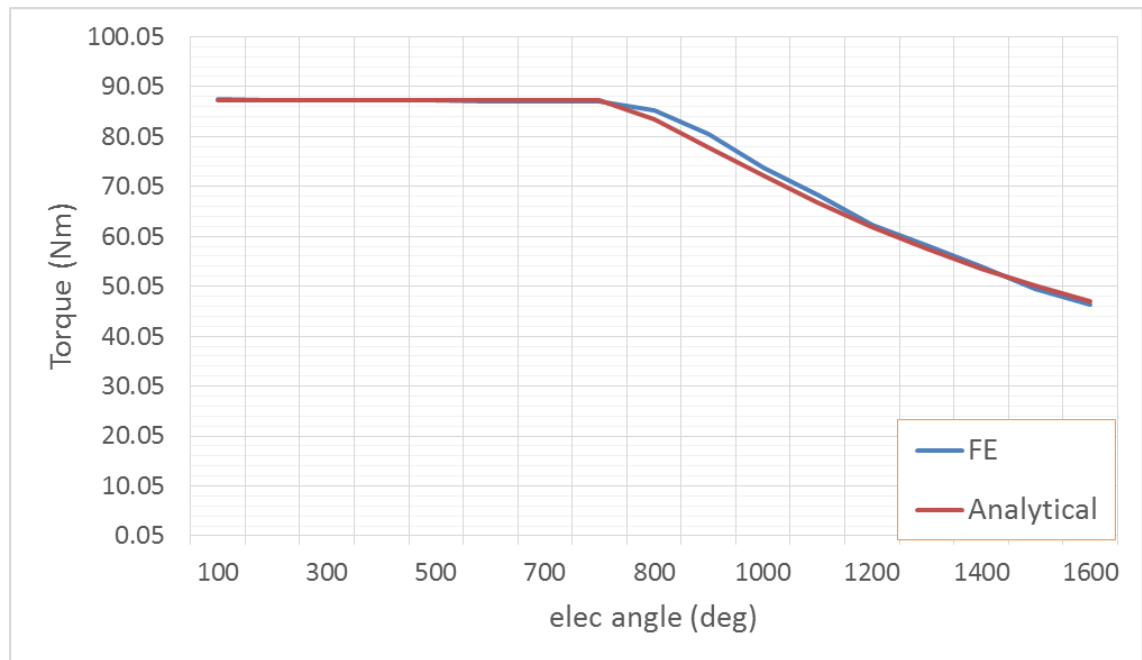


Figure 3-122 The torque-speed curve of the BMM comparison

The finite element method

The inductance of the BMM stays nearly constant with various values of the current alignment angle β , whereas the inductance in the V-shaped motor varies noticeably with the angle as can be seen from Figure 3-123. In order to accurately calculate the torque and the losses at each speed point, finite element analysis is applied.

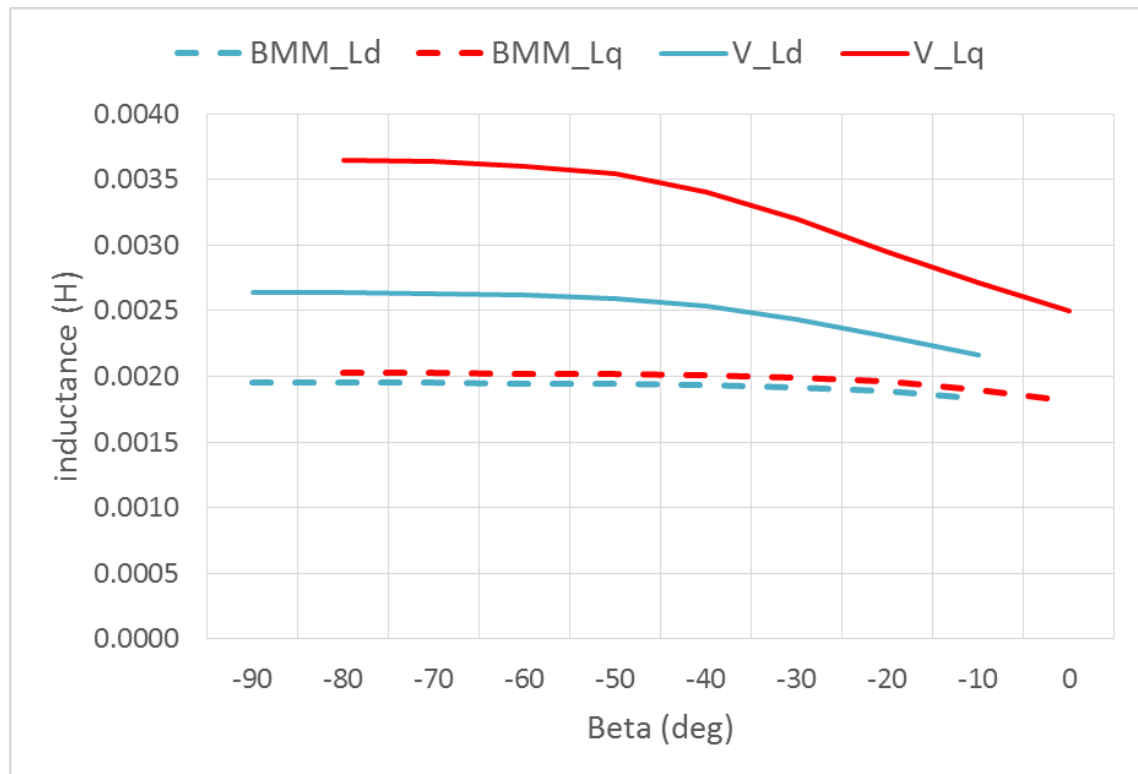


Figure 3-123 The inductance variation with $I_p=30A$

For each speed sampling point, the program to control the FE software, which is written in visual basics, searches for the right current input value to give maximum torque (both magnitude and alignment angle) without exceeding its constraints (rated output power or the terminal voltage limit). It is firstly solved in 2D transient. If the output does not satisfy the constraints, the current values are adjusted and the program iterates.

Each simulation takes a few minutes to solve. For each speed sampling point beyond the base speed, the current value is typically varied 10 times before a satisfactory output is reached. Depending on the required control accuracy, the tolerance of the current magnitude and alignment angle could be from $\pm 1A$ and $\pm 1^\circ$ to $\pm 10A$ and $\pm 10^\circ$. The FE method takes 3-12 hours to generate a torque against speed curve trading between the accuracy and computational time. There are two main control methods programed:

The constant output power control

In this method, the constraints are the output power and the voltage limit. The output power above the corner speed is fixed at the rated value obtained at the corner speed with the rated torque. The torque-speed curve is shown in blue in Figure 3-124.

Optimum torque control

In this control method, the constraint is solely the terminal voltage limit. A higher output power can be achieved compared to the first method. Furthermore, because there is only one constraint to be checked, the computational time is shorter in this method. The results are compared in Figure 3-124.

The constant output power control is selected for the coil-turn tuning in the previous section due to fewer iteration compared to the optimum torque control.

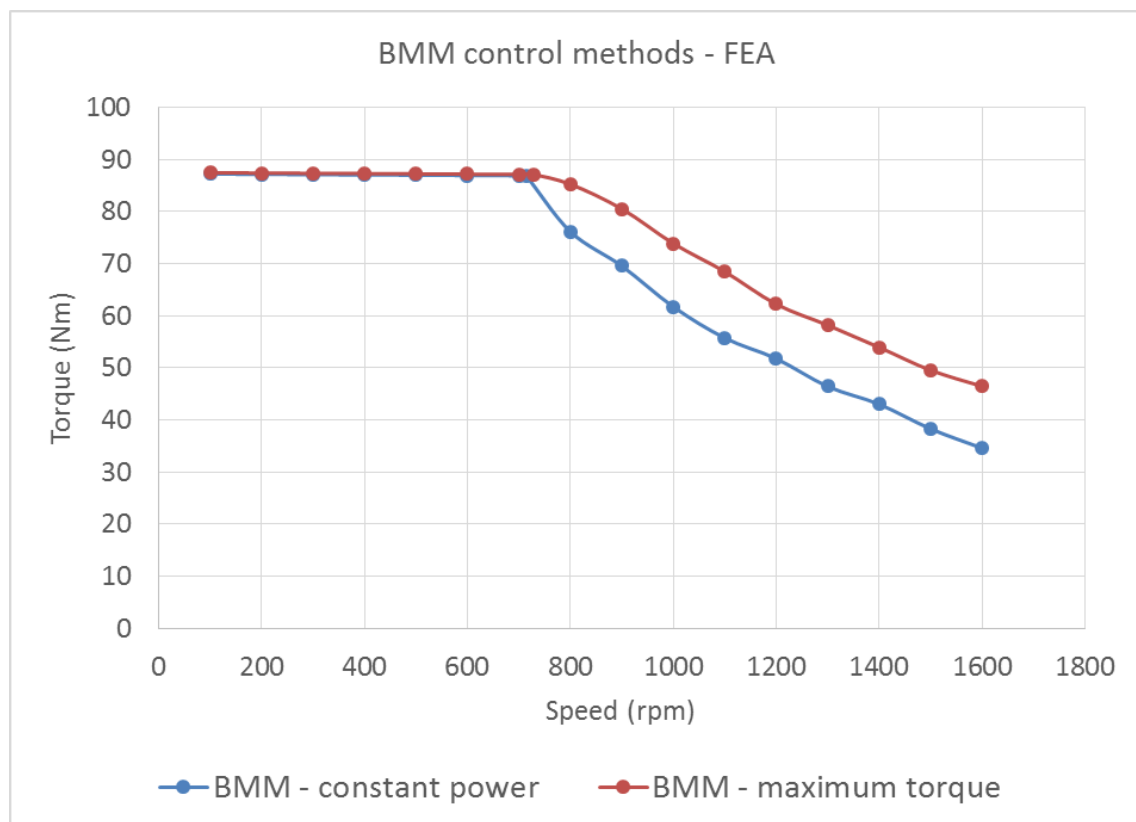


Figure 3-124 Two control methods in FEA

3.5.9. Efficiency map

The efficiency of the motor directly decides the input power for a required output power. For the customer, the more efficient the motor, the more hours of driving per charge. The losses of the motor are manifested as dissipated heat and should be limited due to the tight space within a wheel. Any additional heat is a burden to the cooling system and can potentially jeopardise the magnet's condition (demagnetisation occurs at a lower current at a higher temperature). Hence, the efficiency of the motor at various operation conditions

needs to be closely analysed. The 2D transient FEA is chosen to generate the efficiency map of the region under the torque-speed envelope.

The efficiency map tool consists of two parts: 1. calculating the efficiency at various points via FEA; 2. Plotting the efficiency in the *Matlab* package.

The program is controlled using the optimum torque method. The whole torque-speed envelope is sliced into pieces, by defining the current input and voltage constraint in equal steps as is illustrated in Figure 3-125. After all the required efficiency points are simulated, the data is imported into *Matlab* to generate the map.

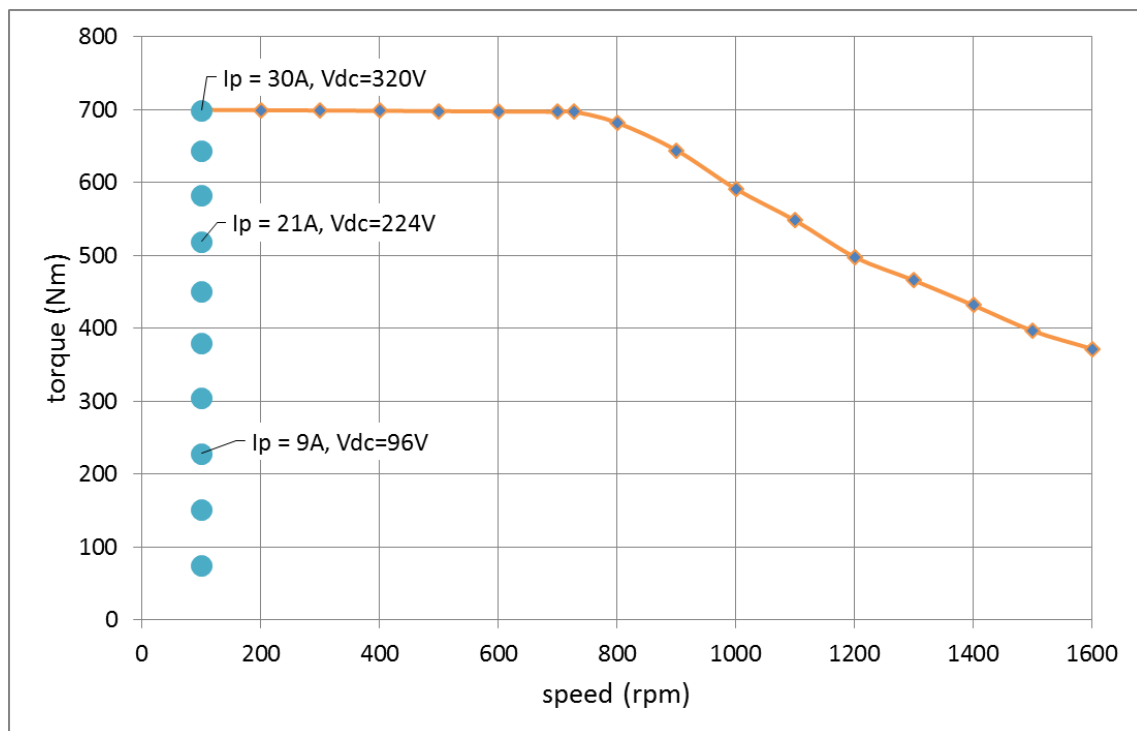


Figure 3-125 The starting point of each slice of the torque-speed envelope

The BMM V-shaped motor is compared with the BMM. The efficiency calculated here does not include the loss of the mechanical parts, the loss from the inverter circuit and the additional AC loss from the coils (discussed in the following section). Two efficiency maps are illustrated in Figure 3-126 and Figure 3-127. The experimental data from the constructed BMM is also shown in Figure 3-128.

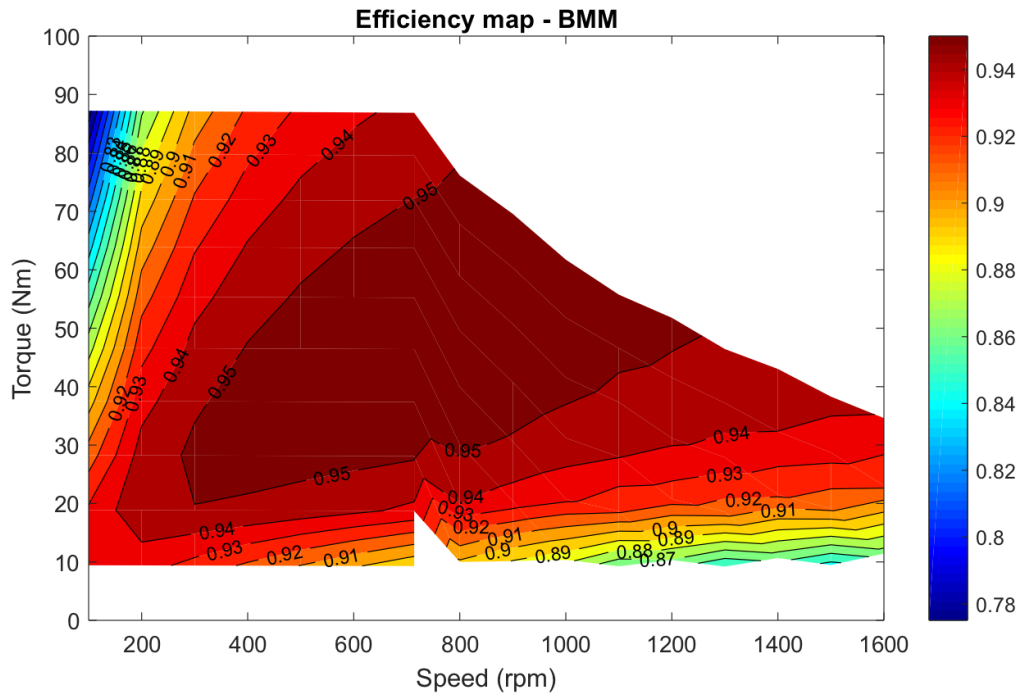


Figure 3-126 The BMM efficiency map

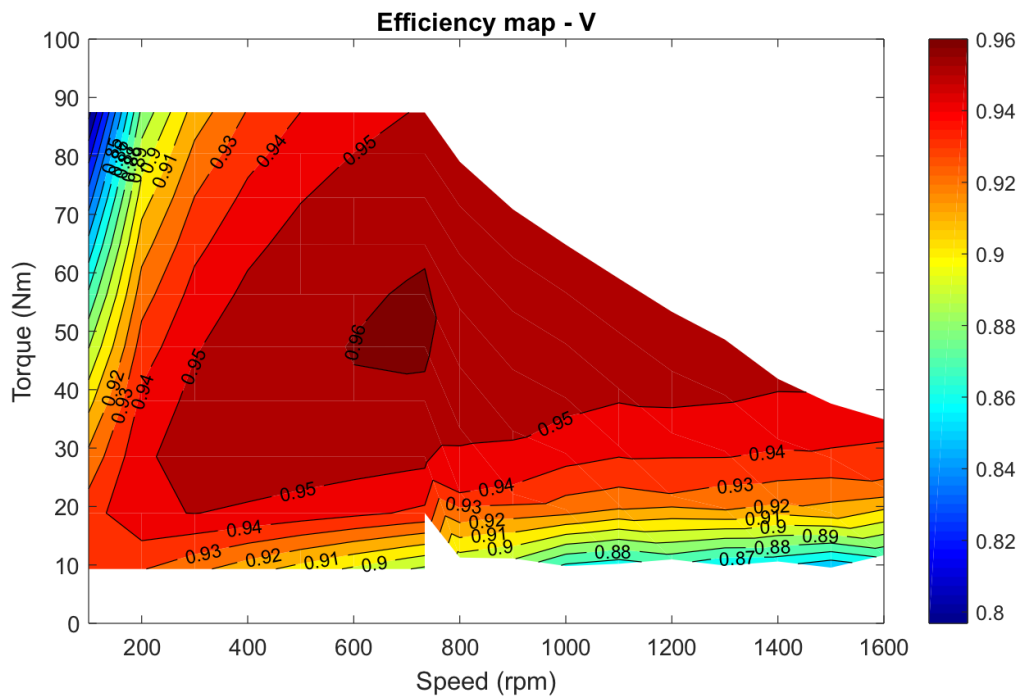


Figure 3-127 The V efficiency map

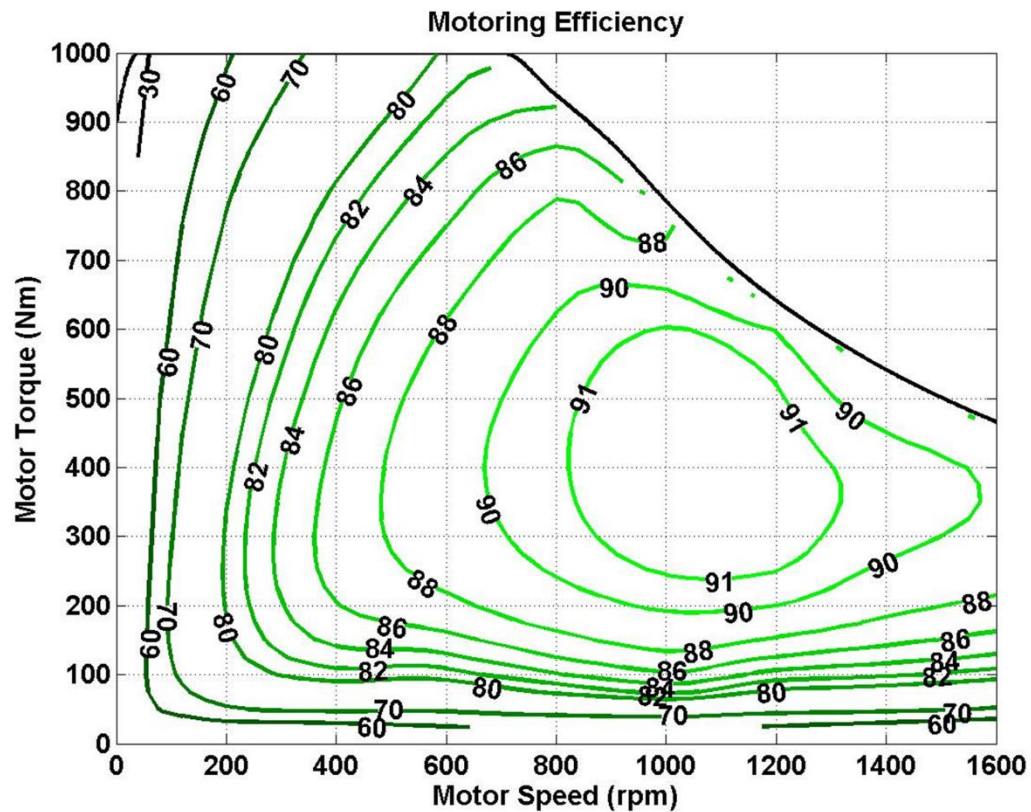


Figure 3-128 The BMM efficiency map provided by Protean

Comments:

- 1) The efficiency of the V is at least 1% higher at most speed ranges, this is due to less copper loss (the number of coil turns is 30 in V compared to 32 in the BMM), stator core loss and magnet loss (this will be discussed in chapter 9).
- 2) The overall efficiency of both in-wheel motors at the frequent operating range 700-1200rpm, 300-700Nm is above 94% in simulation and around 90% in practice, which is as expected for a well-designed permanent magnet machine.
- 3) The efficiency is low at high-torque low-speed in both cases, due to high copper loss.
- 4) The efficiency is high in the constant power region due to reduced copper loss.
- 5) Copper loss is the dominant loss contributor in this torque-speed envelope.

3.5.10. Additional losses

As can be seen from the previous section, the efficiency of the 2D FE model is lower than the experimental data recorded. Because a shorter computational time was aimed for, some motor losses were neglected in the applied FE simulation. They are analysed here separately to show their effect on motor performance.

End-winding effect

There are two ways to include the end-winding effect in the machine loss prediction:

1. The full 3D FE with coils bent and connected at both ends and its simulation;
2. The 2D FE coupled with external impedance accounting for the end-winding effect.

The computation time in the 3D simulation is exponentially raised compared to that in the 2D simulation. Furthermore, the single tooth winding configuration in the in-wheel motors realised a very short end-winding length and hence a relatively low end-winding effect. Therefore, the 2D method is discussed here.

Copper loss is the dominant loss in this motor and is only related to the resistance of the end-winding. Hence only the resistance part of the impedance is calculated. The contribution of the additional DC copper loss is then added to the efficiency map.

The stator with coils is shown in Figure 3-129. In the previous FE model (used to calculate the losses for the efficiency map), the average slot coil length is same as the active length (58.8mm in the BMM motor) and the fill factor is set to 100%. A more accurate model is demonstrated in Figure 3-130 for the analytical estimation. The corrected average coil length, l_{slot}^c , is shown as a black line in Figure 3-130. It is obtained in eq. (3.70) by adding the end-winding length l_{end} .

The end-winding length can be separated into two parts: the circumferential length l_θ and the axial length l_z . The axial length is then calculated from the average coil diameter, 'd', and the axial gap, 'g', between the slot and the coil. In eq. (3.73), the coefficient '0.8' is a correction factor between the end winding length of the actual arc shape and the assumed rectangular shape. In eq.(3.74), the circumferential length is calculated by the average radius $\frac{r_{tn}+r_{tf}}{2}$ and span $\frac{\theta_{tn}+\theta_{tf}}{2}$ from the tooth neck and tooth foot.

The phase length is then calculated by the number of slots per phase $\frac{N_s}{8*3}$, the number of coils per slot $2N_c$ and the additional span from the single linking turn shown in Figure 3-131.

All the calculations (eq. (3.70)-(3.75)) and results are recorded in Table 3-14.

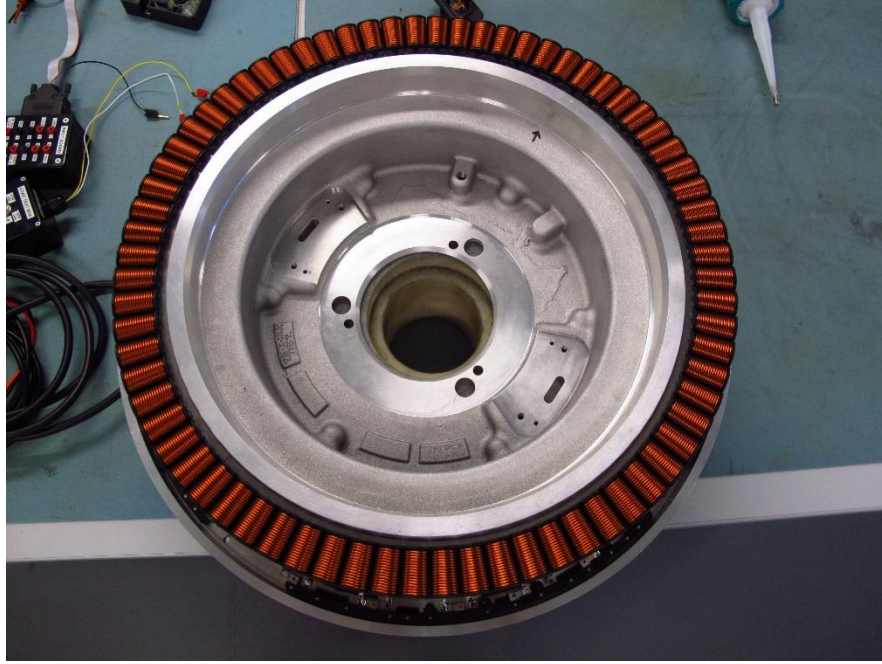


Figure 3-129 The stator of the BMM

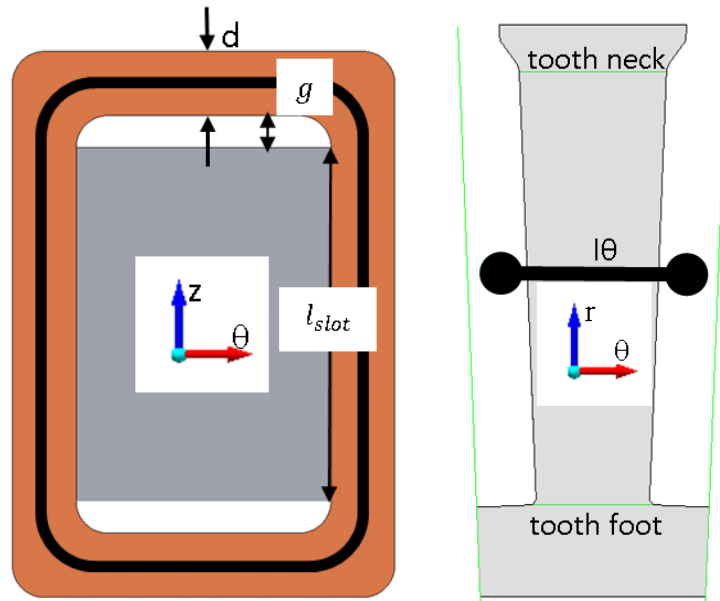


Figure 3-130 The analytical model of the single tooth winding - grey part is the tooth, orange part is the copper conductor.

$$l_{slot}^c = l_{slot} + l_{end} \quad (3.70)$$

$$l_{end} = (l_z + l_{\theta}) \quad (3.71)$$

$$l_z = 0.8\left(\frac{d}{2} + g\right) \quad (3.72)$$

$$l_{\theta} = \left(\frac{\theta_{tn} + \theta_{tf}}{2} + \frac{\frac{2\pi}{N_s} - \frac{\theta_{tn} + \theta_{tf}}{2}}{2} \right) \cdot \frac{r_{tn} + r_{tf}}{2} \quad (3.73)$$

$$l_{ph} = \frac{N_s}{8 * 3} * 2N_c * l_{slot}^c + \frac{2\pi r_{tf}}{8 * 3} \quad (3.74)$$

$$P = I^2 R = \frac{I^2 \rho l_{ph}}{A_{cond}} \quad (3.75)$$



Figure 3-131 The coil drawing for a phase

There are five groups of calculations presented in Table 314. The progression is from the left to the right and then from the first row to the second. Group 1 calculates the diameter of a single conductor. The total area of half slot copper is obtained by space integration from the FE model and then corrected by the fill factor. In group 2, the end-winding length is calculated from the equations derived above. Finally, in group 3 the corrected resistance is calculated and the total loss per phase is obtained from group 4. Its value is then compared to the FE result in group 5. The ratio of the corrected DC copper loss to the one from the simplified FE model is 2.65. The difference is due to the fill factor correction (from 100% to 47%) and the additional end-winding path (24% increase from the active slot length 58.8mm).

To put this corrected copper loss (265% to the one used in the efficiency map), there is a circa 3% additional total loss in the 50Nm 700rpm area bringing the efficiency down from 94.8% to 91.8% in the BMM.

Table 3-14 Calculations for the DC copper loss including end-winding

calculating conductor diameter	m	-	-	kg	kg/m3	2. End-winding length		
	stack leng	fill factor	coil turns	half slot mass	mass dens	d	3.4	mm
	0.0588	47%	32	4.27E-02	8940	tooth neck	2.75	deg
1	m3	m2	m2	m2	m		178.5	mm
	vol	area	active area	cond area	cond dia	tooth foot	2.6	deg
	4.77E-06	8.12E-05	3.82E-05	1.19E-06	1.23E-03		155.7	mm
3	$R = \rho \cdot l / A$					(tn + tf) / 2	167.1	mm
resistance per turn per side	length	turn area	resistivity	resistance			2.68	deg
	m	m2	Ωm	Ω		l0	3.84	deg
	0.07295186	1.19E-06	1.87E-08	1.15E-03			11.2	mm
4	total loss per phase					lz	3.7	mm
coil turns	Rcoil	R_linking coil	coil side	Rph		l_end	14.15	mm
32	3.67E-02	6.41E-04	6	2.21E-01				
dc copper loss	current rms	$I^2 \cdot R$						
	21.21	9.93E+01						
5	FE results fill factor 100%							
	per cond	R_cond	lph rms	loss cond	loss/slot	phase loss	loss ratio	
m2	Ωm	Ω	A	W	W	W	-	
8.12E-05	1.87E-08	2.54E-06	21.21	1.95E-01	6.25E+00	3.75E+01	2.65	

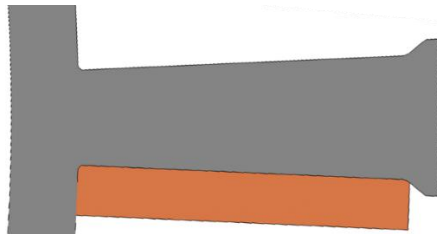


Figure 3-132 The FE model of a half slot copper

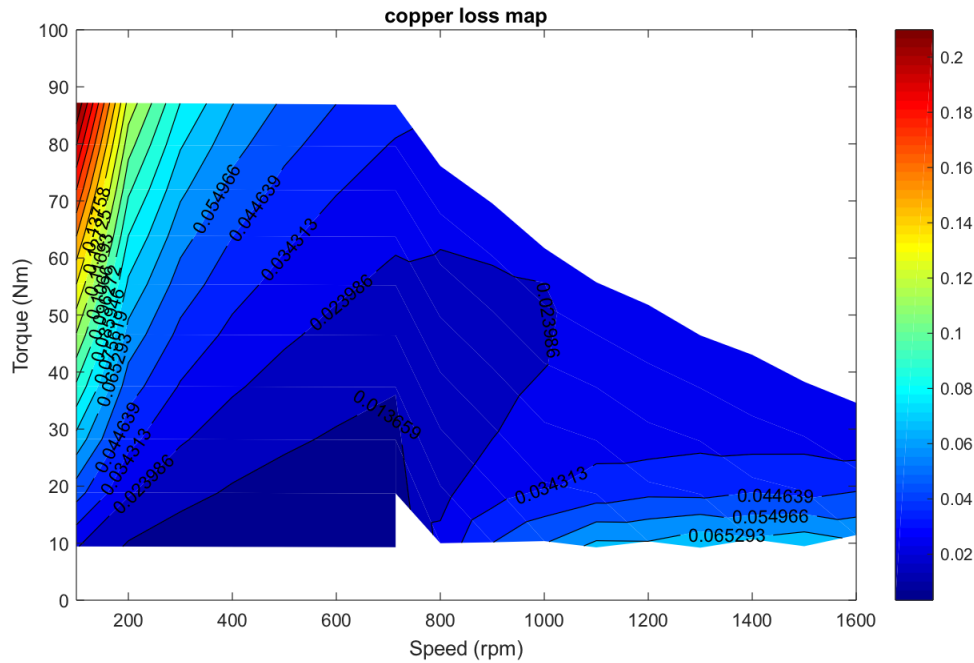


Figure 3-133 The per-unit copper loss in one sub-motor of the BMM

AC loss in the copper

Losses in the copper due to the skin, proximity and slot leakage effects in the alternating current environment can also seriously impact the performance of the machine.

a) Skin effect

Skin effect is the tendency of an alternating electric current to become distributed within a conductor so that the current density is largest near the surface of the conductor, and decreases with greater depth in the conductor. The current flows mainly at the “skin” of the conductor (Figure 3-134), between the outer surface and a level called the skin depth. It increases the resistance of the conductor.

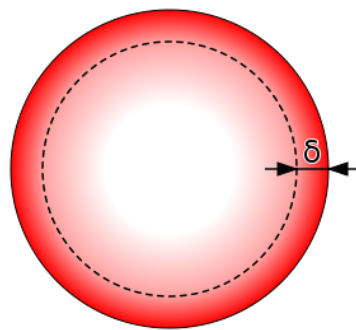


Figure 3-134 The skin depth in a circular conductor

The formula to calculate the skin depth is:

$$\delta = 1/\sqrt{\pi f u \sigma} \quad (3.76)$$

The maximum mechanical speed of the BMM in-wheel motor is 1600rpm. So the electric frequency (32pole pairs) is 853.3Hz. With a copper permeability u of 1.25663e-6 H/m and a conductivity σ of 1/(1.8741e-8) S/m, the minimum conductor skin depth is 2.35mm. The wire diameter is 1.35mm. Therefore, the fundamental AC current frequency alone cannot cause the skin effect.

b) Proximity effect

In a conductor carrying an alternating current, if currents are flowing through one or more of the other nearby conductors, such as within a closely wound coil of wire, the distribution of current within the first conductor will be constrained to smaller regions. The resulting current crowding is termed as the proximity effect.

A changing magnetic field will influence the distribution of an electric current flowing in an electrical conductor, by electromagnetic induction. When an alternating current flows through an isolated conductor, it creates an associated alternating magnetic field around it. The alternating magnetic field induces eddy currents in adjacent conductors, altering the overall distribution of current flowing through them. The result is that the current is concentrated in the areas of the conductor furthest away from the nearby conductors carrying the current in the same direction.

c) The slot-flux leakage effect

When the main magnetic circuit is saturated, the flux in the slot can flow out of the main magnetic path and pass through the conductors via routes illustrated in Figure 3-135. The bigger the red square area enclosed by the red dotted line, the larger the value of the MMF will be and the stronger the magnetic field H is $H=MMF/l$, thus the easier it will be for the flux to leak through the red dotted line and the higher the flux will be.

An FE current density plot of this phenomenon is generated in Figure 3-136. The current density is clearly higher when located closer to the air gap because of a higher, uneven AC resistance created by the higher slot flux leakage and a higher changing magnetic field

near the air gap. Part of the rotor flux from the magnet travels across the air gap and penetrates the conductor close to the air gap as is shown in Figure 3-136.

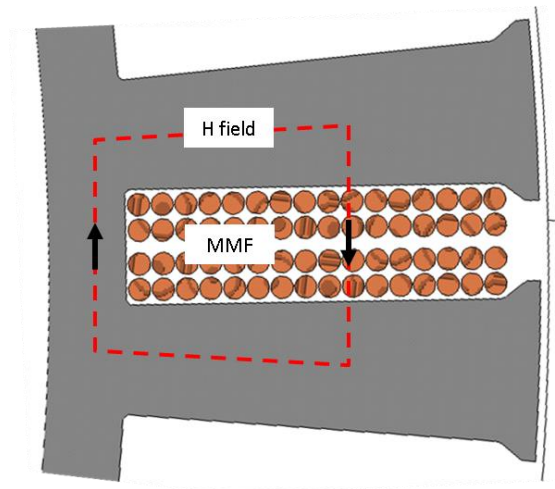


Figure 3-135 The H field loop of the slot flux leakage

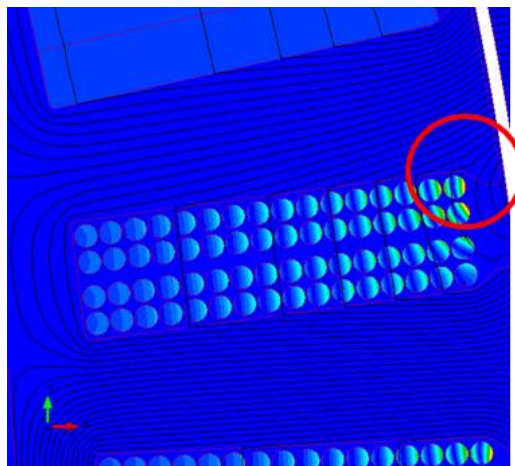


Figure 3-136 The current density plot of an FE model

a) FE result of AC loss in copper

These three effects are combined to generate AC loss of the conductor in the slot. The analytical model of a circular conductor in a uniform magnet field is discussed in [123]. However, due to the geometric complexity, the 2D FE with a separated conductor drawing of the two types of winding (inner-phase winding and inter-phase winding) is generated in Figure 3-137.

The significance of AC loss is assessed at 4 points: 1600rpm top speed with 30Amps rated current and 15Amps; 800rpm near corner speed with 30Amps rated current and 15Amps. The result is shown as bar charts in Figure 3-138.

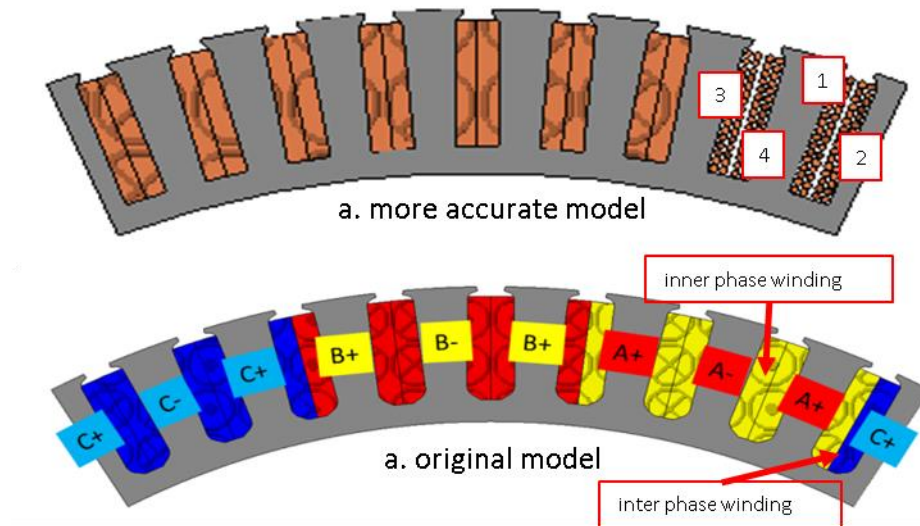


Figure 3-137 The more accurate FE model

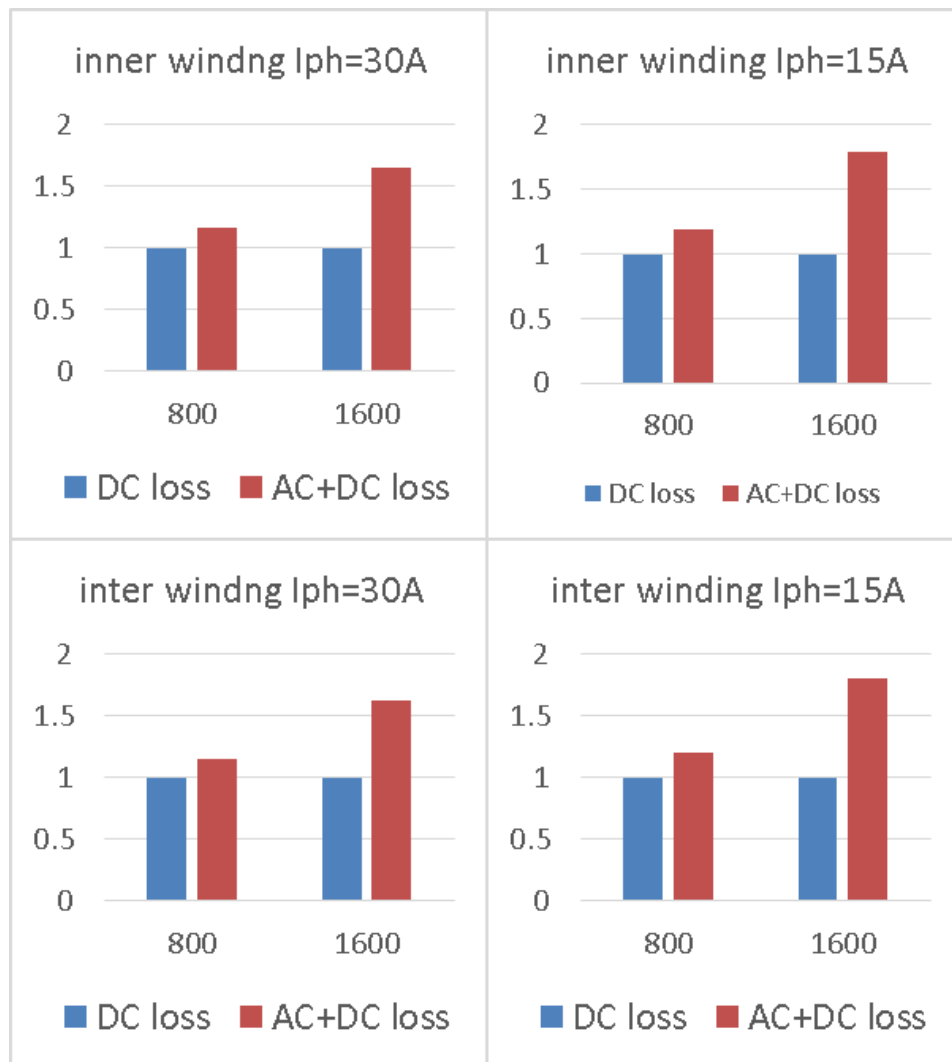


Figure 3-138 The AC loss contribution in the total copper loss

There are a few valuable observations:

- 1) The AC loss increases with the current frequency at a relation of:

$$P_{AC} \propto f^2 \quad (3.77)$$

- 2) The AC loss increases with the current magnitude in a similar relation of:

$$P_{AC} \propto I^2 \quad (3.78)$$

- 3) The AC loss can increase the total copper loss to more than 150% of the value used in the efficiency map at the top speed 1600rpm.

To put this additional AC loss into the efficiency map:

- 1) At high speed, from the copper loss map in Figure 3-133, the DC loss consumes less than 2% of the input power. So the AC loss is equal to less than 1% of the input power.
- 2) At low speed, the DC copper loss is the main loss and it can take 21% of the input power. The AC loss though, due to the reduced frequency, equals 1-2% of the input power.

To conclude, when taking this additional 1% AC loss into account, the BMM efficiency in the 50Nm 700rpm area drops from 91.8% to 90.8% which is close to the experimental data.

3.5.11.the magnet temperature

The magnet loss in V-shaped motor is less than 50% of the BMM, as explained previously. However, because >95% of the loss is from the stator winding and core, there is merely a 1.34°C magnet temperature reduction in the V-shaped motor. The thermal model is made in *ThermNet* and presented here:

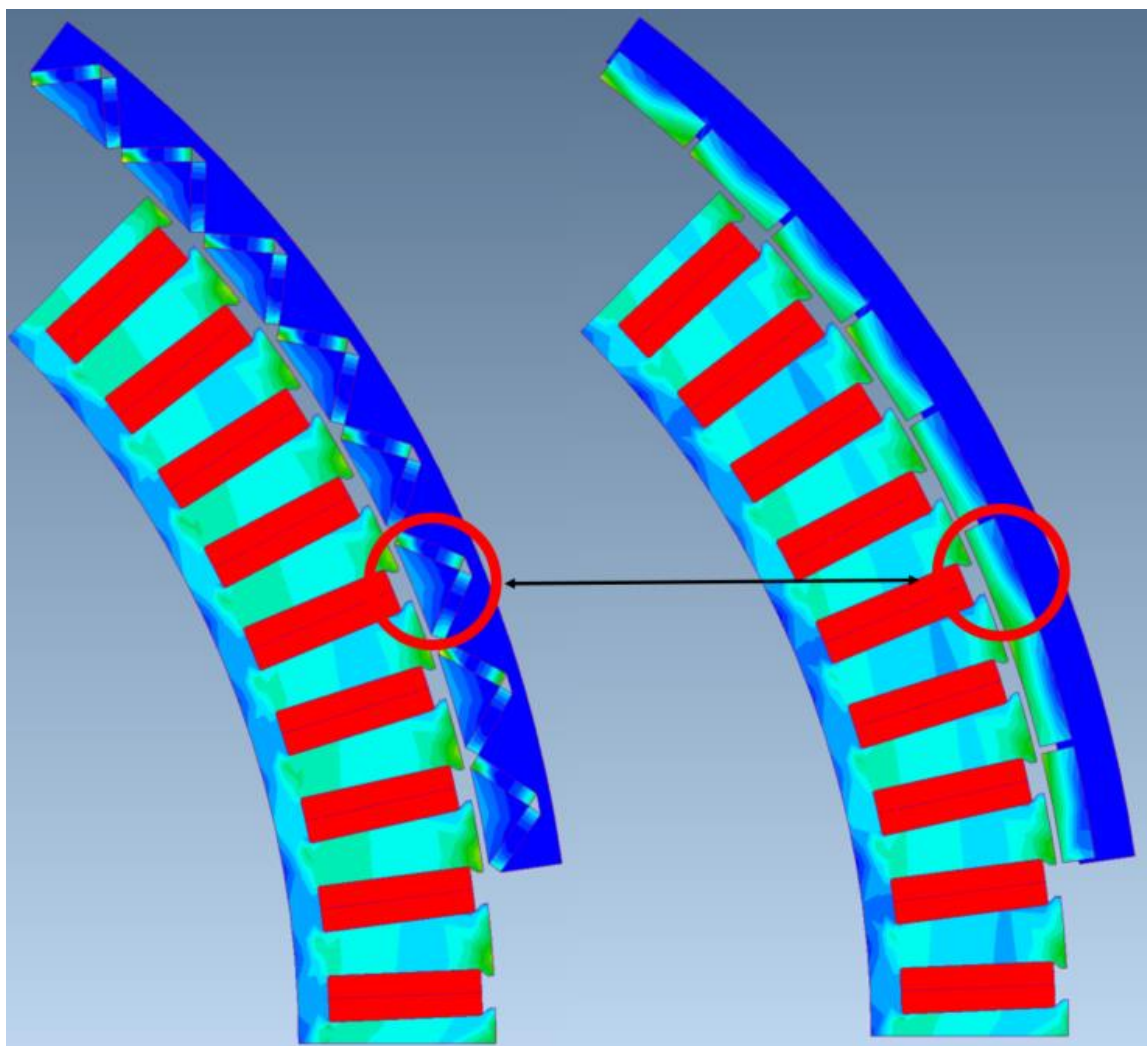


Figure 3-139 field plot of magnet temperature of the BMM and V-shaped motors at rated condition

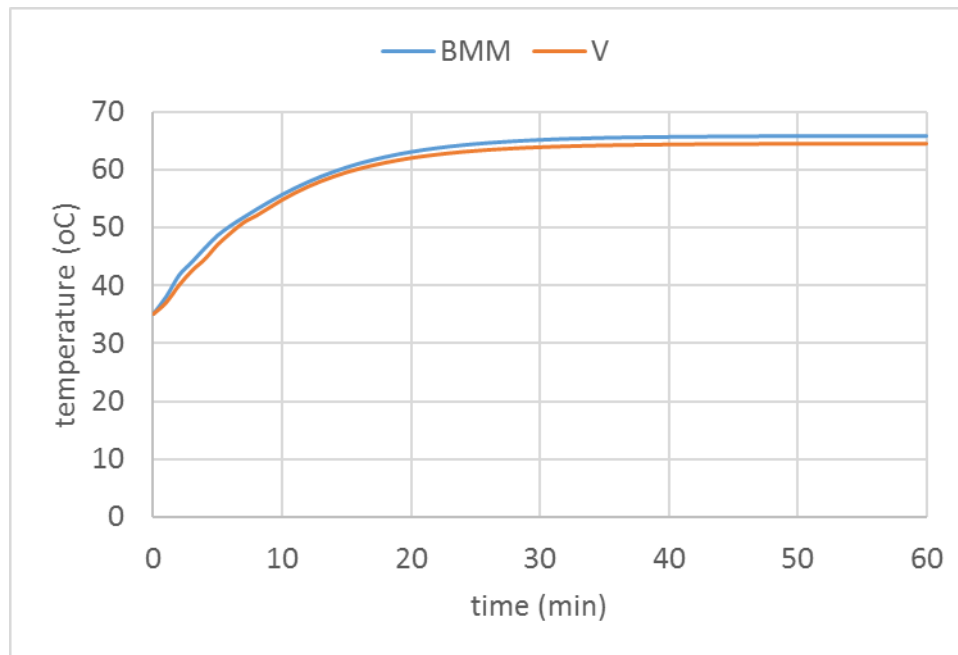


Figure 3-140 magnet temperature vs. time of the BMM and V-shaped motors at rated condition

3.5.12. Conclusion

Various aspects are compared between the V-shaped and the BMM motors. With current-advancing control, the V-shaped motor is shown to have a ~5% higher torque capacity at the rated condition but a 4% lower torque capacity at the over-load condition compared to the BMM. The V-shaped motor possesses a 2 times higher torque ripple (3.5% of the rated torque) and ~1% higher efficiency along the torque-speed curve. Various loss components in FE modelling are discussed to help understand the difference between the FE result and the experimental data in the BMM motor. With careful FE modelling, more accurate loss estimation can be obtained.

3.6. Conclusion

Seven rotor topologies were first analysed. The V-shaped motor gave the highest magnet utilisation value (torque-over-magnet-mass). It also had a shape which was easy to manufacture. Seven V-shaped designs were then created to meet the torque requirement and remain practical. The one with a rectangular magnet and no iron bridge on the end of magnet was selected. Then an analytical study on magnet loss was conducted to better explain demagnetisation resistivity of an interior topology over a surface-mounted one. Insights gained from this study were then applied to finding a suitable segmentation strategy. Finally, the V-shaped motor was optimised to match the torque-speed curve and

avoid demagnetisation in the worst case scenario (<2% area below knee point). All aspects of the V-shaped motor were compared with the BMM in detail and no clear performance disadvantage has been found.

The performance comparison at rated operation is summarised here:

Table 3-15 performance summary of the BMM and V-shaped motors

	BMM	V	
magnet mass	2.38	1.34	kg
line backEMF peak @ 800rpm	306.0	318.2	V
line voltage peak @ 800rpm	360.4	393.6	V
max torque @ rated current	682.2	651.2	Nm
torque ripple pk2pk / rated torque	2.2%	4.8%	-
knee point	754.8	721.3	rpm
magnet loss	1.0	0.32	p.u.

Chapter 4. BUILD AND TEST

4.1. Construction of the V-shaped motor

The essential concept of the V-shaped motor is to remove the steel ribs on all ends of the magnets minimising the flux leakage at a cost to weakening the structural strength of the design. FEA was used to assess its structural integrity under various operating conditions as is shown in section 3.2.3. However, during the motor assembly, unexpected issues were raised. The adhesive, assembly tools and insertion methods were reassessed and a new solution was proposed.

4.1.1. Introduction

The innovation in this V-shape design is the removal of the iron ribs on all ends of the triangular steel component (wedge), which are conventionally used to provide necessary mechanical strength for rotor integrity at the expense of introducing paths of magnetic leakage [100]. In an internal rotor machine, centripetal forces act to pull the magnets away from the centre of rotation. Mechanical rigidity is retained by a combination of magnetic force and stress on the iron ribs. In an external rotor, centripetal force is resisted by the rotor housing, and as a result the ribs are redundant.

The V-shape topology without the ribs, shown in Figure 3-79, possess a higher torque capability (torque per magnet mass) than that with ribs. Nonetheless, compromising the structural strength of the rotor raises unexpected issues during the motor assembly where large unbalanced magnetic forces can be present. Figure 4-1 shows that a few magnetic poles (wedges) have been detached from the rotor after an assembly attempt. Failure to assemble the machine undermines the numerous advantages of this machine design.

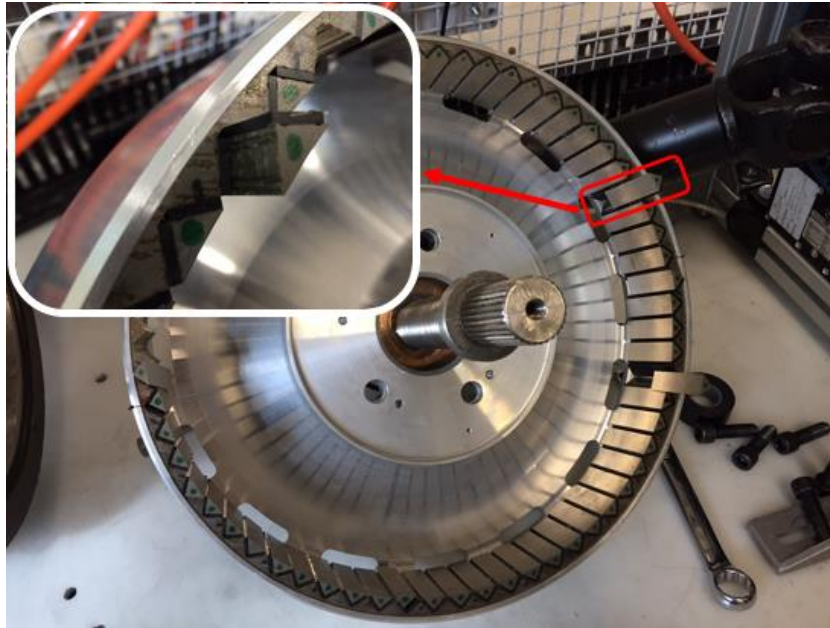


Figure 4-1 The initial rotor assembly attempt

This chapter aims to describe and address the issues presented during the assembly procedure of this novel machine. It includes details of the FEA used to quantify the torque capability advantage gained from the removal of the iron ribs and to investigate the structural integrity in various scenarios. Details of the initial assembly attempt are given, including causes of failure and lessons learnt. In section 4, after careful reassessment, solutions on alternative assembly options are presented. In section 4, assembly results are shown and a summary of the engineering challenges of the assembly is given.

4.1.2. The FEA on the V-shape magnets topology

In [98] seven topologies of the internal rotor permanent magnet synchronous machine were studied for use in an in-wheel motor. Torque capability and magnet mass were used to select and compare topologies. In Figure 4-2, in the existing manufacturing process one topology is presented which is designed to push the lower limit of the thickness of the iron ribs – electrical discharge machining (EDM). The intention is to retain the rotor as a whole while minimising the flux leakage path. The effect of removing the ribs altogether on torque capability is shown in Figure 4-3. There is a 12% torque increase for the same magnet mass, while for the same torque requirement 13.6% less magnet mass is needed compared to the topology with iron ribs. Hence, regarding the material cost, the topology in Figure 3106 is preferable. The next step is to prove it can be built with structural integrity.

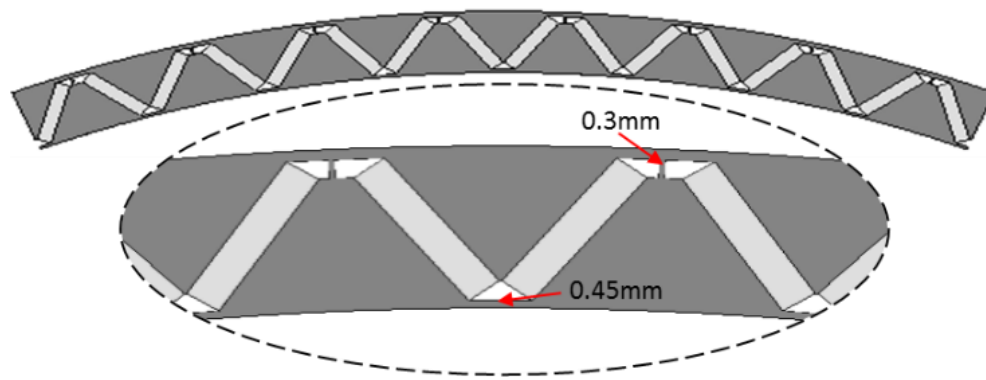


Figure 4-2 The V-shape rotor topology with minimised iron ribs

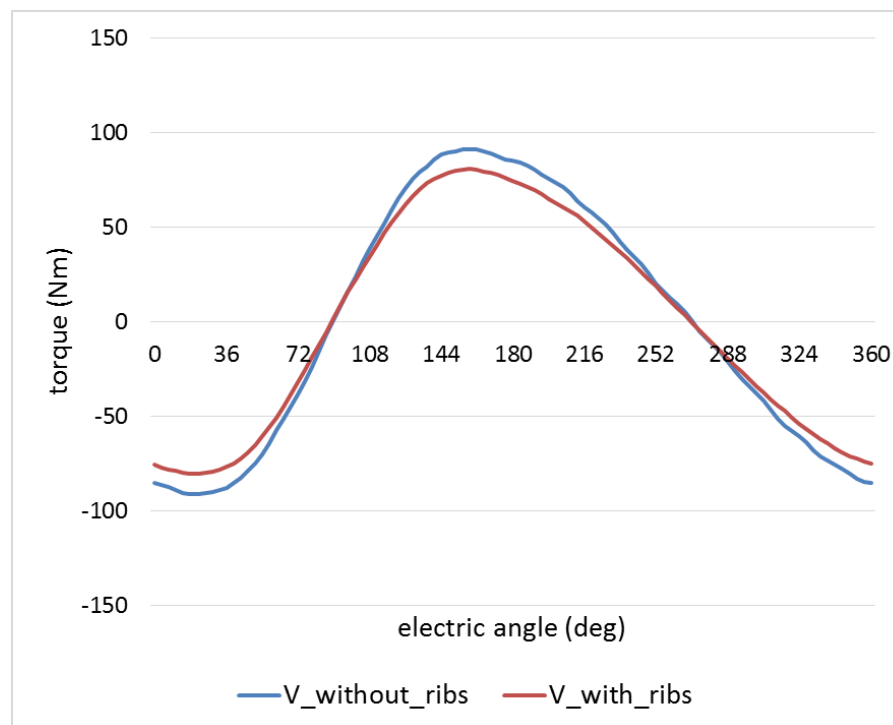


Figure 4-3 The torque waveforms with DC current input and varying rotor position

As illustrated in Figure 4-4, there is no mechanical structure to fix the magnets and the wedges onto the ring shaped rotor back-iron. Instead, the components are directly bonded using adhesive. Clearly, whether the bonding strength provided by the adhesive can hold pieces in place is the deciding factor in the feasibility of this design.

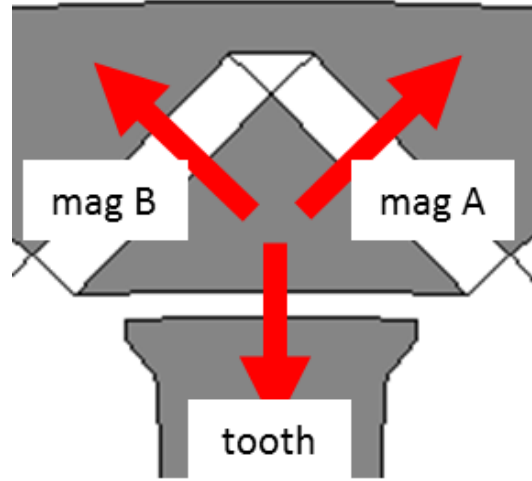


Figure 4-4 The magnetic forces developed on the wedge in the V topology; attraction from the stator tooth and the magnets

One of the advantages of the outer rotor topology is that the centrifugal force is automatically counteracted by the outer rotor housing. Hence, a varying operational speed has no effect on structural integrity.

It is the magnetic forces between components that needs to be analysed. In the established surface-mounted permanent magnet (SPM) design, the force on the magnets is relatively simple: along its magnetising direction - the radial direction.

A lumped-parameter magnetic-circuit model could be used to reveal the relationship between the radial magnetic attractive force and the air gap distance in the open circuit case in SPM: the shorter the air gap distance the stronger the attractive force.

$$B_m = \frac{B_r}{1 + u_r \frac{l_g}{l_m} \frac{A_i}{A_m}} \quad (4.1)$$

$$F = \frac{W_{ag}}{l_g} = \frac{1}{2} \frac{B^2}{u_0} A \quad (4.2)$$

Where, B_m is the flux density in the magnet, B_r is the remanence, u_r is the relative permeance, l_g is the air gap distance, l_m is the magnet length, A_i is the surface area of the iron tooth and A_m is the magnet surface area, shown in Figure 4-5.

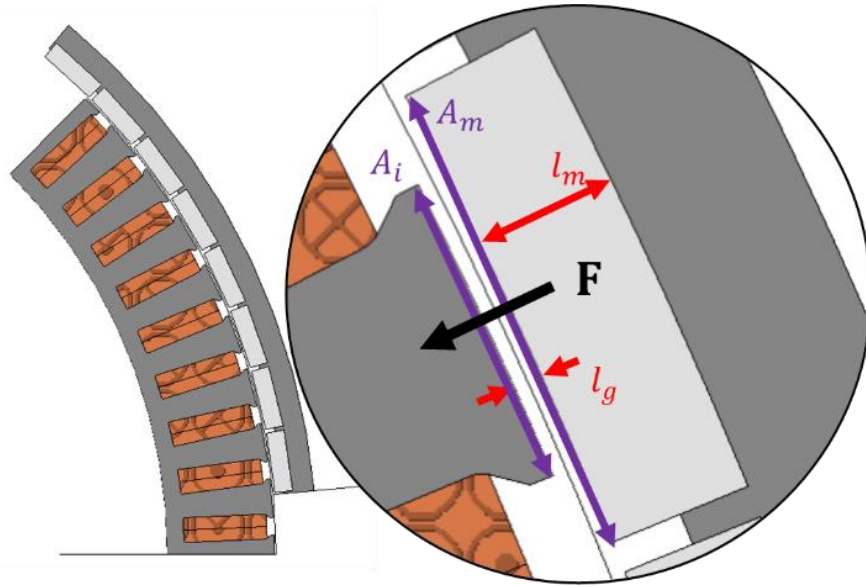


Figure 4-5 The magnetic force exerted on the magnet in the surface-mounted topology
 Due to its geometrical complexity in the V rotor, FEA is used to simulate forces with the following set-up:

1. The current input of the teeth underneath the tested wedge is directed to create an opposite magnetic pole attracting the wedge.
2. The magnitude of the current varies from rated to overloading values.
3. The rotor position is varied as is shown in Figure 46.
4. The air gap distance is varied from nominal to closed (1 -0mm).

Due to the particular stator tooth design, the maximum force is found at rotor position c in Figure 4-6 instead of the expected position a based on the analytical model used above. The direction of the resultant force is pulling the wedge away from the rotor and its magnitude is shown in Figure 4-7.

After converting 592.5N in the worst cases scenario to force per unit area, the average pressure on the wedge surface is 102.1psi, which is well below the typical bonding strength of the adhesive used in the surface-mounted topology [103]. Hence, the conceptual design is proceeded into the construction phase.

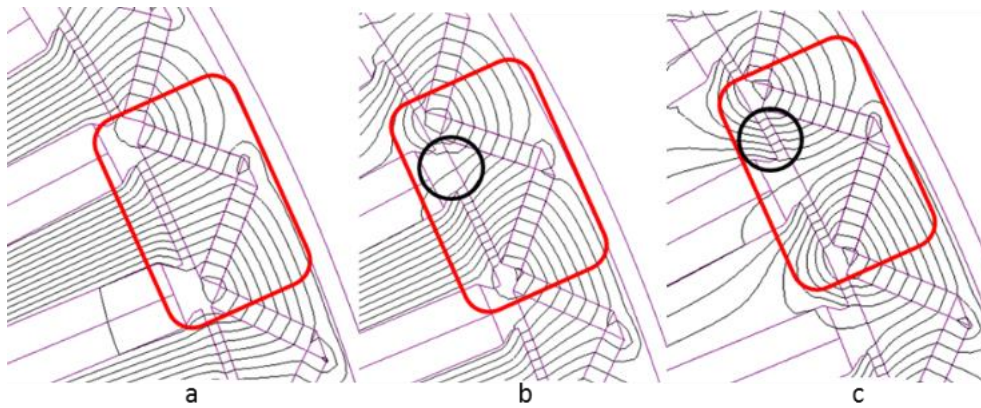


Figure 4-6 Magnetic flux plot in various rotor positions

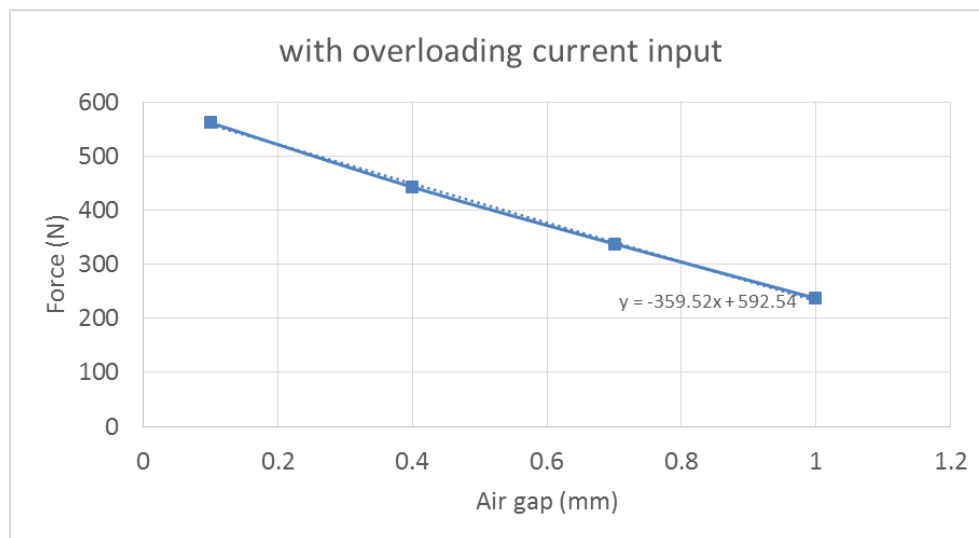


Figure 4-7 Force on the wedge at position c.

4.1.3. Initial assembly and emergent issues

The V magnet rotor consists of the rotor housing, the laminated back-iron, permanent magnets and laminated triangular pieces (wedges) as seen in Figure 4-1 and Figure 4-6. These parts need to be consistently fixed together to produce a structurally sound assembly that will be mounted onto the bearing and, together with the stator, complete the electric motor.

Initially, the back-iron needs to be hot-dropped into the rotor housing. Within the operational temperature range, the two components are rigidly bonded together due to design interference. However, during insertion the rotor housing needs to be heated to 150°C for the diameter of the face relevant to the back-iron to expand and produce a clearance. Due to the existence of thin spots in the back-iron, to accommodate the angled magnets and wedges, the structural failure of the hot-dropped components is of concern. As a result, the interference fit is chosen to be the minimum required to support the output

torque and FEA is conducted to ensure the force applied on the back-iron at the lowest operational temperature is within the limits of the material.

Next, the magnets need to be fixed onto the back-iron using structural adhesive. This decision is based on the fact that fixing the magnets onto the wedges first would require the creation of a positioning tool, which goes against the minimisation of cost and time spent in the prototype stage. As seen in Figure 4-8, each back-iron slot is filled with a pair of magnets, contacting their north or south faces. The contesting forces created cause the repelling of magnets in proximity. Since two-part adhesives take several hours to cure and become able to support large forces, a combination of strong and fast-acting adhesives is applied on each magnet. The magnet is then slid on the desired back-iron face. Two channels on each back-iron face ensure that the adhesive is not extensively wiped off during placement. Each magnet is held manually in place for several minutes, to allow the fast-acting adhesive to be able to support the forces developed during assembly. The two-part adhesive will then cure in time and provide high level structural support.

A similar procedure is followed for the placement of the wedges (Figure 4-9) onto the fixed magnets. In this case, the magnetic forces align to attract the wedge in position and make the assembly simpler.

Finally, the cured rotor needs to be mounted onto the bearing/stator assembly. A tool has been designed that ensures the gradual insertion of the rotor by restricting motion on the x and y axis while controlling the distance between the stator and the rotor using a threaded shaft. The shaft is placed into the stator bearing and fixed in place using a screw. The rotor is mounted onto the shaft through a flange. As the flange is rotated, the thread carries the rotor towards the stator, shown in Figure 4-10.

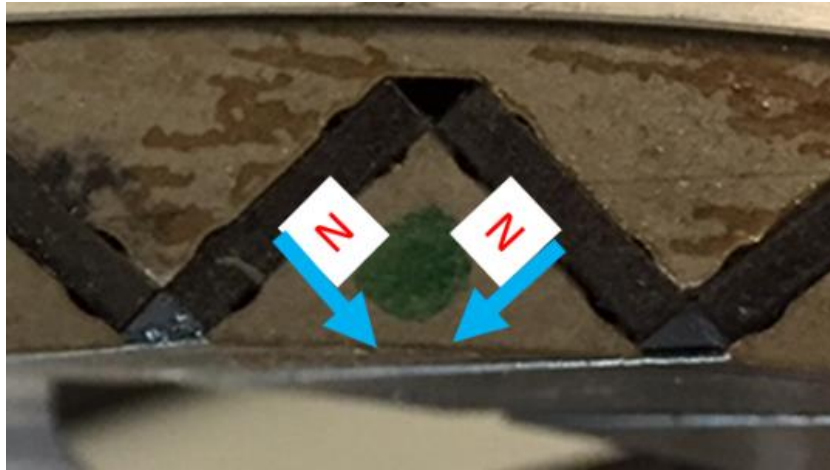


Figure 4-8 The V-shape slot on the back-iron



Figure 4-9 The two channels on the wedge

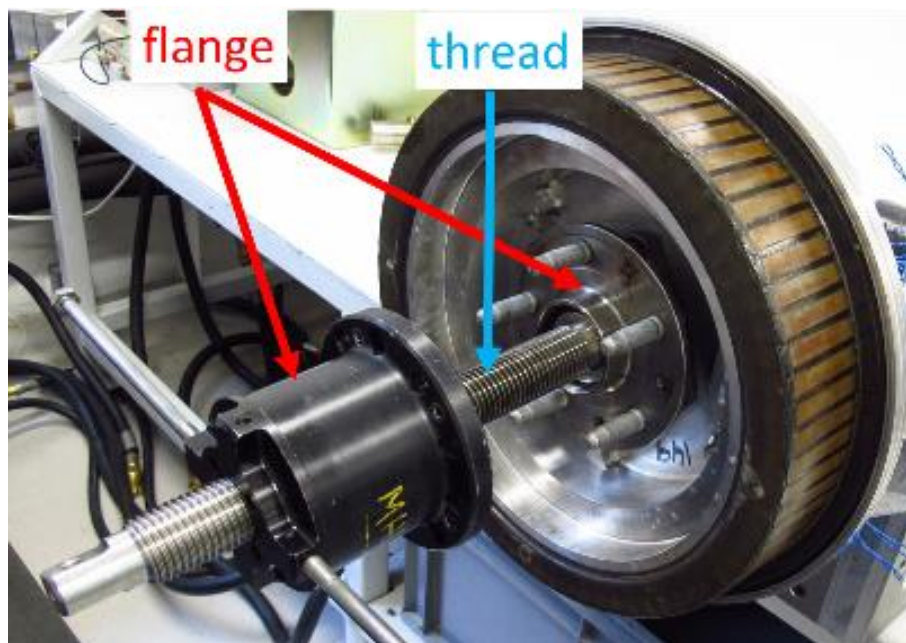


Figure 4-10 The rotor insertion tool

Following the methodology detailed above the motor assembly could not be successfully completed. During the insertion of the rotor onto the stator a relative angle was observed, illustrated in Figure 4-11, that resulted in wedge/stator contact at different points. Roughly half-way through the insertion, excessive friction was developed in the wedge/stator

contacts that led to the failure of multiple adhesive bonds, shown in Figure 4-1. Therefore, a new procedure was needed to reduce the insertion angle, as well as improve the adhesive bonds between components.

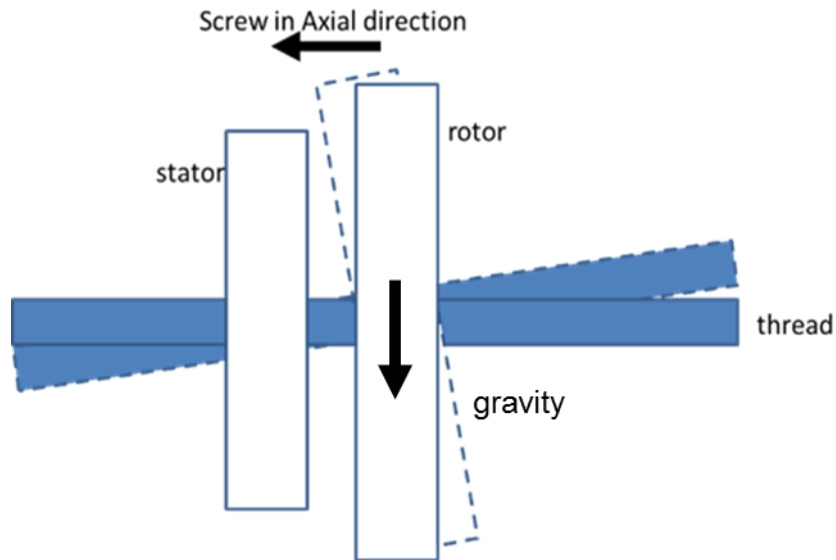


Figure 4-11 Illustration on rotor tilting during insertion

4.1.4.Improved methodology

In order for the rotor to be successfully mounted onto the stator a number of improvements are applied to the original procedure. These improvements can be separated into two categories: insertion and adhesion.

During insertion, the relative angle between the rotor and the stator can be attributed to a number of parameters. The insertion tool, mounting flange and housing tolerances can build up to significant levels. It is important to ensure the sum of tolerances along the shaft/bearing support and the rotor housing remains trivial. To counter these issues, a new rotor insertion tool has been designed with focus on minimising tolerances.

The strong attractive force of the rotor magnets can cause deformation of the rotor housing and promote component contact and friction escalation. Hence, the mounting points of the flange and the rotor housing have been moved to a higher diameter in order to provide better support and reduce the effect that attraction between the magnets and the stator can have on the insertion angle. Finally, a rigid rotor housing is used and weight reduction machining is avoided to improve structural integrity.

Regarding adhesion, back-iron/magnet and magnet/wedge contact bonding has been upgraded drastically. Firstly, the magnet surfaces were sand blasted to remove the coating and provide a rougher texture, as recommended by the magnet supplier [124]. Secondly, all relevant faces were treated with abrasive paper and IPA solvent to be cleaned of any debris. Thirdly, dual adhesive, as well as slide-on methods were abandoned. The quality of the fast-acting adhesive bond was not suitable for the present application and was only used as a positioning solution for the initial manual component assembly. As a result, tools to consistently handle components for the adhesive curing stage need to be created.

Furthermore, the decision was made that the magnets should be bonded to the wedge first, which is shown in Figure 4-12 1.a). In the initial method, Figure 4-12 1.b), due to imperfect manual build, the magnetic centre line of two magnets in some of the slots were not aligned with the centre line of the slot, creating an asymmetric magnetic field. An unbalanced repelling force was then experienced when positioning wedges into the back-iron/magnet slots. Consequently, some of the wedges ended up in asymmetric positions as illustrated in Figure 4-12 2.b) if clamping was not applied while curing.

FEA has been conducted to investigate the effect of the two different methods on the resultant force during wedge insertion in both symmetric and asymmetric positions (Figure 4.13). In a symmetric position, when the magnets are preassembled on the wedge the force is always attractive, whereas in the scenario where the magnets are preassembled on the back-iron, the force is changing from attractive to repulsive when the wedge is approaching the slot. Furthermore, in an asymmetric position, the force acts towards the centre of the slot, i.e. the symmetric position, in the improved method, whereas it is pushing away from the centre of the slot in the initial method, which is illustrated by the red arrow in 2.a and 2.b in Figure 4-13. Hence, bonding the magnets onto the wedge first presents significant advantages.

Initially, a slotted base would have to be built to assist with fixing the magnets on the wedges consistently. First, the magnets are mounted on the base and an appropriate two-part adhesive is applied to the relevant faces. Then, a wedge is pushed into the slot using a custom tool, as shown in Figure 4-14 to avoid wiping any adhesive out of the interface. The assembly is then supported with a clamp, so that pressure is applied on the adhesive, and it is placed in an oven for curing as per supplier instructions. In order to ensure the magnets stay well below the demagnetising temperature limit, the oven temperature needs

to be chosen accordingly. The assembled wedges/magnets are subsequently placed onto the back-iron, again using the custom tool and the push-on method described above.

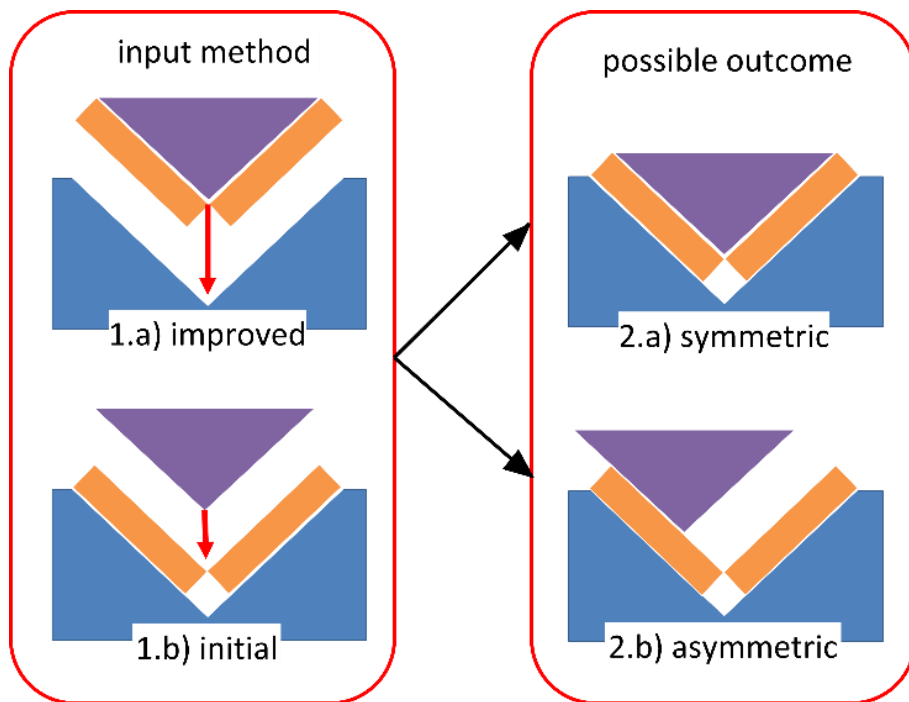


Figure 4-12 1.a) Improved insertion method – magnets adhered on the wedge prior to the insertion; 1.b) Initial insertion method – magnets adhered on the rotor prior to the insertion; 2.a) the anticipated outcome with a symmetric position; 2.b) the asymmetric position experienced in the initial method

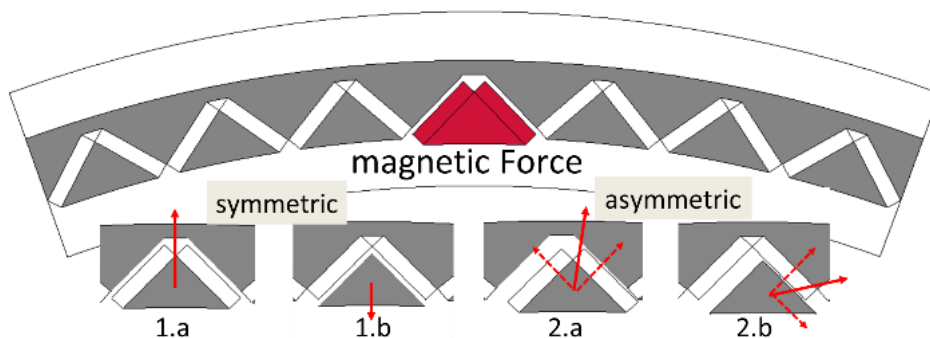


Figure 4-13 The force for the a. improved method and b. initial method at 1. symmetric and 2. asymmetric positions

With the completion of this stage, the rotor is ready to be inserted onto the stator. A new adaptor was made to plug the rotor onto the collet of the lathe. The stator was clamped onto the bed and its position was adjusted to be centre-aligned with the rotor in the inserting direction. The main advantage of using a lathe is that the inserting direction can be aligned with gravity to eliminate any potential gravitational effects on misalignment. Also a more rigid rotor housing is used in this insertion to make sure the rotor shape doesn't change due to the increasing attractive force during and after insertion. The

complete assembly of the outlined V magnet motor is successful and is shown in Figure 4-16.



Figure 4-14 The tool for the push-on method



Figure 4-15 Rotor insertion with the new adaptor

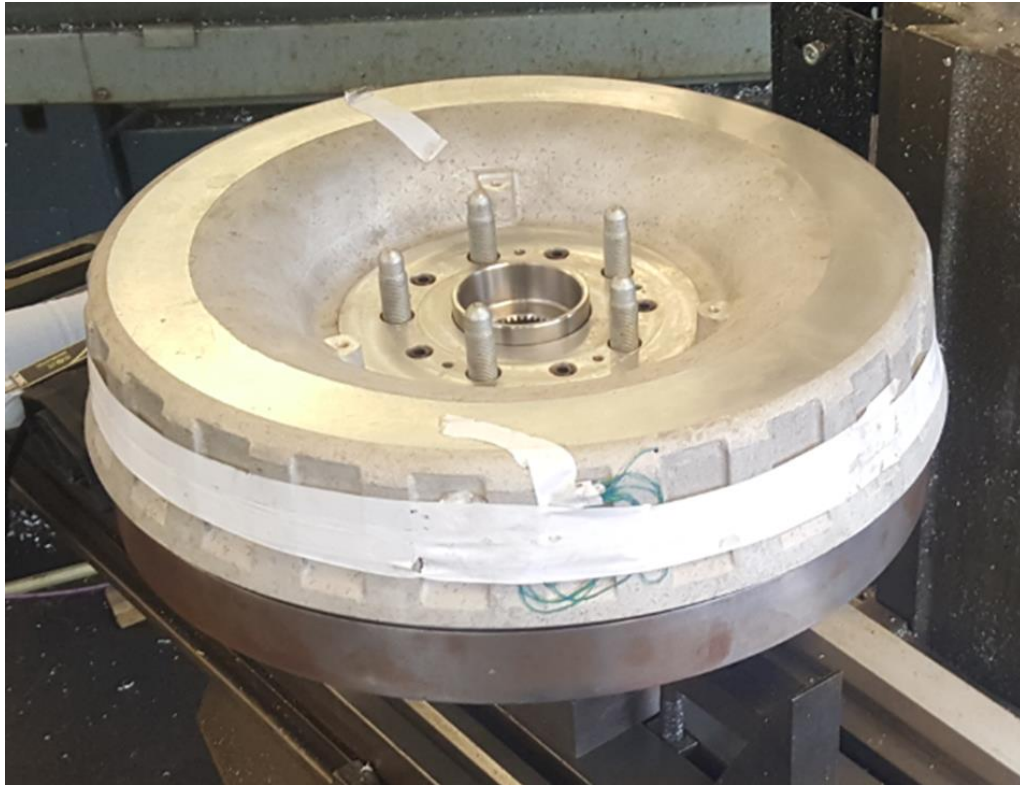


Figure 4-16 The successfully assembled motor

4.1.5. Conclusion

The V-shape magnet rotor design can greatly reduce magnet mass (cost) or, alternatively, improve performance compared to the surface-mounted magnet design. In outer rotor machines it is possible to further improve performance by removing the retaining iron ribs that hold the magnets in place. However, this increases manufacturing complexity. In this chapter, the difficulties arising from attempting to prototype such a machine are described. Learning from the initial assembly attempt, these difficulties have been overcome by: a. improving the insertion process, i.e. bonding the magnets onto the wedge first, using the push-on method, a new rotor insertion tool, changed insertion direction and a stiffer rotor housing; b. the conditions for adhesive bonding of components, i.e. a higher grade adhesive and rougher bonding surfaces. As a result, the assembly of a high performance V-shape magnet design has been made possible, establishing the standard process for future production.

4.2. Test of the V-shaped motor

In this chapter, the prototype V-shaped motor will be tested and the results will be compared with the benchmark surface-mounted motor. Measured data will also be compared with finite element analysis to validate the simulation. Tests include: active short current, drag torque, back EMF and torque against q-axis current.

The testing of the prototype machine was conducted at the Protean Electric testing centre, where a high level test rig was set up with the capability of carrying out various machine tests. Figure 4-17 is the layout of the rig showing the points of connection and the instrumentation needed to log the measured data.

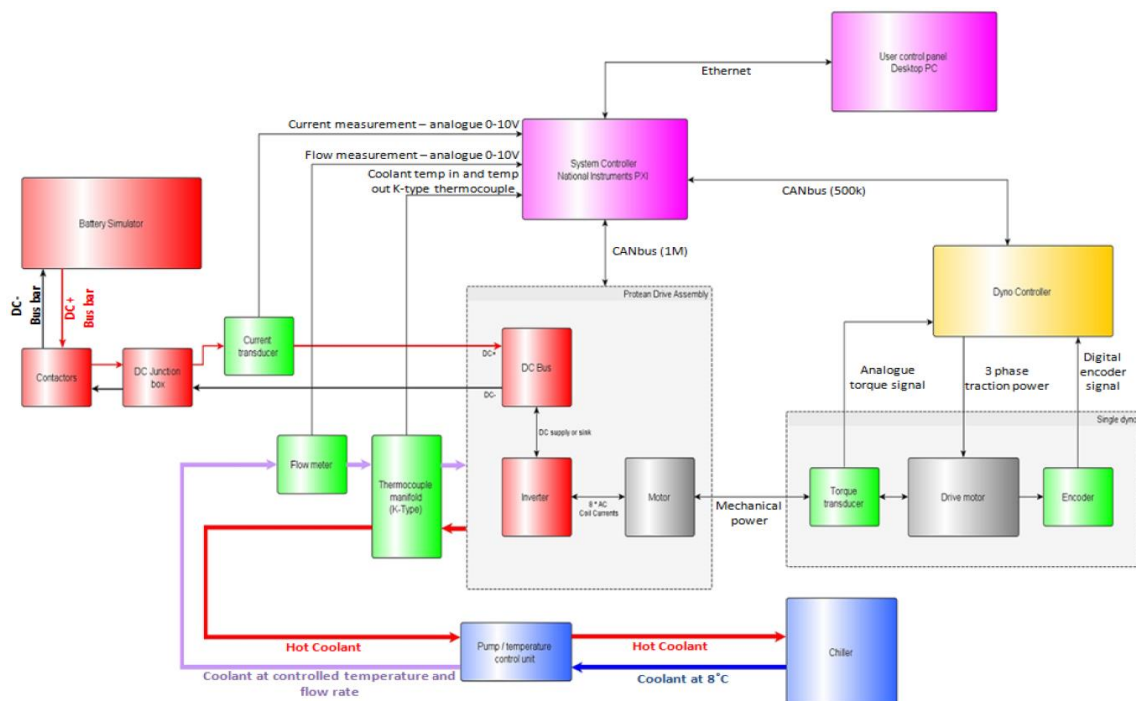


Figure 4-17 Schematic diagram of the Protean Electric test rig [109]

4.2.1.Active short current test

In this test, the motor is connected to and driven by a dynamometer. All three phases of one sub motor are short circuited while the remaining seven sub motors are open circuited. In Figure 4-18, the phase peak-to-peak currents are plotted against the speed. As discussed previously, the inductance is higher in the V-shaped motor due to a thinner equivalent air gap. It means that the short-circuited current is lower in the V-shaped motor, which is represented by the black line in the graph.

The reason why the current is lower at low speed and starts climbing and plateaus when the speed is higher than a certain point can be explained by the phasor diagram shown in Figure 4-19. In the shorted circuit, the back EMF is induced by the rotating flux from the rotor and it is proportional to the speed. The inductive reactance is also proportional to the rotor with inductance given as a constant. However, resistance is not proportional to speed. Hence, when the speed is low, the current value is determined by the simple equation V/R and is proportional to the speed. However, when the speed increases, the $\omega L I$ term quickly increases making the RI term's contribution to the terminal voltage insignificant. Using equations based on this diagram and simulation data from Chapter 3, the result is compared with the experimental data and shown in Figure 4-20. The short-circuited current remains lower than the simulation in the V-shaped motor. The simulation result is 10% and 2% higher than the experimental result in the V-shaped motor and the BMM, respectively. The difference comes from the neglected end-effect when using 2D FE simulation, the manufacturing tolerance. The reason why there is a much higher difference in the V-shaped motor is because the V-shaped motor boring layer was not simulated and the reluctance of the magnet circuit in practise is much higher than the simulation.

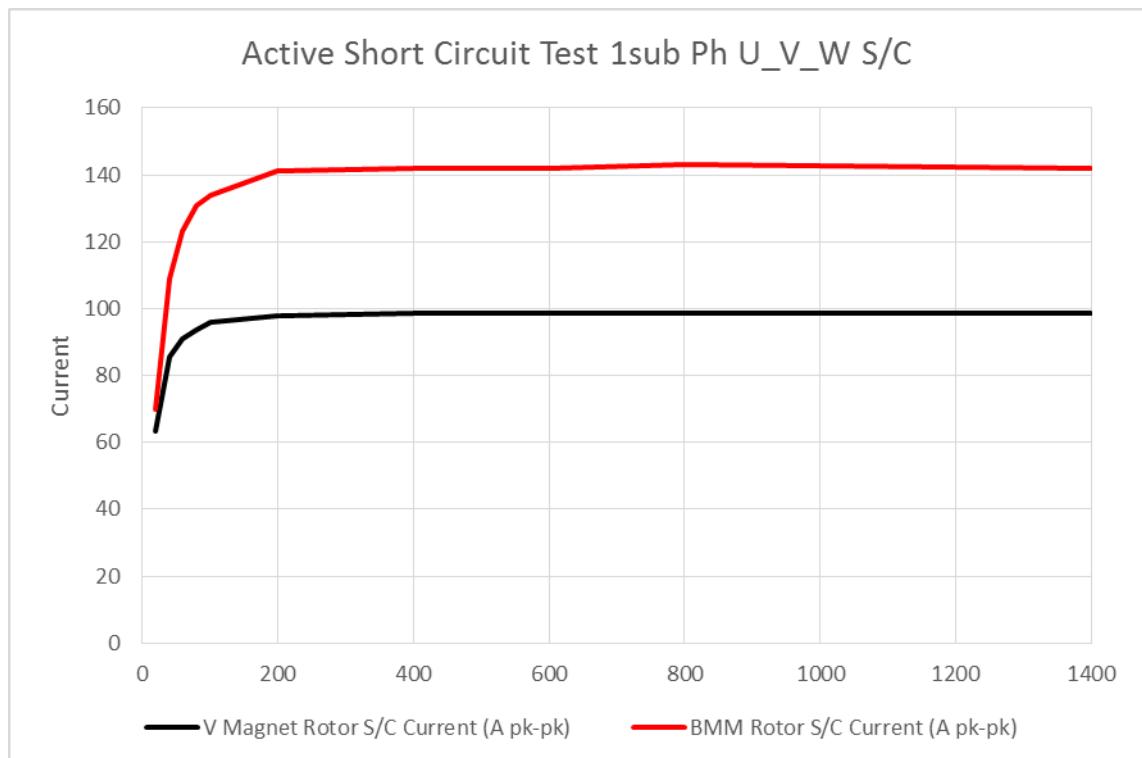


Figure 4-18 The experimental result of the active short circuit test

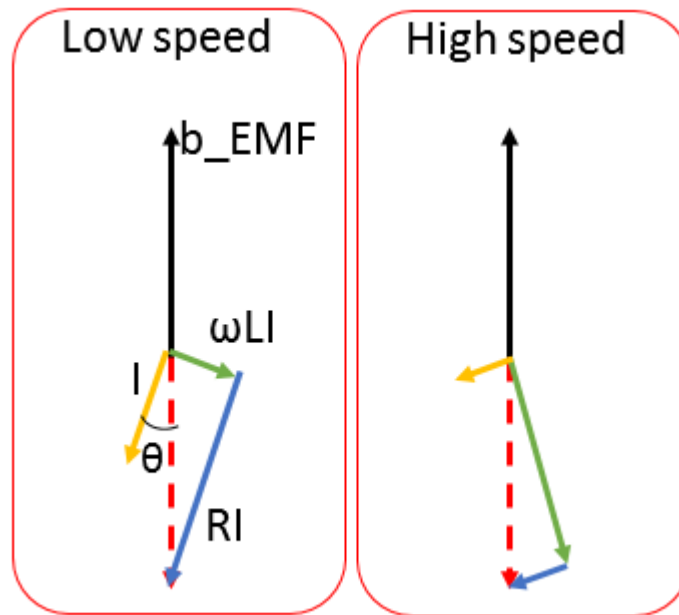


Figure 4-19 The voltage phasor diagram of the short circuited coil

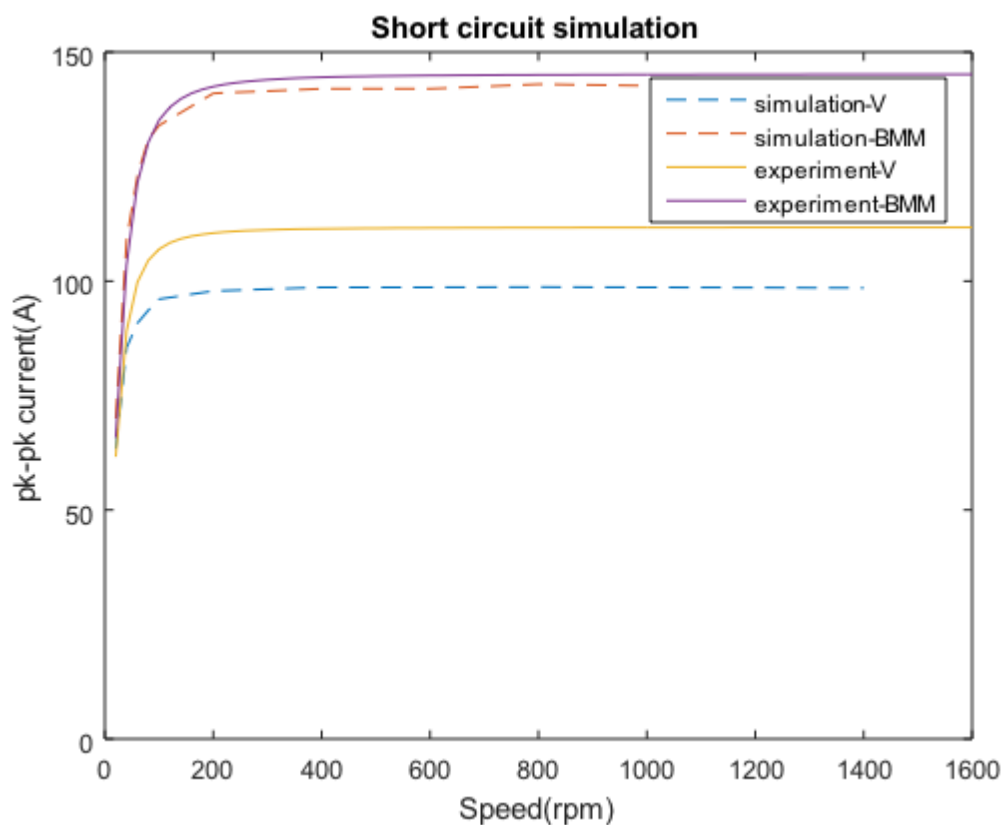


Figure 4-20 The simulation result of the short circuit test

4.2.2. Drag torque test

The drag torque test is presented in Figure 4-21, in which the dynamometer again was used as the prime mover and all phases were disconnected. So The torque, therefore is solely

produced due to the windage and friction loss neglecting the small iron losses. Due to both rotors having the same dimension and a similar weight (the V-shaped motor has less magnet but more iron lamination), the drag torque from both rotors is quite similar. The drag torque comes from both mechanical loss and iron loss. An analytical drag torque model is not developed to compare with the test data. This test data could be used to directly generate curve-fit formula describing these motors' no load losses.

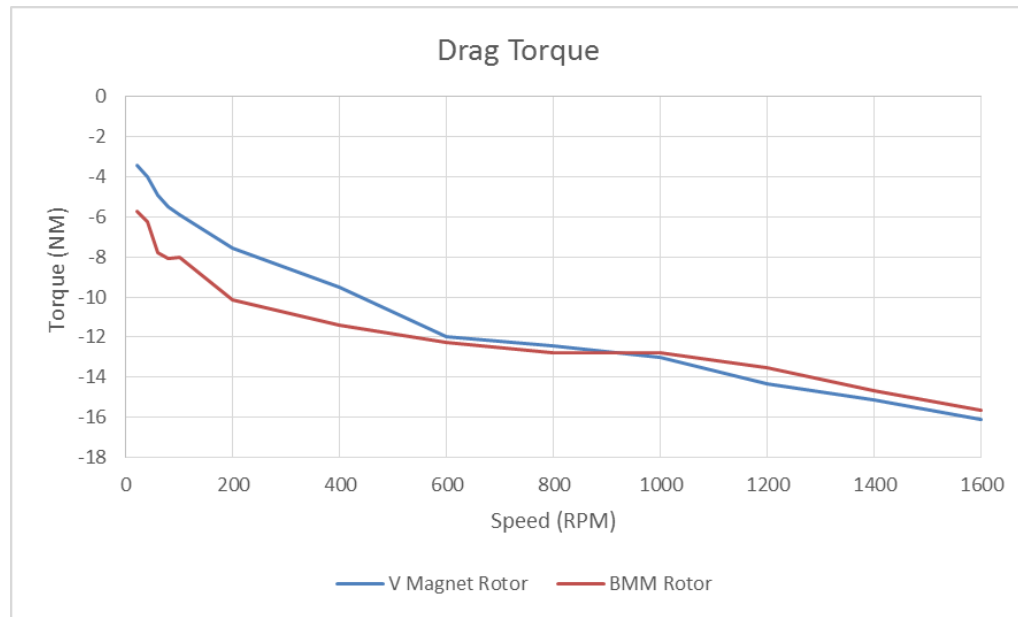


Figure 4-21 The experimental result of drag torque test

4.2.3. Back EMF test

The back EMF test uses the same set up as the drag torque test. As seen in Figure 4-22, it is clear that the back EMFs in these two motors are closely matched meaning that the V-shaped motor when compared to the benchmark motor can provide the same flux linkage with 56% of the magnet material. The experimental results in both motors are 5% lower than the FE simulation result due to the neglected end-winding effect. In both cases, the back EMF of the V-shaped motor is 1.6% higher than the BMM.

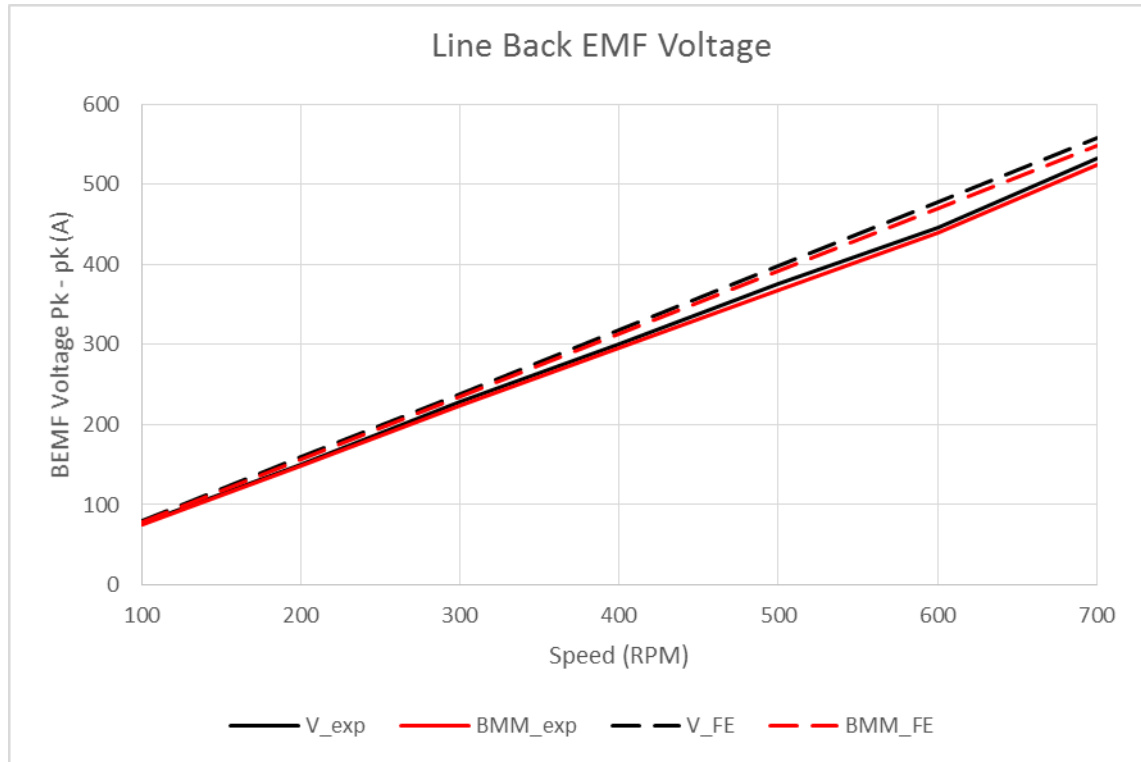


Figure 4-22 Comparison of the simulation and experimental results of the back EMF test

4.2.4. Transient torque test

The torque against the peak q-axis current for both motors are plotted as solid lines in Figure 4-23. As stated in [109], it was noticed that there is a consistent 12% reduction from electromagnetic torque simulated in FE to experimentally measured shaft torque due to mechanical power loss. With this taken into account, the FE results are reduced by 12% and plotted as a dotted line and they are accurately matched with the experimental data shown by a solid line. The biggest difference between the experiment and the simulation of the V-shaped motor is 4.4% and this can come from the unexpected thick bonding layer or the difference between the actual magnet temperature and the simulation. As can be seen from the graph, the V-shaped motor's torque performance is comparable with the BMM at 30Amps rated condition. However, when the motor runs deep into the overloaded region, it quickly saturates and gives noticeably less torque compared to the benchmark motor.

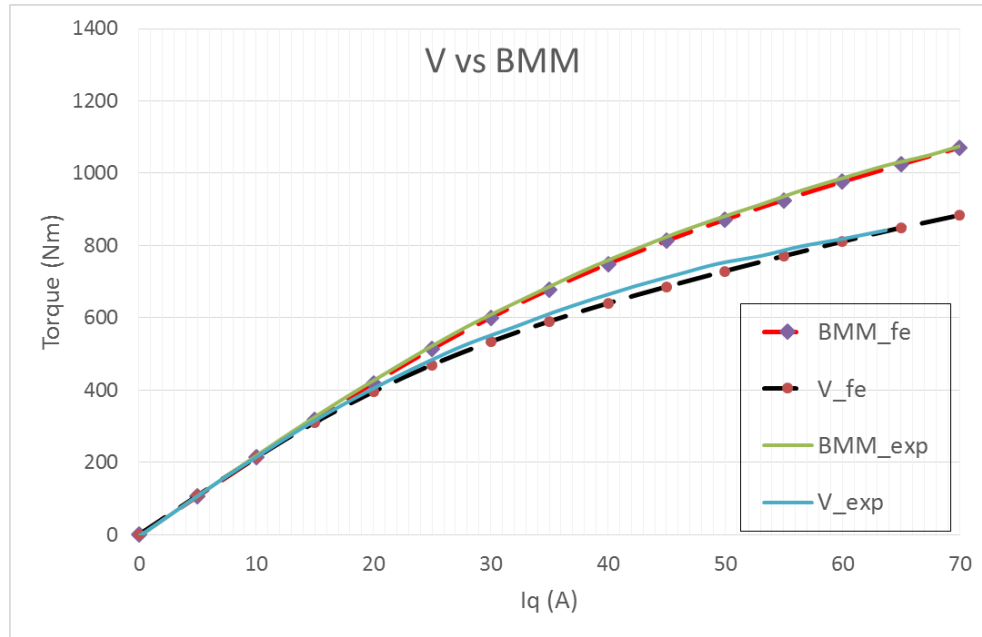


Figure 4-23 Comparison of the simulation and experimental results of transient torque test

4.2.5. Conclusion

There were four tests conducted to verify the FEA results. The result shows that the V-shaped motor gives a lower short-circuited current (68% of the BMM). The reduction of the short current can further reduce the fault torque, the demagnetisation flux and the copper loss at a fault condition. Both motors have the same drag torque meaning both the no-load iron loss and the windage loss of the V-shaped motor is at the same level compared to BMM. The back EMF magnitude of the V-shaped motor has a <2% difference compared to the BMM. This is strong proof that the torque of the V-shaped motor can still be at similar level compared to the BMM. In the last test, the load test, the V-shaped motor can provide 95.6% of the torque of the BMM at 30A peak phase current of rated condition. But, as expected, when the current keeps on being increased above 30A to 60A, the V-shaped motor generates merely 83% of the BMM torque due to early saturation.

4.3. Conclusion

In this chapter, the prototype of the V-shaped motor has been built. During the construction, issues due to removal of the ribs forced a second review and new assembly methods, tools, materials were implemented to solve the issues. The tests conducted all show good agreement with the simulation. From this experience, it is now known that the next generation of V-shaped motor will focus more on improvement of overloading capability.

Chapter 5. PAPER STUDY ON DESIGN IMPROVEMENTS

5.1. Introduction

Fractional slot, concentrated-winding (FSCW) machines, like the BMM and V-shaped motors, are being researched extensively for vehicle traction motors, this is because of the several advantages they have over conventional integral-slot distributed-winding (ISDW) machines: [106]

1. Short end-winding length in both axial and circumferential directions – the active to total axial length ratio can be increased, hence the torque density. The copper mass and loss are also reduced, resulting an improved efficiency. This could be a critical advantage in the in-wheel vehicle traction motor application [98].
2. Modularity – the coil can first be wound onto the tooth, then assembled onto the stator yoke individually, which greatly reduces the manufacturing complexity, saves manufacturing time, labour costs and opens up the possibility of automatic winding assembly. [125]
3. High fill factor – the increased fill factor can reduce winding resistance, hence copper loss, and remove the air gaps between conductors in the slot, hence improving winding thermal conductivity. [71]
4. High fault tolerance – for each phase, windings are concentrated in one stator position. Hence the phase-phase and tooth-tooth electromagnetic couplings are intrinsically lower than ISDW. [126]
5. Increased synchronous inductance – this leads to the reduced characteristic current for fault tolerance and improved constant power operation range in the electric vehicle application. [127, 128]

Aiming to improve the torque density, a salient rotor can be used to provide an additional torque component - the reluctance torque [98]. However, there are two universally-found phenomena related to their torque performance.

First, with the same salient rotor, they exhibit a lower reluctance torque than the integral-slot distributed-winding (ISDW) machines. Second, FSCWs exhibit a higher torque ripple when they use a salient rotor compared to the non-salient one.

This chapter identifies the root cause of these phenomena and explores potential solutions. A popular double layer magnet rotor topology similar to the BMW-i3 motor is used to demonstrate the significant difference of the achievable reluctance torque. Next, the current sheet method is implemented and an analytical expression is proposed to reveal the cause. Then, general rules are summarised to help retain the reluctance torque capability of FSCW by selecting certain pole-slot combination and modifying the stator slot-opening width. Lastly, the concept is demonstrated through modifications of the prototyped V-shaped motor.

5.2. Reluctance torque in fractional-slot concentrated-winding machines with saliency

It is speculated that a lower achievable reluctance torque could be due to rich stator MMF harmonics in FSCWs compared to integral-slot distributed-winding. As stated in [129], by changing the winding arrangement of an FSCW from two layer winding to four layer winding, the torque density can be significantly improved due to an increase in machine saliency and reluctance torque. This is because of the reduction of the sub-harmonics, which is also demonstrated in [130].

Methods are evolved to minimise the stator MMF harmonics including increasing the winding layers [131, 132], stator shifting [133], magnet barrier [134, 135] and rotor shaping [136], and choosing odd numbered stator slots [137]. In literature, there is no work which is able to explain the exact cause of this torque reduction phenomenon and draw a clear relation between it and stator harmonics. This chapter aims to explicitly explain the cause of this torque reduction.

The section is organised as follows: In sub-section 1, one ISDW and three FSCW models with identical rotor and stator MMF input but different winding arrangements and stator slot number are designed to demonstrate the significant difference in reluctance torque. In sub-section 2, the current sheet method of finite element analysis is used to explore the relationship between stator harmonics and reluctance torque. In sub-section 3, based on the insight gained from FEA, an analytical expression to calculate the flux across the air

gap, which is later used to calculate the torque, is devised and verified. In sub-section 4, a case study is used to propose general rules and design advice on mitigating the torque reduction effect is given. Finally, the conclusion of the chapter will be drawn in sub-section 5.

5.2.1.A lower reluctance torque in FSCW

To demonstrate the reluctance torque difference between FSCWs and ISDWs, an ISDW stator of 48 slots and three FSCW stators of 6 slots, 9 slots and 12 slots are designed primarily without optimisation and illustrated in Figure 5-1. Notice, the slot opening width to stator pole pitch ratio is slightly different in model D.

In Figure 5-2, one rotor of 8 magnetic poles with a similar topology to the BMW-i3 traction motor [138], the most state of the art motor in the current electric vehicle industry, is used to be paired with these four stators for torque output simulation. The electric loading (stator MMF) in all models is identical.

In Figure 5-3, the flux of the statically solved model A is plotted when the current advancing angle is set to 0 degrees, i.e. aligned on the q axis. This is used to check whether the model is at a reasonable saturation level to ensure a practical design while selecting the highest possible MMF input to load the motor. 1.6 Tesla is the knee point for the lamination material.

After the MMF input is determined, both the stator and rotor laminations in the four models are then switched to an infinitely permeable magnetic material. This rules out an inconsistent saturation effect due to any different and unoptimised stator geometry in the four models when comparing their torque capability. The rotor is modified slightly in order to take out the saturation effect when applying different ranges and combinations of stator harmonics. A geometric comparison is shown in Figure 5-4. The reason why the iron ribs are cut out is to prevent an infinite amount of flux short circuiting when switched to an infinitely permeable material. The curves of torque against current advancing angle between the saturable and unsaturable models are plotted in Figure 5-11 to demonstrate that there is little torque difference between these two.

In Figure 5-5, two simulation points are selected, both of which will be used to compare the level of reluctance torque in the four models. One is on the q axis for maximum

alignment torque, i.e. the torque generated solely by the magnet's interaction with the stator MMF. The second point is selected at the current advancing angle of -45° , which is the exerting point of the maximum reluctance torque.

As can be seen from Figure 5-6, it is clear that the ISDW model possesses the highest ratio of reluctance torque to alignment torque (61%). The reluctance torque is merely 15% of the alignment torque in model D – p8s6. Even for the highest ratio in three FSCWs (47% of the alignment torque) model B - p8s12, there is a 23% reluctance torque reduction compared to their distributed-winding counterparts. Notice that, the difference in alignment torque among these four models is due to their winding factor difference. The winding factor of models p8s48, p8s12, p8s9 and p8s6 is 0.966, 0.866, 0.945 and 0.866.

Significant torque reduction occurs when switching from ISDW to FSCW.

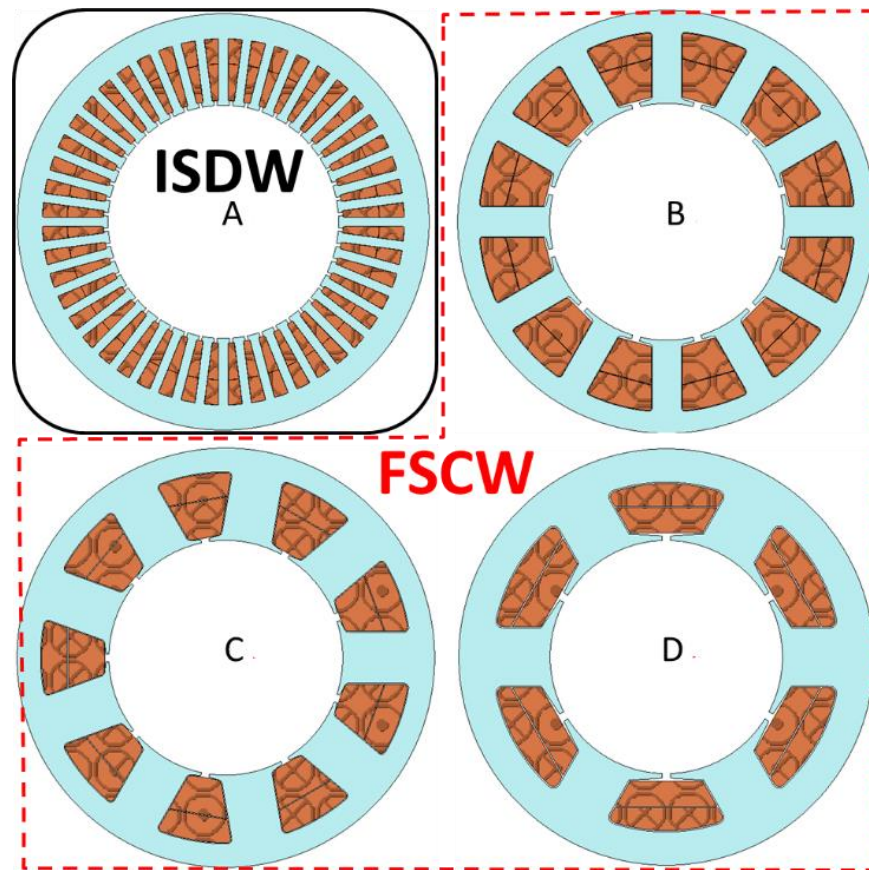


Figure 5-1 Four stator models: A. 48slots, B. 12slots, C. 9slots, D. 6slots

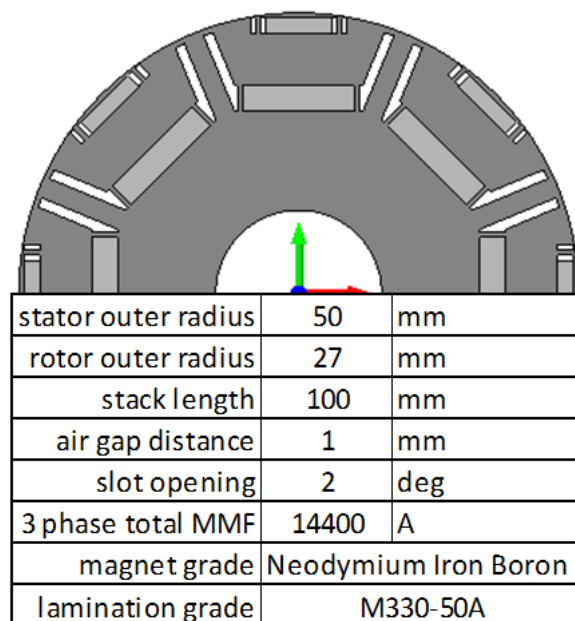


Figure 5-2 Double-layer magnets rotor

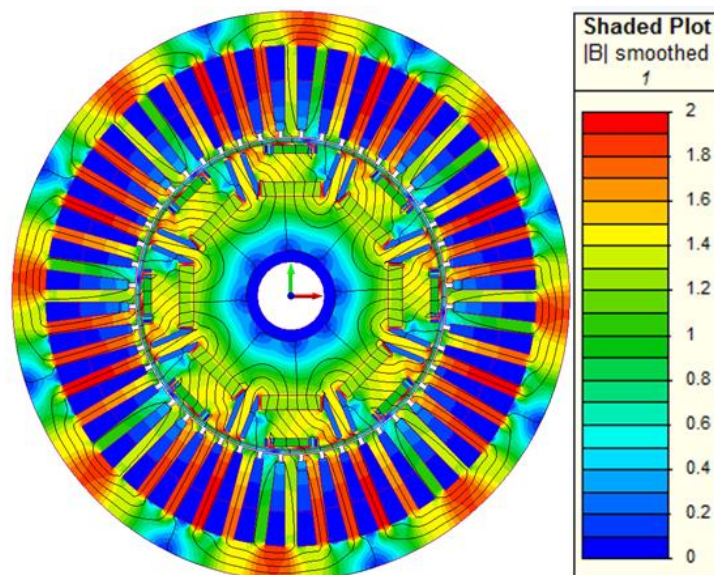


Figure 5-3 Flux plot on Q axis

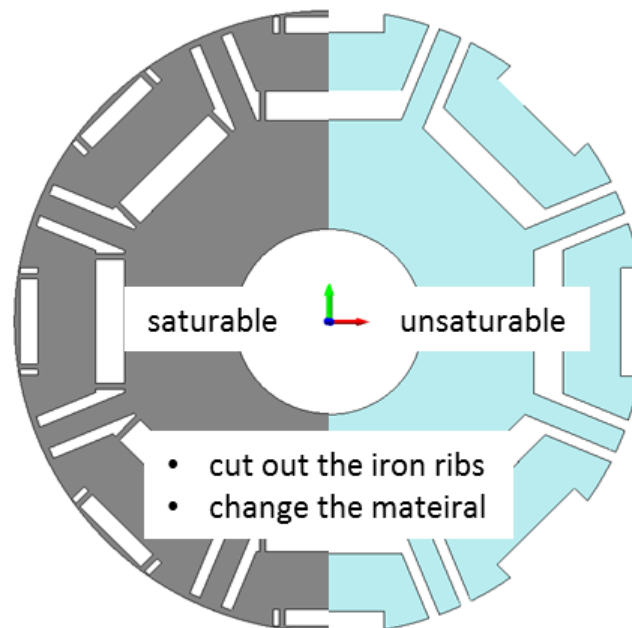


Figure 5-4 Rotor modification

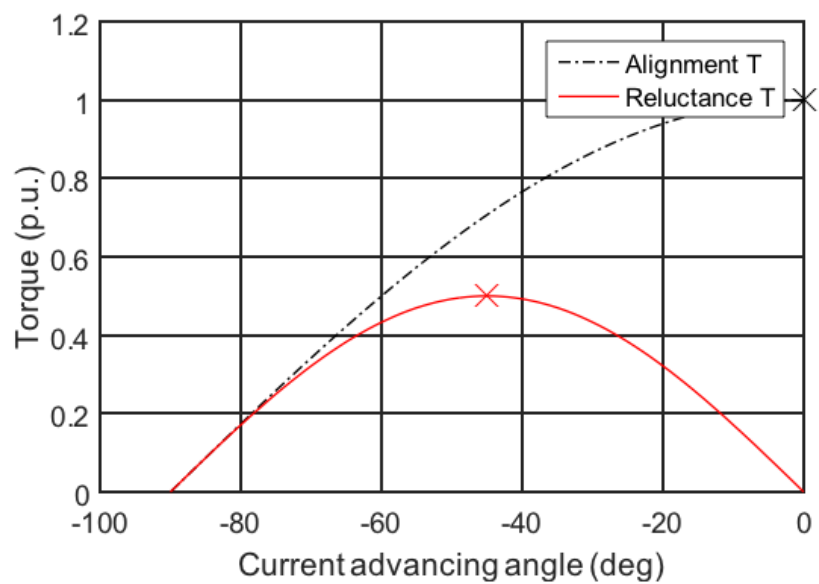


Figure 5-5 Two checkpoints defined on the graph as torque vs. the current advancing angle

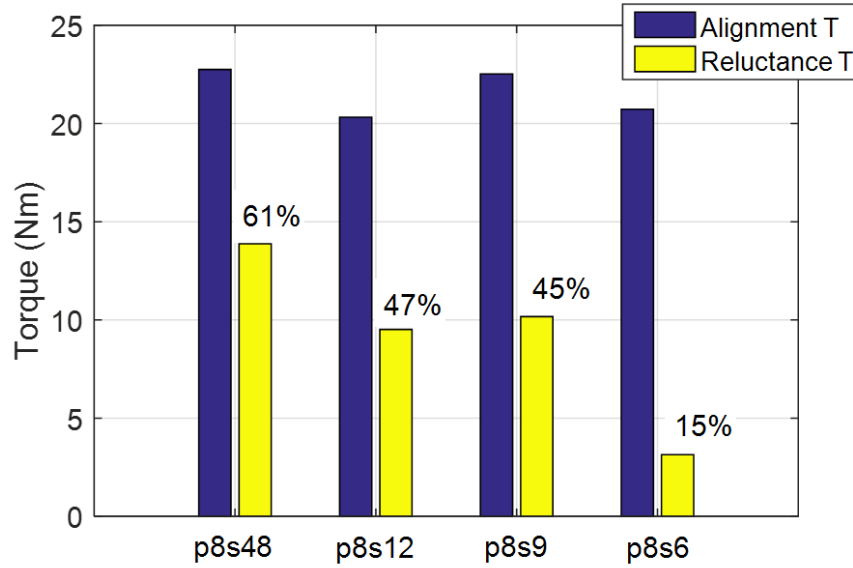


Figure 5-6 Torque comparison between four models

5.2.2. The stator harmonic effect

To understand the cause of this phenomenon, the stators are replaced with a conductor sheet as is shown in Figure 5-7. The idea is to represent the stator MMF of an actual stator as a range of Fourier transferred harmonics is fed into the current sheet to obtain the same torque output. Torque responses to various harmonic inputs can be analysed.

The current input for each coil is calculated analytically from the tangential magnetic field harmonics of the stator, the details were previously presented in [104]. The stator harmonic spectra of model A (ISDW) and D (FSCW) for the current input are demonstrated in Figure 5-8. The harmonic contents are much richer in the FSCW.

To validate this method, the comparative results of the alignment torque at $\beta = 0^\circ$ and the reluctance torque at $\beta = -45^\circ$ in model D are shown in Figure 5-9 and Figure 5-10, respectively. The blue line is the result from the model with the actual stator and the red line is from the current sheet one. The current sheet model can represent the actual stator model at a satisfactory level of accuracy.

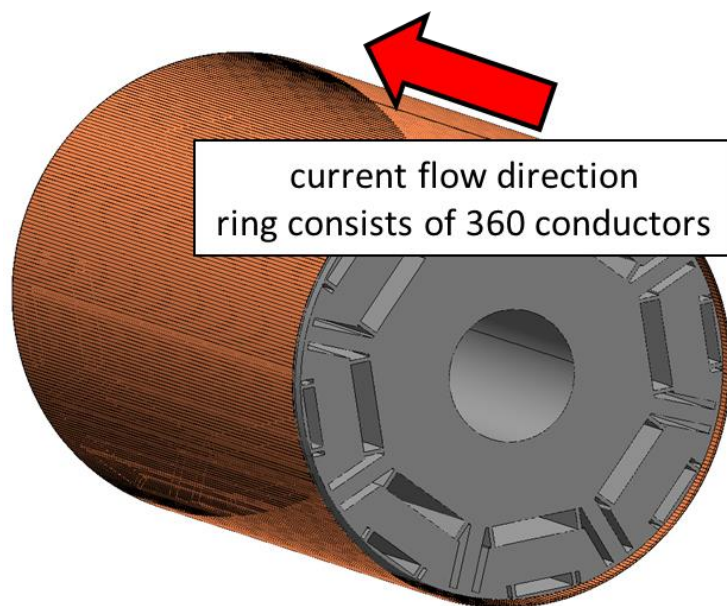


Figure 5-7 Current sheet model

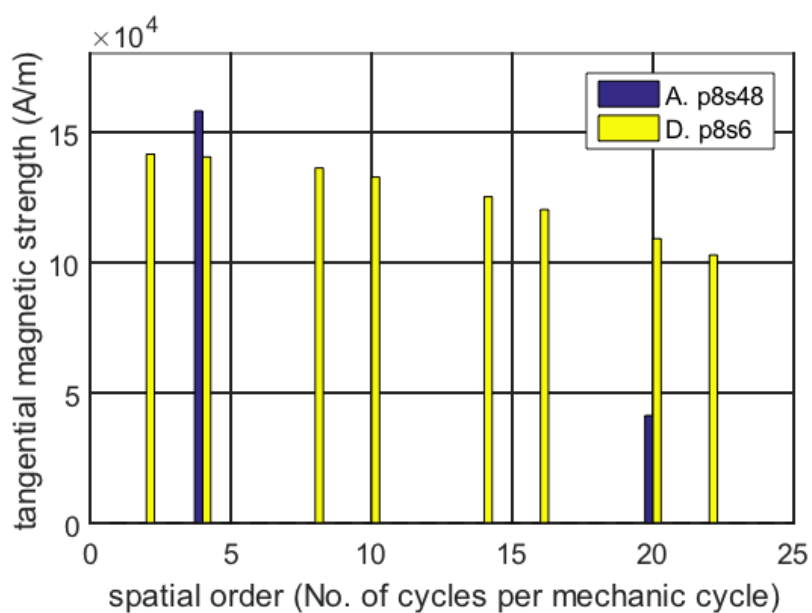


Figure 5-8 Stator H_t harmonic spectra

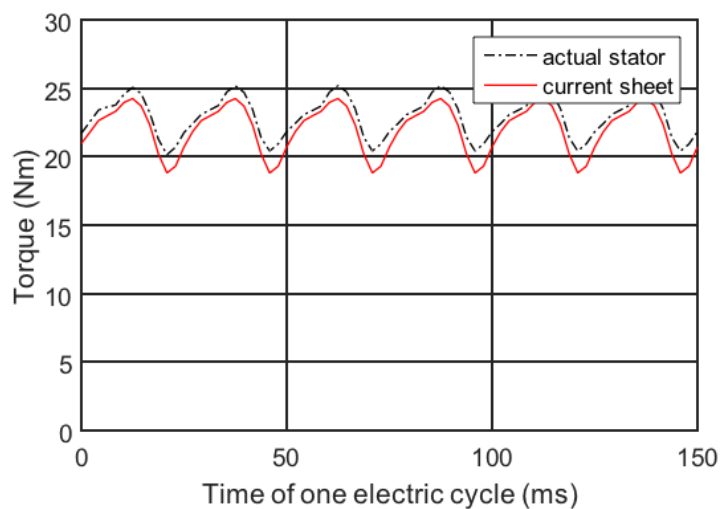


Figure 5-9 Torque vs. time with maximum alignment torque of model D

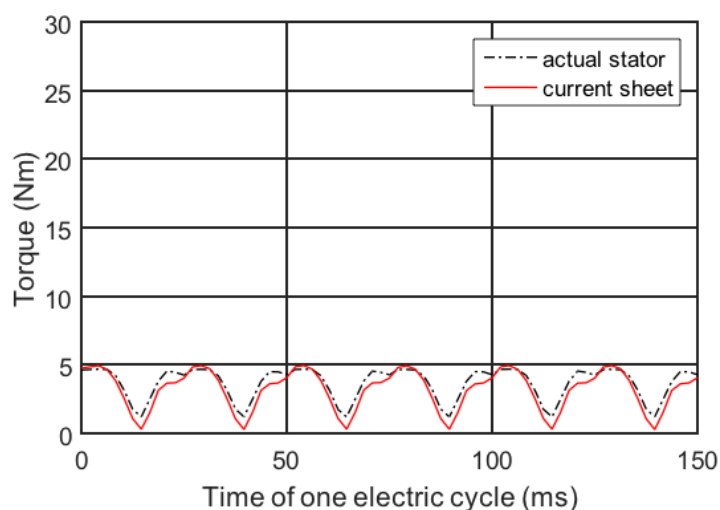


Figure 5-10 Torque against time with reluctance torque of model D

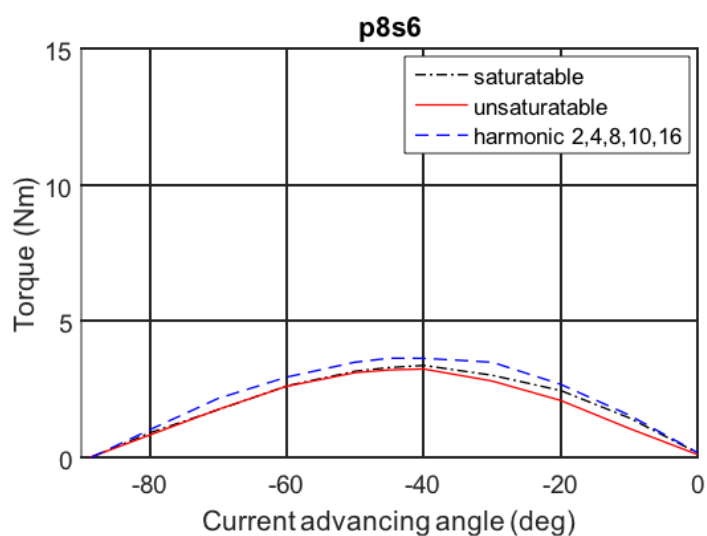


Figure 5-11 Torque against the current advancing angle from three models of current sheet

As described in 3.3.1, after injecting various ranges and combinations of harmonics into the current sheet model, certain groups of harmonics that can cause torque reduction are located. The graph of the time average torque against the current advancing angle is plotted for three FSCW models in Figure 5-14. Notice, due to a clean harmonic spectrum, there is virtually no torque reduction in the ISDW model.

Shown as the black line in Figure 5-12, the reluctance torque of the full stator MMF harmonics is firstly reduced to its essential harmonics (4, 8, 16, 20, 28) with little change of its value compared to the full range result. The torque against current advancing angle curve from the essential harmonics is also plotted in Figure 5-11 to prove it contributes to the majority of the total torque. Then the essential harmonics are broken into three parts:

- The main torque producing harmonic (4^{th}), which rotates synchronously with the rotor;
- The $8^{\text{th}}+16^{\text{th}}$ harmonic group;
- The $20^{\text{th}}+28^{\text{th}}$ harmonic group.

Both of the last two groups reduce the reluctance torque generated by the first part. The same phenomenon is found in the other two FSCW models but for different harmonics. Furthermore, as is found in [139], two stator harmonics interact with the saliency of the secondary rotor and generate torque ripple. Similarly, it can be proven that the reluctance torque is reduced by the interaction between the two stator harmonics and the first rotor saliency.

It is clear now there are certain harmonic groups in the rich harmonic contents of FSCWs that worsen the reluctance torque. In order to understand this effect in greater detail and predict how it varies with different parameters and in different FSCWs, the analytical expression will be deduced and general rules of the interaction summarised in the next two sections.

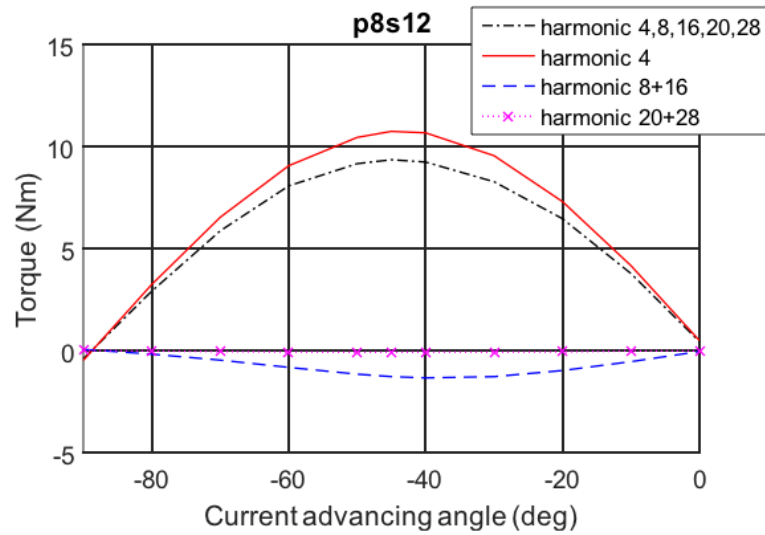


Figure 5-12 Torque components breakdown in the p8s12 FSCW

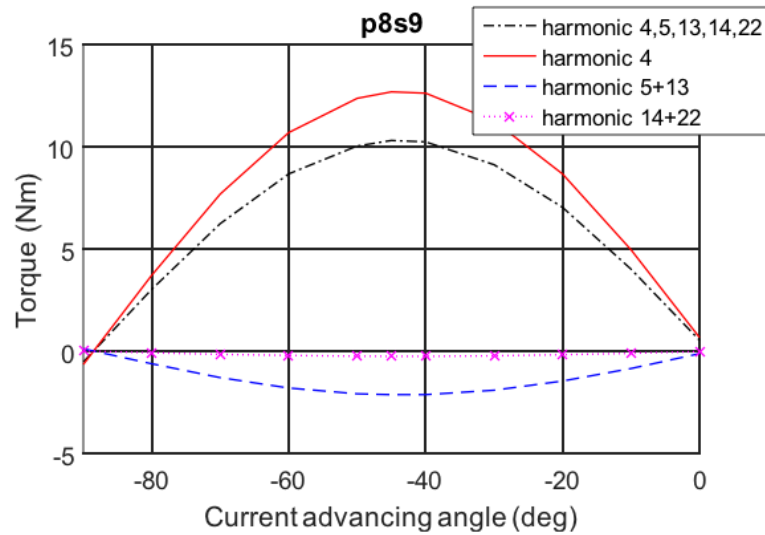


Figure 5-13 Torque components breakdown in the p8s9 FSCW

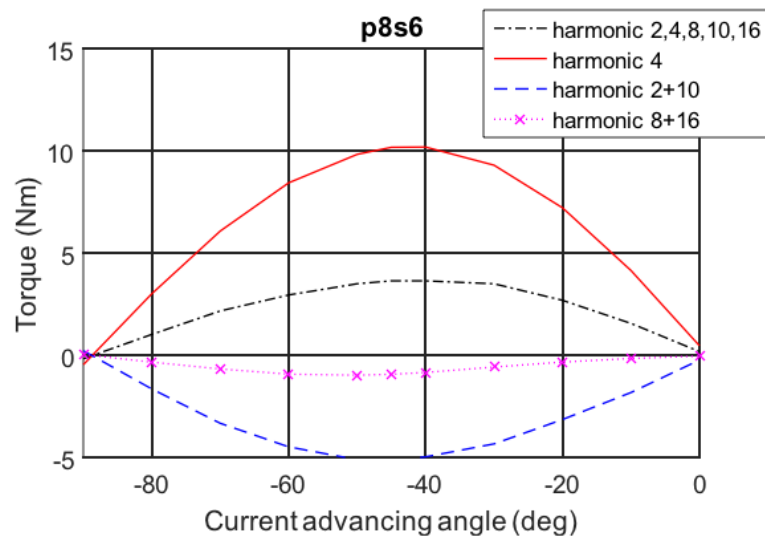


Figure 5-14 Torque components breakdown in the p8s6 FSCW

5.2.3. The analytical expression on the flux across the air gap

In this section, an analytical expression to calculate the magnetic flux across the air gap in the radial direction is developed.

To start with, the classic torque calculation based on Maxwell's stress tensor equation is laid out in eq. (11.1-3) taken from [140]. The tangential stress tensor from the v th magnetic field harmonic is σ_t^v . It is related to both the tangential magnetic field H_t^v and the normal (radially crossing the air gap) magnetic flux density B_n^v . The torque can then be obtained by integrating the stress tensor around the air gap circumference with radius r_{ag} and stack length l_{stk} .

$$\begin{cases} \sigma_t^v(\theta) = B_n^v \cdot H_t^v \\ \sigma_t(\theta) = \sum_{v=1}^{\infty} \sigma_t^v(\theta) \end{cases} \quad (5.1)$$

$$T = l_{stk} \cdot r_{ag} \sum_{v=1}^{\infty} \int_0^{2\pi} \sigma_t(\theta) \cdot r_{ag} d\theta \quad (5.2)$$

$$\begin{cases} H_t^m = h^m \sin(m\theta + \theta_t^m) \\ B_n^n = b^n \sin(n\theta + \theta_n^n) \end{cases} \quad (5.3)$$

The key point here is that in order to have a non-zero value torque, the B_n and H_t , which are defined in eq. (5.3), need to be at the same spatial order meaning ' $m = n$ '. Only by meeting this requirement, can the spatial variable ' $m\theta$ ' be cancelled out after carrying out a trigonometric multiplication in eq. (5.1). Otherwise, after integration over 2π in eq. (5.2) it would result in zero torque value.

The H_t is known from the stator current input. Normally, the B_n is provided from the rotor magnets, but, in the reluctance torque case, it is from the interaction between the rotor saliency and the H_t . Eq. (5.4) is proposed for this calculation. The idea behind this equation is to change the route the flux travelled from a circumferential to a radial direction.

The reciprocal of the air gap distance l_{ag} can be defined as Fourier series in eq. (5.5). p is the number of rotor pole pair.

$$\begin{aligned}
B_n^v &= u_o \frac{MMF_v}{2l_{ag}} = \int_{\theta-\frac{\pi}{v}}^{\theta} H_t^v \cdot r d\theta \cdot \frac{u_o}{2l_{ag}} \\
&= -\frac{u_o r}{2v} H_t^v \cdot \cos(v\theta \pm \omega_e t + \theta_v) * \frac{1}{l_{ag}}
\end{aligned} \tag{5.4}$$

$$\frac{1}{l_{ag}} = a + \sum_{v=1}^{\infty} r^v \sin(v2p\theta - 2v\omega_e t + \theta_r^v) \tag{5.5}$$

To test this expression, it is compared with the current sheet method of FEA and results are illustrated in Figure 5-15. The rotor used in (a.) is an outer salient rotor with a sinusoidally varying air gap distance of 16 cycles, i.e. the 2nd rotor saliency of an 8 pole rotor. The input is 2nd tangential magnetic field strength H_t . In part (b), the input is changed to the 1st H_t harmonic and the number of rotor cycles is halved to 8 (the 1st rotor saliency). Then input H_t harmonics are combined in part (c), and a square rotor saliency is used in part (d).

In all of these tests, the analytically calculated H_n curves are closely matched with the FE results in terms of both phase and magnitude.

After the information of B_n is obtained, the torque can then be calculated using eq. (11.1-3). Verification and more details of this torque calculation method can be found in [136]. , The torque calculation of the p8s9 FSCW is deduced in the next section in an aim to understand the effect of each parameter in this torque reduction phenomenon.

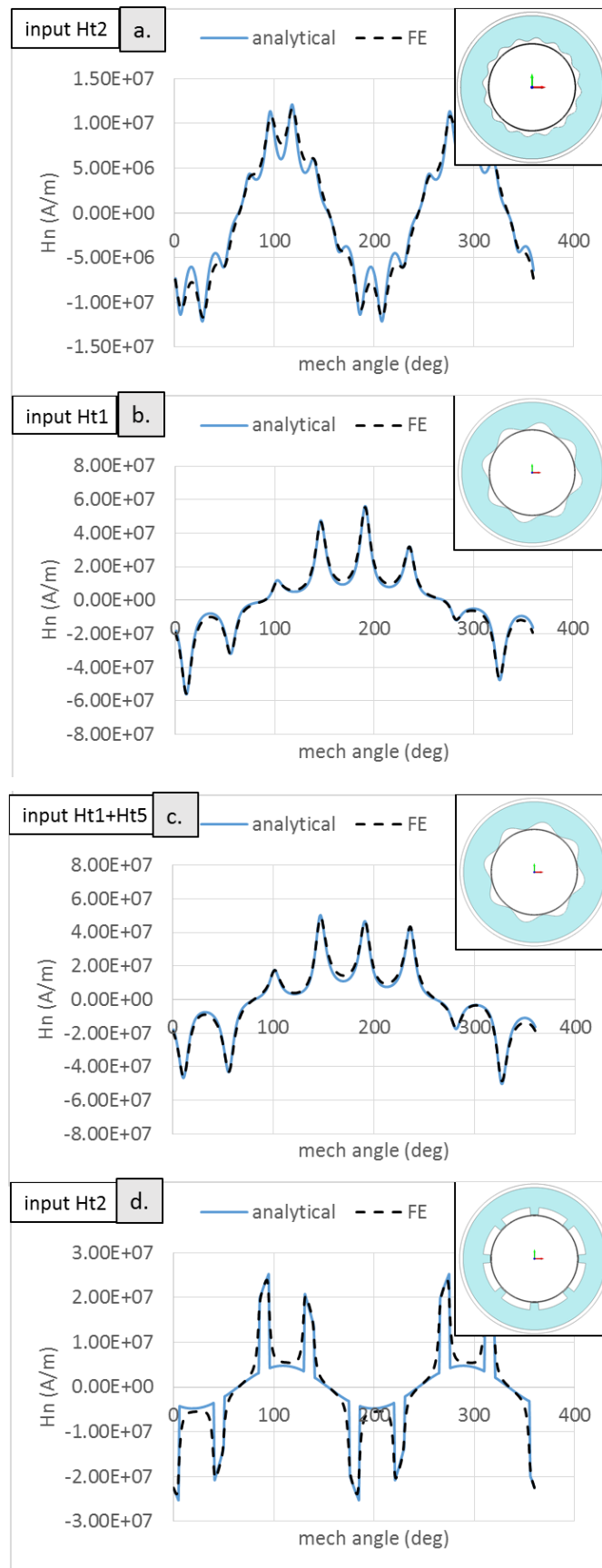


Figure 5-15 H_n curve comparison between FE and analytical calculation

5.2.4. General rules of stator harmonic interaction

The 5th+13th harmonic group in the p8s9

This harmonic group develops a negative time average torque opposite to the reluctance torque when interacting with the 1st rotor saliency. These harmonics are defined as:

$$\begin{cases} H_t^5 = h^5 \sin(5\theta + \omega_e t + \theta_t^5) \\ H_t^{13} = h^{13} \sin(13\theta - \omega_e t + \theta_n^{13}) \\ (1/l_{ag})^{v=1} = r^1 * \sin(8\theta - 2\omega_e t + \theta_r^1) \end{cases} \quad (5.6)$$

The rotating direction varies in Ht harmonics ('+' in the 5th and '-' in the 13th) but the speed is synchronised with the rotating rotor and fixed at ω_e . In the rotor saliency harmonic, the speed is proportional to the spatial order and it is doubled for the 1st harmonic compared to the Ht speed. Its direction is fixed to the physical rotor rotating direction and is always '-'.

In the classic trigonometric identity equation eq. (5.7), when two sine waves multiply, two new sine waves appear in addition. By putting the spatial term in, it means that the 5th Ht can interact with the 1st rotor saliency in order to raise the Bn of the 13th spatial order. This is the same for the 13th Ht. Hence, two torque components can be generated.

$$\begin{cases} \sin(x) \cos(y) = \frac{1}{2} (\sin(x+y) + \sin(x-y)) \\ \sin(x) \sin(y) = \frac{1}{2} (\cos(x-y) - \cos(x+y)) \end{cases} \quad (5.7)$$

To calculate the first torque component, the B_n is obtained by eq. (5.4), from which the 5th harmonic is first integrated and then multiplied by the rotor saliency. The result of the 13th order B_n is shown on the left side in eq. (5.8). Next, the multiplication of the 13th H_t and B_n is shown in eq. (5.9). The spatial variable 13 θ is cancelled out. With the term on the right side of eq. (5.9), a constant negative torque over time can be obtained. In these two equations, both variables K and L do not depend on the harmonic number.

$$B_n^{r+5} = -\frac{1}{5} h^5 r^1 \sin(13\theta - \omega_e t + \theta_t^5 + \theta_r^1) K \quad (5.8)$$

$$B_n^{5*r} H_t^{13} = -\frac{1}{5} h^5 h^{13} r^1 \cos(\theta_t^5 + \theta_r^1 - \theta_t^{13}) L \quad (5.9)$$

The second torque component is positive in sign and smaller in magnitude compared to the first one due to the smaller coefficient '1/13'.

$$B_n^{r-13} = -\frac{1}{13} h^{13} r^1 \sin(-5\theta - \omega_e t + \theta_r^1 - \theta_t^{13}) K \quad (5.10)$$

$$B_n^{13-r} H_t^5 = \frac{1}{13} h^5 h^{13} r^1 \cos(\theta_t^5 + \theta_r^1 - \theta_t^{13}) L \quad (5.11)$$

When adding up these two components, the total torque for this harmonic group is negative assuming the cosine term is positive.

The same calculation for the main harmonic (4th), the reluctance torque producing harmonic, is also conducted and the result is shown in eq. (11.12,13). Its value is positive.

$$B_n^{r-4} = -\frac{1}{4} h^4 r^1 \sin(4\theta - \omega_e t + \theta_r^1 - \theta_t^4) K \quad (5.12)$$

$$B_n^{r-4} H_t^4 = \frac{1}{4} h^4 h^4 r^1 \cos(\theta_r^1 - 2\theta_t^4 + 180) L \quad (5.13)$$

Here the angle ' $-2\theta_t^4 + 180$ ' equals to ' $\theta_t^5 - \theta_t^{13}$ ', meaning the reduction torque generated by the harmonic group is always opposite to the reluctance torque generated by the main harmonic.

The general rules

The general rules of this stator MMF harmonic caused torque reduction phenomenon are summarized as:

- All slot harmonics defined in eq. (5.14) can generate the reduction torque and their magnitudes are relatively high. N_s is the number of the stator slot.

$$v_s = n \cdot N_s \pm p (n = 0, 1, 2 \dots) \quad (5.14)$$

In the case of the p8s9, they are the: 4th, 5th, 13th, 14th...

- The rest of the harmonics, are negligible although they can generate the time average torque. This is because they are low in magnitude, as illustrated in the small spikes between the slot harmonics in Figure 5-16.

- The combination of the harmonic group is always that the lower harmonic rotates opposite to the main harmonic and the higher one rotates with the main harmonic. The spatial order difference should be the same as the order of the first rotor saliency.

In the case of the p8s9, they are the: 5th+13th, 14th+22nd, 23rd+31st...

- The angle of the cosine term in the reduction torque, i.e. $\cos(\theta_t^5 + \theta_r^1 - \theta_t^{13})$ in eq.(9), is always equal to the term in the main reluctance torque, i.e. $\cos(\theta_r^1 - 2\theta_t^4 + 180)$ in eq.(13), for all slot harmonic groups.

This means all torque components including the reluctance torque vary with ' θ_r^1 ' at the same rate. When the main reluctance torque reaches its maximum value, the reduction torque is also at its minimum value. To prove angle equality, one can start from the Ht harmonic equation proposed in the author's earlier paper [104].

- There is a reciprocal term of the spatial order of the harmonic in the calculated Bn, which means that the higher the spatial order of the stator harmonic the lower the reduction torque it can generate is.

In the case of the p8s9, p8s6 and p8s12, only the first 2 harmonic groups have any observable reduction effect on the main reluctance torque.

- The slot opening also affects torque reduction as stated in [139]: the wider the slot opening, the more rapidly the harmonic magnitude will drop when increasing the harmonic spatial order. This phenomenon only affects the higher order harmonics, the main harmonic and the lower ones remain virtually the same.

As can be seen from the stator harmonic Ht spectra of the three FSCW models in Figure 5-16, the magnitude of the slot harmonics in the p8s6 drops much more slowly than the other two models due to having a much smaller slot opening design. This results in a much higher reduction torque and lower reluctance torque in the p8s6 model compared to other two FSCWs.

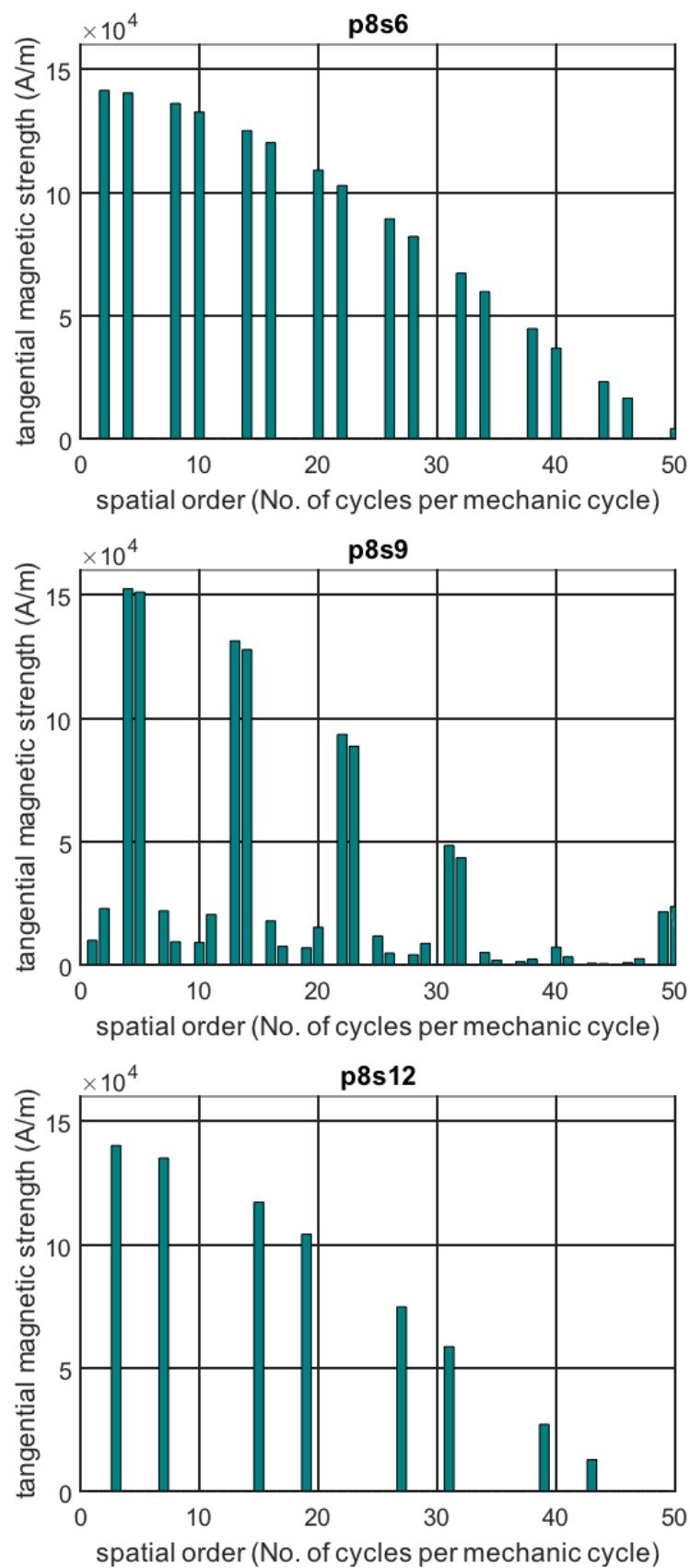


Figure 5-16 Stator harmonic spectra of FSCWs

5.2.5.Design advice on mitigating the torque reduction effect

The torque reduction effect is the reason why the achievable reluctance torque is lower in most of the FSCWs compared to its distributed-winding counterpart. Besides the aforementioned methods to reduce the harmonic content, two additional pieces of design advice are given to help minimise this effect:

Select FSCWs with the right pole to slot ratio. For instance, when it is $2/3$, e.g. p4s6, p8s12, p10s15 etc. FSCWs have a much cleaner harmonic spectrum as is shown in Figure 5-16. It means that the harmonic groups are shifted further to the right on the harmonic spectrum compared to other FSCWs, in other words, a lower torque reduction. However, this type of FSCW generally possesses a higher torque ripple. Hence a careful selection of pole-slot combination needs to be made depending on the motor application.

Having a wider slot-opening design will reduce both the torque reduction effect and the 6th order torque ripple [139] caused by rich stator harmonics.

5.2.6.Conclusion

This section gives an explicit explanation of the well know phenomenon that fractional-slot concentrated-winding machines cannot achieve the same level of reluctance torque compared to integral-slot distributed-winding machines with the same salient rotor. The reluctance torque in FSCWs has been compared to that of ISDW. It is much lower in FSCWs. This is due to the interaction between certain harmonic groups and the 1st rotor saliency. The analytical expression for flux in a normal direction is then devised in order for the stator harmonic model to cooperate with with the classic Maxwell stress equation. General rules about this reduction torque have been given. Besides the existing methods to reduce the stator harmonics, two additional pieces of advice are given for designing FSCWs with a better reluctance torque: 1. FSCWs with a pole-slot ratio of $2/3$ are particularly good at achieving high reluctance torque due to clean harmonic content; 2. A wider slot opening design can also help to improve the reluctance torque level in FCSWs.

5.3. Torque ripple analysis

When equipped with an anisotropic rotor, its torque ripple is higher than FSCWs without rotor saliency. As discussed in chapter 3, the one with a V-shaped rotor has a torque ripple of 4%, which is double the one with the surface-mounted rotor (2%), shown in Figure 5-17. Also, for a synchronous reluctance machine with FSCW used in [136], its torque ripple is also much more significant compared to a distributed-winding one. Hence, there should be a type of torque ripple stemmed from the interaction between stator harmonics and rotor saliency.

Torque ripple can be separated into two components:

- Torque ripple resulting from the interaction between stator saliency and rotor magnets - cogging torque;
- Torque ripple resulting from the interaction between rotor saliency and stator MMF harmonics (RSSH).

Cogging torque is well understood, but the underlying origin of the RSSH torque ripple remains unclear. FSCWs, like those in [126, 141-146], tend to produce a 6th harmonic torque ripple per electric cycle. With many winding configurations, such as those with three teeth per pole pair, there is a large, backwards rotating, 2nd harmonic stator winding MMF produced. If the rotor has a 2nd harmonic of saliency, then this harmonic interacts with the rotor to produce the observed torque ripple. However, the 9slot, 8pole machine in question does not have a second harmonic MMF and so another source must exist.

Methods have been evolved to reduce this torque ripple by reducing the stator harmonics as described in section 11.1. However, most of the methods attempt to suppress stator harmonics indistinguishably and there is no existing paper that has been able to identify the exact harmonic(s) that cause this peculiar torque ripple. Hence, the aim of this chapter is to explain the mechanism of this particular torque ripple and propose new means of torque reduction based on deeper insight.

This section is organised as follows: In section 1, the RSSH torque ripple is discussed and an analytical model is developed based on two cases of different slot/pole combination. The rules and principles that govern the RSSH torque ripple are summarised. In section 2, an index indicating the RSSH torque ripple magnitude in any FSCW is introduced and a guidance table for slot/pole number selection including this index in FSCWs is proposed. The analytical predictions are then verified by finite element analysis (FEA) in both actual

stator and current sheet represented models. In section 3, using the guidance table, the pole number of an existing V shape in-wheel design is modified to reduce the RSSH torque ripple and the effectiveness of skewing is assessed via FEA. In the last section, the influence of the width of the slot opening, is investigated.

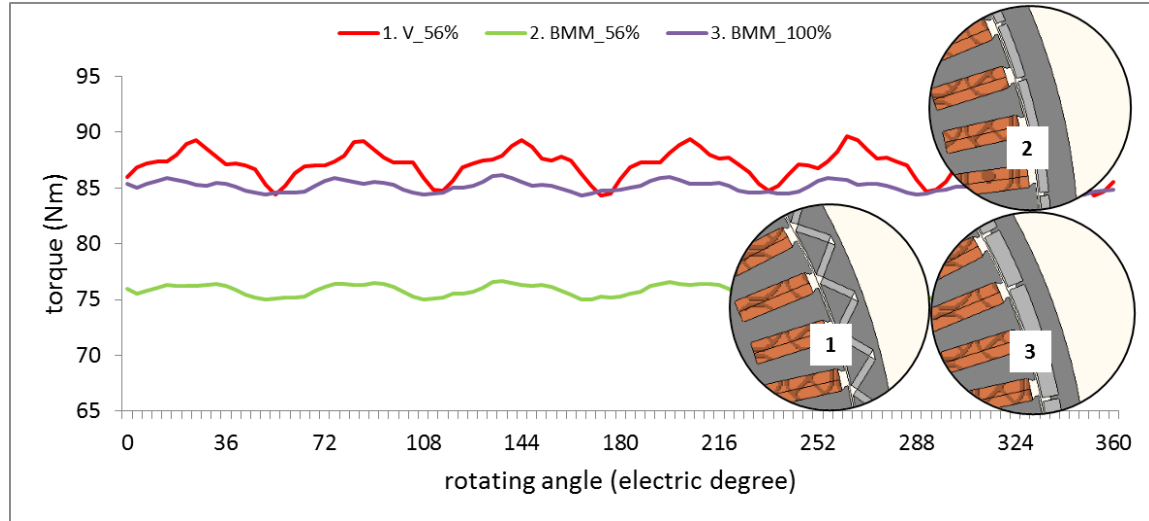


Figure 5-17 Rated torque comparison between 1. V-shaped design with 56% magnet mass, 2. benchmark motor with 56% magnet mass and 3. benchmark motor with 100% magnet mass of 1/8 of the BMM in-wheel motor. Current input condition: $I_q = 30A$ peak, $I_d = 0A$ (rated load)

1.1.1. The RSSH torque ripple forming mechanism

FE analysis using the current sheet method

The origin of this torque ripple has been carefully investigated as follows:

- Through modelling the motor with un magnetized magnets and observing that the torque ripple remained, it was established that torque ripple is related to the salient nature of the rotor.
- A finite element model was created with the stator replaced by a current sheet which contained all the spatial harmonics of the MMF created by the windings. Once more the torque ripple remained, indicating that the cogging torque was not the source.
- Each of the spatial harmonics created by stator winding were applied in turn. However, none of these harmonics in isolation produced any torque ripple. Torque ripple only resulted when certain pairs of spatial harmonic were applied together.

From the above, it became clear that torque is produced through two spatial harmonics of different pole numbers interacting via the saliency of the rotor. This is closely analogous to torque production in doubly fed reluctance machines [147] and magnetic gearing machines [148-150]. Each harmonic interacts with the salient rotor to produce two magnetic flux (B_n) harmonics flowing normally across the air gap: one with pole number equal to the sum of the MMF harmonic order and the order of the rotor saliency, and the other equal to the difference. The resulting B_n harmonics can then interact with another stator harmonic, H_t , of the same spatial order to produce torque or torque ripple, depending on the rotating direction of these two fields.

To verify the explained mechanism, a machine with nine slots for every 8 poles and a fractional slot, concentrated winding (FSCW) are analysed. The FE model is illustrated as model O in Figure 5-18. Model A replaces the iron with an infinitely permeable iron neglecting saturation effect to simplify the analysis.

The stator is replaced by a current sheet in model B, as outlined above. The full harmonic spectrum of this FSCW and an explanation of the current sheet method is given in [104]. Figure 5-19 shows the spectrum of harmonics produced by the winding, including both sub and super harmonics of the torque producing 8 pole field.

After testing various harmonic groups, it was deduced that two pairs of the stator H_t harmonic groups are responsible for torque ripple. These are:

- a. The combination of the 2 pole pair and 14 pole pair harmonics.
- b. The combination of the 5 pole pairs and 11 pole pair harmonics.

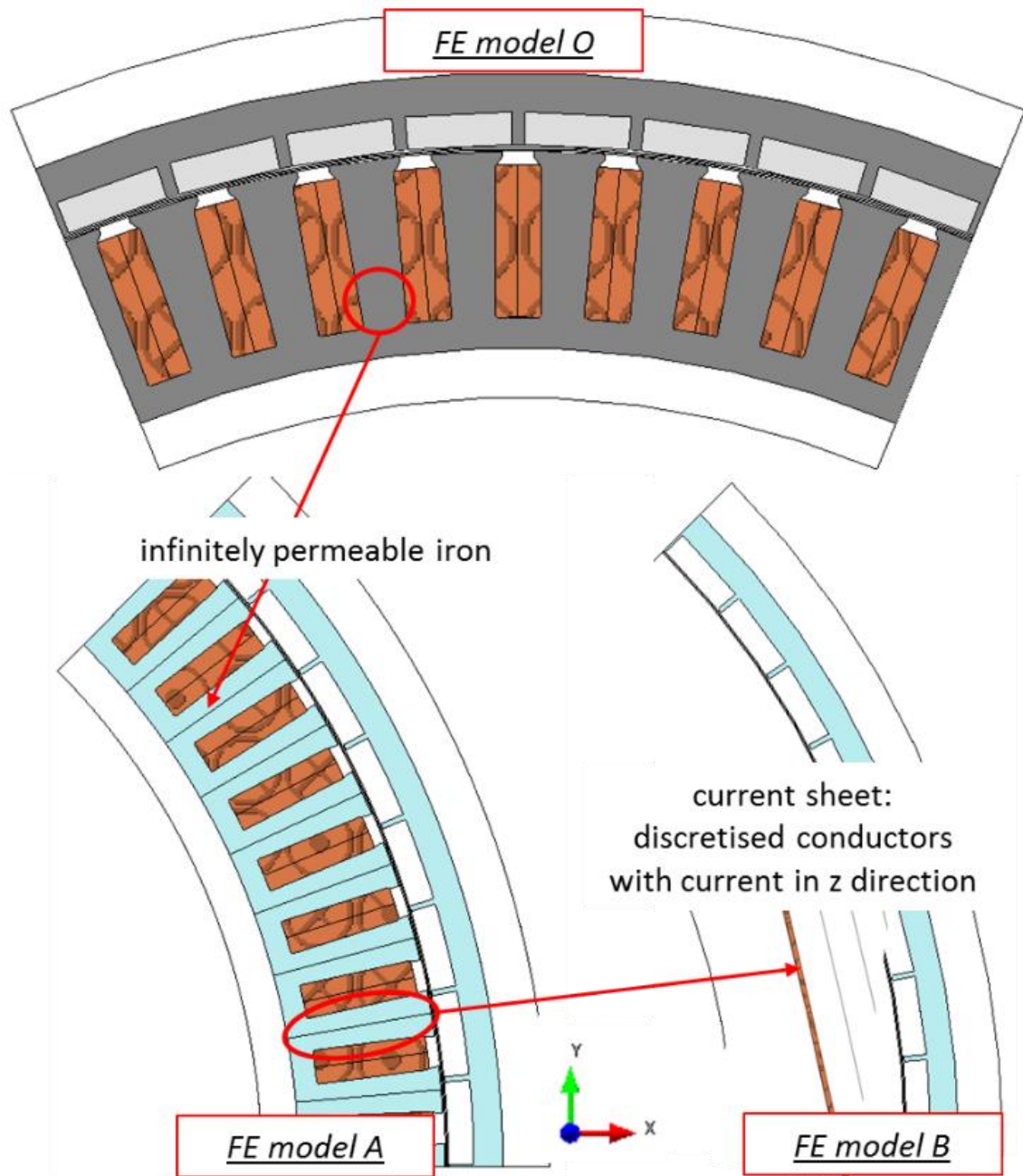


Figure 5-18 Model O – the original FE model from [43]; model A – the simplified model; model B – the current sheet converted model

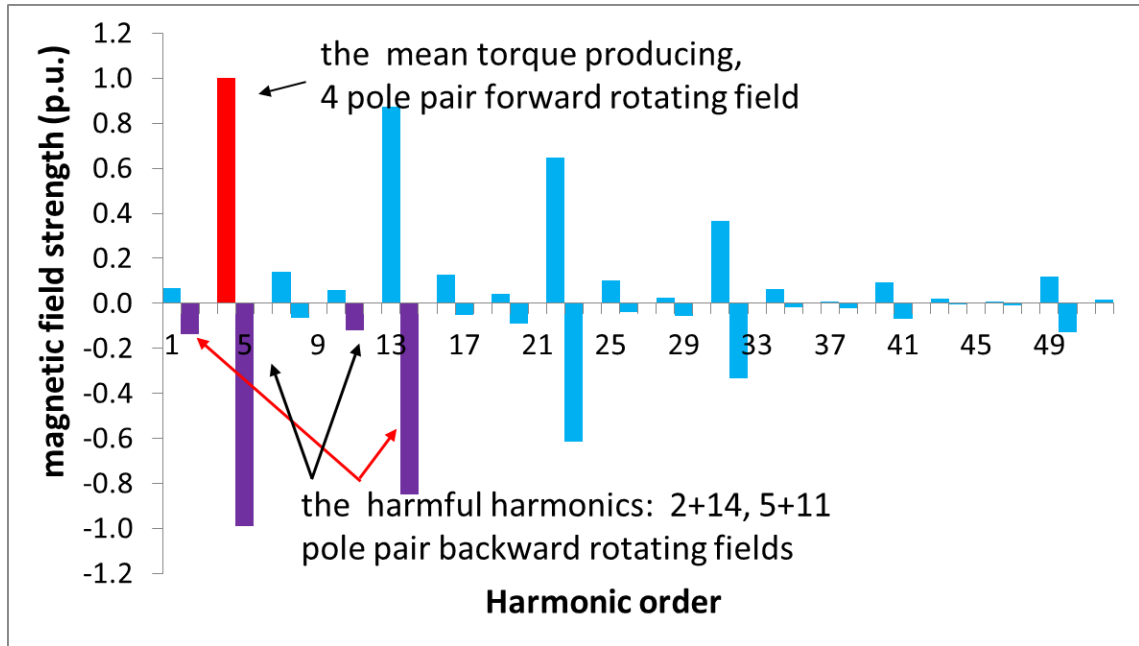


Figure 5-19 The spatial harmonics of magnetising field strength created by the model A shown in Figure 518

It was not immediately obvious how the rotor saliency could produce the interaction observed. To aid understanding, the rotor was replaced with one which had a sinusoidally varying air-gap, seen in Figure 5-20, hence almost eliminating any spatial harmonics of saliency. This revealed that the fundamental component of saliency does not give rise to the torque ripple – it is the second harmonic of saliency which is responsible. This saliency has 16 cycles per revolution i.e. it is a 16 pole pair variation.

The torque ripple comparison between these harmonics in model B and the full range of harmonics in model A is given in Figure 5-21, indicating the validity of the current sheet model and how it is simply these harmonics producing torque ripple.

In essence, the 2 pole pair, backwards rotating H field interacts with the forward rotating 16 pole pair rotor saliency harmonic to produce a 14 pole and an 18 pole resultant air-gap flux density. The 14 pole flux density then interacts with the 14 pole H field generated by stator winding to produce torque. Because the two 14 pole fields are not rotating synchronously the resultant torque from their interaction is oscillatory.

A similar situation works with the 5 pole pair harmonic, which interacts with the 16 pole pair rotor saliency to produce 11 and 21 pole pair flux densities. The 11 pole pair flux density interacts with the 11th harmonic MMF to produce torque ripple.

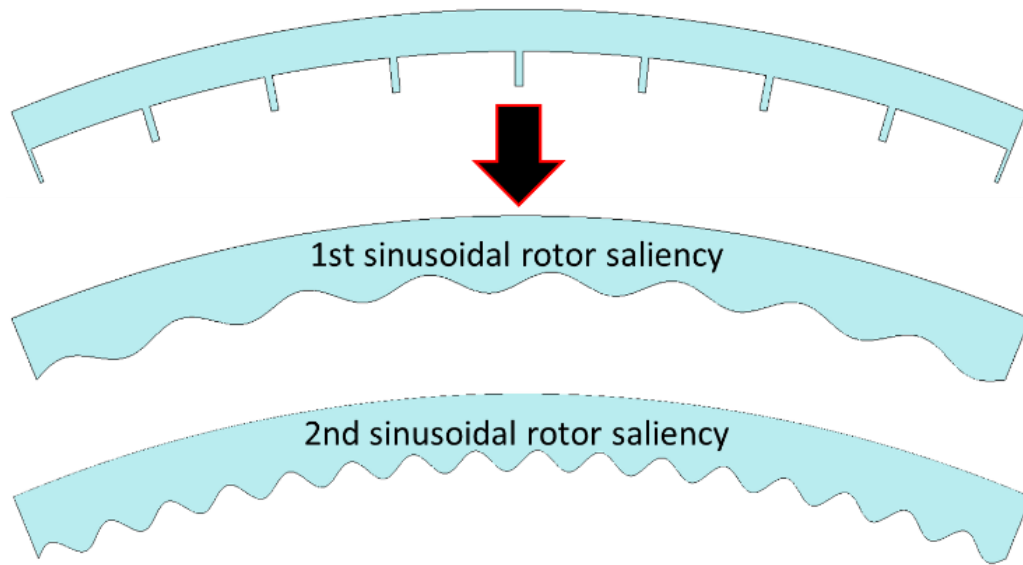


Figure 5-20 The sinusoidal rotor

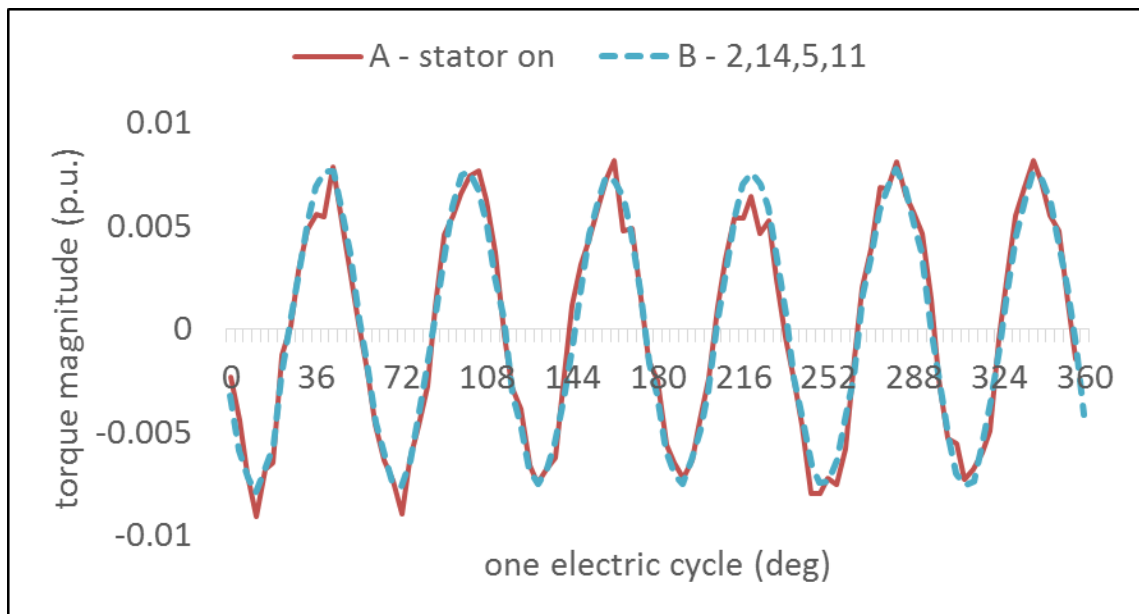


Figure 5-21 Torque ripple comparison between model A and B

In Figure 5-22, the magnitude of individual stator harmonics from this 9slot 8pole (s9p8) FSCW is shown. The main stator (4th) harmonic links to the 8 pole rotor field to produce the mean torque. The two groups of stator harmonics in this s9p8 FSCW which can be modulated by the 2nd order rotor saliency harmonic forming the 6th order RSSH torque ripple are marked out by dotted black lines. Each group contains one from the left side of the 1st rotor saliency and one from the right side of it. To support the FEA, the analytical model of the torque ripple is derived and demonstrated on two cases with a different slot-pole combination.

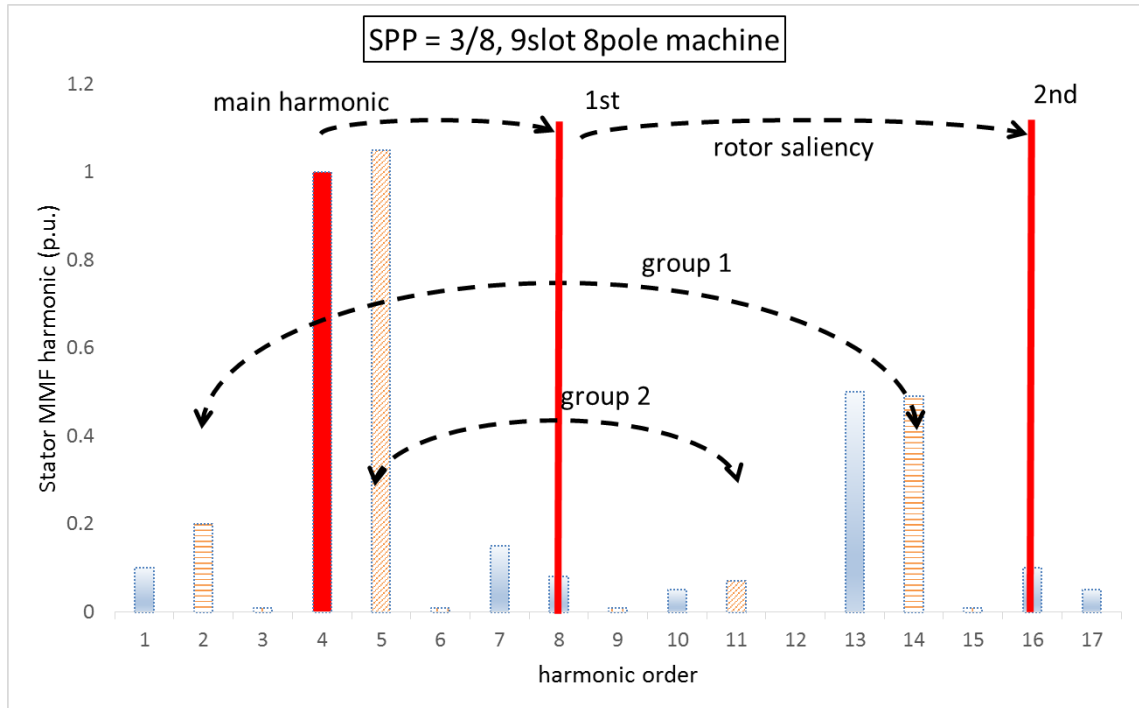


Figure 5-22 The stator H_t harmonic spectrum of the s9p8 machine

The analytical explanation

The normal field

Seen from Figure 5-23, the stator MMF can induce magnetic flux flowing in both tangential and normal directions in the air gap. The tangential field travel path shown using a blue line is identical in both non-salient and salient cases. However, the permeance of the normal field in these two cases is different. In the salient case, the salient air gap permeance is a function varying with rotor position and it modulates both the spatial and temporal frequency of the MMF source field. The resultant normal field would then interact with the tangential field generating torque or/and torque ripple. However, in the non-salient case, the permeance is a constant and there is no modulation effect. The normal field is 90° phase shifted from the tangential field and the inaction between these two gives no torque output.

The temporal frequency

The rotating speed (m/s) of the stator harmonic is inversely proportional to its wavelength due to a fixed electric frequency from the phase current, ω_e rad/s shown in eq. (5.15). For instance, the 2nd stator harmonic travels double the distance along the circumferential direction in the air gap compared to the 4th harmonic in a given period of time. However, the rotating speed of the rotor saliency harmonic is fixed with the rotor's mechanical

rotating speed. The rotor saliency's spatial frequency is two times higher than the rotor magnetic field, i.e. one rotor pole forms a full cycle of the rotor saliency. For the 2nd rotor saliency ($\nu = 2$), it pulsates at four times the stator harmonic rate which is $4\omega_e$ rad/s, again shown in the last line of eq. (5.15). To make the torque output vary with time, there is a certain way to arrive at the 6th order torque ripple. Here are two case examples.

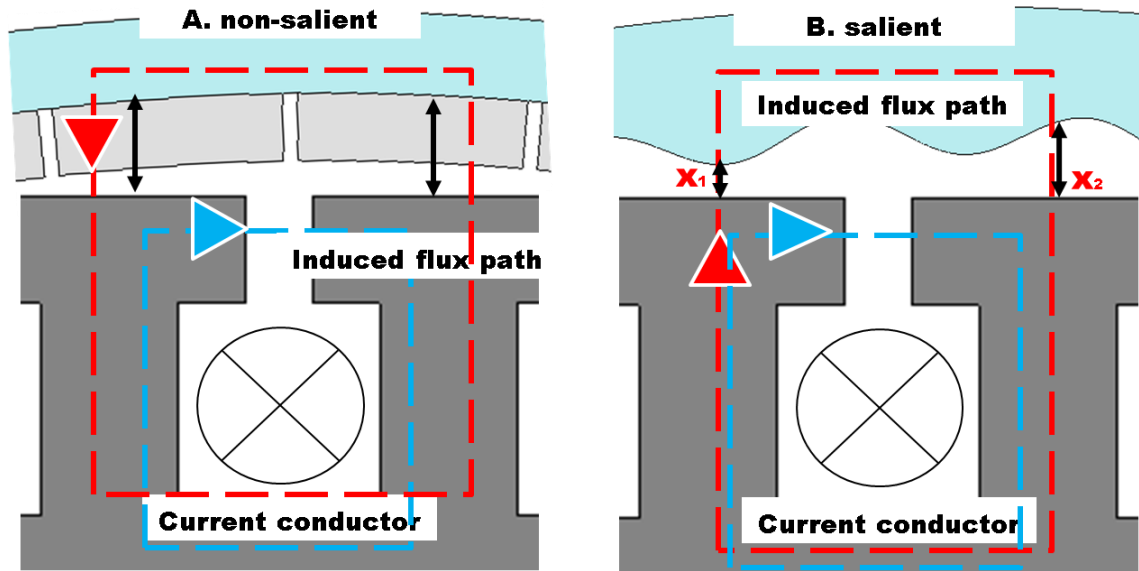


Figure 5-23 The magnetic field strength H defined in non-salient and salient cases

Case A – torque ripple in an s9p8 FSCW

Take the 2nd+14th of the slot9 pole8 FSCW shown in Figure 5-19 as an example:

The 2nd and 14th of the stator harmonic and the 2nd rotor saliency are defined in eq. (5.15). To form the normal field, both of the stator harmonics are first integrated and then multiplied by the rotor saliency, in which their spatial and temporal frequencies are modulated obeying the trigonometric identities law in eq. (5.7). The resultant normal field is presented in eq. (5.16). K is a variable that doesn't depend on the harmonic order. Then these two B_n would interact with H_t with the same spatial frequency to generate the 6th order torque ripple. Eq. (5.17) is the exact torque ripple expression showing the temporal frequency term $6\omega_e t$. The second group of harmonics, 5th+11th, works under the same principle.

$$\begin{cases} H_t^2 = \sin(2\theta + \omega_e t + \theta_t^2) \\ H_t^{14} = \sin(14\theta + \omega_e t + \theta_t^{14}) \\ (1/l_{ag})^{v=2} = r^2 * \sin(16\theta - 4\omega_e t + \theta_r^2) \end{cases} \quad (5.15)$$

$$\begin{cases} B_n^{r+2} = \frac{K}{2} [\sin(-14\theta + 5\omega_e t - \theta_t^2 + \theta_r^2)] \\ B_n^{r+14} = \frac{K}{14} [\sin(-2\theta + 5\omega_e t - \theta_t^{14} + \theta_r^2)] \end{cases} \quad (5.16)$$

$$T_{2,14} = -\frac{16u_0 r_{ag}^3 \pi \hat{K}_{14} \hat{K}_2 C}{2l_{stk} \cdot (14.2)} \cos(6\omega_e t + \theta_{2+14-r}) \quad (5.17)$$

Case B - torque ripple in an s6p4 FSCW

A much larger stator torque ripple can be found in the s6p4 FSCWs with rotor saliency. Using the current sheet FE method, the 2nd and 10th harmonics are found to be the RSSH torque ripple source with a harmonic spectrum shown in Figure 5-24. Their interaction with the rotor saliency can be summarised in eq. (5.18), (5.19).

$$\begin{cases} H_t^2 = \sin(2\theta - \omega_e t + \theta_t^2) \\ H_t^{10} = \sin(10\theta + \omega_e t + \theta_t^{14}) \\ (1/l_{ag})^{v=2} = r^2 * \sin(8\theta - 4\omega_e t + \theta_r^2) \end{cases} \quad (5.18)$$

$$\begin{cases} B_n^{r+2} = \frac{K}{2} [\sin(10\theta - 5\omega_e t + \theta_t^2 + \theta_r^2)] \\ B_n^{r-10} = \frac{K}{10} [\sin(-2\theta - 5\omega_e t - \theta_t^{10} + \theta_r^2)] \end{cases} \quad (5.19)$$

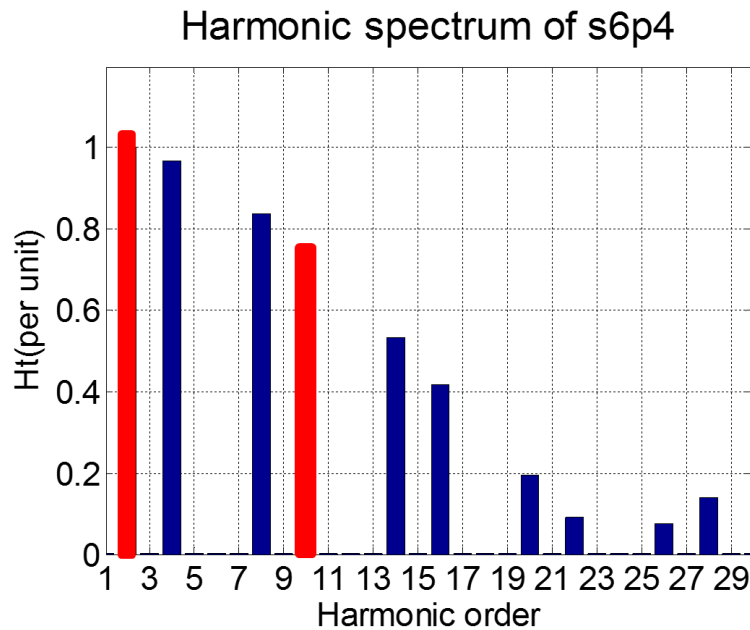


Figure 5-24 Stator harmonic spectrum of a s9p4 FSCW

1.1.2.Rules for RSSH torque ripple

Modulation classification

As can be seen from these cases, there can be several groups of harmonics generating the same frequency (6th) torque ripple. Each group consists of a pair of harmonics. There are two different modulations:

Mod A

In this type of modulation, the two working harmonics must rotate against the main harmonic. The rotating direction of every harmonic can be defined from Table 5-1. Furthermore, as illustrated in Figure 5-22, two working harmonics must sit on both sides of the fundamental rotor saliency and have equal distance to the fundamental which is a multiple of 3.

Table 5-1 Stator harmonic type

Type	Harmonic order	Rotate direction (+ / -)
a	$v_a = 3k + 1$	+
b	$v_b = 3k + 2$	-

Exception: FSCWs with rotor pole pair = 3, 6, 9..., in which the harmonic order in odd multiples of 3 rotates in one direction and the harmonic order in even multiple of 3 rotates in the opposite direction

The relationship between the rotor saliency and working harmonics can be illustrated in Figure 5-25. Assuming the main harmonic, v_m , type a from Table 5-1 rotates clockwise with direction '+'. Then the second rotor saliency, ξ_2 , is defined and linked with the first working harmonic, v_1 , in type b. The second working harmonic, v_2 , can be obtained by subtraction.

Applying this process in the s9p8 FSCW, the 4th harmonic is the main harmonic and the 8th is the fundamental rotor saliency, ξ_1 , so the working harmonic group can be calculated as 5th + 11th (k=1) and 2nd + 14th (k=2). It matches with the FE simulation from the case study.

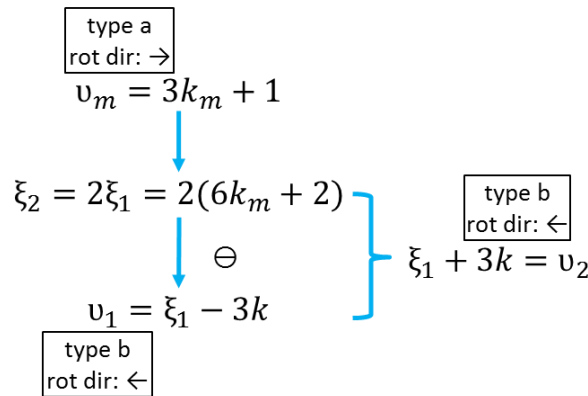


Figure 5-25 Rotor saliency modulation of type A

Mod B

In Mod B, one of the working harmonics is the main harmonic, v_m . The other working harmonic is in the order of 5 times the main harmonic, $5v_m$. The modulation process can be illustrated in Figure 5-26. This time, the interaction between the lower order working harmonic and the rotor saliency is not subtraction but addition.

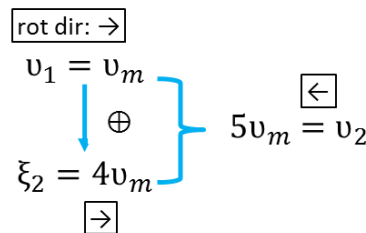


Figure 5-26 Rotor saliency modulation B

Applying this process in the s6p4 machine, the 2nd harmonic is the main harmonic, so the working harmonic group is the 2nd + 10th. It matches with what was found in case study B.

FSCW classification

The working harmonics in modulation B can have a relatively high magnitude as can be seen in Figure 5-24. They belong to the so-called ‘slot harmonic’ which is a group of harmonics sharing the same winding factor with the main harmonic and having high magnitudes. Only in FSCWs with $SP=3/(2k)$, can both working harmonics be slot harmonics. Hence, according to the SP value, FSCWs can be classified into two groups:

$$SP=3/(2k)$$

When $SP=3/2$ ($k=1$), there is no harmonic with a significant magnitude between the order of the main harmonic and the fundamental rotor saliency. Hence, torque ripple is mainly generated by modulation B shown in Figure 5-27. However, when $SP=3/(2k)$ ($k=2,3,4,\dots$), both types of modulation processes contribute to the ripple shown in Figure 5-28.

$$SP \neq 3/(2k)$$

When $SP \neq 3/(2k)$, $v_2 = 5v_m$ is not a slot harmonic. Due to its high order and low magnitude, the torque ripple generated by the type B modulation is not significant and the dominate modulation is type A in this group of FSCWs.

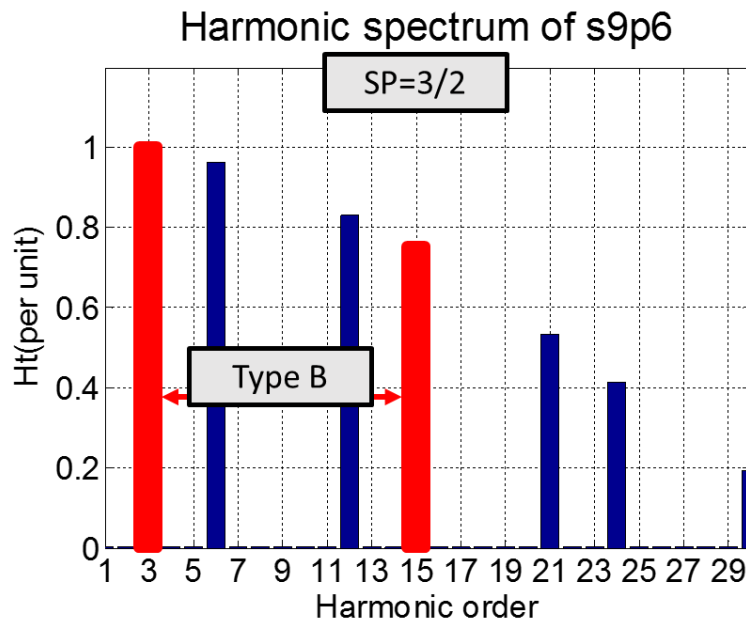


Figure 5-27 Modulation B in an s9p6 FSCW

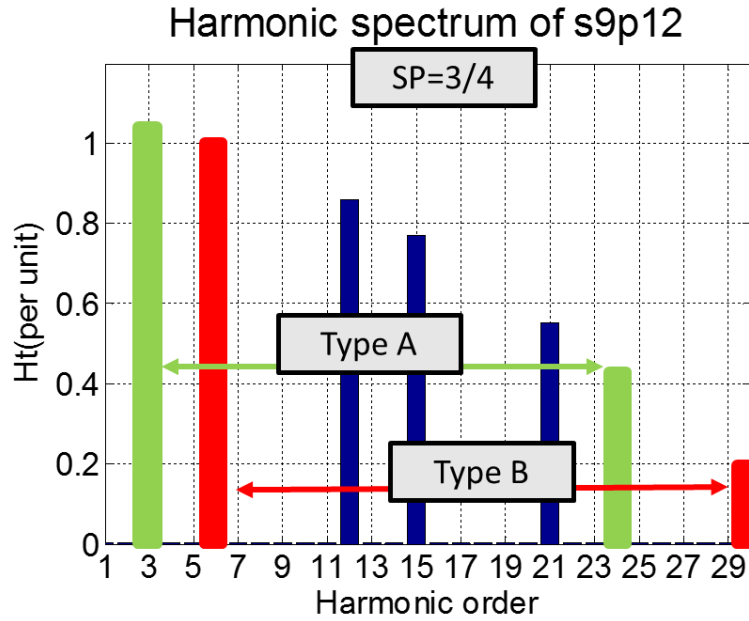


Figure 5-28 Both modulations in an s9p12 FSCW

Other aspects

Torque ripple magnitude

Eq. (5.20) is simplified from eq. (5.17), the torque ripple magnitude of a harmonic group is proportional to the product of the working harmonic magnitudes, rotor saliency constant C , the order of the main harmonic and is inversely proportional to the product of the order of the working harmonics. It is proportional to the input current squared, whereas the mean alignment torque is only proportional to the input current. This means that the relative magnitude of the RSSH torque ripple increases when the PM machine's electric loading is increasing.

$$\hat{T} \propto \frac{\hat{v}_m \hat{H}_1 \cdot \hat{H}_2 \cdot C}{v_1 \cdot v_2} \quad (5.20)$$

The phase information of the torque ripple is related to its harmonic group, for example the angle θ_{2-r+14} is only for the torque ripple formed by harmonic group $2^{\text{nd}}+14^{\text{th}}$. So, torque ripples from individual working groups are summed as vectors to obtain the total torque ripple.

Other rotor saliency harmonics

In this analytical derivation, only the 2^{nd} rotor saliency ($v = 4pp$) is considered. Consequently, only the 6^{th} order torque ripple is formed per electric cycle. If including other rotor saliencies, a different order of torque ripple can be found. Nonetheless, both

the stator harmonics and the rotor saliency are attenuated rapidly moving to a higher order, there is no significant torque ripple formed by higher order saliency in FSCWs with $SP \neq 3/(2k)$. However, when considering the ripple in $SP=3/2$ FSCWs, the 3rd rotor saliency significantly contributes to the 6th order torque ripple. Consequently, the torque ripple magnitude is not constant consistent with different alignment angles, since the torque ripple angle of the 3rd rotor saliency varies differently with the alignment angle compared to the 2nd rotor saliency angle.

For instance, the frequency and phase information of the main harmonic, 3rd rotor saliency and the $5v_m$ are given in eq. (5.21). The angle of the torque ripple depends on θ_r^3 , whereas it is θ_r^2 for the ripple formed by the 2nd rotor saliency. If the alignment angle were to be advanced by 10° , θ_r^2 would increase $4 \times 10^\circ$, while θ_r^3 would increase $6 \times 10^\circ$. As a result, the magnitude of the total torque ripple would vary with the alignment angle.

$$\begin{cases} (3k+1)\theta - \omega t + \theta_m \\ 6(3k+1)\theta - 6\omega t + \theta_r^3 \\ 5(3k+1)\theta + \omega t + \theta_{5m} \end{cases} \quad (5.21)$$

1.1.3.Design guidance table with STI

In applications that require precise position control, such as servo and robotics, the torque ripple needs to be minimised [151]. Knowing the relative torque ripple magnitude in various FSCWs would be helpful in selecting a suitable slot/pole number at the beginning stage of motor design. A stator torque index (STI) is introduced in this section to indicate the RSSH torque ripple magnitude based on the eq. (5.20) .

Table 5-2 is the design guidance table for all basic three phase FSCWs in a double layer winding configuration. The columns in this table are the pole number of a FCSW and the row represents the slot number. Inside each FSCW box defined by the slot and pole numbers, there are four parameters –SP ratio (S/P), winding factor (Kw), least common multiple (LCM) and stator torque index (STI). To explain this table, the size of the table is firstly discussed.

Table 5-2 The guidance table for SP selection in FSCWs

slot								
pole	s/p	4	6	8	10	12	14	16
SP	6	3/2		3/4	3/5		3/7	3/8
Kw		86.60%		86.60%	50%		50%	86.60%
LCM		12		24	30		42	48
STI		3.409		2.0912				
	9		3/2	9/8	9/10	3/4	9/14	9/16
			86.60%	94.50%	94.50%	86.60%	61.70%	32.80%
			18	72	90	36	126	144
			2.281	1.1518	0.5294	1.3775		
	12			3/2	6/5		6/7	3/4
				86.60%	93.30%		93.30%	86.60%
				24	60		84	48
				1.7043	0.7078		0.1932	1.0331
	15			5/8	3/2		15/14	15/16
				71.10%	86.60%		95.10%	95.10%
				120	30		210	240
					1.3688		0.6951	0.4434
	18					3/2	9/7	9/8
						86.60%	90.20%	94.50%
						36	126	144
						1.1003	0.0451	0.5697
	21						3/2	21/16
							86.60%	89.00%
							42	336
							0.9777	0.069
	24							3/2
								86.60%
								48
								0.8262
		boundary		good		bad		

The table size – SP range

This slot/pole range of FSCWs is chosen to cover all of the FSCWs with double layer winding and it is based on three principles:

1. The SP ratio

The SP ratio is provided in the first row of each FSCW in Table 5-4. It must be no smaller than $3/2$ in order to have a good coil span to link the rotor flux. When the ratio is $3/2$, assuming the rotor pole span is 180° in electric degrees, the stator tooth span is 120° . Any span shorter than this critical ratio will result in a winding factor less than 86.6%. For example, the winding factor of the s15p8 FSCW is 71.1%. Any FSCW from the lower part of the red diagonal line in the table is not considered and therefore left blank.

2. A higher pole number

The pole number is directly related to the main harmonic order. Only low order stator MMF harmonics are considered as the main harmonic for a certain winding arrangement, due to higher harmonic attenuation. For example, in the stator harmonic spectrum from Figure 5-28, though all of the slot harmonics share the same fundamental winding factor, their magnitudes attenuate with an increasing harmonic order. Consequently, less mean torque can be produced if a higher order slot harmonic is chosen as the main harmonic.

In conclusion, all FSCWs with $v_m = k \cdot N_s \pm \frac{N_r}{2}$ ($k > 3$) are ignored. The torque ripple of FSCWs with an integer multiplier of these listed FSCWs in Table 5-2 will be discussed in the later part of this section (e.g. s72p64, s36p32 and s18p16 and s9p8 all share the same SP).

3. Winding factor

The winding factor of each FSCW is calculated by hand using theory introduced in chapter 6. The fundamental winding factor (K_w) is provided in the second row of each FSCW. Any FSCW with K_w less than 0.866, is marked as a red block, left blank and deemed as an unwanted design in the table.

LCM - Cogging torque

The third row in an FSCW block is the least common multiple (LCM) of the slot and rotor pole numbers. This LCM is equivalent to the number of cycles of cogging torque in one full mechanical cycle. The magnitude of the cogging torque is inversely correlated to this number.

By definition of “fractional-slot”, SP ratio is not an integer and the numbers of slot and pole are close to each other due to the ‘concentrated-winding’ concept. Hence, FSCWs intrinsically possess a much higher LCM, which indicates a lower cogging torque

compared to machines with integer-slot and distributed winding with the same pole number.

STI – RSSH torque

The governing equation for STI

The stator torque index (STI) is calculated by eq. (5.22). The higher the STI, the higher the RSSH torque ripple.

$$\left\{ \begin{array}{l} STI(m) = v_m \cdot \sum \left(\frac{\hat{H}_1 \cdot \hat{H}_2}{\hat{H}_m} \right)^{j\theta_0} \\ \hat{H}_m = \hat{H}_{fp} * k_w \end{array} \right. \quad (5.22)$$

In which, \hat{H}_1 and \hat{H}_2 are known inputs from eq. (9.5) in chapter 9. The main \hat{H}_m of each FSCW is the product of \hat{H}_{fp} of a fully-pitched ideal winding configuration and the winding factor K_w . The value of \hat{H}_{fp} is standard and fixed in all models. The term of $j\theta_0$ shows that the torque ripple of each harmonic group is summed as a vector. The STI in s9p8 is 1.15 and is higher than its multiple, s18p16. This can be explained by the harmonic order $v_1 \cdot v_2$ as the denominator in eq. (5.22). Though the magnitude of the harmonic is fixed in both cases, the harmonic order is doubled in s18p16. Hence the STI is reduced by a factor of 2 in s18p16. The value of s18p16 is 0.58, which can be validated by FE analysis.

FE validation

The calculated STI is verified with 2D transient FE analysis. There are two types of model which have been generated by FE software: *MagNet*, *Infolytica*. The fixed parameters for the compared models are listed in Table 5-3.

Table 5-3 The controlled parameters for all FSCW models. In which, the slot opening ratio is the ratio of the slot opening span to the full slot span

FSCW parameters		
air gap radius	30	mm
inner radius	10	mm
outer radius	50	mm
axial length	30	mm
fixed MMF per phase	2000	Amp
magnet span	169	deg
magnet thickness	5	mm
slot opening ratio	0.25	-

The 2DFE current sheet models

A general current sheet is used to represent any stator slot and the rotor is represented by a sinusoidal surface as shown in Figure 5-29. There are 5 SP combinations arbitrarily selected from Table 5-2. As can be seen, the STI is closely related to the torque ripple obtained in the current sheet model. The slight difference is stemmed from the ignorance of any rotor saliency other than the 2nd and the flux leakage.

Table 5-4 The RSSH torque ripple comparison between FE current sheet and STI

FSCW	s6p4	s9p8	s9p10	s12p10	s12s14	s15p14	s15p16
FE-CS	8.19	3.11	1.49	1.88	0.46	1.50	1
STI	7.69	2.60	1.19	1.60	0.44	1.57	1

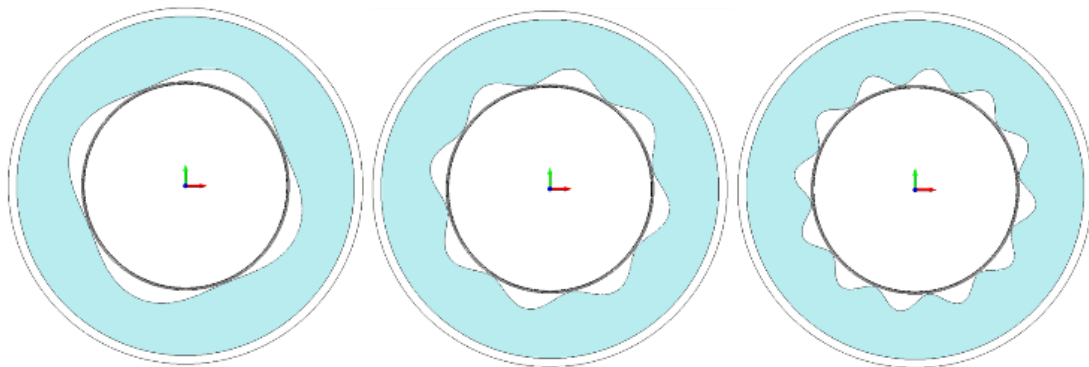


Figure 5-29 Current sheet with rotor saliency of 2 pole, 4 pole and 8 pole rotor

The model with the actual stator

The original FSCW models with the actual stator and infinitely permeable iron are shown in Figure 5-30. The comparison between 2DFE RSSH torque ripple and the STI of three

arbitrarily selected FSCWs is shown in Table 5-5. It demonstrates that the STI can accurately indicate the torque ripple magnitude in the original FSCW models.

The torque output with DC input current and rotating rotor is given in Figure 5-31 to show that these three FSCWs are all able to achieve a similar maximum torque with differences due to the winding factor. The torque ripple is provided in Figure 5-32 to show the common 6th order and the magnitude that corresponds to the STI. The DC value of this graph is due to the reluctance torque. In Table 5-5. From s9p8 to s18p16, the torque ripple is halved as is expected and the s15p10, which has $SP = 3/2$ and possesses the highest torque ripple in FE even though it has a higher number of slots and poles.

In conclusion, the new STI introduced to the guidance table can represent the RSSH torque ripple component in FSCWs with double layer winding. This index work can also be easily extended to the single layer winding models.

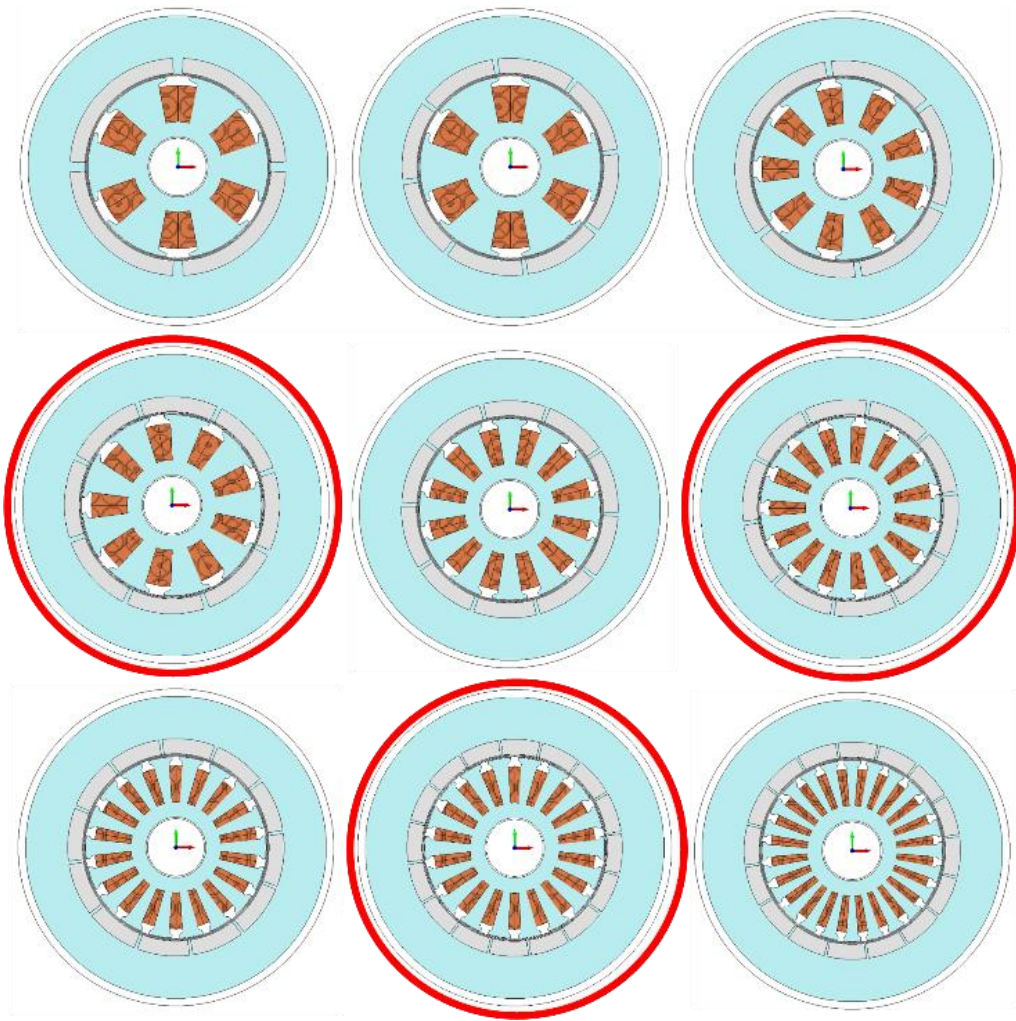


Figure 5-30 The arbitrarily selected FSCW models

Table 5-5 The RSSH torque ripple comparison between FE original and STI

FSCW	s9p8	s15p10	s18p16
FE - Ori	230	265	1
STI	202	240	1

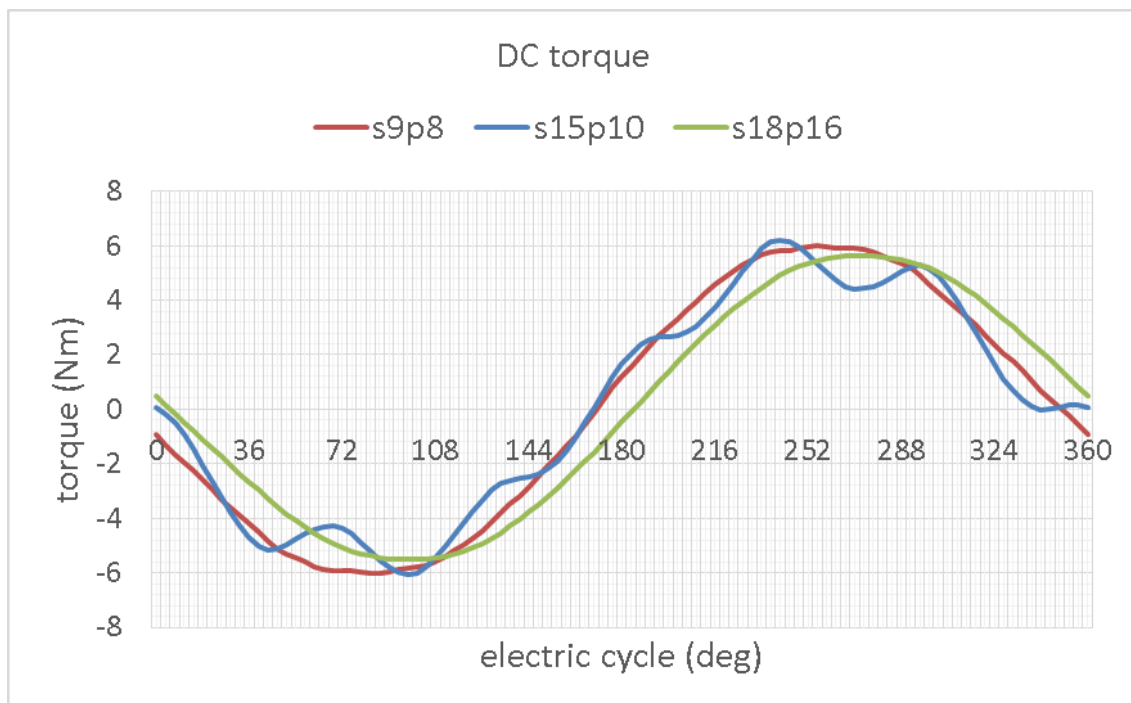


Figure 5-31 The torque output of a DC current input and rotating rotor

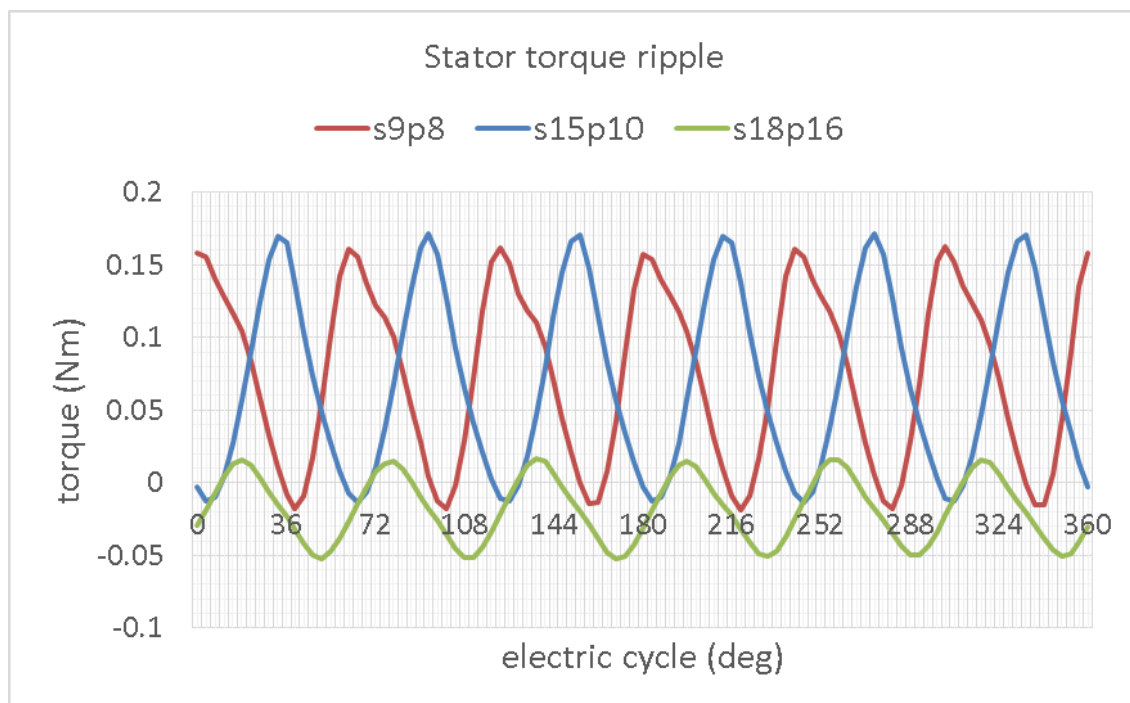


Figure 5-32 The torque ripple in the rated operating condition

1.1.4. Torque reduction in SP selection

The V-shaped in-wheel motor design is the s9p8 combination. Despite all of its advantages compared to the surface-mounted permanent magnet design, the torque ripple in the V shape is twice as high in the rated condition due to increased rotor saliency.

In order to reduce the stator torque ripple, two new combinations: s9p10 and s12p14 are selected from Table 5-2. Together with the SPM, all four models are presented in Figure 5-33. The magnet masses in all three V designs are fixed at 56% of the SPM. The RSSH torque ripples in the 3 V-shaped designs are demonstrated in Figure 5-34 with the magnet unmagnetised. The DC value of the torque is again due to the reluctance torque. It is clear that both new combinations give good torque ripple reduction. The s9p10 is chosen over the s12p14 due to less saturation in the front iron of the magnets, thus giving a better torque performance. Furthermore, there are fewer teeth and magnets in s9p10 which is advantageous in manufacturing. The torque of s9p10 is then compared to the SPM and the V s9p8 in Figure 5-35. A 50% overall torque ripple reduction and 9% mean torque increase can be achieved in s9p10 with the fewest design modifications.

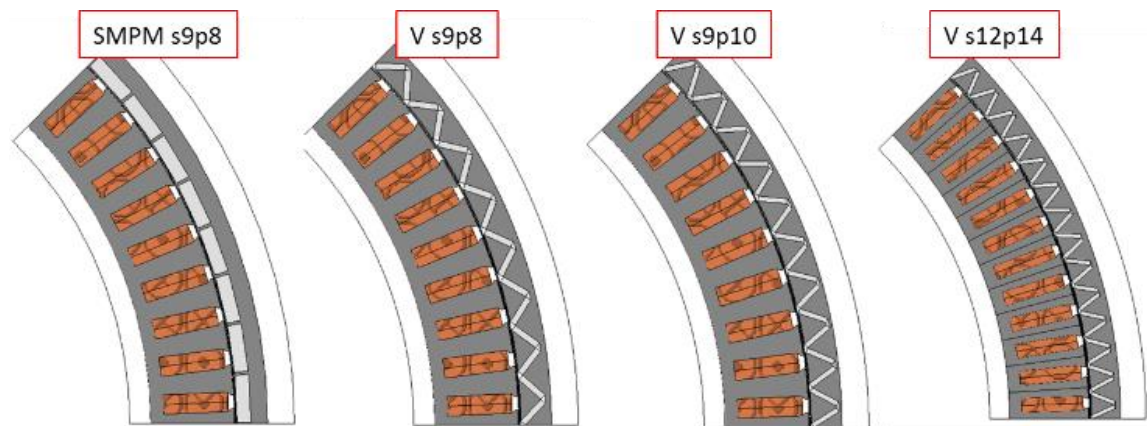


Figure 5-33 The four models

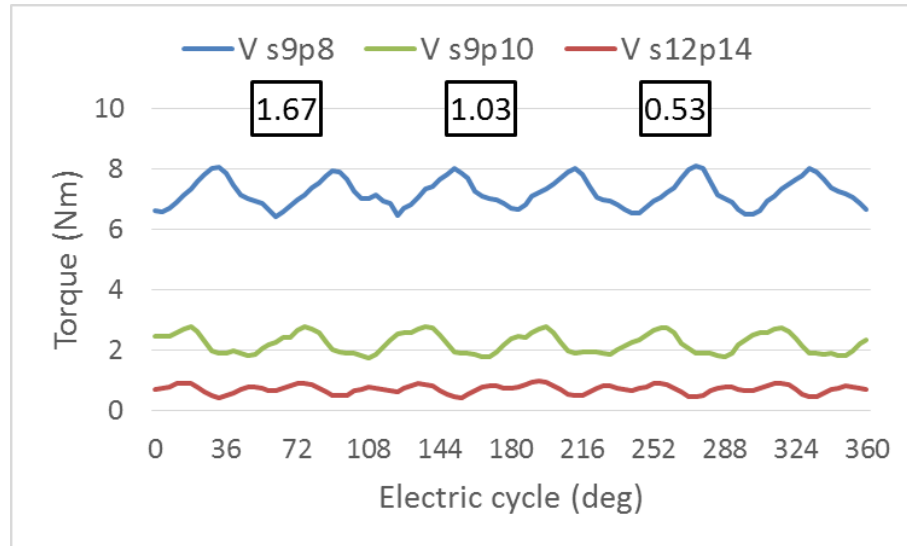


Figure 5-34 The RSSH component of the torque ripples

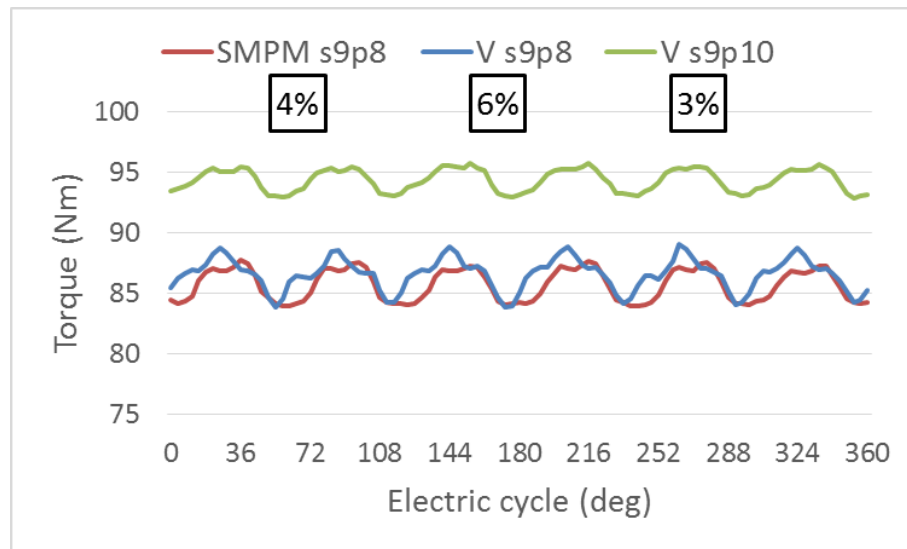


Figure 5-35 The torque at $I_q=30A$ $I_d=0A$

1.1.5. Torque reduction in an FSCW with fixed SP

Spatial harmonics of the MMF can only produce torque if one of the harmonics interacts with the rotor to produce a field of or pole number equal to the second of the harmonics. The key to reducing this torque ripple is to either suppress the MMF harmonics produced by the windings or, alternatively, to minimise the saliency of the second harmonic. This can be achieved by:

1. Careful rotor design to reduce the harmonics of the rotor saliency function [137].
2. Current waveform shaping to inject certain harmonic currents [152].

3. Use of multilayer and fractional-slot winding configurations to reduce the stator harmonic content. [132, 142]
4. Modification of the stator magnetic geometry to reduce the impact of the harmonics

After the SP ratio of a machine is decided, there are still other options to further reduce the torque ripple. In this section the last of these options will be considered through:

- 1) Rotor magnet skewing
- 2) Modification of the stator slot openings

Rotor magnet Skewing

The purpose of skewing is to physically break down a whole stator/rotor into a few parts along the axial direction and place them at a slightly different angle relative to each. Consequently, the torque generated from each part will have a slight phase difference in time. Particular torque ripple harmonics can be cancelled out when summing together these torque parts. When comparing stator skewing to rotor skewing; the latter one is more popular. Stator skewing increases winding difficulty, introduces undesired gaps in the slot and reduces the slot fill factor, whereas, rotor skewing is relatively easy to implement as demonstrated in Figure 5-36, which shows examples of 1, 2 and 3 axial magnet segments. The required skewing angle is determined by the torque ripple frequency for cogging torque reduction.

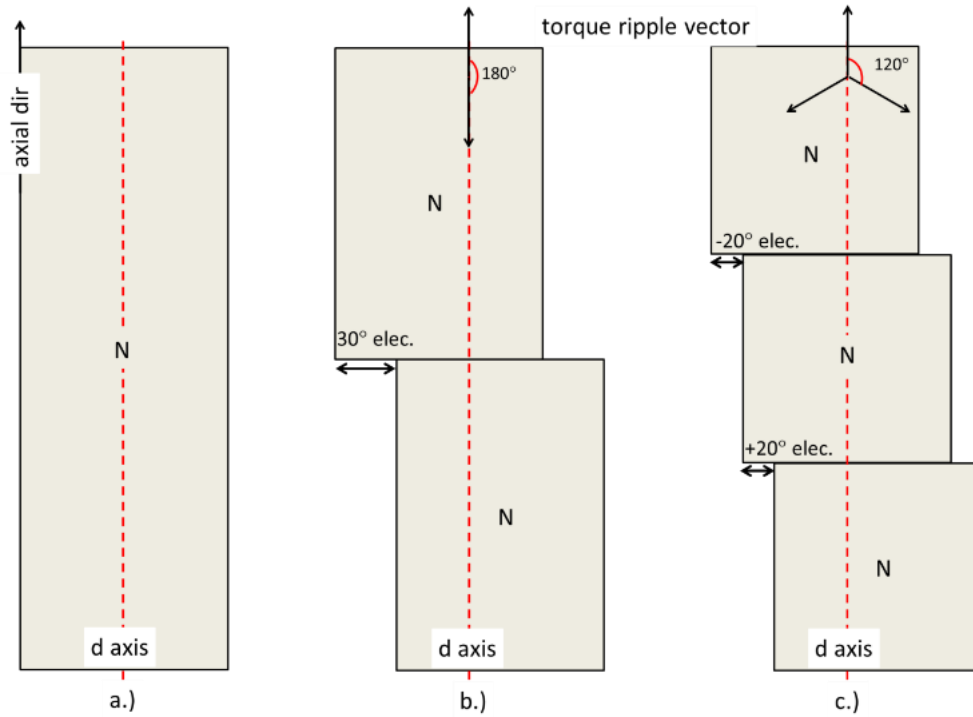


Figure 5-36 Rotor skewing with angle $\xi_{cog} = 60^\circ$

a.) unskewed; b.) 2pieces; c.) 3 pieces

A. Rotor skewing for cogging torque

The cycles of cogging torque, n_{cog} , in a full mechanical revolution are calculated by the least common multiple of the number of stator slots and rotor poles. In the in-wheel motor with 9 slots and 8 poles, there are 72 cycles of cogging torque per mechanical rotation. To minimise cogging torque, the skewing angle in mechanical degrees is set to 5° , this corresponds to 20 electrical degrees. Three pieces are then chosen to be skewed at $-20^\circ/3$, 0° , and $20^\circ/3$ electric angles. The comparison between the skewed and un-skewed cogging torque ripple is shown in Figure 5-36. It is clear that the torque ripple in the skewed case is much lower than the un-skewed.

Skewing also affects the mean torque of the machine due to the different current alignment angle of each rotor axial section relative to the D axis. In the skewed machine the torque is proportional to the average of the $\cos\theta_{1,2,3}$, where $\theta = -20/3^\circ, 0^\circ, 20/3^\circ$. Consequently, the mean rated torque is 0.5% lower in the skewed case than in the original design.

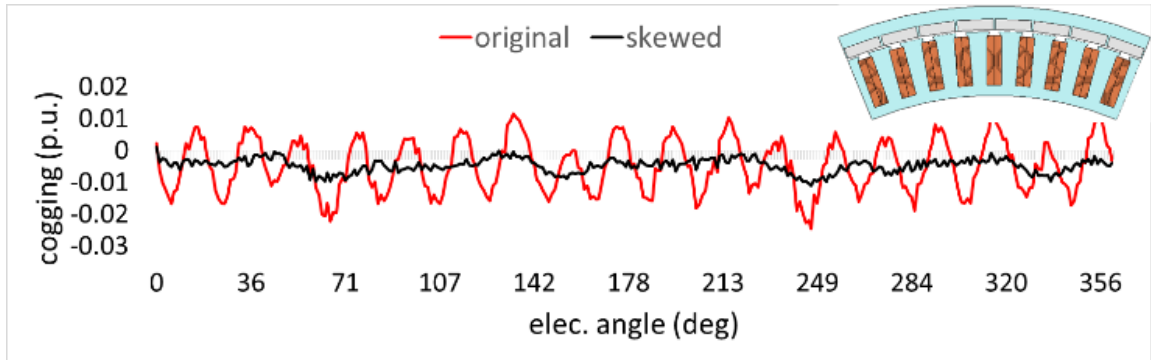


Figure 5-37 Effect of rotor skewing on cogging torque

To conclude, the cogging torque can be effectively reduced by rotor skewing with negligible loss to its mean torque.

B. Rotor skewing for the RSSH torque ripple

To minimise torque ripple due to the interaction of stator MMF harmonics with the rotor saliency there are two viable approaches: a. introduce skew to eliminate the MMF harmonics; or b. introduce skew to remove the second harmonic of rotor saliency.

Option (a) is not chosen because there are multiple harmonic groups and any one skew angle can only eliminate one of them.

The rotor has eight poles, with the first harmonic of saliency which has 8 pole pairs. The second harmonic of saliency, which is the source of the torque ripple, has 16 pole pairs. Hence the mechanical skew angle needed to minimise the RSSH torque ripple is: 22.5° .

This corresponds to 90 electrical degrees. Note, however, that this large skewing of the rotor results in an almost 9 % drop in mean torque. Step skewing in three axial lengths, each displaced 30 degrees from the next is equivalent to a 90 degrees continuous skew. The impact upon RSSH torque ripple is shown in Figure 5-38.

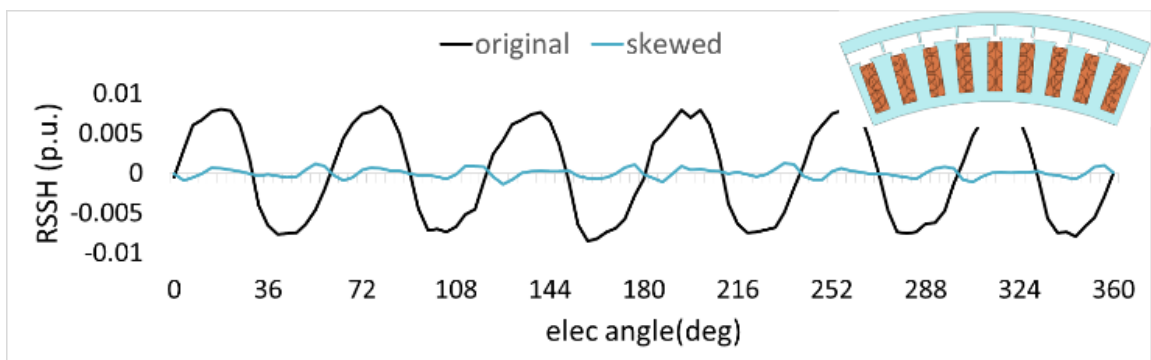


Figure 5-38 Effect of rotor skewing on the RSSH torque ripple

Note that skewing the rotor through 22.5 mechanical degrees is equivalent to 4.5 cycles of cogging torque. Whilst this will not completely eliminate the cogging torque, it will reduce it to only 7.5 % of the unskewed level.

Hence in summary, a 22.5 degrees skew will eliminate the RSSH torque ripple and reduce cogging torque by 92.5%, but will produce a corresponding reduction of 9% in mean torque.

The effect of the slot opening width

This method is developed based on the harmonic equation of the tangential magnetic field created by the stator slot current which varies with time t and space θ . It was introduced in chapter 9 and is recalled here:

$$H_t(\theta, t) = \sum_{v=1}^{\infty} \sum_{m=1}^{slotno} \frac{H_t(t, m)}{v\pi} \sin\left(v \frac{(\theta_b - \theta_a)}{2}\right) \cdot \cos\left(v \left(\frac{(\theta_b + \theta_a)}{2} + m\lambda_s - \theta\right)\right) \quad (5.23)$$

$$\begin{cases} H_t(t, m) = \frac{MMF(t, m)}{r_{ag} \cdot (\theta_b - \theta_a)} \\ \theta_{a,b}(m) = \theta_{a,b} + (m - 1)\lambda_s \end{cases} \quad (5.24)$$

In which, θ_a and θ_b are the angles between the slot opening; $MMF(t, m)$ is the slot magnetomotive force; v is the harmonic number and m is the slot number; λ_s is the slot pitch in radians.

The total H field consists of all the individual stator harmonics. Each stator harmonic is summed up by the slot harmonic vectors, their magnitudes are determined by $\frac{H_t(t, m)}{v\pi} \sin\left(v \frac{(\theta_b - \theta_a)}{2}\right)$ and their angles are given from $v \left(\frac{(\theta_b + \theta_a)}{2} + m\lambda_s - \theta\right)$. These slot vectors for any given harmonic order can be summarised into a single vector, which is illustrated as the thick purple line in Figure 5-39. There are three points that can be made:

- 1) The phase difference between two consecutive slots is $vm\lambda_s$;
- 2) Each slot vector is rotating in the same direction and at the same speed, so their spatial phase difference is time invariant;
- 3) The change in the slot opening $(\theta_b - \theta_a)$ will not create any non-zero DC term in eq. (3), as long as the slot opening is identical for each slot.

To reduce the RSSH torque ripple is to reduce the harmful harmonics, i.e. 2nd+14th and 5th+11th in the s9p8 FSCW. It can be achieved by either reducing the magnitude term or manipulating the phase angle of each slot vector.

The phase angle ($v \frac{(\theta_b + \theta_a)}{2} + vm\lambda_s$) can be manipulated by changing the slot opening position, i.e. making the phase difference between each consequent slot no longer λ_s but with a slight phase shift of around λ_s . This slight difference will have an effect on the vector summation. However, the manipulation of the vector angle is complex and will have potential side effects on the cogging torque. This again can be explained by vector cancellation in the cogging torque. Imagine that each slot has a vector, originally they are of equal magnitude and evenly spaced out. Therefore, the collective result is zero until the frequency reaches LCM to create the cogging torque. However, after the manipulation, the vectors could be unequal in magnitude and unevenly spaced out. Thus, additional cogging torque can be formed.

Hence, only the manipulation on the magnitude of the vector is developed, assuming all slot openings are identical.

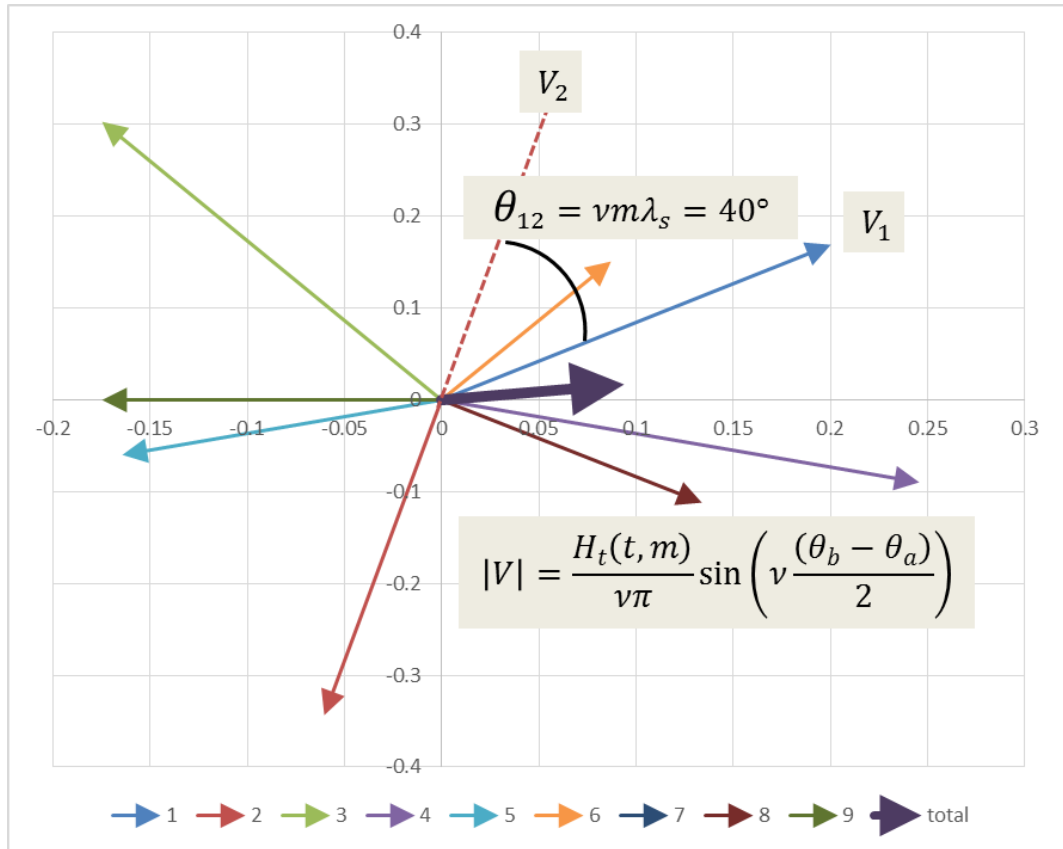


Figure 5-39 The 1st harmonic of the s9p8 FSCW

A. The even slot opening span

The magnitude term, $\frac{H_t(t,m)}{n\pi} \sin\left(v \frac{(\theta_b - \theta_a)}{2}\right)$, can be expanded to:

$$\frac{H_t(t,m)}{v\pi} \sin\left(v \frac{(\theta_b - \theta_a)}{2}\right) = \frac{MMF(t,m)}{v\pi} \cdot \frac{1}{\theta_b - \theta_a} \sin\left(v \frac{(\theta_b - \theta_a)}{2}\right) \quad (5.25)$$

The $\frac{MMF(t,m)}{v\pi}$ can be seen as a constant from a given winding configuration. The angle, $(\theta_b - \theta_a)$, ranges from 0 to $\frac{\lambda_s}{2}$, which is 0-20° in a 9s8p machine. Hence, to reduce the harmonic content, $\frac{1}{\theta_b - \theta_a} \sin\left(\frac{v}{2}(\theta_b - \theta_a)\right)$ needs to be reduced by changing the slot opening span $(\theta_b - \theta_a)$. Interestingly, when $\frac{v}{2} \cong 1$, the magnitude coefficient $\frac{1}{\theta_b - \theta_a} \sin\left(\frac{v}{2}(\theta_b - \theta_a)\right)$ is analogous to the cardinal sine function, $\sin(x)/x$, which does not change with the slot opening span if the angle, x , is small.

Take the main harmonic, $v_m = 4$ and the magnitude of its maximum slot opening angle, $\frac{v}{2}(\theta_b - \theta_a)$, is 45° meaning that the magnitude of $\frac{1}{\theta_b - \theta_a} \sin\left(\frac{v}{2}(\theta_b - \theta_a)\right)$ is nearly independent of the slot opening span variation. Consequently, the effect of increasing the slot opening span on the main torque is negligible. Whereas the higher harmonics can be attenuated by it.

The discrete nature of the slot opening positions is the principle cause of lower order spatial harmonics produced by the winding. However, it is the width of the slot opening which is dominant in determining the magnitude of the higher order harmonics. When the slot opening is very narrow then the surface H field is much greater, but over a smaller angle. This results in larger high order harmonics, as shown in Figure 5-40.

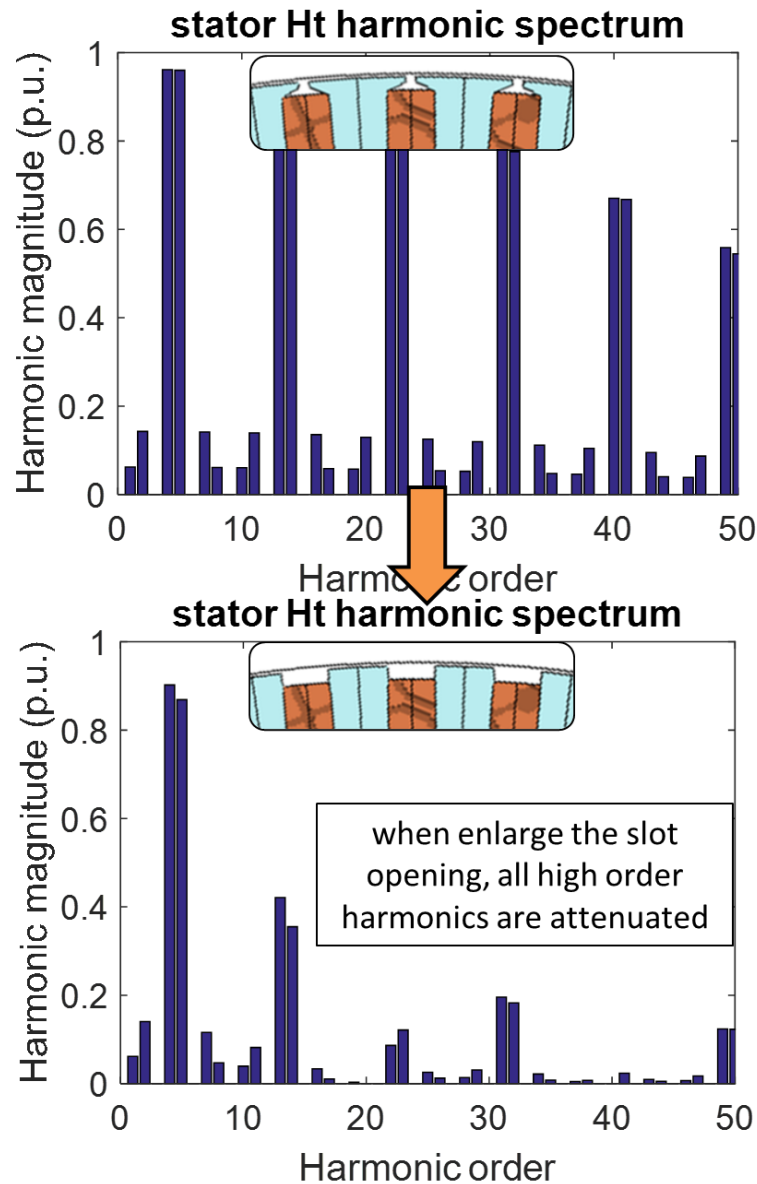


Figure 5-40 Effect of the slot opening width upon the stator magnetising field strength harmonics

Recall first that the RSSH torque ripple occurs due to the interaction of two pairs of harmonics: the 2nd combined with the 14th and the 5th combined with the 11th. It was found that when increasing the slot-opening from almost closed to fully open, the 2nd and 5th harmonics remain above 93%, whilst the 14th and 11th drop to less than 50% of their original value. Consequently, the RSSH can be reduced by a similar amount.

FE simulation of the torque ripple in the nine slot, eight pole motor confirms the effectiveness of this method, see Figure 5-41. By opening the slot from its original value to a fully open slot the RSSH torque ripple is reduced by 63%.

Note that using a wider slot opening can cause some potential side-effects:

1. Increased cogging torque due to the stronger slotting effect;
2. Increased AC loss in the conductors near to the slot opening.
3. Increased rotor magnet eddy-current loss.
4. A small reduction in mean torque as the air-gap reluctance is increased.

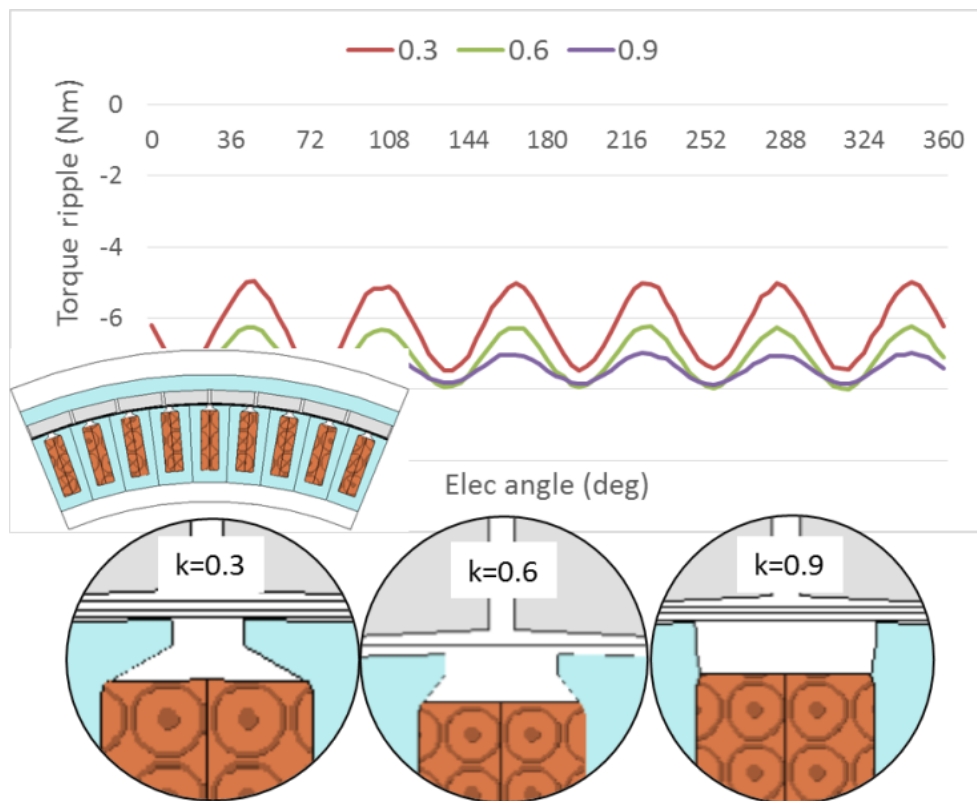


Figure 5-41 Impact of the slot opening upon RSSH torque ripple

B. Uneven slot opening span

There are other slot opening manipulation methods that could potentially reduce the torque ripple. Here is an example of using an uneven slot opening span.

Figure 5-42 demonstrates two different types of harmonic vector: both are harmful to the s9p8. The 11th harmonic is the non-slot harmonic and its magnitude is small, whereas the 14th is the slot harmonic with a large magnitude. The magnitude and phase angle of each slot vector are shown in Figure 5-42. In the 14th harmonic case, the way to reduce the magnitude of the summed vectors is to increase the slot opening since all of the slot vectors are pointing in a similar direction. However, in the case of the 11th harmonic, a slight increase in the slot vectors pointing opposite to the summed and a slight reduction on the other side can help to reduce the summed vectors significantly.

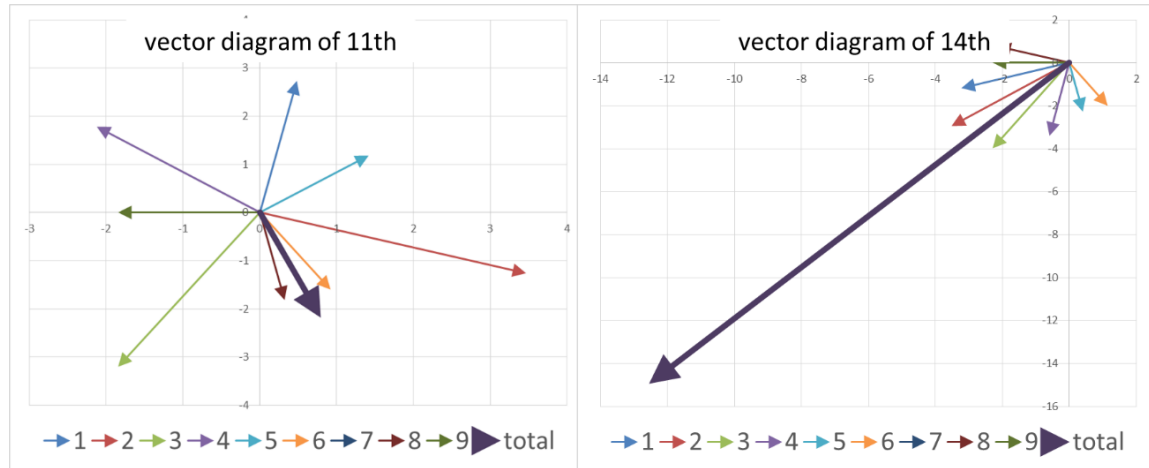


Figure 5-42 The vector diagram of 11th and 14th harmonic

An example is given in Figure 5-43. In diagram (a.), the harmonic magnitude of the 11th is 1 unit with the slot half opened ($k=0.3$). Then the slot opening changes to fully open ($k=1$) in (b.) resulting in 0.52 unit harmonic magnitude. The uneven slot opening is used in (c.), it can reduce the 11th harmonic to 0.28 unit. In (d.), the value of ‘ k ’ for each slot is tuned more individually, resulting in 0.09 unit of the original harmonic.

The RSSH torque ripple of the harmonic group ‘5th+11th’ is then checked with a current sheet model. It agrees with the analytical indication, as shown in Figure 5-44. However, unlike the evenly pitched slot opening, the effect of the uneven pitching on other harmonics is not simply inversely proportional to k as explained by Figure 5-42. Remember there is a type B modulation, i.e. the main harmonic plus the one with a five times higher order. After checking the harmonic vector diagram, it can be seen that the ratio of the $5v_m$ harmonic in case a, b, and c is 1:0.12:1.32. Taking the phase shift between torque groups into account, the analytical prediction for the total RSSH torque ripple is made in Table 5-6. The FE simulation in Figure 5-45 using the current sheet method and Figure 5-46 with the original model confirms the analytical prediction.

To conclude, the uneven slot opening shows some promising effects on particular harmonic reduction. However, it could also increase other harmonics. Hence, instead of focusing on one harmonic reduction for one group of torque ripple at a time, the total torque ripple should be evaluated collectively for each set of individually pitched values of ‘ k ’. A slightly more complex algorithm is required to select the optimum ‘ k ’ for each slot. However, due to the time constraint of this project, this approach is merely introduced here without further development.

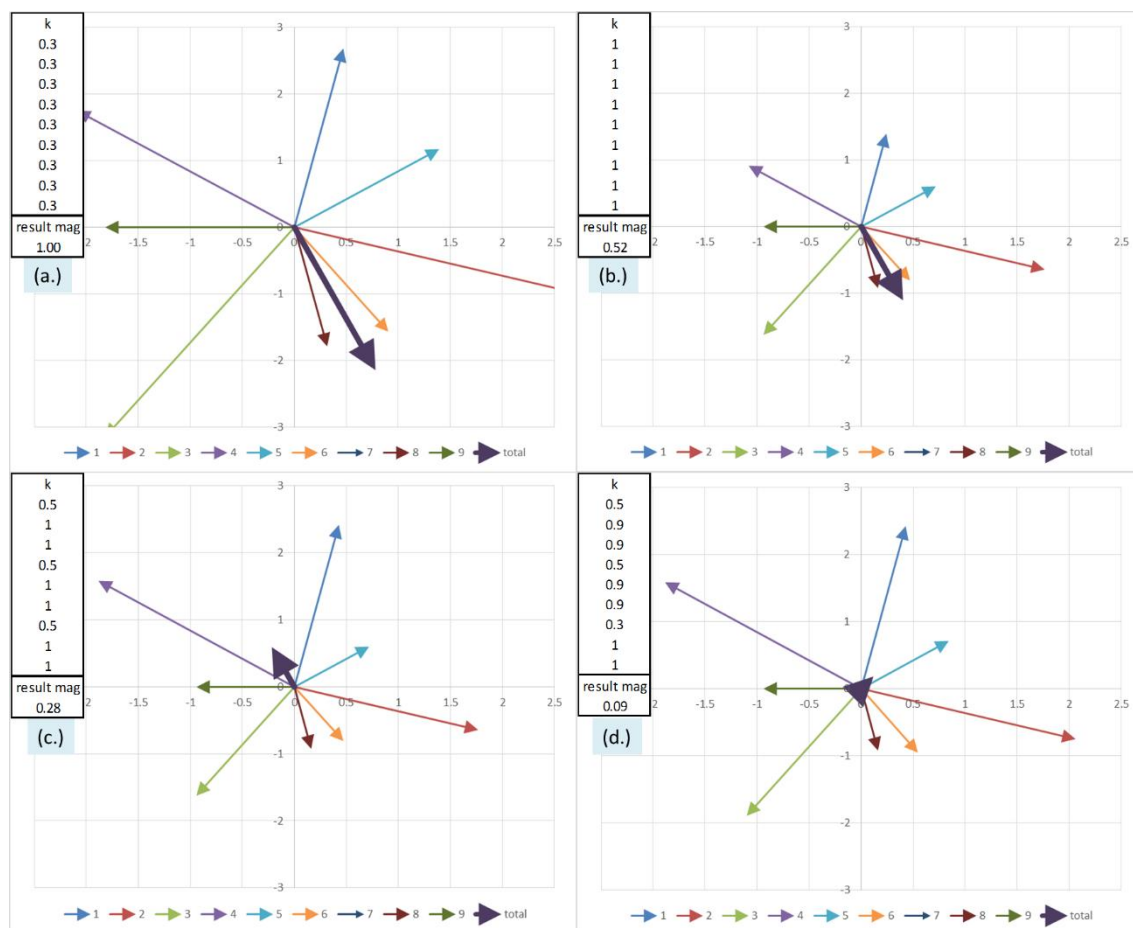


Figure 5-43 The uneven slot opening with 11th harmonic

Table 5-6 The RSSH torque index in an s9p8

	a			b			c		
harmonic	2+14	5+11	4+20	2+14	5+11	4+20	2+14	5+11	4+20
torque index	41.50	22.30	11.44	8.60	7.31	1.41	11.54	6.36	15.14
phase	132.86	132.87	-42.98	133.30	133.39	-223.68	133.22	-46.98	-223.24
result		52.40			17.31			20.31	

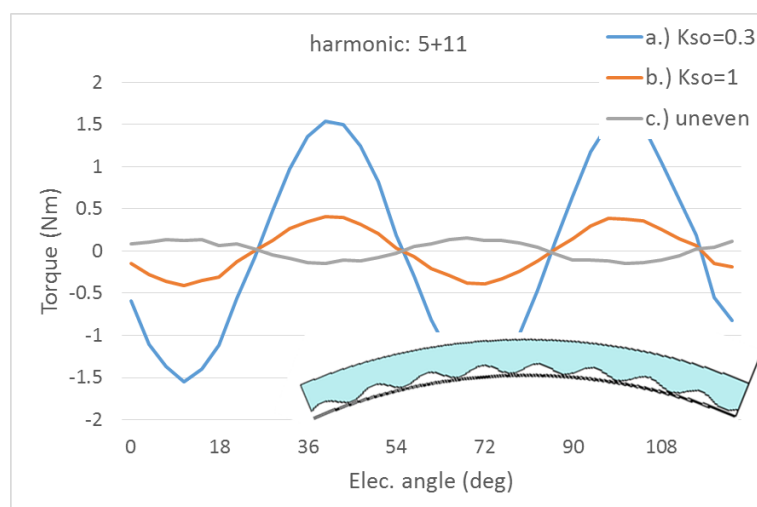


Figure 5-44 The RSSH torque output from the 5th and 11th harmonics in an s9p8

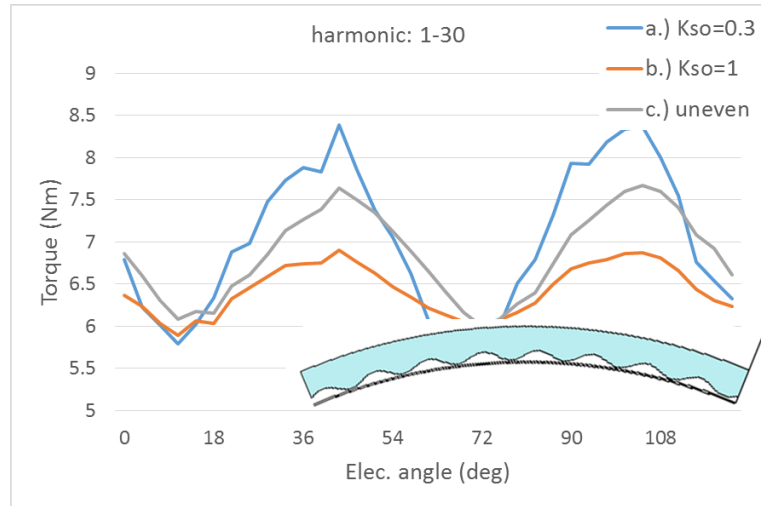


Figure 5-45 The RSSH torque output from all harmonics in an s9p8 current sheet model

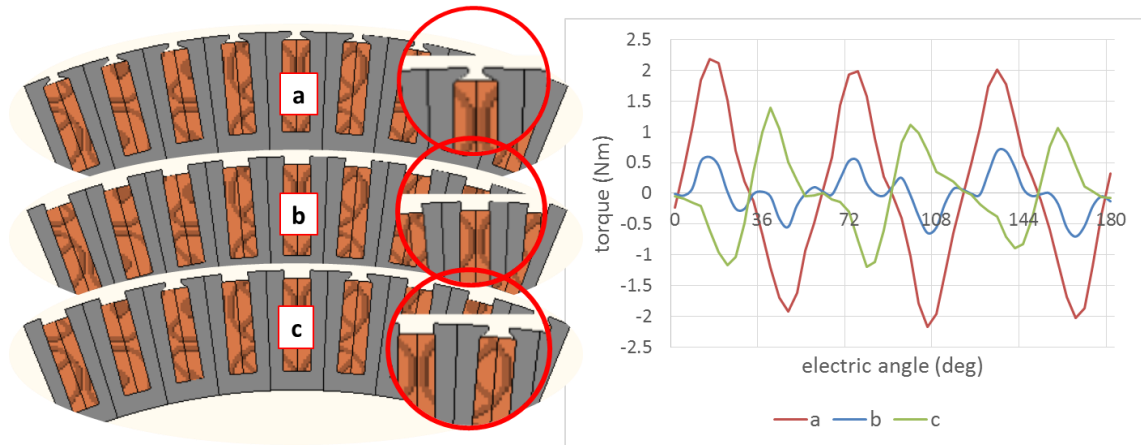


Figure 5-46 The RSSH torque output from all harmonics in an s9p8 model with actual stator

1.1.6. Conclusion

In this section, the torque ripple, in particular the one caused by interactions between the rotor saliency and the stator harmonics (RSSH) in fractional-slot concentrated-winding (FSCW) machines with rotor saliency has been discussed. In some machines the torque ripple occurs due to the interaction of two stator harmonics of different pole numbers which then interact through the rotor saliency. The fundamentals of this process are very similar to that which produces torque in doubly fed reluctance machines.

Based on the generalised rules, an analytically calculated stator torque index has been proposed and a guidance table to help choose the suitable slot-pole numbers of an FSCW has been formulated. Using the current-sheet method and the original FE model, all analytical models were verified and the accuracy of the STI was confirmed.

Selecting from the guidance table, the V-shaped motor has been modified to successfully reduce the torque ripple. After the slot-pole number has been fixed, the torque ripple can be further reduced by careful modifications such as skewing, profiling and shaping. New ideas of manipulating the slot opening design have been proposed and verified.

5.4. Conclusion

In this chapter, the interaction between the stator winding harmonic and the rotor saliency has been studied to explain two phenomena: lower reluctance torque compared to ISDW and higher torque ripple compared to non-salient rotor. The reluctance torque reduction can be recovered by selecting a pole-slot ratio of $2/3$ and using a wider slot-opening. The torque ripple can also be reduced by using a wider slot-opening and selecting the ‘right’ SP combination. Methods like skewing and tooth shaping are also useful at the detailed design stage. The s8p10 design shows a 50% overall torque ripple reduction and 9% mean torque increase with $I_q=30A$ $I_d=0A$ compared to the s9p8 V-shaped prototype.

Chapter 6. CONCLUSION AND FUTURE WORK

The benchmark in-wheel motor from Protean Electric is compact with a high torque capability, because it is required to be integrated with other components and directly drive the vehicle. A rare-earth magnet is used. However, the sources of Neodymium are scarce, its price fluctuates greatly depending on the local government's policy. Its price can increase by 1800% and drop back to normal in less than 3 months as seen in 2011. The uncertainty of future prices of the material motivates the author to research potential means to reduce the usage of the magnet for the next generation motor.

6.1. Conclusion

In this thesis, the background of electric vehicle technology was briefly introduced and the challenges of the in-wheel motor design were laid out. A few magnet-free motor types were then explored to seek machines with a higher torque density, including the transverse flux machine, the switched reluctance machine and the induction machine. Designed in the FE model, both the induction machine and the switched reluctance machine provided less torque density compared to the benchmark permanent magnet motor, however the permanent magnet type was still chosen.

In terms of using outer or inner rotor topology, an analytical model was used to prove that an outer-rotor topology can offer a higher torque density compared to the conventional inner-rotor topology. The air gap radius of the BMM was proved to be near optimum. Six different magnet topologies were then researched and compared. The V-shaped motor was selected due to its high reluctance torque, high resistance to demagnetisation and better manufactural practicality (simple, rectangular shape; rotor back iron made from one piece).

To make it easier to manufacture, seven V magnet shapes were designed and analysed to reach a balance between the torque density and the manufactural practicality. The selected rotor design consists of a single back iron ring, 128 rectangular magnets and 64 triangular front iron laminations. It uses 56% the magnet material of the benchmark motor and generates 95.6% of the BMM torque at the rated condition. It can also withstand a demagnetising field in the worst possible faulty scenario.

Using less magnet material, made demagnetisation a top potential issue. Reducing magnet loss can reduce magnet temperature and hence improve the magnet's resistance to demagnetisation. Segmentation was used. Analytical models of magnet loss were made to help determine how to segment the magnet. By segmenting the BMM circumferentially from one-piece-per-pole to two-pieces-per-pole, magnet loss was able to be reduced by 65%. The V magnet topology is two-pieces-per-pole and hence is proved to have less magnet loss compared to the BMM. Furthermore, the V-shaped magnets are less exposed to the asynchronous rotating stator harmonics by hiding behind the front iron giving it a much higher demagnetisation resistance.

During the assembly, failure magnet adhesion failure occurred. The type of adhesive, gluing procedure for the magnets and the assembly tools were all improved on. The V-shaped motor was then successfully assembled. With the measurements from experimental tests, the FE simulation results were verified. A lower overloading capability was found to be a major cost in reducing the magnet mass.

In the paper study, an analytical model was derived to explain the generally lower reluctance torque in fractional-slot concentrated-winding machines (FSCW). It was then extended to help explain a particular type of torque ripple found in FSCWs. Methods to reduce the torque ripple and increase the reluctance torque were proposed. By changing from a 9slot-8pole combination to a 9slot-10pole combination the torque ripple was reduced by 50% and the average torque was improved by 9%.

Overall, compared to the BMM, the V-shaped motor reduced magnet mass mainly by introducing reluctance torque and improving demagnetisation resistance. Therefore, much thinner magnets could be used in the V-shaped motor. Also, in order to minimise the flux leakage, it was decided that ribs for structural strength should be taken away. This posed a large difficulty for the assembly process. More sophisticated assembly techniques needed to be implemented for mass production.

6.2.Future work

The V-shaped motor design is focused on matching the torque output at the rated operating condition. However, it generates noticeable less torque under the overload condition compared to the benchmark motor. The key reason for this drawback is the reduced equivalent air gap distance. Therefore, for the same electric loading, more armature flux

can be generated in the V-shaped motor leading to a higher saturation. Future works can be carried out to increase the torque output in the saturated region.

Due to assembly difficulties, optimisation of the V rotor design for manufacturability, e.g. the slotted design, can also be considered. The full cost evaluation including other system components and manufactural price can also be included into the optimisation.

The reluctance torque of both the prototype and the BMM is relatively low compared to integral-slot distributed-winding machines shown in chapter 5. Consequently, the attempts were made to use the new distributed winding design to increase the reluctance torque.

The current stator coil can be replaced with a patented compressed coil technology from Protean Electric to increase the fill factor and reduce copper loss. This means that more current can be forced into the coil to produce a higher torque. Design on the assembly procedure and material property analysis under stress are necessary.

The tooth design theorized in chapter 5 can be researched further to derive a set of rules for the optimum tooth tip width of each tooth to minimise the torque ripple.

The mass on the hub is critical for in-wheel technology. Research on the minimisation of the mass of the motor can be conducted. Look at areas of the steel which are not well utilised and remove them. This may not be manufacturable or cost-effective but will generate some possibilities for lowering mass without lowering the quality of significant performance.

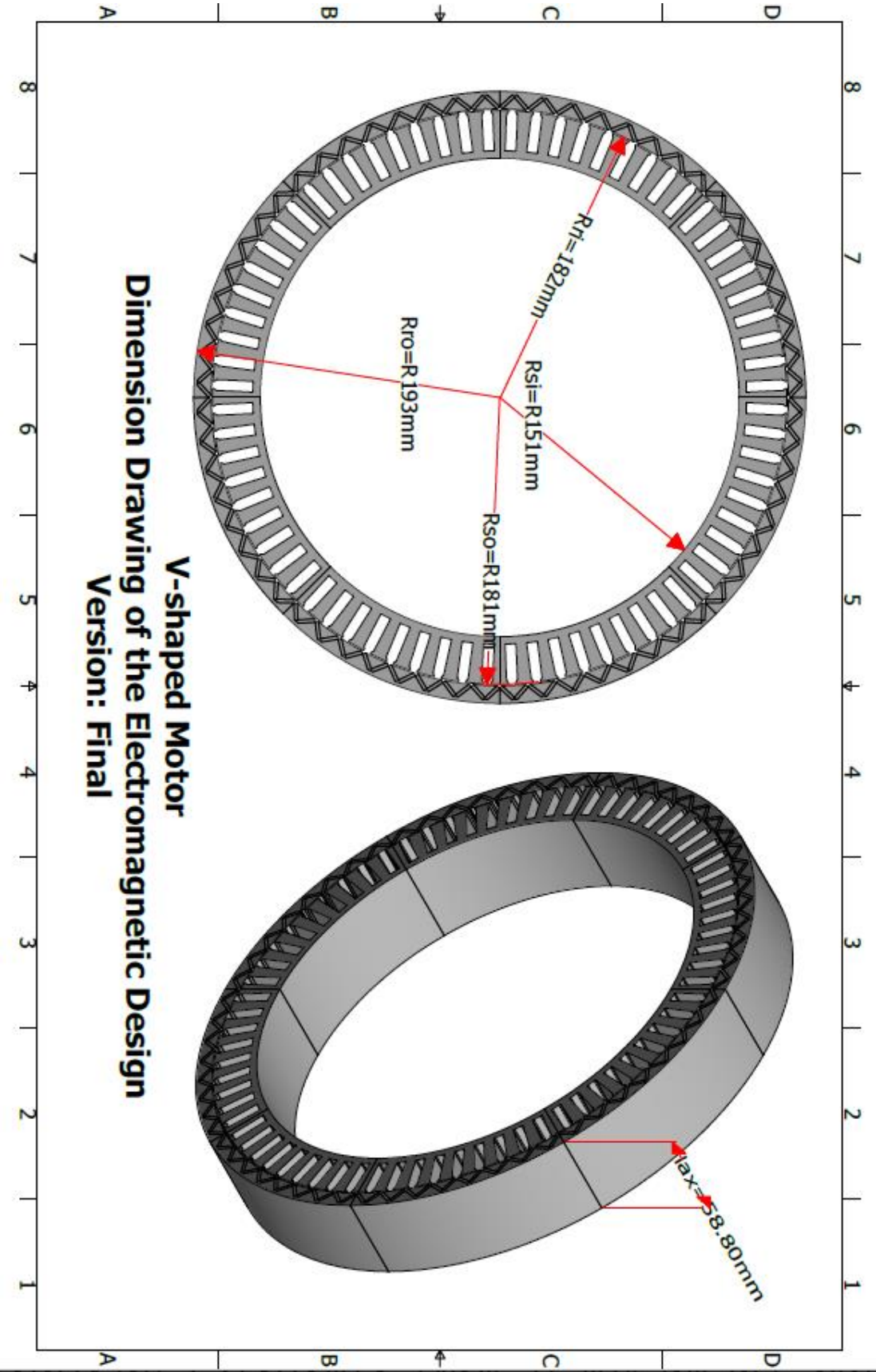
Halbach array is known for its high air-gap flux concentration ability. A motor with this topology could be researched to further improve the torque density of the in-wheel motor to see if this is a higher torque density option for customers who are less price sensitive and what challenges would there be in such a motor.

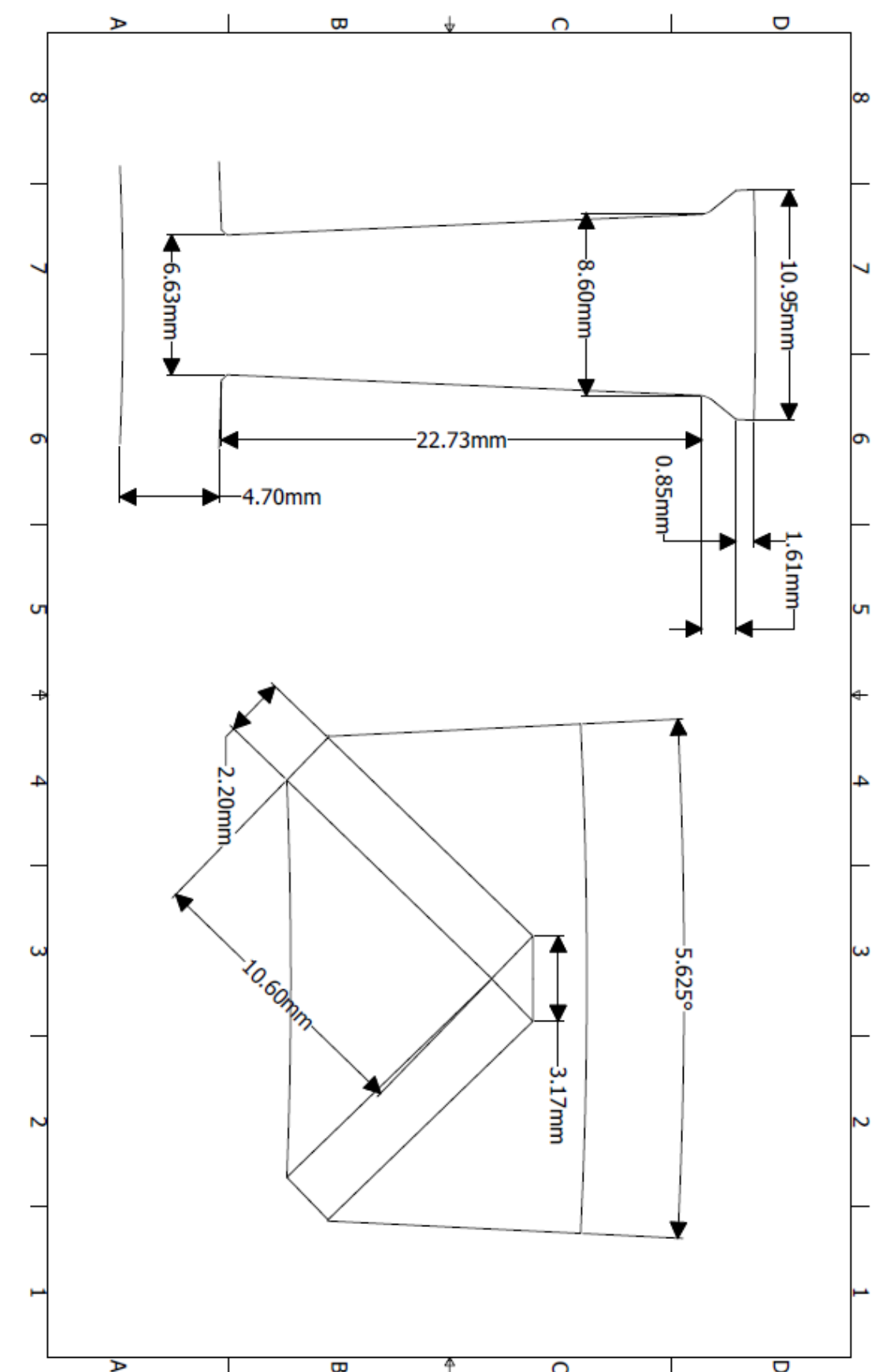
The axial flux technology can also be explored for its pancake shape. The potential larger cooling area may help the machine to achieve a higher torque with the same thermal constraint. The dual stator/rotor topology is also known for its high torque density.

Other research suggestions are: development of a high speed motor version for use with a geared drive; re-optimisation machine design in the absence of constraints on the stator

shape and air gap diameter; re-optimisation of the surface mounted topology using techniques like magnet shaping.[153]

APPENDIX A: V-SHAPED MOTOR DIMENSION DRAWING





APPENDIX B: INVERTER CONTROL SCHEME - SVPWM

Fig. a demonstrates the DC to AC 3 phase inverter circuit used to link the battery and the motor. The control scheme used is the space vector pulse width modulation (SVPWM) [154]. 6 insulated-gate-bipolar-transistors (IGBT) are switched on and off to generate 3 phase sinusoidal current which can be defined as 8 states in Fig. b. Table. a is given to show the ratio between phase to phase, phase to neutral, d/q voltage and the DC voltage source at each switching state.

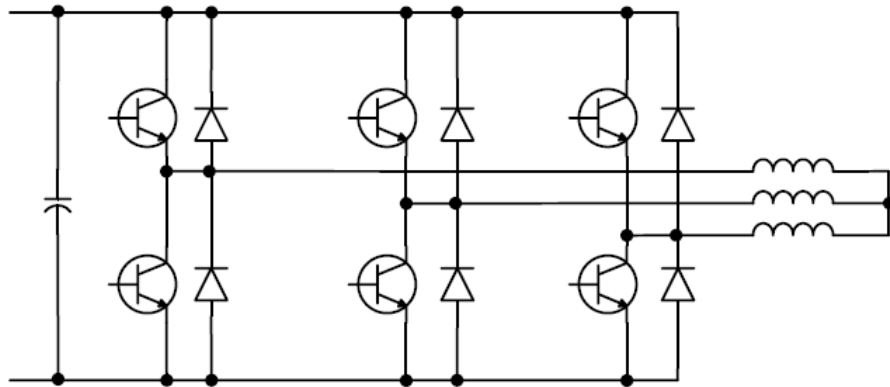


Fig. a DC to AC 3 phase inverter circuit with voltage source

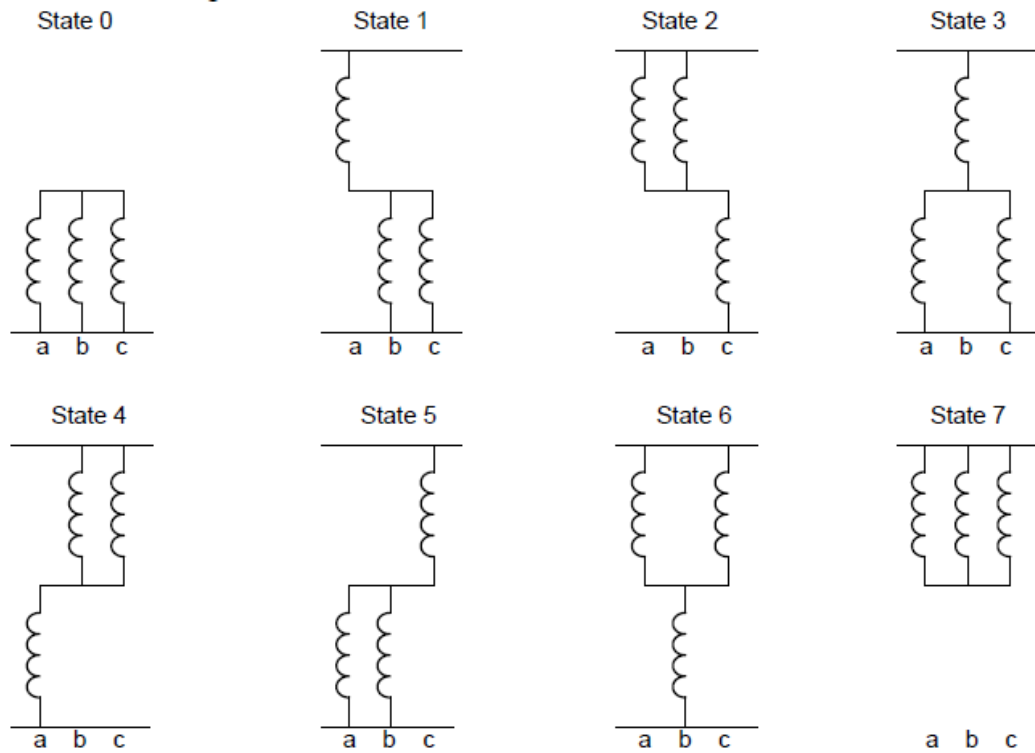


Fig. b Switching states associated with a 6-transistor inverter circuit [155]

Table. a Switching states of 3-phase inverter [155]

State	Vector	$\frac{v_{ab}}{V_{dc}}$	$\frac{v_{bc}}{V_{dc}}$	$\frac{v_{ca}}{V_{dc}}$	$\frac{v_{an}}{V_{dc}}$	$\frac{v_{bn}}{V_{dc}}$	$\frac{v_{cn}}{V_{dc}}$	$\frac{v_d}{V_{dc}}$	$\frac{v_q}{V_{dc}}$
000	\bar{v}_0	0	0	0	0	0	0	0	0
100	\bar{v}_1	1	0	-1	2/3	-1/3	-1/3	2/3	0
110	\bar{v}_2	0	1	-1	1/3	1/3	-2/3	1/3	1/√3
010	\bar{v}_3	-1	1	0	-1/3	2/3	-1/3	-1/3	1/√3
011	\bar{v}_4	-1	0	1	-2/3	1/3	1/3	-2/3	0
001	\bar{v}_5	0	-1	1	-1/3	-1/3	2/3	-1/3	-1/√3
101	\bar{v}_6	1	-1	0	1/3	-2/3	1/3	1/3	-1/√3
111	\bar{v}_7	0	0	0	0	0	0	0	0

The collective effect of the 3 phase current on the resultant magnetic field is mapped as a circle in Fig. c. The 6 states except state '000' are the space vector segmenting the circle. By controlling the circulating vector shown as red line to project an arbitrary space vector onto two adjacent basic states, shown in Fig. d, the magnitude of modulation indexes for these two basic states can be calculated to switch the 3 bridges on and off which is shown in Fig. e and Fig. f. In normal operation, the trajectory of the vector is a circle, and the sinusoidal magnetic field is rotating in the air gap. When overloading is required, the circle can be extended to a hexagon and a 15.4% fundamental increase can be achieved.

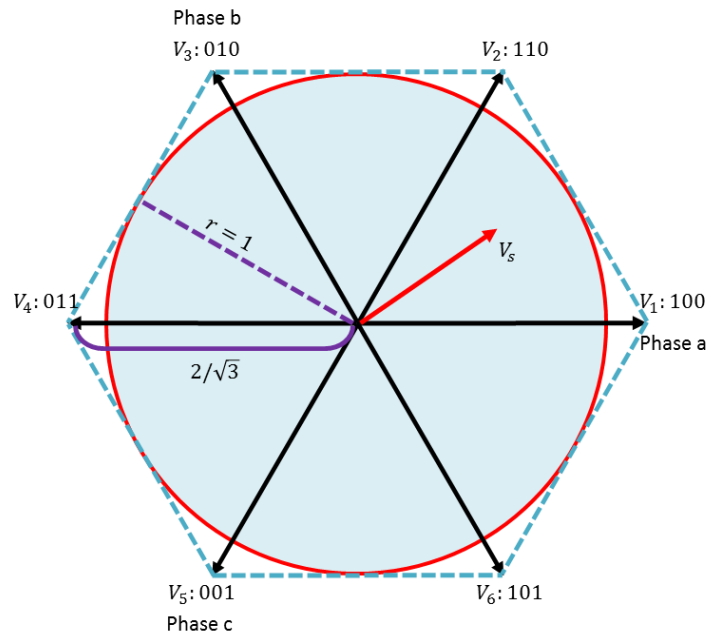


Fig. c Space Vector Circulating Trajectory

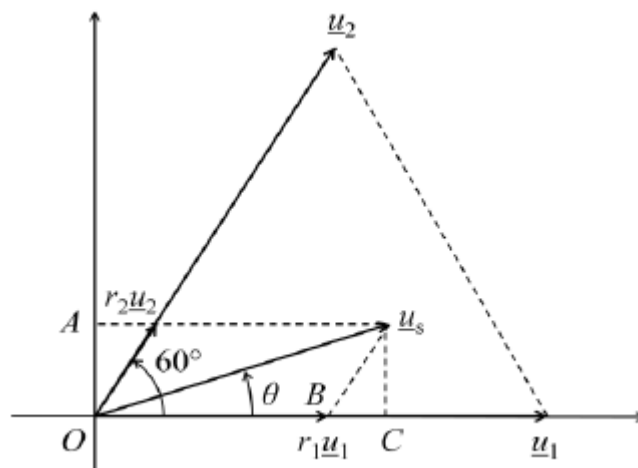


Fig. d Approximation of an arbitrary voltage space vector using base vectors [156]

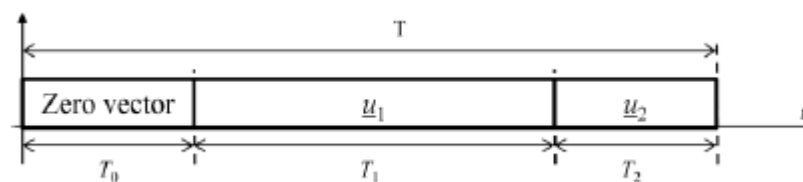


Fig. e Combination of vectors using time division

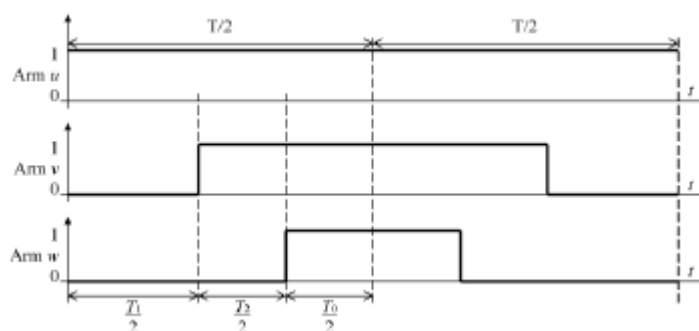


Fig. f PWM switching sequence using symmetric pulsation

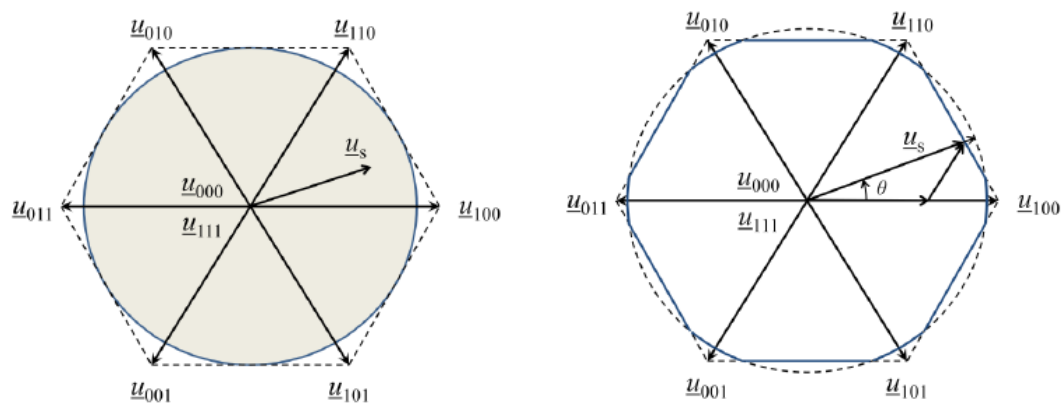


Fig. g Two modulation operation for SVPWM control [156]

Seen from Fig. c, when the vector is at the '100 state, it is $2/\sqrt{3}$ of the normal vector radius. Looking up Table. a, the peak phase voltage, V_{an} , is $2/3$ of V_{dc} . Therefore, for the normal modulation, the vector radius, which is the available peak phase voltage in normal modulation mode can be calculated by eq.a.

$$V_{ph-pk} = \frac{1}{2/\sqrt{3}} \cdot \frac{2}{3} V_{dc} = \frac{V_{dc}}{\sqrt{3}} \quad (a)$$

APPENDIX C: MATERIAL DATA



N45SH

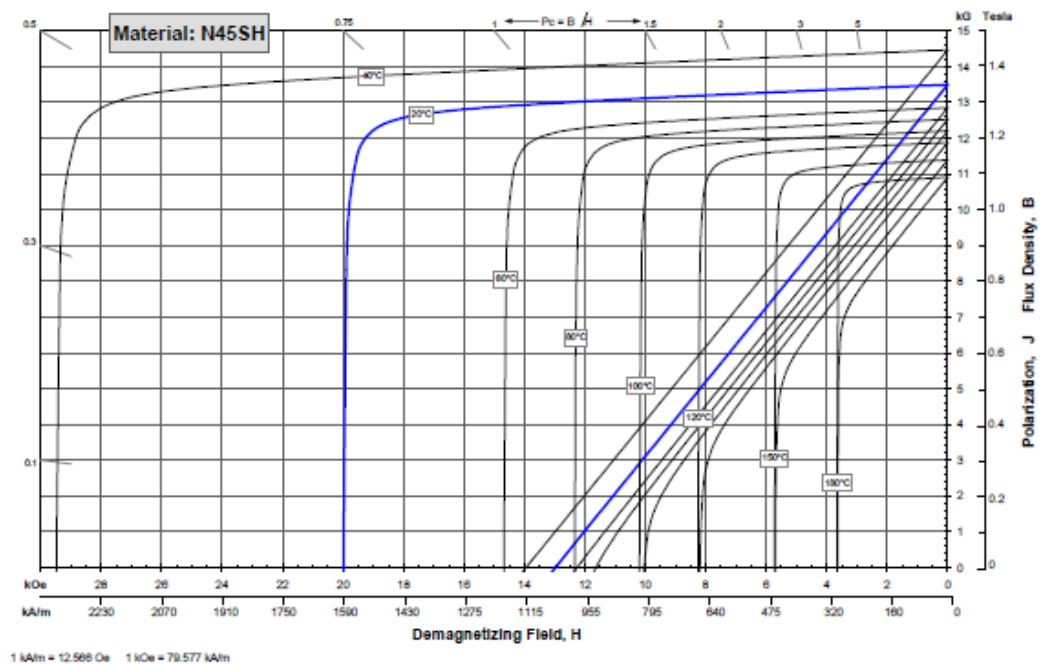
Sintered Neodymium-Iron-Boron Magnets

These are also referred to as "Neo" or NdFeB magnets. They offer a combination of high magnetic output at moderate cost. Please contact Arnold for additional grade information and recommendations for protective coating. Assemblies using these magnets can also be provided.

Characteristic	Units	min.	nominal	max.
Br , Residual Induction	Gauss	13,200	13,500	13,800
	mT	1320	1350	1380
H_{CB} , Coercivity	Oersteds	12,400	12,800	13,200
	kA/m	987	1,019	1,050
H_{CI} , Intrinsic Coercivity	Oersteds	20,000		
	kA/m	1,592		
BHmax , Maximum Energy Product	MGoe	43	45	46
	kJ/m ³	342	354	366

Characteristic	Units	C //	C ⊥
Thermal Properties	Reversible Temperature Coefficients ⁽¹⁾		
	of Induction, α(Br)	%/°C	-0.12
	of Coercivity, α(H _C)	%/°C	-0.55
	Coefficient of Thermal Expansion ⁽²⁾	ΔL/L per °C x 10 ⁻⁶	7.5
Other Properties	Thermal Conductivity	cal/inh/°C	5.3
	Specific Heat ⁽³⁾	cal/g/°C	0.11
	Curie Temperature, T _C	°C	340
	Flexural Strength	psi	41,300
		MPa	285
	Density	g/cm ³	7.5
	Hardness, Vickers	Hv	620
	Electrical Resistivity, ρ	μΩ · cm	180

Notes: (1) Coefficients measured between 20 and 150 °C
(2) Between 20 and 200 °C
(3) Between 20 and 140 °C

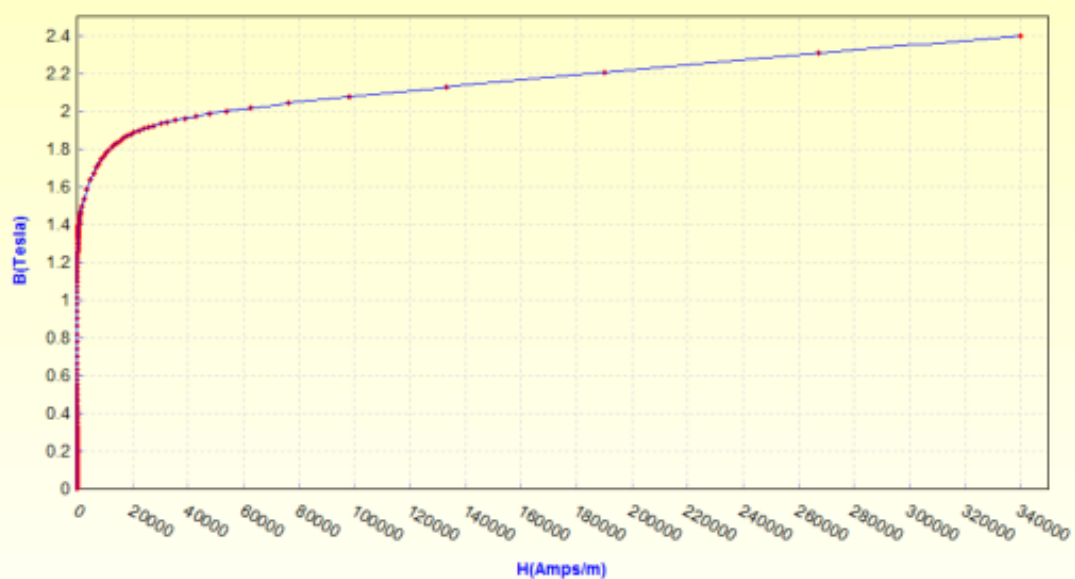


Notes The material data and demagnetization curves shown above represent typical properties that may vary due to product shape and size. Demagnetization curves show nominal Br and minimum H_{CI}. Magnets can be supplied thermally stabilized or magnetically calibrated to customer specifications. Additional grades are available. Please contact the factory for information.

Grade EN 10106	Thickness mm	Maximum specific total loss at 50 Hz		Minimum magnetic polarization at 50 Hz		
		$\hat{J} = 1,5 \text{ T}$ W/kg	1,0 T** W/kg	$\hat{H} = 2500$ T	5000 T	10000 A/m T
M235-35A	0,35	2,35	0,95	1,49	1,60	1,70
M250-35A	0,35	2,50	1,00	1,49	1,60	1,70
M270-35A	0,35	2,70	1,10	1,49	1,60	1,70
M300-35A	0,35	3,00	1,20	1,49	1,60	1,70
M330-35A	0,35	3,30	1,30	1,49	1,60	1,70
M700-35A*	0,35	7,00	3,00	1,60	1,69	1,77
M250-50A	0,50	2,50	1,05	1,49	1,60	1,70
M270-50A	0,50	2,70	1,10	1,49	1,60	1,70
M290-50A	0,50	2,90	1,15	1,49	1,60	1,70
M310-50A	0,50	3,10	1,25	1,49	1,60	1,70
M330-50A	0,50	3,30	1,35	1,49	1,60	1,70
M350-50A	0,50	3,50	1,50	1,50	1,60	1,70
M400-50A	0,50	4,00	1,70	1,53	1,63	1,73
M470-50A	0,50	4,70	2,00	1,54	1,64	1,74
M530-50A	0,50	5,30	2,30	1,56	1,65	1,75
M600-50A	0,50	6,00	2,60	1,57	1,66	1,76
M700-50A	0,50	7,00	3,00	1,60	1,69	1,77
M800-50A	0,50	8,00	3,60	1,60	1,70	1,78
M940-50A	0,50	9,40	4,20	1,62	1,72	1,81
M310-65A	0,65	3,10	1,25	1,49	1,60	1,70
M330-65A	0,65	3,30	1,35	1,49	1,60	1,70
M350-65A	0,65	3,50	1,50	1,49	1,60	1,70
M400-65A	0,65	4,00	1,70	1,52	1,62	1,72
M470-65A	0,65	4,70	2,00	1,53	1,63	1,73
M530-65A	0,65	5,30	2,30	1,54	1,64	1,74
M600-65A	0,65	6,00	2,60	1,56	1,66	1,76
M700-65A	0,65	7,00	3,00	1,57	1,67	1,76
M800-65A	0,65	8,00	3,60	1,60	1,70	1,78
M1000-65A	0,65	10,00	4,40	1,61	1,71	1,80
M600-100A	1,00	6,00	2,60	1,53	1,63	1,72
M700-100A	1,00	7,00	3,00	1,54	1,64	1,73
M800-100A	1,00	8,00	3,60	1,56	1,66	1,75
M1000-100A	1,00	10,00	4,40	1,58	1,68	1,76

* This grade does not appear in the standard EN 10106.

** The values of losses at 1,0 T are given as indicative.



REFERENCE

- [1] A. T. de Almeida, F. J. T. E. Ferreira, and J. A. C. Fong, "Standards for Efficiency of Electric Motors," *Industry Applications Magazine, IEEE*, vol. 17, pp. 12-19, 2011.
- [2] M. Ehsani, Y. Gao, and A. Emadi, *Modern Electric Hybrid Electric, and Fuel Cell Vehicles - Fundamentals, Theory and Design*, 2010.
- [3] Amsterdam Roundtables Foundation and M. Company, "Electric vehicles in Europe: gearing up for a new phase?," 2012.
- [4] "The European Economic Recovery Plan," E. Commission, Ed., ed, Dec. 2008.
- [5] ENERGY.GOV, "DOE Announces \$15 Million to Accelerate the Deployment of Energy Efficient Transportation Technologies," ed, 2016.
- [6] J. Hildermeier, "Electric Vehicles in Europe - approaching adolescence," Clean Vehicles and E-mobility Transport & Environment 2016.
- [7] N. Lutsey. (Sep, 2015, Transition to a global zero-emission vehicle fleet: a collaborative agenda for governments.
- [8] J. Chu. (2015, RE 100 - china's fast track to a renewable future.
- [9] c. a. driver. Hybrid and Electric Cars 2016-2017: The Best and the Rest [Online]. Available: <http://www.caranddriver.com/best-hybrid-electric-cars>
- [10] J. Parnell. (Dec 06, 2013, Obama sets 20% renewables target for US government by 2020. Available: http://www.pv-tech.org/news/obama_sets_20_renewables_target_for_us_government_by_2020
- [11] *Energy density*. Available: https://en.wikipedia.org/wiki/Energy_density
- [12] A. T. d. Almeida, F. J. T. E. Ferreira, and J. A. C. Fong, "Standards for Super-Premium Efficiency class for electric motors," in *Conference Record 2009 IEEE Industrial & Commercial Power Systems Technical Conference*, 2009, pp. 1-8.
- [13] C. J. Ifedi, B. C. Mecrow, S. T. M. Brockway, G. S. Boast, G. J. Atkinson, and D. Kostic-Perovic, "Fault-Tolerant In-Wheel Motor Topologies for High-Performance Electric Vehicles," *IEEE Transactions on Industry Applications*, vol. 49, pp. 1249-1257, 2013.
- [14] A. Fraser. IN-WHEEL ELECTRIC MOTORS - The Packaging and Integration Challenges.
- [15] A. T. D. Almeida, F. J. T. E. Ferreira, and A. Q. Duarte, "Technical and Economical Considerations on Super High-Efficiency Three-Phase Motors," *IEEE Transactions on Industry Applications*, vol. 50, pp. 1274-1285, 2014.
- [16] Long-Term Global Warming Trend Continues [Online]. Available: <http://earthobservatory.nasa.gov/IOTD/view.php?id=80167>
- [17] Global Temperatures [Online]. Available: <http://earthobservatory.nasa.gov/Features/WorldOfChange/decadaltemp.php>
- [18] V. Ramanathan and Y. Feng, "Air pollution, greenhouse gases and climate change: Global and regional perspectives," *Elsevier*, 2008.
- [19] N. Brown. The Tesla Model S Is Almost Maintenance Free [Online]. Available: <http://cleantechnica.com/2013/09/27/tesla-model-s-almost-maintenance-free/>
- [20] a. v. t. activity. How Do Gasoline & Electric Vehicles Compare?
- [21] The EV Wedge: How Electric Vehicle Fuel Savings Vary By Country (and car). Available: <http://shrinkthatfootprint.com/electric-vehicle-fuel-savings>

- [22] M. Lavelle. (2012, How to Compare the Cost of Electric and Gas Cars. Available: <http://energyblog.nationalgeographic.com/2012/10/01/how-to-compare-the-cost-of-electric-and-gas-cars/>
- [23] J. CHU. (Sep, 2015, Electric Vehicle vs. Gas vs. Hybrid Cars: A Comparison of Maintenance, Fuel, Insurance and Other Costs. Available: <https://www.nerdwallet.com/blog/loans/electric-hybrid-gas-how-they-compare-costs-2015/>
- [24] A. M. El-Refaie, "Motors/generators for traction/propulsion applications: A review," *IEEE Vehicular Technology Magazine*, vol. 8, pp. 90-99, 2013.
- [25] U. o. C. scientists, "Cleaner Cars from Cradle to Grave - How Electric Cars Beat Gasoline Cars on Lifetime Global Warming Emissions," 2016.
- [26] D. Norman. (Feb, 2014, What Noise Does the Electric Car Make?
- [27] The sound of silence [Online]. Available: <http://www.economist.com/node/13606446>
- [28] Government incentives for plug-in electric vehicles [Online]. Available: https://en.wikipedia.org/wiki/Government_incentives_for_plug-in_electric_vehicles
- [29] S. EVANS. (2015, Electric vehicle batteries 'already cheaper than 2020 projections'.
- [30] K. Bullis. (2015, Why We Don't Have Battery Breakthroughs. Available: <https://www.technologyreview.com/s/534866/why-we-dont-have-battery-breakthroughs/>
- [31] M. Green. (2015, New Study Reveals When, Where and How Much Motorists Drive. Available: <http://newsroom.aaa.com/2015/04/new-study-reveals-much-motorists-drive/>
- [32] D. J. v. Schalkwyk and M. J. Kamper, "Effect of Hub Motor Mass on Stability and Comfort of Electric Vehicles," in *2006 IEEE Vehicle Power and Propulsion Conference*, 2006, pp. 1-6.
- [33] M. Anderson and D. Harty. Unsprung mass with in-wheel motors - myths and realities.
- [34] C. C. Chan, "The state of the art of electric and hybrid vehicles," *Proceedings of the IEEE*, vol. 90, pp. 247-275, 2002.
- [35] G. Goetchius. (2011) Leading the Charge – The Future of Electric Vehicle Noise Control. *The Noise and Vibration Control Magazine*.
- [36] C. Hilton, "the effects of torque ripple from a wheel motor ", S. Yang, Ed., ed: Protean Ltd., 2016.
- [37] D. K. Perovic, "Making the Impossible, Possible – Overcoming the Design Challenges of In Wheel Motors," 2010.
- [38] G. Liu, J. Yang, W. Zhao, J. Ji, Q. Chen, and W. Gong, "Design and Analysis of a New Fault-Tolerant Permanent-Magnet Vernier Machine for Electric Vehicles," *IEEE Transactions on Magnetics*, vol. 48, pp. 4176-4179, 2012.
- [39] Q. Chen, G. Liu, J. Yang, W. Gong, and W. Zhao, "Comparison Of Two Interior Permanent-Magnet Motors With Improved Fault-Tolerance," in *IECON 2012 - 38th Annual Conference on IEEE Industrial Electronics Society*, 2012, pp. 4093-4098.
- [40] Q. Chen, G. Liu, L. Sun, Y. Jiang, and J. Yang, "Comparison of five topologies rotor permanent magnet motors with improved fault-tolerance," in *Industrial Electronics (ISIE), 2013 IEEE International Symposium on*, 2013, pp. 1-5.

- [41] J. Wang, K. Atallah, Z. Q. Zhu, and D. Howe, "Modular Three-Phase Permanent-Magnet Brushless Machines for In-Wheel Applications," *IEEE Transactions on Vehicular Technology*, vol. 57, pp. 2714-2720, 2008.
- [42] A. M. E.-. Refaie and T. M. Jahns, "Optimal flux weakening in surface PM machines using fractional-slot concentrated windings," *IEEE Transactions on Industry Applications*, vol. 41, pp. 790-800, 2005.
- [43] C. J. Ifedi, B. C. Mecrow, S. T. M. Brockway, G. S. Boast, G. J. Atkinson, and D. Kostic-Perovic, "Fault-Tolerant In-Wheel Motor Topologies for High-Performance Electric Vehicles," *Industry Applications, IEEE Transactions on*, vol. 49, pp. 1249-1257, 2013.
- [44] C. J. Ifedi, "A HIGH TORQUE DENSITY, DIRECT DRIVE IN-WHEEL MOTOR FOR ELECTRIC VEHICLES," Ph.D., EEE school, newcastle university, 2013.
- [45] G. Pellegrino, A. Vagati, B. Boazzo, and P. Guglielmi, "Comparison of Induction and PM Synchronous Motor Drives for EV Application Including Design Examples," *IEEE Transactions on Industry Applications*, vol. 48, pp. 2322-2332, 2012.
- [46] S. Williamson, M. Lukic, and A. Emadi, "Comprehensive drive train efficiency analysis of hybrid electric and fuel cell vehicles based on motor-controller efficiency modeling," *IEEE Transactions on Power Electronics*, vol. 21, pp. 730-740, 2006.
- [47] J. Gieras, *Advancements in Electric Machines*: Springer Science & Business Media, 2008.
- [48] F. Caricchi, F. Crescimbeni, E. Fedeli, and G. Noioa, "Design and construction of a wheel-directly-coupled axial-flux PM motor prototype for EVs," in *Proceedings of 1994 IEEE Industry Applications Society Annual Meeting*, 1994, pp. 254-261 vol.1.
- [49] (2016). *Protean Electric Announces Manufacturing in China's Tianjin Binhai Hi-Tech Industrial Development Area*. Available: <http://www.proteanelectric.com/protean-electric-announces-manufacturing-in-chinas-tianjin-binhai-hi-tech-industrial-development-area/>
- [50] *Protean Electric Ltd*. Available: <http://www.proteanelectric.com/>
- [51] *elaphe in-wheel motor*. Available: <http://in-wheel.com/>
- [52] *ECOMOVE*. Available: <http://ecomove.dk/>
- [53] S. P. Nikam, V. Rallabandi, and B. G. Fernandes, "A High-Torque-Density Permanent-Magnet Free Motor for in-Wheel Electric Vehicle Application," *IEEE Transactions on Industry Applications*, vol. 48, pp. 2287-2295, 2012.
- [54] R. Madhavan and B. G. Fernandes, "Axial Flux Segmented SRM With a Higher Number of Rotor Segments for Electric Vehicles," *IEEE Transactions on Energy Conversion*, vol. 28, pp. 203-213, 2013.
- [55] Z. Q. Zhu and D. Evans, "Overview of recent advances in innovative electrical machines — With particular reference to magnetically geared switched flux machines," in *2014 17th International Conference on Electrical Machines and Systems (ICEMS)*, 2014, pp. 1-10.
- [56] Y. Maeda, T. Kosaka, and N. Matsui, "Design study on hybrid excitation flux switching motor with permanent magnet placed at middle of field coil slot for HEV drives," in *2016 XXII International Conference on Electrical Machines (ICEM)*, 2016, pp. 2522-2528.
- [57] Y. Tang, J. J. H. Paulides, and E. A. Lomonova, "Automated design of DC-excited flux-switching in-wheel motor using magnetic equivalent circuits," in *Ecological*

- Vehicles and Renewable Energies (EVER), 2014 Ninth International Conference on*, 2014, pp. 1-10.
- [58] M. R. Harris, G. H. Pajooman, and S. M. A. Sharkh, "The problem of power factor in VRPM (transverse-flux) machines," in *Electrical Machines and Drives, 1997 Eighth International Conference on (Conf. Publ. No. 444)*, 1997, pp. 386-390.
 - [59] Y. S. Hsu and M. C. Tsai, "Development of a Novel Transverse Flux Wheel Motor," *IEEE Transactions on Magnetics*, vol. 47, pp. 3677-3680, 2011.
 - [60] M. Zeraoulia, M. E. H. Benbouzid, and D. Diallo, "Electric Motor Drive Selection Issues for HEV Propulsion Systems: A Comparative Study," *Vehicular Technology, IEEE Transactions on*, vol. 55, pp. 1756-1764, 2006.
 - [61] M. Hodowanec and W. R. Finley, "Copper versus aluminum-which construction is best? [induction motor rotors]," *Industry Applications Magazine, IEEE*, vol. 8, pp. 14-25, 2002.
 - [62] J. Goss, M. Popescu, and D. Staton, "A comparison of an interior permanent magnet and copper rotor induction motor in a hybrid electric vehicle application," in *Electric Machines & Drives Conference (IEMDC), 2013 IEEE International*, 2013, pp. 220-225.
 - [63] A. Goodrich. Selection of Rotor Material for Industrial Induction Motors: The Case for Copper.
 - [64] D. G. Dorrell, A. M. Knight, M. Popescu, L. Evans, and D. A. Staton, "Comparison of different motor design drives for hybrid electric vehicles," in *Energy Conversion Congress and Exposition (ECCE), 2010 IEEE*, 2010, pp. 3352-3359.
 - [65] M. G. Say, *Alternating Current Machines*. London, United Kingdom: January 1, 1976, 1976.
 - [66] T. A. Lipo, *Introduction to AC machine design*. University of Wisconsin-Madison, 2004.
 - [67] P. Mishra and S. Saha, "Design modeling and simulation of low voltage squirrel cage induction motor for medium weight electric vehicle," in *Advances in Computing, Communications and Informatics (ICACCI), 2013 International Conference on*, 2013, pp. 1697-1704.
 - [68] F. F. a. X. Tang, *Induction machine design handbook*: China Machine Press, 2002.
 - [69] I. Boldea and S. A. Nasar, *The induction machines design handbook*, 2nd ed. Boca Raton, FL: CRC Press/Taylor & Francis, 2010.
 - [70] J. Pyrhönen, T. Jokinen, and V. Hrabovcová, *Design of rotating electrical machines*, Second edition. ed. Chichester: Wiley, 2014.
 - [71] C. M. Spargo, B. C. Mecrow, J. D. Widmer, and C. Morton, "Application of Fractional-Slot Concentrated Windings to Synchronous Reluctance Motors," *Industry Applications, IEEE Transactions on*, vol. 51, pp. 1446-1455, 2015.
 - [72] A. M. El-Refaie and M. R. Shah, "Comparison of Induction Machine Performance with Distributed and Fractional-Slot Concentrated Windings," in *Industry Applications Society Annual Meeting, 2008. IAS '08. IEEE*, 2008, pp. 1-8.
 - [73] A. S. Abdel-Khalik and S. Ahmed, "Performance Evaluation of a Five-Phase Modular Winding Induction Machine," *Industrial Electronics, IEEE Transactions on*, vol. 59, pp. 2654-2669, 2012.
 - [74] B. Virlan, S. Benelghali, A. Munteanu, A. Simion, and R. Outbib, "Multi-speed induction motor for direct drive applications," in *Electrical Machines (ICEM), 2012 XXth International Conference on*, 2012, pp. 1928-1934.
 - [75] K. Ki-Chan, K. Kwangsoo, K. Hee-jun, and L. Ju, "Demagnetization Analysis of Permanent Magnets According to Rotor Types of Interior Permanent Magnet

- Synchronous Motor," *Magnetics, IEEE Transactions on*, vol. 45, pp. 2799-2802, 2009.
- [76] W. Aimeng, J. Yihua, and W. L. Soong, "Comparison of Five Topologies for an Interior Permanent-Magnet Machine for a Hybrid Electric Vehicle," *Magnetics, IEEE Transactions on*, vol. 47, pp. 3606-3609, 2011.
- [77] M. Kamiya, "Development of Traction Drive Motors for the Toyota Hybrid System," *IEEJ Transactions on Industry Applications, Volume 126, Issue 4*, pp. 473-479 (2006). 2006.
- [78] K.-j. Lee, K. Kim, S. Kim, J.-S. Ahn, S. Lim, and L. Ju, "Optimal magnet shape to improve torque characteristics of interior permanent magnet synchronous motor," *Journal of Applied Physics*, vol. 97, pp. 10Q505-10Q505-3, 2005.
- [79] D. Evans, Z. Azar, L. J. Wu, and Z. Q. Zhu, "Comparison of optimal design and performance of PM machines having non-overlapping windings and different rotor topologies," in *Power Electronics, Machines and Drives (PEMD 2010), 5th IET International Conference on*, 2010, pp. 1-7.
- [80] K. Yamazaki, M. Kumagai, T. Ikemi, and S. Ohki, "A Novel Rotor Design of Interior Permanent-Magnet Synchronous Motors to Cope with Both Maximum Torque and Iron-Loss Reduction," *Industry Applications, IEEE Transactions on*, vol. 49, pp. 2478-2486, 2013.
- [81] S. Ishii, Y. Hasegawa, K. Nakamura, and O. Ichinokura, "Characteristics of novel flux barrier type outer rotor IPM motor with rare-earth and ferrite magnets," in *Renewable Energy Research and Applications (ICRERA), 2012 International Conference on*, 2012, pp. 1-4.
- [82] S. Y. Lim and L. Ju, "A design for improved performance of interior permanent magnet synchronous motor for hybrid electric vehicle," *Journal of Applied Physics*, vol. 99, pp. 08R308-08R308-3, 2006.
- [83] D. G. Dorrell, H. Min-Fu, and A. M. Knight, "Alternative Rotor Designs for High Performance Brushless Permanent Magnet Machines for Hybrid Electric Vehicles," *Magnetics, IEEE Transactions on*, vol. 48, pp. 835-838, 2012.
- [84] F. Chaaban, "Determination of the optimum rotor-stator diameter ratio of permanent magnet machines," *Electric Power Applications*, 1994.
- [85] J. D. Ede, Z. Q. Zhu, and D. Howe, "Optimal split ratio for high-speed permanent magnet brushless DC motors," in *Electrical Machines and Systems, 2001. ICEMS 2001. Proceedings of the Fifth International Conference on*, 2001, pp. 909-912 vol.2.
- [86] S. Yang and Z. Q. Zhu, "Analytical Prediction of Optimal Split Ratio for Fractional-Slot External Rotor PM Brushless Machines," *Magnetics, IEEE Transactions on*, vol. 47, pp. 4187-4190, 2011.
- [87] J. Kennedy and R. Eberhart, "Particle swarm optimization," in *Neural Networks, 1995. Proceedings., IEEE International Conference on*, 1995, pp. 1942-1948 vol.4.
- [88] M. L. Eckart Zitzler, and Stefan Bleuler. A tutorial on evolutionary multiobjective optimization.
- [89] N. Bianchi and S. Bolognani, "Design optimisation of electric motors by genetic algorithms," *Electric Power Applications, IEE Proceedings -*, vol. 145, pp. 475-483, 1998.
- [90] M. Ashabani, Y. A. R. I. Mohamed, and J. Milimonfared, "Optimum Design of Tubular Permanent-Magnet Motors for Thrust Characteristics Improvement by Combined Taguchi–Neural Network Approach," *Magnetics, IEEE Transactions on*, vol. 46, pp. 4092-4100, 2010.

- [91] L. F. ALVAREZ, "design optimisation based on genetic programming," PhD., department of civil and environmental engineering, University of bradford UK, 2000.
- [92] K. Yamazaki, M. Kumagai, T. Ikemi, and S. Ohki, "A Novel Rotor Design of Interior Permanent-Magnet Synchronous Motors to Cope with Both Maximum Torque and Iron-Loss Reduction," *IEEE Transactions on Industry Applications*, vol. 49, pp. 2478-2486, 2013.
- [93] J. S. Hsu;, C. W. Ayers;, and C. L. Coomer, "Report on toyota/Prius motor design and manufacturing assessment," Oak Ridge National Laboratory2004.
- [94] K. Sung-Il, C. Jinwoo, P. Sunghyuk, P. Taesang, and L. Seongtaek, "Characteristics Comparison of a Conventional and Modified Spoke-Type Ferrite Magnet Motor for Traction Drives of Low-Speed Electric Vehicles," *Industry Applications, IEEE Transactions on*, vol. 49, pp. 2516-2523, 2013.
- [95] C. Qian, L. Guohai, Z. Wenxiang, S. Longgang, S. Mingming, and L. Zhengmeng, "Design and Comparison of Two Fault-Tolerant Interior-Permanent-Magnet Motors," *Industrial Electronics, IEEE Transactions on*, vol. 61, pp. 6615-6623, 2014.
- [96] W. Q. Chu and Z. Q. Zhu, "On-Load Cogging Torque Calculation in Permanent Magnet Machines," *Magnetics, IEEE Transactions on*, vol. 49, pp. 2982-2989, 2013.
- [97] W. Q. Chu and Z. Q. Zhu, "Average Torque Separation in Permanent Magnet Synchronous Machines Using Frozen Permeability," *Magnetics, IEEE Transactions on*, vol. 49, pp. 1202-1210, 2013.
- [98] S. Yang, N. J. Baker, B. C. Mecrow, C. Hilton, G. Sooriyakumar, D. Kostic-Perovic, *et al.*, "Cost reduction of a permanent magnet in-wheel electric vehicle traction motor," in *Electrical Machines (ICEM), 2014 International Conference on*, 2014, pp. 443-449.
- [99] J. B. Kim, K. Y. Hwang, and B. I. Kwon, "Optimization of Two-Phase In-Wheel IPMSM for Wide Speed Range by Using the Kriging Model Based on Latin Hypercube Sampling," *Magnetics, IEEE Transactions on*, vol. 47, pp. 1078-1081, 2011.
- [100] R. Akaki, Y. Takahashi, K. Fujiwara, M. Matsushita, N. Takahashi, and M. Morita, "Effect of Magnetic Property in Bridge Area of IPM Motors on Torque Characteristics," *Magnetics, IEEE Transactions on*, vol. 49, pp. 2335-2338, 2013.
- [101] Z. Wenliang, Z. Fei, T. A. Lipo, and K. Byung-il, "Optimal Design of a Novel V-Type Interior Permanent Magnet Motor with Assisted Barriers for the Improvement of Torque Characteristics," *Magnetics, IEEE Transactions on*, vol. 50, pp. 1-4, 2014.
- [102] K. Ki-Chan, L. Ju, K. Hee Jun, and K. Dae-Hyun, "Multiobjective Optimal Design for Interior Permanent Magnet Synchronous Motor," *Magnetics, IEEE Transactions on*, vol. 45, pp. 1780-1783, 2009.
- [103] adhesive - LOCTITE AA 326 [Online]. Available: <http://www.loctite.co.uk/loctite-4087.htm?nodeid=8802624110593>
- [104] S. Yang, N. J. Baker, B. C. Mecrow, D. Smith, G. Atkinson, C. Hilton, *et al.*, "Magnet Losses and Demagnetisation in a Permanent Magnet In-wheel Electric Vehicle Traction Motor," presented at the IEMDC 2015, Idaho, USA, 2015.
- [105] T. J. Juha Pyrhonen, Valeria Hrabovcova, "Design of Rotating Electrical Machines," ed, 2008, pp. 105-122.

- [106] A. M. El-Refaie, "Fractional-Slot Concentrated-Windings Synchronous Permanent Magnet Machines: Opportunities and Challenges," *Industrial Electronics, IEEE Transactions on*, vol. 57, pp. 107-121, 2010.
- [107] N. Bianchi and E. Fornasiero, "Impact of MMF Space Harmonic on Rotor Losses in Fractional-Slot Permanent-Magnet Machines," *Energy Conversion, IEEE Transactions on*, vol. 24, pp. 323-328, 2009.
- [108] K. Yamazaki and A. Abe, "Loss Investigation of Interior Permanent-Magnet Motors Considering Carrier Harmonics and Magnet Eddy Currents," *Industry Applications, IEEE Transactions on*, vol. 45, pp. 659-665, 2009.
- [109] C. J. Ifedi, "A high torque density, direct drive in-wheel motor for electric vehicles," Ph.D., Electrical and electronic engineering, Newcastle university, 2013.
- [110] J. Blum, J. Merwerth, and H. G. Herzog, "Magnet eddy-current losses in interior permanent magnet machines with concentrated windings - analysis and reduction of the major source," in *Power Electronics, Machines and Drives (PEMD 2014), 7th IET International Conference on*, 2014, pp. 1-6.
- [111] Z. Azar, L. J. Wu, D. Evans, and Z. Q. Zhu, "Influence of rotor configuration on iron and magnet losses of fractional-slot IPM machines," in *Power Electronics, Machines and Drives (PEMD 2010), 5th IET International Conference on*, 2010, pp. 1-6.
- [112] G. J. Atkinson, "HIGH POWER FAULT TOLERANT MOTORS FOR AEROSPACE APPLICATIONS," Ph.D., Electrical and electronic engineering school, Newcastle university, 2007.
- [113] R. L. Stoll, *The analysis of eddy currents*: Clarendon Press, 1974.
- [114] D. J. B. Smith, "HIGH SPEED HIGH POWER ELECTRICAL MACHINES," Ph.D., Electrical and electronic engineering, Newcastle University, 2014.
- [115] B. Aslan, E. Semail, and J. Legranger, "General Analytical Model of Magnet Average Eddy-Current Volume Losses for Comparison of Multiphase PM Machines With Concentrated Winding," *Energy Conversion, IEEE Transactions on*, vol. 29, pp. 72-83, 2014.
- [116] M. Mirzaei, A. Binder, B. Funieru, and M. Susic, "Analytical Calculations of Induced Eddy Currents Losses in the Magnets of Surface Mounted PM Machines With Consideration of Circumferential and Axial Segmentation Effects," *Magnetics, IEEE Transactions on*, vol. 48, pp. 4831-4841, 2012.
- [117] H. Wan-Ying, A. Bettayeb, R. Kaczmarek, and J. C. Vannier, "Optimization of Magnet Segmentation for Reduction of Eddy-Current Losses in Permanent Magnet Synchronous Machine," *Energy Conversion, IEEE Transactions on*, vol. 25, pp. 381-387, 2010.
- [118] B. C. Mecrow, A. G. Jack, D. J. Atkinson, S. R. Green, G. J. Atkinson, A. King, *et al.*, "Design and testing of a four-phase fault-tolerant permanent-magnet machine for an engine fuel pump," *Energy Conversion, IEEE Transactions on*, vol. 19, pp. 671-678, 2004.
- [119] D. J. Atkinson, S. Green, B. C. Mecrow, A. G. Jack, and J. R. Coles, "Fault tolerant fuel pump drives for the all electric aircraft," in *All Electric Aircraft (Digest No. 1998/260), IEE Colloquium on*, 1998, pp. 1/1-1/6.
- [120] T. A. Lipo, *Analysis of Synchronous Machines*, June 25, 2012.
- [121] Y. S. Chen, Z. Q. Zhu, and D. Howe, "Calculation of d- and q-axis inductances of PM brushless ac machines accounting for skew," *Magnetics, IEEE Transactions on*, vol. 41, pp. 3940-3942, 2005.

- [122] *The user manual of MagNet from Infolytica Corporation.* Available: <http://www.infolytica.com/secured/customer/elite/livedocs/MagNet/#06-Coils/USC-OutputCharacteristics/Inductance.htm?Highlight=inductance>
- [123] C. R. Sullivan, "Computationally efficient winding loss calculation with multiple windings, arbitrary waveforms, and two-dimensional or three-dimensional field geometry," *Power Electronics, IEEE Transactions on*, vol. 16, pp. 142-150, 2001.
- [124] *Arnold Magnetics Technologies.* Available: <http://www.arnoldmagnetics.com/en-us/>
- [125] W. Jiabin, K. Atallah, Z. Q. Zhu, and D. Howe, "Modular Three-Phase Permanent-Magnet Brushless Machines for In-Wheel Applications," *Vehicular Technology, IEEE Transactions on*, vol. 57, pp. 2714-2720, 2008.
- [126] N. Bianchi, S. Bolognani, Pre, x, M. D., and G. Grezzani, "Design considerations for fractional-slot winding configurations of synchronous machines," *Industry Applications, IEEE Transactions on*, vol. 42, pp. 997-1006, 2006.
- [127] R. Dutta, L. Chong, and M. F. Rahman, "Design and Experimental Verification of an 18-Slot/14-pole Fractional-Slot Concentrated Winding Interior Permanent Magnet Machine," *Energy Conversion, IEEE Transactions on*, vol. 28, pp. 181-190, 2013.
- [128] A. M. El-Refaie and T. M. Jahns, "Optimal flux weakening in surface PM machines using fractional-slot concentrated windings," *Industry Applications, IEEE Transactions on*, vol. 41, pp. 790-800, 2005.
- [129] P. B. Reddy, A. M. E.-. Refaie, and K. K. Huh, "Effect of Number of Layers on Performance of Fractional-Slot Concentrated-Windings Interior Permanent Magnet Machines," *IEEE Transactions on Power Electronics*, vol. 30, pp. 2205-2218, 2015.
- [130] A. M. El-Refaie and T. M. Jahns, "Impact of Winding Layer Number and Magnet Type on Synchronous Surface PM Machines Designed for Wide Constant-Power Speed Range Operation," *IEEE Transactions on Energy Conversion*, vol. 23, pp. 53-60, 2008.
- [131] W. Jiabin, V. I. Patel, and W. Weiya, "Fractional-Slot Permanent Magnet Brushless Machines with Low Space Harmonic Contents," *Magnetics, IEEE Transactions on*, vol. 50, pp. 1-9, 2014.
- [132] L. Alberti and N. Bianchi, "Theory and Design of Fractional-Slot Multilayer Windings," *Industry Applications, IEEE Transactions on*, vol. 49, pp. 841-849, 2013.
- [133] P. B. Reddy, H. Kum-Kang, and A. M. El-Refaie, "Generalized Approach of Stator Shifting in Interior Permanent-Magnet Machines Equipped With Fractional-Slot Concentrated Windings," *Industrial Electronics, IEEE Transactions on*, vol. 61, pp. 5035-5046, 2014.
- [134] H. Seok-Hee, T. M. Jahns, and W. L. Soong, "Torque Ripple Reduction in Interior Permanent Magnet Synchronous Machines Using the Principle of Mutual Harmonics Exclusion," in *Industry Applications Conference, 2007. 42nd IAS Annual Meeting. Conference Record of the 2007 IEEE*, 2007, pp. 558-565.
- [135] M. Barcaro and N. Bianchi, "Torque ripple reduction in fractional-slot Interior PM machines optimizing the flux-barrier geometries," in *Electrical Machines (ICEM), 2012 XXth International Conference on*, 2012, pp. 1496-1502.
- [136] C. M. Spargo, B. C. Mecrow, and J. D. Widmer, "A Seminumerical Finite-Element Postprocessing Torque Ripple Analysis Technique for Synchronous Electric Machines Utilizing the Air-Gap Maxwell Stress Tensor," *Magnetics, IEEE Transactions on*, vol. 50, pp. 1-9, 2014.

- [137] H. Seok-Hee, T. M. Jahns, W. L. Soong, M. K. Guven, and M. S. Illindala, "Torque Ripple Reduction in Interior Permanent Magnet Synchronous Machines Using Stators With Odd Number of Slots Per Pole Pair," *Energy Conversion, IEEE Transactions on*, vol. 25, pp. 118-127, 2010.
- [138] H. Schilp, P. Schlag, M. Kohnh, x00E, and user, "Optimized handling of permanent magnets within the mass production of electric traction drives," in *Electric Drives Production Conference (EDPC), 2013 3rd International*, 2013, pp. 1-6.
- [139] S. Yang, B. C. Mecrow, N. J. Baker, C. Hilton, D. K. Perovic, and I. Kakavas, "Torque ripple reduction in fractional-slot concentrated-winding machines with saliency," presented at the PEMD2016, Glasgow, 2016.
- [140] T. J. Juha Pyrhonen, Valeria Hrabovcova, *Design of Rotating Electrical Machines*: Wiley-Blackwell, 2008.
- [141] J. Jae-Woo, H. Jung-Pyo, and K. Young-Kyoun, "Characteristic Analysis and Comparison of IPMSM for HEV According to Pole and Slot Combination," in *Vehicle Power and Propulsion Conference, 2007. VPPC 2007. IEEE*, 2007, pp. 778-783.
- [142] W. Yawei, Q. Ronghai, and L. Jian, "Multilayer Windings Effect on Interior PM Machines for EV Applications," *Industry Applications, IEEE Transactions on*, vol. 51, pp. 2208-2215, 2015.
- [143] P. Ponomarev, I. Petrov, and J. Pyrhonen, "Influence of Travelling Current Linkage Harmonics on Inductance Variation, Torque Ripple and Sensorless Capability of Tooth-Coil Permanent-Magnet Synchronous Machines," *Magnetics, IEEE Transactions on*, vol. 50, pp. 1-8, 2014.
- [144] L. Sun-Kwon, K. Gyu-Hong, H. Jin, and K. Byoung-Woo, "Stator and Rotor Shape Designs of Interior Permanent Magnet Type Brushless DC Motor for Reducing Torque Fluctuation," *Magnetics, IEEE Transactions on*, vol. 48, pp. 4662-4665, 2012.
- [145] N. Saito, R. Kijima, and S. Shimomura, "The design method to minimize torque ripple in interior permanent magnet synchronous motor with concentrated winding," in *Power Electronics Conference (IPEC), 2010 International*, 2010, pp. 1293-1298.
- [146] Z. Azar, Z. Q. Zhu, and G. Ombach, "Influence of Electric Loading and Magnetic Saturation on Cogging Torque, Back-EMF and Torque Ripple of PM Machines," *Magnetics, IEEE Transactions on*, vol. 48, pp. 2650-2658, 2012.
- [147] A. M. Knight, R. E. Betz, and D. G. Dorrell, "Design and Analysis of Brushless Doubly Fed Reluctance Machines," *Industry Applications, IEEE Transactions on*, vol. 49, pp. 50-58, 2013.
- [148] K. Ikuta, S. Makita, and S. Arimoto, "Non-contact magnetic gear for micro transmission mechanism," in *Micro Electro Mechanical Systems, 1991, MEMS '91, Proceedings. An Investigation of Micro Structures, Sensors, Actuators, Machines and Robots. IEEE*, 1991, pp. 125-130.
- [149] K. Atallah and D. Howe, "A novel high-performance magnetic gear," *Magnetics, IEEE Transactions on*, vol. 37, pp. 2844-2846, 2001.
- [150] Z. Z. Wu and Z. Q. Zhu, "Analysis of Air-Gap Field Modulation and Magnetic Gearing Effects in Switched Flux Permanent Magnet Machines," *Magnetics, IEEE Transactions on*, vol. 51, pp. 1-12, 2015.
- [151] M. S. Islam, R. Islam, and T. Sebastian, "Experimental Verification of Design Techniques of Permanent-Magnet Synchronous Motors for Low-Torque-Ripple

- Applications," *Industry Applications, IEEE Transactions on*, vol. 47, pp. 88-95, 2011.
- [152] J. Y. Hung and Z. Ding, "Design of currents to reduce torque ripple in brushless permanent magnet motors," *Electric Power Applications, IEE Proceedings B*, vol. 140, pp. 260-266, 1993.
- [153] J. Ofori-Tenkorrang and J. H. Lang, "A comparative analysis of torque production in Halbach and conventional surface-mounted permanent-magnet synchronous motors," in *Industry Applications Conference, 1995. Thirtieth IAS Annual Meeting, IAS '95., Conference Record of the 1995 IEEE*, 1995, pp. 657-663 vol.1.
- [154] F. S. LIMITED. (2011, Space Vector Pulse Width Modulation.
- [155] Dave. Atkinson. (2012, Control of Electric Drives.
- [156] P. D.-I. R. Kennel, "Power Electronics Exercise: Space Vector Modulation," 2012.